Understanding Advanced Materials for Solar Panels: Interplay of Composition, Structure and Optoelectronic Properties in New Metal-Halide Semiconductors



Leonardo Rocco Vittorio Buizza

University College

University of Oxford

A thesis submitted for the degree of

Doctor of Philosophy

Trinity 2021

Acknowledgements

First, I would like to thank the Engineering and Physical Sciences Research Council Centre for Doctoral Training in New and Sustainable Photovoltaics, the Department of Physics at the University of Oxford, and the Oxford-Radcliffe Scholarship for their funding of my studentship.

I am truly grateful to my supervisor, **Professor Laura Herz**, who has taught me to become a better physicist and a better researcher, and I am thankful for her unerring guidance and mentorship. **Professor Michael Johnston** has also been kind and supportive, and I am thankful to him for all of the help and advice he has provided to me.

Thank you to those who have taught and inspired me along the path to studying physics and becoming a physicist: Stephen Brown, for his ability to make problem-solving and maths fun for a young child; Peter Sammut, for making me realise that studying physics at university was not just an option, but what I would love to do; and Robert Dillon, who made my undergraduate study of physics so fun.

Taking on the challenge of a PhD has been made far, far easier by the wonderful colleagues and friends I have had in the Herz/Johnston research group. A heartfelt thank you goes to: Alex Knight, Becky Milot, Chelsea Xia, Chris Davies, Djamshid Damry, Elisabeth Duijnstee, Hannah Eggimann, James Ball, Jay Patel, Juliane Borchert, Karim Elmestekawy, Kilian Lohmann, Kimberley Savill, Kun Peng, Marcello Righetto, Mathias Rothmann, Michael Trimpl, Robbie Oliver, Sabrina Sterzl, Silvia Motti, Tim Crothers and Vincent Lim. Thank you also to the great CDT-PV gang from C4, who have accompanied me all along the way these past four years.

I am particularly thankful to **Adam Wright**, whose hard work, careful attention to detail and incredibly high standards as a researcher have been an inspiring example to follow. I am also hugely grateful to **Harry Sansom**: exploring a family of totally undiscovered materials together has been an exciting, sometimes frustrating and yet wonderful experience. Finally, thank you to **Alex Ulatowski** for becoming a THz buddy, a brilliant lab-mate and a lovely friend.

Working towards a PhD is not a purely academic endeavour, and I have had a brilliant experience in Oxford alongside my research. A big thank you and hug must go to my housemates and friends over the years: Nik, Dan, Tash, Oli, Rellie, Bernd and Marko. Thank you to Univ for providing a friendly, supportive collegiate environment where it has been a pleasure to kick a football around with the MCR team, to row with UCBC, to quiz with Oli, Abi, Anisah and Willem (Up *Los Lelos*!), and to be a Convenor of the Martlets Society. Thank you also to the other close friends I've made along the way, who have been a wonderful bubble of support, kindness and 'brains trust' in times of need: Tom, Eli, Ben, Sam, James and Anna.

Finally, thank you to my family for understanding, supporting and loving me, throughout this PhD and beyond. **Ludzy**, you are silly, smart and sometimes highly frustrating, fulfilling every expectation of the role of younger brother. **Cat**, setting aside the occasional elder-sibling bout of stubbornness, you are forever inspiring as you drive towards the things you seek. Grazie **Mamma**, mi hai sempre capito perfettamente e sei un'ispirazione enorme; mi hai insegnato tantissimo, da come affrontare una sfida a come rispettare e capire le altre persone. **Papà**, grazie per i tuoi consigli e il tuo supporto, e per avermi seguito con cosi tanto affetto e attenzione. Vi amo un sacco. **Charlotte**, having you in my life fills it with happiness, joy and love, and I am so grateful for it.

Abstract

Interest in metal-halide semiconductors has risen rapidly over the past decade, notably due to the success of lead-halide perovskites in solar cells, whose efficiencies have risen to rival those of best-in-class commercial materials. Alongside this improvement in device-based performance, a detailed understanding of the underlying optoelectronic properties of such materials has developed, focusing on the most successful lead-halide perovskite materials. This thesis provides insights into how the composition and structure of such materials influence their optoelectronic properties, focusing especially on charge-carrier dynamics and transport. The materials investigated for this thesis all move beyond conventional lead-halide perovskites, pushing the boundaries of materials discovery and thus making a clear understanding of their fundamental properties crucial to their successful deployment in optoelectronic and energy applications.

Materials that combine the high charge-carrier lifetimes and mobilities, strong absorption, and good crystallinity of three-dimensional perovskites with the stability of two-dimensional perovskites are promising candidates for use in solar cells. To fully understand the optoelectronic properties of these 2D–3D hybrid perovskite systems, materials with general composition $BA_x(FA_{0.83}Cs_{0.17})_{1-x}Pb(I_{0.6}Br_{0.4})_3$ are investigated. Small amounts of butylammonium (BA) are found to help to improve crystallinity and passivate grain boundaries, reducing trap-mediated charge-carrier recombination and enhancing charge-carrier mobilities. For low amounts of BA, the benevolent effects of reduced recombination and enhanced mobilities yield charge-carrier diffusion lengths up to 7.7 µm, making these 2D-3D hybrid materials highly promising for solar-cell applications.

Due to concerns around the toxicity of lead, an interest in lead-free alternatives has developed in recent years, with a particular focus on silver-bismuth-halide materials. The optoelectronic properties of the lead-free semiconductor Cu_2AgBiI_6 are studied using temperature-dependent spectroscopy. Ultrafast charge-carrier localization effects are observed, evident from picosecond-scale THz photoconductivity decays and a rise in intensity with decreasing temperature of long-lived, highly Stokes-shifted photoluminescence. Together, these observations point towards strong charge-lattice couplings and the formation of small polaron states in Cu_2AgBiI_6. Intriguingly, similar charge-carrier localisation and temperature-activated hopping transport is also observed in the closely related double perovksite material $Cs_2AgBiBr_6$.

Finally, the charge-carrier dynamics and transport properties of five compositions along the $AgBiI_4$ – CuI solid solution line are investigated. Increasing copper content is found to enhance photoluminescence intensity and charge-carrier transport, and this is shown to derive from reduced cation disorder and improved electronic connectivity due to the presence of Cu^+. Further, increased Cu^+ content enhances the band curvature around the valence band maximum, resulting in lower charge-carrier effective masses, reduced exciton binding energies and higher mobilities. Ultrafast charge-carrier localisation is observed across all compositions investigated, lowering the charge-carrier mobility and leading to Langevin-like bimolecular recombination. Together with the above temperature-dependent results, these findings indicate that charge-carrier localisation is intrinsically linked to the presence of silver and bismuth in these materials, drawing a clear experimental link between the electronic dimension of a material and the likelihood of charge-carrier localisation taking place.

Contents

List of Publications vii

List of Abbreviations viii

1 Introduction 1

2 Background and Fundamentals 7

2.1 Introduction to Metal-Halide Perovskites . . . 8

2.1.1 Structure and Stoichiometry . . . 8

2.1.2 Optoelectronic Properties and Charge-Carrier Dynamics . . . 10

2.1.3 Double Perovskites and Novel Ag-Bi-I Materials . . . 14

2.1.4 The Importance of Electronic Dimension and Lone Pairs . . . 17

2.2 Polarons and Charge-Carrier Localisation in Metal-Halide Semiconductors . . . 19

2.2.1 Polaron theory: a brief introduction . . . 23

2.2.1.1 The 'large' polaron of Landau and Fröhlich . . . 23

2.2.1.2 The 'small' polaron . . . 26

2.2.1.3 Emin and Holstein's evaluation of polaronic regimes . . . 27

2.2.1.4 The role of dimension in charge-carrier localisation . . . 28

2.2.1.5 Applying polaron theory to metal-halide semiconductors 29

2.2.2 Polarons in metal-halide semiconductors . . . 31

2.2.2.1 Bulk three-dimensional metal-halide perovskites . . . 31

2.2.2.2 Perovskite nanocrystals . . . 36

2.2.2.3 Double perovskites . . . 38

2.2.2.4 Ruddlesden-Popper layered perovskites . . . 40

2.2.2.5 Non-perovskite metal-halide semiconductors . . . 45

2.2.2.6 Vacancy-ordered perovskites . . . 45

2.2.2.7 Quasi-zero dimensional metal-halides . . . 46

2.2.2.8 Other metal-halide semiconductors . . . 48

2.2.2.9 The role of structural distortion and low dimension in non-perovskite metal-halides . . . 48

2.3 Conclusions . . . 49

3 Experimental Theory and Methods **51**
3.1 Absorption Spectroscopy . . . 52
3.1.1 Fitting of Absorption Spectra According to Elliott's Theory . . . 54
3.2 Photoluminescence Spectroscopy . . . 55
3.2.1 Steady-State PL Measurements . . . 56
3.2.2 Time-Correlated Single Photon Counting . . . 57
3.2.2.1 Fitting to TCSPC Data . . . 58
3.3 Terahertz Spectroscopy . . . 59
3.3.1 Time-Domain Terahertz Spectroscopy (TDTS) . . . 61
3.3.2 Optical-Pump Terahertz-Probe Spectroscopy (OPTPS) . . . 61
3.3.2.1 Time resolution and instrument response of OPTPS . . . 62
3.3.3 Details of experimental system . . . 63
3.3.4 Calculation and modelling of dielectric function in the THz frequency range . . . 65
3.3.5 Direct calculation of the charge-carrier mobility . . . 67
3.3.6 Fitting to OPTP transient decays . . . 69
3.3.6.1 Long-time (nanosecond) fitting . . . 69
3.3.6.2 Early-time fitting in cases of charge-carrier localisation . . . 71
3.3.7 Drude factor calculation for photoconductivity . . . 74
3.4 X-Ray Diffraction . . . 74
3.4.1 Pawley Fitting . . . 75
3.5 Sample Fabrication . . . 76
3.5.1 $BA_x(FA_{0.83}Cs_{0.17})_{1-x}Pb(I_{0.6}Br_{0.4})_3$ Thin Films used in Chapter 4 . . . 76
3.5.2 Cu_2AgBiI_6 Thin Films used in Chapter 5 . . . 77
3.5.3 $Cs_2AgBiBr_6$ Thin Films used in Chapter 5 . . . 77
3.5.4 $Cu_{4x}(AgBi)_{1-x}I_4$ Thin Films used in Chapter 6 . . . 78

4 Interplay of Composition and Optoelectronic Properties of 2D-3D Hybrid Lead-Halide Perovskites **80**
4.1 Introduction and Background . . . 81
4.2 Experimental Details . . . 83
4.3 Understanding of Butylammonium Inclusion . . . 84
4.4 Main Experimental Results and Discussion . . . 86
4.4.1 Structural changes occuring with increasing BA content . . . 86
4.4.2 Trends in emission and absorption with increasing BA content . . . 88
4.4.3 Material aging and stability against light-induced halide segregation 92
4.4.4 Trap-mediated charge-carrier recombination . . . 97
4.4.5 Bimolecular (band-to-band) charge-carrier recombination . . . 100
4.4.6 Effective charge-carrier mobility and diffusion lengths . . . 106
4.5 Summary and Conclusion . . . 108

5 Temperature-Dependent Studies of Charge-Carrier Localisation and Transport in Cu_2AgBiI_6 and $Cs_2AgBiBr_6$ 109
5.1 Introduction and Background . . . 110
5.2 Experimental Details . . . 113
5.3 Materials Synthesis and Understanding of Crystal Structure . . . 113
5.4 Main Experimental Results and Discussion . . . 118
5.4.1 Understanding the steady-state optoelectronic properties of Cu_2AgBiI_6 118
5.4.2 Charge-carrier dynamics: photoexcitation, localisation and emission 122
5.4.3 Temperature-dependent OPTPS investigation of charge-carrier localisation and transport . . . 127
5.4.4 Comparison with charge-carrier localisation in $Cs_2AgBiBr_6$ . . . 138
5.5 Summary and Conclusion . . . 143

6 Interplay of Structure, Charge-Carrier Localisation and Dynamics in Copper-Silver-Bismuth-Halide Semiconductors 145
6.1 Introduction and Background . . . 146
6.2 Experimental Details . . . 148
6.3 Main Experimental Results and Discussion . . . 149
6.3.1 Structural discontinuity and enhanced electronic connectivity with increasing copper content . . . 149
6.3.2 Influence of copper on the electronic structure . . . 153
6.3.3 Charge-carrier localisation and energetics are intrinsically linked to the presence of Ag and Bi . . . 157
6.3.4 Observation of ultrafast charge-carrier localization and small-polaron formation . . . 161
6.3.5 Unravelling the sequence of charge-carrier relaxation, localisation and recombination . . . 163
6.3.6 Influence of Cu^+ on charge-carrier mobility and transport . . . 172
6.3.7 Understanding, mitigating and tailoring charge-carrier localisation 176
6.4 Summary and Conclusion . . . 179

7 Conclusion and Outlook 180

References 186

List of Publications

L. R. V. Buizza, T. W. Crothers, Z. Wang, J. B. Patel, R. L. Milot, H. J. Snaith, M. B. Johnston, L. M. Herz. Charge-Carrier Dynamics, Mobilities and Diffusion Lengths of 2D-3D Hybrid Butylammonium-Cesium-Formamidinium Lead Halide Perovskites. *Advanced Functional Materials* **2019**, *29* (35), 1902656.

L. R. V. Buizza, A. D. Wright, G. Longo, H. C. Sansom, C. Q. Xia, M. J. Rosseinsky, M. B. Johnston, H. J. Snaith, L. M. Herz. Charge-Carrier Mobility and Localization in Semiconducting Cu_2AgBiI_6 for Photovoltaic Applications. *ACS Energy Letters* **2021**, *6* (5), 1729-1739.

L. R. V. Buizza and L. M. Herz. Polarons and Charge Localization in Metal-Halide Semiconductors for Photovoltaic and Light-Emitting Devices. *Advanced Materials* **2021**, *33* (24), 2007057.

L. R. V. Buizza, H. C. Sansom, A. D. Wright, A. M. Ulatowski, M. B. Johnston, H. J. Snaith, L. M. Herz. Interplay of Structure, Charge-Carrier Localisation and Dynamics in Silver-Bismuth-Halide Semiconductors. *Advanced Functional Materials* **2021**, *32*, 2108392.

J. M. Ball, **L. R. V. Buizza**, H. C. Sansom, M. D. Farrar, M. T. Klug, J. Borchert, J. B. Patel, L. M. Herz, M. B. Johnston, H. J. Snaith. Dual-Source Coevaporation of Low-Bandgap $FA_{1-x}Cs_xSn_{1-y}Pb_yI_3$ Perovskites for Photovoltaics. *ACS Energy Letters* **2019**, *4* (11), 2748-2756.

A. M. Ulatowski, A. D. Wright, B. Wenger, **L. R. V. Buizza**, S. G. Motti, H. J. Eggimann, K. J. Savill, J. Borchert, H. J. Snaith, M. B. Johnston, L. M. Herz. Charge-Carrier Trapping Dynamics in Bismuth-Doped Thin Films of $MAPbBr_3$ Perovskite. *The Journal of Physical Chemistry Letters* **2020**, *11* (9), 3681-3688.

G. Longo, S. Mahesh, **L. R. V. Buizza**, A. D. Wright, A. J. Ramadan, M. Abdi-Jalebi, P. K. Nayak, L. M. Herz, H. J. Snaith. Understanding the Performance-Limiting Factors of $Cs_2AgBiBr_6$ Double-Perovskite Solar Cells. *ACS Energy Letters* **2020**, *5* (11), 2200-2207.

M. J. Trimpl, A. D. Wright, K. Schutt, **L. R. V. Buizza**, Z. Wang, M. B. Johnston, H. J. Snaith, P. Müller-Buschbaum, L. M. Herz. Charge-Carrier Trapping and Radiative Recombination in Metal Halide Perovskite Semiconductors. *Advanced Functional Materials* **2020**, *30* (42), 2004312.

H. C. Sansom, G. Longo, A. D. Wright, **L. R. V. Buizza**, S. Mahesh, B. Wenger, M. Zanella, M. Abdi-Jalebi, M. J. Pitcher, M. S. Dyer, T. D. Manning, R. H. Friend, L. M. Herz, H. J. Snaith, J. B. Claridge, M. J. Rosseinsky. Highly Absorbing Lead-Free Semiconductor Cu_2AgBiI_6 for Photovoltaic Applications from the Quaternary CuI-AgI-BiI_3 Phase Space. *Journal of the American Chemical Society* **2021**, *143* (10), 3983-3992.

A. D. Wright, **L. R. V. Buizza**, K. J. Savill, G. Longo, H. J. Snaith, M. B. Johnston, L. M. Herz. Ultrafast Excited-State Localization in $Cs_2AgBiBr_6$ Double Perovskite. *The Journal of Physical Chemistry Letters* **2021**, *12* (13), 3352-3360.

R. D. J. Oliver, P. Caprioglio, F. Peña-Camargo, **L. R. V. Buizza**, F. Zu, S. G. Motti, S. Mahesh, A. J. Ramadan, M. M. McCarthy, J. H. Warby, Y.-H. Lin, N. Koch, S. Albrecht, L. M. Herz, M. B. Johnston, D. Neher, M. Stolterfoht, H. J. Snaith. Understanding and Suppressing Non-Radiative Losses in Methylammonium-Free Wide-Bandgap Perovskite Solar Cells. *Energy & Environmental Science* **2021**, Accepted for Publication.

H. C. Sansom, **L. R. V. Buizza**, M. Zanella, J. Gibbon, M. J. Pitcher, M. S. Dyer, T. D. Manning, V. R. Dhanak, L. M. Herz, H. J. Snaith, J. B. Claridge, M. J. Rosseinsky. Chemical Control of the Dimensionality of the Octahedral Network of Solar Absorbers from the CuI-AgI-BiI_3 Phase Space by Synthesis of 3D $CuAgBiI_5$. *Inorganic Chemistry* **2021**, *60* (23), 18154-18167.

List of Abbreviations

1D . . . . . One-Dimensional
2D . . . . . Two-Dimensional
3D . . . . . Three-Dimensional
BA . . . . . Butylammonium Ion, $(C_4H_9NH_3)^+$
c-c . . . . . Charge-Carrier
DFT . . . . . Density Functional Theory
E_B . . . . . Exciton Binding Energy
FA . . . . . Formamidinium Ion, $CH(NH_2)_2^+$
FACs . . . . . Formamidinium-Caesium
FWHM . . . . . Full Width at Half Maximum
IR . . . . . Infrared
k_B . . . . . Boltzmann Constant
L_d . . . . . Charge-Carrier Diffusion Length
LED . . . . . Light-Emitting Diode
MA . . . . . Methylammonium Ion, $CH_3NH_3^+$
MHP . . . . . Metal-Halide Perovskite
n . . . . . Excited Charge-Carrier Density
OPTPS . . . . . Optical-Pump Terahertz-Probe Spectroscopy
PL . . . . . Photoluminescence
PEA . . . . . 2-Phenylethylammonium Ion, $C_6H_5(CH_2)_2NH_3^+$
PV . . . . . Photovoltaic
SEM . . . . . Scanning Electron Microscopy
SPAD . . . . . Single-Photon Avalanche Diode
THz . . . . . Terahertz
TCSPC . . . . . Time-Correlated Single-Photon Counting
TDTS . . . . . Time-Domain Terahertz Spectroscopy
TRMC . . . . . Time-Resolved Microwave Conductivity
UV . . . . . Ultraviolet
XRD . . . . . X-Ray Diffraction

1

Introduction

Three key topics set the scene for the work presented in this thesis: energy use, innovation and the challenge of decarbonisation. Rising energy use has historically led to increasing incomes and enhanced prosperity and well-being for a population [1, 2]. Underpinning such advances in energy use have been innovations and new technologies that allow humanity to exploit sources of energy more easily and cheaply [3, 4], and which also lead to general improvements in human flourishing [5, 6]. Unfortunately, over the past two centuries increases in energy use have been underpinned by carbon-intensive sources of energy such as coal, oil and natural gas, the burning of which leads to the release of carbon dioxide [7, 8]. Increases in the atmospheric concentration of carbon dioxide lead to rising average global temperatures, which are expected to have catastrophic impacts on human wellbeing, the built environment, biodiversity and the natural world [9, 10]. Innovations that allow for a decoupling of energy production and use from the emission of carbon dioxide are, therefore, a key aspect in achieving decarbonisation and the realisation of a 'net-zero' society and economy [11–13]. A key example of such innovation is that of solar photovoltaic panels, which allow for the direct conversion of sunlight into useful electricity without emitting carbon dioxide in the process. Thus, innovation and research

that leads to reductions in price or improvements in the efficiency of energy-related processes can help to achieve a society that is both more sustainable and prosperous.

The last decade has seen a remarkable increase in interest in a class of materials known as metal-halide perovskites (MHPs), notably when applied as the main absorbing layer in a solar cell device [14, 15]. Metal-halide perovskite materials are able to combine highly promising properties for application in solar panels, notably strong absorption of visible light and easy movement of charges in these materials (as discussed in Chapter 2), alongside cheap, scalable and low-energy processing techniques [14, 16]. When applied to solar panels, perovskite-based solar cell devices have reached a power conversion efficiency (PCE) of over 25% [17], comparable to the best silicon-based devices, after just a decade of research and there are now multiple companies attempting to commercialise this technology successfully [18]. Innovation in the industry of solar photovoltaics is heavily linked to this impressive combination of low cost and rising efficiency. The current incumbent material for commercial applications, silicon, has over the past decade moved closer to its technological efficiency limit [19] whilst simultaneously achieving staggering decreases in processing costs [20]. Due to this, the production costs associated with the silicon material itself are now a small proportion of the total costs for a solar panel module [21], and thus attention is now focused on improving the efficiency of solar panel devices as the optimal strategy for continuing to reduce the unit costs of energy produced by solar panels [22]. A key approach to achieving this is by producing perovskite-silicon tandem solar cells, which would add a small amount of MHP-based material on top of a conventional silicon solar panel — an approach that could lead to substantial increases in overall module efficiency with little associated rise in processing costs [23]. This makes MHPs and other similar metal-halide materials outstanding candidates for next-generation solar panels [14, 16]. Further, the same outstanding optoelectronic properties and low-cost, easy manufacturing of perovskite materials also

make them highly promising for next-generation highly-efficient LEDs [24], as well as a variety of other optical and semiconducting applications [25].

Metal-halide perovskites, which typically have the stoichiometry ABX_3, display a range of highly promising properties for applications in optoelectronic devices. However, several challenges remain to be overcome. Many promising candidate compositions display instabilities that are a barrier to commercialisation [26]: mixed-halide perovskites are unstable to phase mixing under illumination [27, 28]; methylammonium-based perovskites suffer from thermally- and moisture-induced degradation [26, 29]; tin-based perovskites form tin vacancies easily, inhibiting device performance [30–32]. Further, the most successful MHP solar cell and light-emitting devices make use of lead-based compositions, raising concerns around the toxicity of lead and its potential harmful impacts on the environment [33, 34]. These challenges have led to a widening of materials exploration horizons [35], with a variety of alternative chemical compositions and structures being explored [36–39] which display a range of promising properties ranging from strong light emission [38] to good stability [39] and lead-free compositions [33].

For every new material that is discovered, proposed or modelled, understanding how the chemical composition, crystal structure and electronic properties of the material interact is crucial in determining its suitability for specific applications. Specifically, making use of spectroscopic techniques to understand how charges that are excited following illumination behave in a semiconductor, i.e. studying *charge-carrier energetics, dynamics and transport*, is a key way to determine the fundamental properties of new semiconducting materials. In Chapter 2 a brief introduction to conventional metal-halide perovskites is given, followed by a more in-depth review of a range of related 'metal-halide' semiconductors alongside an introduction to the process of charge-carrier localisation and polaron formation, which is often observed in many such ionic materials. Three contributing factors are found to influence the process of charge-carrier localisation [36]:

the chemical composition of a material; its structural and electronic dimension; and the ease of structural distortion of the material.

Chapter 3 outlines the experimental techniques used in the studies presented here. The key technique used for the work presented in this thesis is that of optical-pump terahertz-probe spectroscopy (OPTPS), which gives insights into charge-carrier transport in a material as well as the dynamics of charge carriers over the first few hundred picoseconds following photoexcitation. Experiments based on UV-visibile absorption and photoluminescence spectroscopy also provide valuable information, and in Chapter 5 additional insights are obtained through temperature-dependent measurements for all three of these techniques.

The first experimental chapter of this thesis, Chapter 4, focuses on exciting 'hybrid 2D-3D' perovskite materials with a general composition $BA_x(FA_{0.83}Cs_{0.17})_{1-x}Pb(I_{0.6}Br_{0.4})_3$. These materials are expected to combine the excellent optoelectronic properties of conventional bulk 3D MHPs with the enhanced stability and moisture-resistant properties of layered 2D Ruddlesden-Popper perovskites. By studying a wide range of compositions, the optimal amount of 'hybridisation' is found to include a small amount of the 2D layered perovskites. For this optimal composition, the introduction of a small amount of butylammonium (BA) is found to lead to an improvement in material crystallinity, increased defect passivation and improved charge-carrier mobilities, indicating highly suitable properties for applications in solar panel devices. Calculations of the charge-carrier diffusion lengths in these materials reveal a clear peak for BA fractions between $x = 0.091 - 0.167$, and yield values well above 1 µm, more than sufficient for high-performance solar panel devices.

Chapter 5 moves on to discuss the interesting new lead-free, silver-bismuth based material Cu_2AgBiI_6. By combining temperature-dependent absorption, photoluminescence and optical-pump terahertz-probe spectroscopy measurements, a detailed understanding

of the fundamental properties of this novel material is obtained. Optical absorption measurements reveal a band gap and exciton binding energy that are highly suitable for materials used as the top absorber layer in tandem photovoltaic devices. Temperature-dependent photoluminescence measurements show a long-lived, highly Stokes-shifted band that is typical of the emission from localised charge-carrier states. Further, an ultrafast decrease in THz photoconductivity is observed over a few picoseconds in the OPTPS measurements, corresponding to the localisation of charge carriers into a small polaron state. The small polaron mobility rises with increasing temperature, typical of the temperature-activated 'hopping' transport in such localised states, up to a value above $1\,cm^2V^{-1}s^{-1}$. Taken together, these properties highlight Cu_2AgBiI_6 as a promising material for optoelectronic applications. Further, a comparison is drawn with the temperature-dependent OPTPS measurements carried out for $Cs_2AgBiBr_6$, highlighting several similarities in charge-carrier localisation and transport properties across these two silver-bismuth-halide semiconductors, correlating well with theoretical predictions based on the electronic dimension of such materials.

The work in Chapter 6 builds upon that in the previous chapter, studying the semiconducting properties of five silver-bismuth-halide materials with composition $Cu_x(AgBi)_{1-x}I_4$. The replacement of Ag^+ and Bi^{3+} with Cu^+ is found to enhance photoluminescence intensity, lower exciton binding energy and improve charge-carrier transport. By making use of X-ray diffraction and optical and THz spectroscopy measurements, this change in optoelectronic properties is linked to a transition in octahedral network of the lattice structure, and to a reduction in charge-carrier effective masses with rising Cu^+ content. Further, OPTPS measurements reveal that ultrafast charge-carrier localisation takes place across the entire compositional range studied and this process is found to be intrinsically linked to the presence of Ag^+ and Bi^{3+}. The formation of such small polarons reduces charge-carrier mobilities and also leads to Langevin-type bimolecular

(radiative) recombination in these silver-bismuth materials. The chapter concludes with a discussion of how such charge-carrier localisation effects can be tailored or mitigated for silver-bismuth materials, depending on the specific optoelectronic application.

Finally, Chapter 7 summarises the work presented in this thesis, drawing conclusions around the interplay between the composition, crystal structure and optoelectronic properties of novel metal-halide semiconductors, and highlights potential areas of future work.

Overall, the work presented in this thesis studies how such optoelectronic properties interact for a range of promising new materials for solar panels, and addresses four key questions:

1. To what extent can conventional 3D MHPs be 'hybrised' with 2D perovskites to form materials that combine the beneficial properties of both material classes?

2. Do novel Cu-Ag-Bi-I based materials have the right mix of optoelectronic properties to be applied in solar panels?

3. How do charge carriers move in silver-bismuth-halide materials, and how does this influence their suitability for optoelectronic devices?

4. Can an experimental link be drawn between theoretical predictions of the electronic dimension of new materials and the charge-carrier dynamics and transport therein, especially in the case of silver-bismuth-halide semiconductors?

2

Background and Fundamentals

Contents

2.1 Introduction to Metal-Halide Perovskites 8
2.1.1 Structure and Stoichiometry 8
2.1.2 Optoelectronic Properties and Charge-Carrier Dynamics 10
2.1.3 Double Perovskites and Novel Ag-Bi-I Materials 14
2.1.4 The Importance of Electronic Dimension and Lone Pairs 17
2.2 Polarons and Charge-Carrier Localisation in Metal-Halide Semiconductors 19
2.2.1 Polaron theory: a brief introduction 23
2.2.1.1 The 'large' polaron of Landau and Fröhlich 23
2.2.1.2 The 'small' polaron 26
2.2.1.3 Emin and Holstein's evaluation of polaronic regimes . 27
2.2.1.4 The role of dimension in charge-carrier localisation . . 28
2.2.1.5 Applying polaron theory to metal-halide semiconductors 29
2.2.2 Polarons in metal-halide semiconductors 31
2.2.2.1 Bulk three-dimensional metal-halide perovskites . . . 31
2.2.2.2 Perovskite nanocrystals 36
2.2.2.3 Double perovskites 38
2.2.2.4 Ruddlesden-Popper layered perovskites 40
2.2.2.5 Non-perovskite metal-halide semiconductors 45
2.2.2.6 Vacancy-ordered perovskites 45
2.2.2.7 Quasi-zero dimensional metal-halides 46
2.2.2.8 Other metal-halide semiconductors 48
2.2.2.9 The role of structural distortion and low dimension in non-perovskite metal-halides 48
2.3 Conclusions 49

This chapter gives an introduction to the fundamental properties of metal-halide semiconductors, beginning with a brief overview of 'typical' metal-halide perovskites (referred to as 'bulk three-dimensional MHPs') in Section 2.1 that summarises their composition, structure, optoelectronic properties and charge-carrier dynamics. Following this, an overview of charge-carrier localisation and the formation of polarons in metal-halide materials is provided in Section 2.2. This covers the background theory of polarons and provides an overview of the current understanding of polarons and charge-carrier localisation across a wider variety of metal-halide semiconductors.

2.1 Introduction to Metal-Halide Perovskites

2.1.1 Structure and Stoichiometry

The term 'perovskite' typically refers to materials with general composition ABX_3, which share a crystal structure with the archetypal material $SrTiO_3$ and were first described by Gustav Rose in 1839 through the discovery of $CaTiO_3$ [40], and named after the Russian mineralogist Lev Perovski. Metal-halide perovskites (MHPs), a specific subset of perovskites that are often applied to solar cells, are typically artificial, i.e. they do not occur naturally and are synthesised in a chemical laboratory. Currently, the highest-performing MHPs incorporate a methylammonium ($CH_3NH_3^+$, also referred to as MA^+), formamidinium ($HC(NH_2)_2^+$, also referred to as FA^+) or caesium cation, or mixture thereof, at the A site [41, 42]. For the B-site cation, lead (Pb^{2+}) is the most commonly used [16], although solar cells based on tin (Sn^{2+}) or tin-lead mixtures have also been attempted as these allow for lower band gaps to be obtained [32, 43]. Finally, iodide, bromide and chloride anions, or mixtures thereof, are used at the X site, allowing for a high degree of band gap tunability [42, 44].

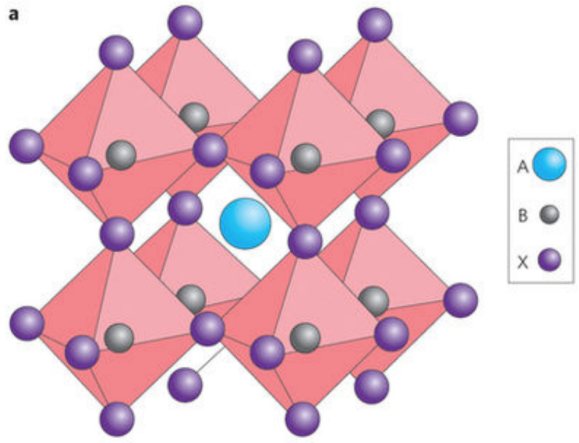


Figure 2.1: Perovskite crystal structure. Cubic crystal structure of typical MHPs. A tends to be a monovalent cation, B is a divalent metal cation, typically lead or tin, and X is a halide anion. Reprinted with permission from Springer Nature: Nature Photonics, Ref. [16] Copyright (2014).

The ideal perovskite crystal structure has a cubic unit cell (shown in Figure 2.1), although tetragonal and orthorhombic unit cells also form, with the precise structure depending strongly on composition, synthesis route and temperature and pressure of the material [16, 35, 40, 45]. The size of ions that can be placed at the A, B and X sites depends on the material having a Goldschmidt tolerance factor $0.8 \leq t \leq 1$ [16], where t is defined as:

$$t = \frac{R_{\mathrm{A}} + R_{\mathrm{X}}}{\sqrt{2}\,(R_{\mathrm{B}} + R_{\mathrm{X}})}. \tag{2.1}$$

Here R_{A}, R_{B} and R_{X} are the ionic radii of the A, B and X-site ions, respectively. (A tolerance factor $t = 1$ would indicate that the spherical ions would stack perfectly into an ideal cubic perovskite structure.) When t takes values outside of the range 0.8 – 1, lower-symmetry or lower-dimensional perovskite structures, or entirely non-perovskite structures, can form.

2.1.2 Optoelectronic Properties and Charge-Carrier Dynamics

Although MHPs incorporate organic components in their composition, the lack of contributions to the band extrema from such organic small molecules [46] leads to the ionic metal-halide sublattice determining much of the optoelectronic properties of MHPs. This allows the behaviour of charge carriers in these materials to be well described by conventional semiconductor theory, with the overall behaviour somewhat similar to that observed in other ionic semiconductors such as gallium arsenide [47–49]. For the production of efficient, low-cost thin-film (sub-micron thickness) solar cell devices the absorber layer must be thick enough to absorb the vast majority of incident sunlight, but also thin enough to enable efficient charge extraction. Typically MHPs have direct band gaps with strong optical absorption [16, 47], meaning that films of $\sim 500\,\text{nm}$ are able to absorb effectively across most of the solar spectrum [16, 41]. Further, high electron and hole mobilities [49–51] and long charge-carrier lifetimes [48, 52, 53] combine to give very large charge-carrier diffusion lengths [54, 55], which together with high absorption coefficients satisfy the criteria required for highly efficient solar cell devices. The most commonly investigated material, $MAPbI_3$, has been shown to exhibit favourable properties for optoelectronic use including shallow trap states [56, 57], low Urbach energies [58] and small phonon energies [59, 60], demonstrating the benign structure and chemistry of MHPs. Finally, MHPs are easily processable, usually via spin-coating of precursor solutions [61] or the evaporation of precursors in a vacuum chamber [62].

The contributions to electronic states at the edges of the valence and conduction bands in MHPs primarily arise from the electronic orbitals of the B- and X-site ions [46]. In the case of $MAPbI_3$, the band gap is governed by the overlap of the B- and X-site orbitals: the valence band maximum (VBM) arises from the antibonding states of Pb $6s$ and I $5p$, and the conduction band minimum (CBM) is formed by empty Pb $6p$ orbitals or Pb $6p$ – I $5p$ interactions [63, 64]. Given this, substitutions of the B-

and X-site ions are the most direct way to tune the band gap of MHPs for specific applications, although variations in the size of the A-site cation will cause changes in the crystal structure of a material, which in turn may lead to alterations in the band gap [42, 65]. This strong tunability of the band gap of makes MHPs ideal for a variety of optoelectronic applications including solar cells and LEDs.

With regards charge-carrier dynamics, charge carriers in semiconductors can undergo a variety of processes: stimulated absorption, stimulated emission, spontaneous emission (sometimes referred to as bimolecular, or radiative, emission), Auger recombination, and trap-mediated recombination [66]. Stimulated absorption follows from the absorption of a photon with an energy above the band gap, which leads to the excitation of an electron from the valence band to the conduction band and the generation of an electron-hole pair. Following this, the four remaining processes determine how charge carriers relax back to the ground state, i.e. four different pathways for charge-carrier recombination. Three such processes, of trap-mediated, bimolecular (radiative), and Auger recombination are shown schematically in Figure 2.2.

Both stimulated and spontaneous emission lead to the emission of a photon as an electron relaxes from the conduction band back down to the valence band, with the photon having an energy equivalent to the difference in energy between the initial and final states. Stimulated emission requires an incident photon with an equivalent energy to initiate the process, whereas spontaneous emission does not [66]. For the metal-halide semiconductors studied in this thesis, stimulated emission is not observed at any of the excitation intensities used, and therefore this type of emission is not discussed further. Spontaneous emission is typically referred to as radiative recombination in semiconductors, with the rate of this process proportional to the square of the photoexcited charge-carrier density, n^2, and in general for MHPs radiative recombination has been shown to be the inverse of absorption [67]. The dependence on n^2 follows from the fact that the

rate will depend on the number of photoexcited charge carriers n in the conduction band, and the number of states available to relax back into in the valence band. The latter is simply the number of holes, p; for an intrinsic semiconductor, every absorbed photon leads to the generation of one electron-hole pair, meaning that $p = n$, and leading to the bimolecular (radiative) recombination rate being proportional to n^2. Given the band-to-band nature of such recombination in metal-halide perovskites [67], radiative recombination is an *intrinsic* process that depends on the precise nature of the band structure at and close to the band edge in a semiconductor.

Trap-mediated recombination involves the recombination of one free charge carrier with a localised or 'trapped' carrier of the opposite charge at a trapping site (often a defect, impurity or vacancy state in a material) [48, 66, 68, 69]. Such recombination rarely leads to the emission of a photon, and the excess energy is typically dissipated as phonons [66, 68, 69]. Trap-mediated recombination is a monomolecular process, i.e. it can

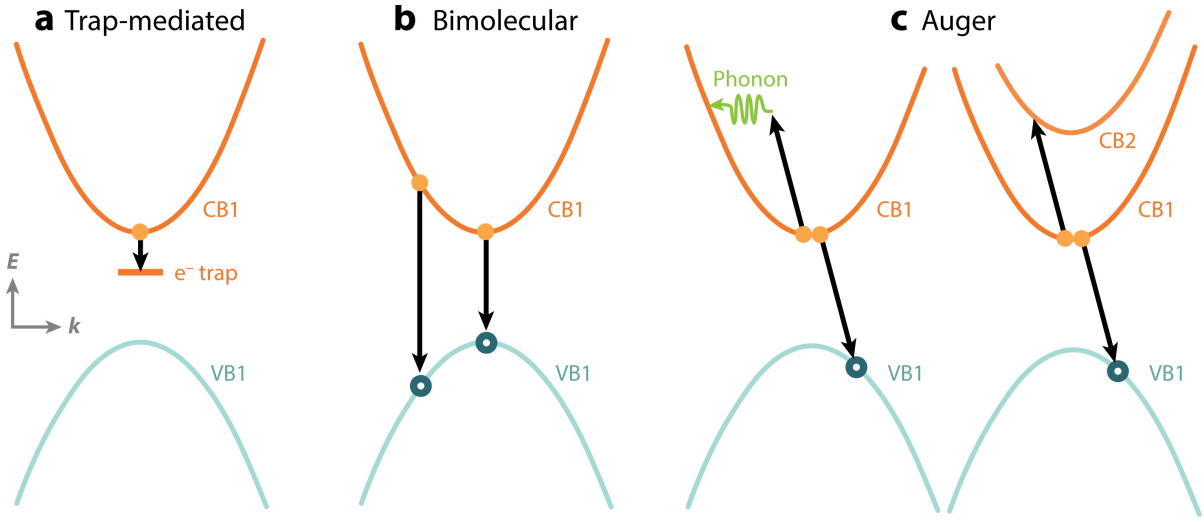


Figure 2.2: Schematic of three recombination processes in MHPs. (a) Trap-mediated monomolecular recombination, in which an electron is trapped in a state between the valence and conduction bands (a mid-gap trap state). (b) Bimolecular (radiative) recombination, in which an electron and hole recombine and emit a photon, with the photon energy determined by the position of the charge carriers in the bands. (c) Auger recombination, in which an electron and hole recombine non-radiatively, with the excess energy and momentum transferred to a third charge carrier (in this case, a conduction-band electron). Taken from Ref. [48], used with permission from Annual Reviews via the Copyright Clearance Center.

be shown to depend linearly on n [66, 68, 69]: if the number of traps filled with a given charge type is fixed, then the likelihood of a charge carrier of the opposite type becoming 'trapped' is simply proportional to the number of photoexcited charge carriers, n. Given that this dependence is linear, at high-enough photoexcited charge carrier densities ($n \gtrsim 10^{16}\,\mathrm{cm}^{-3}$), such monomolecular recombination quickly becomes less important relative to higher-order processes such as bimolecular (radiative) or Auger recombination. It should be noted that, in certain circumstances, monomolecular recombination can lead to PL emission, such as in the case of so-called 'colour centres' [70–72], where a localised defect state can lead to the emission of a photon, typically with an energy significantly below the band gap energy (i.e. with a large Stokes shift). Such localised-state emission is relevant for the discussion of the result in Chapters 5 and 6. Finally, an important aspect of trap-mediated recombination is that this is an *extrinsic* process: it is not related to the electronic structure and instead depends strongly on properties such as the defect density, energetic disorder, energetic distribution of trap states or the material crystallinity.

Finally, Auger recombination is a tri-molecular process that involves an additional charge carrier that carries away excess energy and momentum released by the non-radiative recombination of an electron and a hole. Given that three charge carriers are required for such recombination, the overall rate is thus proportional to n^3, and the strong dependence on the precise nature of the band structure of a semiconductor make Auger recombination a highly *intrinsic* process. For the charge carrier densities in the research presented in this thesis ($n \lesssim 1 \times 10^{19}\,\mathrm{cm}^{-3}$), the contribution from Auger recombination is found to be negligible and is typically not accounted for.

Combining the three main contributions to charge-carrier recombination in a semiconductor, one can describe the dynamics of charge carriers using the following rate equation:

$$\frac{\mathrm{d}n}{\mathrm{d}t} = G(t) - k_1 n - k_2 n^2 - k_3 n^3 = G(t) - nR(n). \tag{2.2}$$

Here n is the charge carrier density, k_1, k_2 and k_3 are the recombination rate constants for mono-, bi- and tri-molecular recombination, $G(t)$ is the generation rate of photoexcited charge carriers and $R(n)$ is the overall recombination rate. The generation rate $G(t)$ will depend on the precise nature of the illumination source: for the experiments used here, given that the pulse width of the excitation lasers used is typically much less than both the instrument response function of the experimental system and less than the dynamics being investigated, photoexcitation is regarded as being effectively instantaneous. This means that, for times $t > 0$, one can assume that $G(t) = 0$, allowing Equation 2.2 to be solved in order to extract values of k_1, k_2 and k_3 from time-resolved photoluminescence and terahertz spectroscopic measurements, as outlined in Chapter 3.

2.1.3 Double Perovskites and Novel Ag-Bi-I Materials

Although lead-halide perovskites yield excellent semiconducting materials and high-performance solar cells [16], there remain a variety of challenges to their successful commercialisation. The presence of lead leads to concerns around toxicity [33, 34], the most successful MHPs rely on the use of MA or FA organic cations, leading to temperature- and moisture-related instabilities [26, 29], and mixed-halide compositions are prone to phase mixing when exposed to light [27, 28]. Given this, one strategy to search for alternatives for semiconducting applications should be to seek out fully inorganic materials that are based on a single halide anion, and that do not make use of lead.

If the lead in conventional MHPs is replaced by heterovalent cation pairs which are isoelectronic to B^{2+} (i.e., a mono- and tri-valent cation), this yields materials with a general composition of $A_2B'B''X_6$ known as 'double perovskites'. These materials have a similar structure to conventional MHPs, but with alternating metal ions at the centre of adjacent corner-sharing octahedra, as shown in Figure 2.7 (b). Double perovskites allow for the exploration of a much wider compositional range and are of great interest for the

exploration of lead-free compositions [33, 35], with the most commonly studied material being $Cs_2AgBiBr_6$ [73–75]. However, although this material satisfies the requirements above, it has a very high direct band gap above 3 eV [73, 75, 76], too high even for tandem solar cell applications, and a very large exciton binding energy of several hundred meVs [73, 77] that yields strongly bound excitons present at room temperature, which are not ideal for solar cell applications. Replacing bromide with iodide should lead to a lowering of the band gap [33, 78], but Cs_2AgBiI_6 does not form a stable phase that is suitable for optoelectronic applications at room temperature [79].

Tertiary Ag-Bi-I materials have also been investigated as an alternative lead-free strategy for solar cell applications, with $AgBiI_4$ having strong optical absorption and a band gap of 1.6 – 1.8 eV [80–82], suitable as the top cell in tandem solar cells (other materials with varying Ag:Bi ratios have also been investigated, see Refs. [81, 83]). Building on this research, the addition of copper to such materials opens up a new phase space of potential semiconducting materials, as has been shown in recent papers by Sansom et al. [84, 85]. The wide range of materials in the CuI-AgI-BiI_3 phase space is shown in Figure 2.3, along with their known crystal structures, which all include a close-packed iodide sublattice as well as silver and bismuth cations are located in the octahedral sites facilitated by the close-packed iodide sublattice (except for in AgI), and copper cations are located in the tetrahedral sites facilitated by the close-packed iodide sublattice. A common theme for the Cu-Ag-Bi-I materials in this phase space is the presence of edge-sharing octahedral networks, and a significant amount of cation disorder, as shown by the partial occupancy levels for the Cu^+, Ag^+, Bi^{3+} cations in Figure 2.3.

Chapter 5 focuses on Cu_2AgBiI_6, which is a lower-bandgap, low-exciton binding energy, stable alternative to the archetypal double perovskite $Cs_2AgBiBr_6$ [84, 86]. This material has a partially-layered structure, with rows of edge-sharing octahedra, and copper located at the tetrahedral sites (see also Figure 5.1 (a)). Chapter 6 studies the

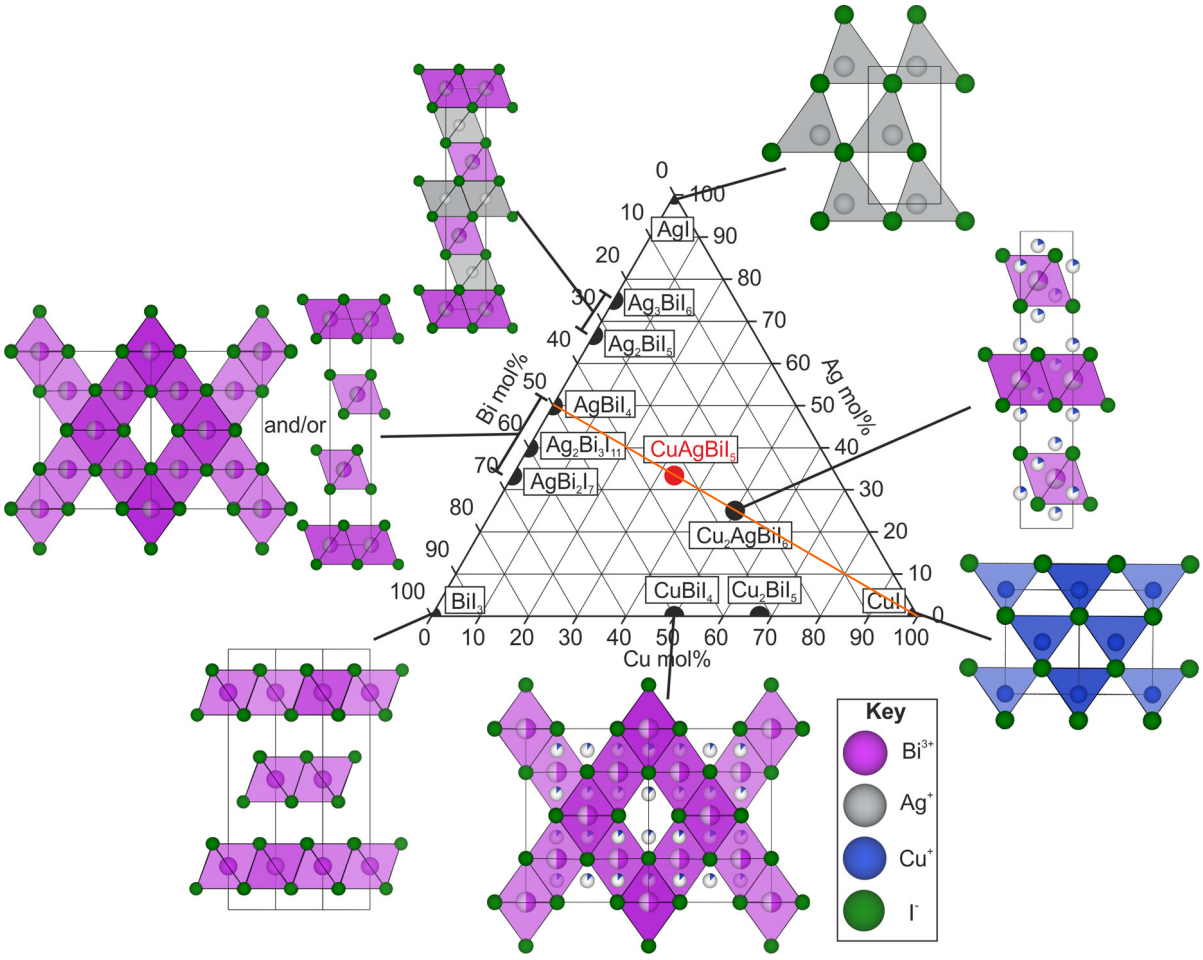


Figure 2.3: Crystal structures of materials across the CuI-AgI-BiI_3 phase space. Reported structures for materials in the CuI-AgI-BiI_3 phase space, which all consist of a close-packed iodide sublattice, as well as a variety of Cu^+, Ag^+, Bi^{3+} cations filling octahedral and tetrahedral sites. This includes the materials studied in Ref. [85] ($CuAgBiI_5$), Refs. [84, 86] (Cu_2AgBiI_6), and Ref. [87] ($Cu_{4x}(AgBi)_{1-x}I_4$, solid solution line highlighted in orange). Adapted with permission from Ref. [85]. Copyright (2021) American Chemical Society.

$Cu_{4x}(AgBi)_{1-x}I_4$ solid solution line, highlighted in orange in Figure 2.3, with values of x = 0, 0.09, 0.2, 0.33, 0.6. The crystal structure for x = 0.2 ($CuAgBiI_5$) instead includes a fully three-dimensional network of edge-sharing octahedra, in a spinel-type motif, as well as copper at the tetrahedral sites as in Cu_2AgBiI_6. For x = 0 ($AgBiI_4$) the octahedral network, with silver and bismuth located at the centre of the octahedra, can take on either the partially-layered or the spinel-type structures, with no copper cations present. Thus, although the structures for x = 0.09 and 0.6 have not been fully studied and confirmed yet, work to date shows that, for $Cu_{4x}(AgBi)_{1-x}I_4$ as x increases there is a

transition from a 3D to a 2D octahedral motif (also shown schematically in Figure 6.4). This is discussed in more detail in Ref. [85] and in Chapter 6, including the impact of such a change in crystal structure on the optoelectronic properties of these materials.

2.1.4 The Importance of Electronic Dimension and Lone Pairs

The prominence of lead electronic states in the band structure of lead-halide perovskites [46, 65] mean that its replacement in double perovskites and other metal-halide semiconductors is a delicate process, requiring a careful balancing of electronic and structural considerations [35]. Further, given the wide range of materials classed as MHPs, and also in the wider category of metal-halide semiconductors (discussed in more detail below), unifying principles that describe the general properties of such materials are of great value. A recent study by Fabini et al. [88] highlights the importance of the presence of lead lone-pair s^2 electrons in conventional MHPs. For an ion, the term 'lone pair' is used to describe a pair of valence-shell electrons that do not contribute to the formation of ionic bonds. It is argued that their presence leads to favourable band alignment, low charge-carrier effective masses (and thus high charge-carrier mobilities), strong dielectric screening and also lattice anharmonicity [88] — properties that have previously been linked to the excellent optoelectronic performance of MHPs [49, 89, 90].

This observation is closely linked to studies by Xiao et al. [91, 92] and Zhao et al. [93] that highlight how the lone-pair nature of the B' and B" metal ions in double perovskites help to determine their band structure and electronic properties. Depending on whether the ions at the B' and B" sites have an s^2 lone-pair electron configuration, Zhao et al. separate double perovskites into three classes [93], which helps to distinguish these materials based on their electronic dimension and thus the quality of their charge-carrier transport properties [92]. Electronic dimension is different to structural dimension: structural dimension describes whether the crystal structure of a material has symmetry

along each lattice dimension (e.g. the 3D network of octahedra present in MHPs); electronic dimension instead describes how well connected the atomic orbitals contributing to the VBM and CBM are. An as-yet unanswered question in this field is the extent to which this concept of electronic dimension, and the presence or absence of lone-pair states, can be linked to the likelihood of charge-carrier localisation taking place in metal-halide semiconductors — one which is addressed in Chapters 5 and 6.

When both B' and B" ions in a double perovskite material contribute lone-pair states (e.g. in $Cs_2InBiCl_6$), it can be considered as electronically three-dimensional, analogous to $MAPbI_3$, leading to good electronic connectivity and charge transport properties. If only one ion contributes a lone-pair state, then one set of $[BX_6]$ octahedra is electronically isolated from the other, making the double perovskite electronically quasi-zero dimensional, as has been found for $Cs_2AgBiBr_6$ and $Cs_2NaBiCl_6$ [94, 95]. Finally, if neither ion has a lone-pair electronic state, this leads to contrasting contributions to the VBM and CBM [93], as is the case in $Cs_2AgInCl_6$ where the electronic character of the VBM is low-dimensional, with quite flat bands and high hole effective masses, whereas the CBM has very curved bands, more typical of 3D bulk MHPs [93, 96].

The impact of such variations can be seen in Figure 2.4. The high-dimensional material $CsPbBr_3$ (analogously, $Cs_2PbPbBr_6$), where each lead ion at the centre of every octahedron contributes a s^2 lone-pair, has clear spatial overlap between the electronic states at the VBM and at the CBM, providing good electronic connectivity and facile charge transport [97]. Instead in the case of the low-electronic-dimension material $Cs_2SrPbBr_6$, the $[SrBr_6]$ octahedra do not contribute to the VBM or CBM states, leading to adjacent octahedra being electronically isolated from each other. This leads to the lack of spatial overlap in VBM and CBM states, seen clearly in Figure 2.4 (b), greatly inhibiting charge transport and leading to an increased likelihood of charge-carrier localisation, as discussed below. The design and study of new semiconducting materials should be guided, at least initially,

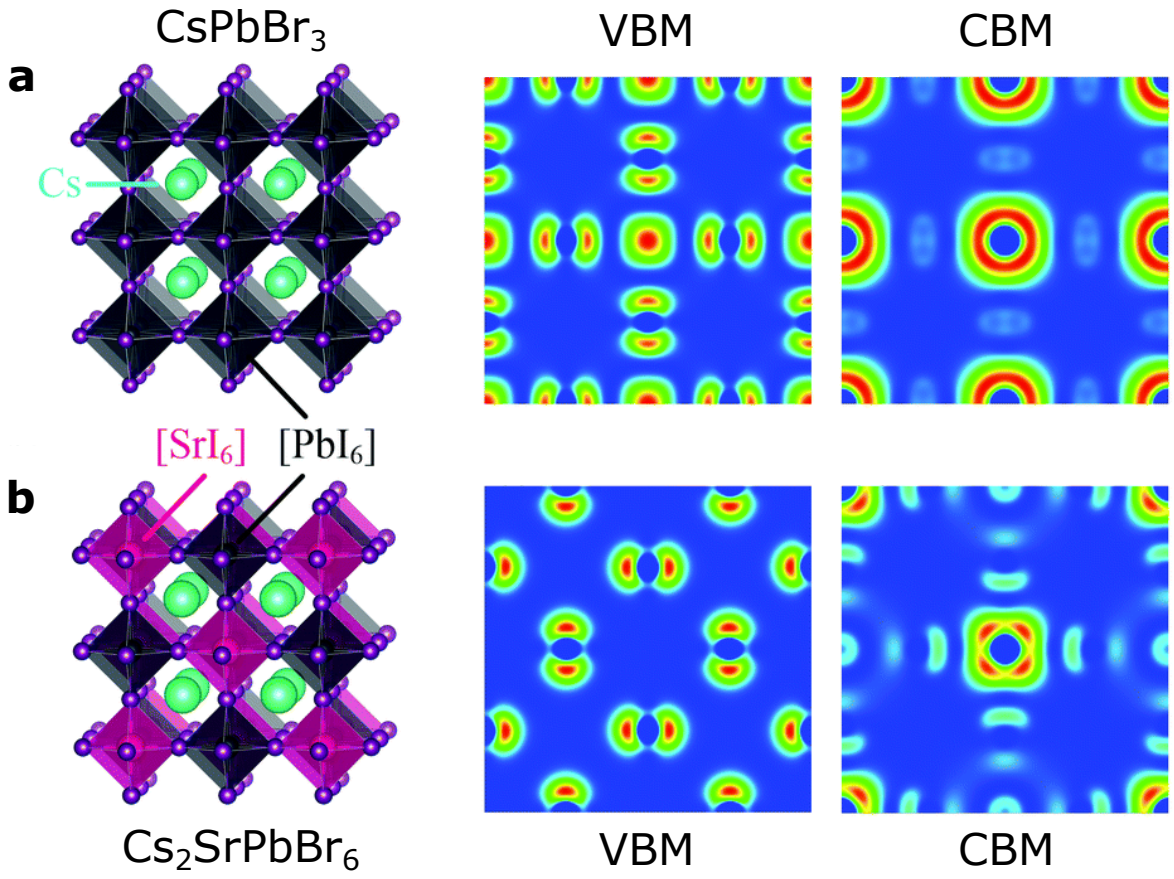


Figure 2.4: Link between electronic dimension and orbital overlap. Crystal structure, and VBM and CBM charge density density maps, for $CsPbBr_3$ (a) and $Cs_2SrPbBr_6$ (b). The former material has a high structural and electronic dimension, yielding good spatial overlap between electronic states at the VBM and CBM. Instead for $Cs_2SrPbBr_6$ the $[SrBr_6]$ octahedra are electronically isolated from the $[PbBr_6]$ octahedra, leading to a low electronic dimension and poor charge-carrier transport properties notwithstanding its high structural dimension. Reproduced from Ref. [91] with permission from the Royal Society of Chemistry.

by considerations of such factors when determining what specific compositions should be synthesised and explored experimentally.

2.2 Polarons and Charge-Carrier Localisation in Metal-Halide Semiconductors

The work presented in this section is based on a review initially published as: L. R. V. Buizza and L. M. Herz. 'Polarons and Charge Localization in Metal-Halide Semiconductors for Photovoltaic and Light-Emitting Devices'. *Advanced Materials* **2021**, *33* (24), 2007057

(Ref. [36]).

On top of the considerations of electronic structure and dimension, discussed above, another key parameter in determining optoelectronic properties of semiconductors is the strength of interactions between charge carriers and the lattice. In recent years a wide range of metal-halide semiconducting materials, closely related to MHPs, has emerged, many of which exhibit similarly advantageous properties for applications in solar panels, LEDs or other devices. Although these materials are not perovskites they often share aspects of the crystal structure, such as octahedral geometries, or have similar chemical compositions, notably the inclusion of halide elements [35, 98, 99]. So far, investigations have included layered Ruddlesden-Popper perovskites [99, 100], vacancy-ordered perovskites [101], double perovskites [73, 74], and quasi zero-dimensional metal-halides [102]. Applications for these metal-halide semiconductors range from solar cells [16] to thermoelectrics [103], and gamma-ray detectors [104] to LEDs [99]. Understanding whether charge carriers in a material recombine radiatively or not, whether they move without encountering obstacles, or whether they can be extracted easily can determine the success of one composition over another when innovative materials for such applications are explored. Thus, in order to predict the suitability of any of these materials for specific optoelectronic applications, a clear understanding of the dynamics of charge carriers, and of their interaction with the crystal lattice, is critical. A fundamental type of charge-lattice interaction manifests as a polaron, which forms when a photoexcited electron or hole interacts with the ions in a polarisable crystal, leading to a displacement in ionic positions. The displaced ions can then couple to the original charge carrier, and the overall lattice polarisation along with the charge are considered as a single quasiparticle, a polaron [105, 106], with the typical effect being that charge-carrier motion is impeded as the lattice distortion moves throughout the lattice along with the charge carrier [107, 108]. A schematic of polaron formation, and the energy associated with

the distortion of the lattice and formation of the polaron, is shown in Figure 2.5, and Ref. [109] provides an excellent theoretical overview of polarons in semiconductors.

The use of new metal-halide materials in solar cells illustrates the links between materials selection, a fundamental understanding of charge-lattice couplings, and innovation in optoelectronics. Initial research focused on the metal-halide perovskite $MAPbI_3$ [16] but has now shifted to more complex, multi-cation MHPs and hybrid 2D-3D perovskites that provide better stability and enhanced crystallinity [51, 110]. Alongside this shift, a thorough understanding of the role of large polarons in MHPs developed [111, 112], providing crucial insights into the costs and benefits of charge-lattice interactions for device applications [89, 113, 114]. Notwithstanding this improved understanding, there is still broad scope for the exploration of new materials beyond MHPs. The desire to avoid the use of toxic lead [33], adjusting band gaps to suit tandem solar cell [42, 76, 115], the introduction of nano-structuring or variation of crystal structures to tailor optoelectronic properties [44, 116], and the push to make use of more stable fully-inorganic compositions [117] all open new avenues for the exploration of novel materials and compositions.

As research has moved beyond $MAPbI_3$ towards other materials, the need to understand the impact of charge-carrier interactions has remained as pressing as ever. For photovoltaics, large polarons appear not to be significantly detrimental, lowering charge-carrier mobilities and introducing some moderate couplings to the lattice but still allowing for efficient charge extraction [111, 112, 118, 119]. On the other hand, small polarons that limit charge-carrier mobilities substantially and lead to charge-carrier self-trapping and fast non-radiative recombination are clearly detrimental for photovoltaics [74, 107, 120]. However, if self-trapped charges lead to broadband, efficient white-light emission, small polarons could be quite beneficial for solid-state lighting [99, 121], as well as other applications such as gamma-ray detection [104, 122]. Recent reviews have emphasised the potential promise of metal-halide semiconductors in lighting applications [24, 123, 124]

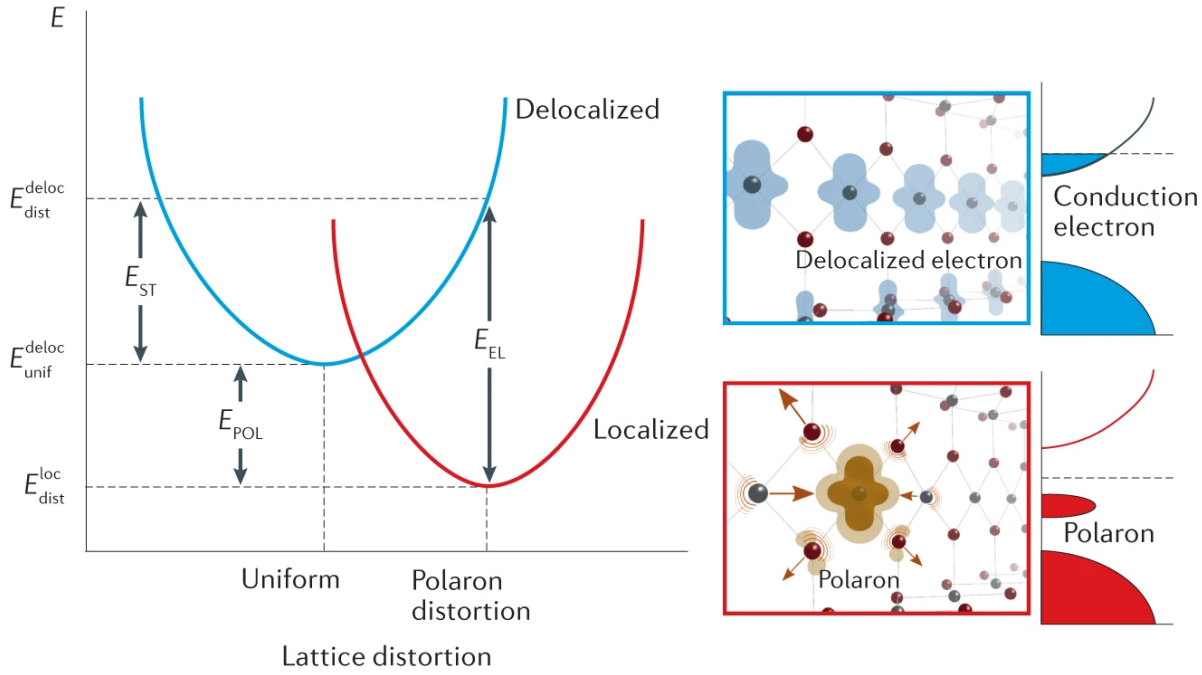


Figure 2.5: Energy-configuration coordinate diagram for polaron formation. Schematic diagram showing the energy levels for a delocalised (conduction) electron, and a polaron (left). E_{ST} is the structural energy associated with deformation of the lattice, E_{EL} is the overall electronic energy of localisation, and E_{POL} is the polaron formation energy. Charge density isosurfaces and corresponding schematic band structures (right). These are shown for a delocalised electron (upper right) and a small polaron, with the polaron peak localised below the Fermi energy (lower right). Reprinted with permission from Springer Nature: Nature Reviews Materials, Ref. [109] Copyright (2021).

and for radiation detection [125, 126], but there has been little focus on the fundamental understanding of polaronic effects and charge localisation which affect the performance of these materials in devices. Thus, understanding the role of charge-lattice interactions is critical in ensuring that new materials for energy innovation are designed rationally and tailored appropriately to specific applications.

In this remainder of this chapter, the state of current understanding of charge-carrier localisation and the role of polarons in a range of metal-halide semiconductors is summarised. First, the evolution of polaron theory and its application to metal-halide perovskites is outlined. Then, a variety of material classes, starting with archetypal bulk three-dimensional (3D) MHPs and moving on to nanocrystal MHPs, double perovskites, Ruddlesden-Popper perovskites, and a range of novel metal-halide semiconductors are

explored. In each case the current understanding of the role of polarons and interactions between charge carriers and the lattice is outlined. As is made clear throughout, polaron formation and charge-carrier localisation in metal-halide semiconductors relies on three complementary factors: the chemical composition of the material, the dimension of the material (both structural and electronic, as outlined above), and the ease of structural distortions in the material.

2.2.1 Polaron theory: a brief introduction

2.2.1.1 The 'large' polaron of Landau and Fröhlich

As a guide for the remainder of this chapter, a short outline of the development of theories to describe polarons is provided, as well as a useful framework in which to consider the formation of large and small polarons. An initial theoretical description of polarons was outlined by Landau in 1933 [105], and later work with Pekar showed how polarons alter the effective mass of charge carriers moving in crystals [106, 127]. Fröhlich, Pelzer and Zienau subsequently developed a quantum mechanical description of polaron theory, introducing electron-phonon couplings in the place of the interaction between a charge carrier and a polarisable continuum [128]. Solutions to their Hamiltonian were then provided by Fröhlich [129], Feynman [108], Hellwarth [130], Ōsaka [131, 132] and others in order to describe a range of electron-phonon interaction strengths [133], focussing specifically on couplings of charges to the macroscopic local electric fields generated by longitudinal-optical (LO) phonons in ionic crystals. This approach describes 'large' polarons for which the interactions are long-range, covering dozens of unit cells, and localisation effects and changes in charge-carrier dynamics are less pronounced [134].

The original Fröhlich Hamiltonian describes a free electron interacting with a single, dispersionless LO phonon [128, 129]. Within this theory one can consider the dimensionless parameter α_F, which is used to quantify the strength of the interaction between the

charge and the LO phonon:

$$\alpha_F = \left(\frac{1}{\epsilon_\infty} - \frac{1}{\epsilon_{static}}\right)\left(\frac{R_y}{\hbar\omega_{LO}}\right)^{1/2}\left(\frac{m^*}{m_e}\right)^{1/2}, \tag{2.3}$$

where $R_y = 13.606$ eV is the Rydberg constant, ω_{LO} is the LO phonon frequency, and $\frac{m^*}{m_e}$ is the ratio of charge-carrier effective mass to the free electron mass. Further, ϵ_∞ and ϵ_{static} are the high-frequency and static limits of the dielectric function with respect to ω_{LO}, typically approximated as the values in the optical and THz frequency ranges, respectively [135]. This parameter is of great value as m^*, ω_{LO}, ϵ_∞ and ϵ_{static} can all be measured or calculated for a material, allowing direct evaluation of the coupling strength, as has been done for some semiconducting perovskite materials [112, 118] (see below and Table 2.1), often making use of formulations by Feynman and Hellwarth [130, 136]. Once the value of α_F is known, it can conveniently be used to calculate the polaron effective mass through $m_p = m^*\left(1 + \frac{\alpha_F}{6} + \frac{\alpha_F^2}{40} + ...\right)$, an approximation first proposed by Feynman [108]. Further, one can also use the Feynman and Hellwarth [130, 136] formulation to calculate polaron mobilities, as has been done by Sendner et al. for bulk 3D lead-halide perovskites [112]. However, there are some limits to the applicability of the Fröhlich description; for example, its simplified assumption of a purely harmonic lattice potential [129] may reduce accuracy for soft MHPs that are expected to exhibit stronger anharmonicities [89, 137, 138].

Ref.	Material	Theory or Experiment	Approach	α_F	m^* (% boost in band mass)	μ ($cm^2V^{-1}s^{-1}$ at 295 K)	p (from $\mu \propto T^p$)
Frost [111]	$MAPbI_3$	Theory	Single-phonon Fröhlich model	2.39 (e) 2.68 (h)	+37 (e) +43 (h)	136 (e) 94 (h)	-0.47
	$CsPbI_3$			1.35	+21	258	
Schlipf et al. [118]	$MAPbI_3$	Theory	Three-phonon Fröhlich polaron model	1.4	+28		-1.5
Poncé et al. [119]	$MAPbI_3$	Theory	Multi-LO phonon coupling	1.91 (e) 1.75 (h)		33 (e) 50 (h)	-1.37
	$CsPbI_3$			1.69 (e) 1.63 (h)		76 (e) 61 (h)	-0.92
	$CsPbBr_3$			2.36 (e) 2.15 (h)		41 (e) 44 (h)	
	$CsSnI_3$			0.75 (e) 0.97 (h)		177 (e) 241 (h)	
	$CsSnBr_3$			1.20 (e) 1.63 (h)		89 (e) 61 (h)	
Sender et al. [112]	$MAPbI_3$	Exp.	Far-IR spectroscopy, then using single-phonon Fröhlich model	1.72	+35	197	
	$MAPbBr_3$			1.69	+35	158	
	$MAPbCl_3$			2.17	+48	58	
Zhao et al. [139]	$MAPbBr_3$	Exp.	THz spectroscopy, then using single-phonon Fröhlich model	1.68 (e) 1.17 (h)		83 (e) 265 (h)	
Lan et al. [140]	$MAPbI_3$	Exp.	THz spectroscopy, then using single-phonon Fröhlich model	2			
Batignani et al. [141]	$MAPbBr_3$	Exp.	Raman spectroscopy, then using single-phonon Fröhlich model	1.84 (e) 1.28 (h)			
Puppin et al. [142]	$CsPbBr_3$	Exp.	ARPES direct measurement of m^*, then using single-phonon Fröhlich model	1.82 (h)	+50 (h)		

Ref.	Material	Theory or Experiment	Approach	α_F	m^* (% boost in band mass)	μ ($cm^2V^{-1}s^{-1}$ at 295 K)	p (from $\mu \propto T^p$)
Neutzner et al. [143]	$(PEA)_2PbI_4$	Exp.	Temperature-dependent PL linewidth measurements, then using single-phonon Fröhlich model	1.67-2.2			
Manna et al. [144]	$Cs_2AgBiCl_6$	Theory	Single-phonon Fröhlich model	2.82 (e) 3.35 (h)	+67 (e) +84 (h)	17 (e) 9 (h)	
	$Cs_2AgIn_{0.25}Bi_{0.75}Cl_6$			2.41 (e) 3.02 (h)	+55 (e) +73 (h)	30 (e) 14 (h)	
	$Cs_2AgIn_{0.75}Bi_{0.25}Cl_6$			3.93 (e) 3.15 (h)	+104 (e) +77 (h)	5 (e) 10 (h)	
	$Cs_2AgInCl_6$			1.99 (e) 4.66 (h)	+43 (e) +132 (h)	52 (e) 2 (h)	
Steele et al. [145]	$Cs_2AgBiBr_6$	Theory	Single-phonon Fröhlich model	2.54 (e) 2.0 (h)			

Table 2.1: Polaronic properties in MHPs. Summary of measurements or calculations of the Fröhlich coupling parameter α_F, polaron effective mass m^* (in terms of its increase with respect to the band effective mass), room-temperature charge-carrier mobility μ and power-law exponent p for the temperature-dependence of the mobility, across a variety of bulk metal-halide perovskite and related materials. Theoretical and experimental studies are labelled separately, and give a brief description of the approach used to calculate the parameters. The term "single-phonon Fröhlich model" is used for the expression for α_F given above in the main text, based on the high-frequency and static dielectric constants ϵ_∞, ϵ_{static}, and the extracted LO-phonon frequency ω_{LO}.

2.2.1.2 The 'small' polaron

Holstein developed an approach for describing short-range interactions that lead to strong charge localisation, and these situations are referred to as 'small' polarons as they are typically limited to approximately a single lattice site [107]. Landau originally suggested that, in cases with strong charge-lattice couplings and slow-moving charges, charge carriers might become immobilised, and thus be described as 'self-trapped' [105]. This state has since been described in much more detail in a variety of materials [146, 147], notably by Williams and Song [72, 120], and is associated with instances of strong localisation. Cases of self-trapping can be purely intrinsic, where the formation of

a self-trapped state automatically leads to a lower-energy configuration, or can be extrinsic, where an already-present lattice defect leads to charge localisation, which induces a further lattice distortion at that site [99]. In some cases, self-trapped charges recombine radiatively with a free charge, at so-called 'colour centres' [148, 149]. Both colour centres and strongly self-trapped charges are often described as a 'molecule in a crystal', i.e. the formation of a covalent bond in an ionic crystal, because their energy levels resemble those of halogen molecule negative ions X_2^- [147–150]. Although the terminology varies, all of these states involve the formation of a polaron and lead to a qualitative change in the properties associated with charges, such as their effective mass, mobility or energetics [105–108, 114, 151].

2.2.1.3 Emin and Holstein's evaluation of polaronic regimes

A useful framework for considering the large and small polaron regimes was outlined by Emin and Holstein [152] and summarised by Stoneham et al. [149] One can consider four contributions to the energy of an electron coupling to a polarisable lattice, via short- and long-range interactions and coupling to a defect state. These contributions depend on the electronic wavefunction length scale L, with $L = 0$ corresponding to an infinitesimally localised state at a lattice site. The kinetic energy of the charge carrier scales as $+L^{-2}$. The short-range interaction scales as $-L^{-d}$ (where d is the number of dimensions of the system); the long-range interaction scales as $-L^{4-d}$; and a cross-term from the short- and long-range interactions scales as $-L^{-2}$. Finally, the defect potential is assumed to be Coulombic, and thus scales as $-L^{-1}$. Overall, using the same notation as Emin and Holstein, the total energy may be expressed as:

$$E(L) = \frac{T_e}{L^2} - \frac{1}{2}\left(\frac{V_{int}^{s}}{L^d} + \frac{V_{int}^{l}}{L^{4-d}} + \frac{V_{int}^{s,l}}{L^2}\right) - \frac{V_d}{L}, \tag{2.4}$$

where T_e, V_d and $V_{int}^{s/l}$ are constants associated with the kinetic energy, defect potential, and the charge-lattice interactions, respectively, and d is the number of dimensions of

the system. For a three-dimensional system, the expression is thus:

$$E(L) = \frac{T_e}{L^2} - \frac{1}{2}\left(\frac{V_{int}^{s}}{L^3} + \frac{V_{int}^{l}}{L} + \frac{V_{int}^{s,l}}{L^2}\right) - \frac{V_d}{L}. \tag{2.5}$$

In the three-dimensional cases, four distinct situations can arise, which are sketched out in Figure 2.6. If the charge-lattice interaction is purely long-range a single minimum exists in the dependence of energy on L, giving only large polarons that are stably bound (Figure 2.6 (a)), and this situation is qualitatively the same whether or not a defect potential is present. In cases with only short-range interactions, the energy has a minimum at $L = 0$, giving a small polaron, and at $L = \infty$, giving a free charge (Figure 2.6 (b)). In the presence of both a defect potential and a short-range charge-lattice coupling, a small polaron state can always form at $L = 0$, and the large polaron state at finite L can be metastable (Figure 2.6 (c)) or unstable (Figure 2.6 (d)).

2.2.1.4 The role of dimension in charge-carrier localisation

There have been suggestions that the formation of small polarons depends on the dimension of the system [72, 152, 153]: two- and three-dimensional systems may have an energetic barrier between free and localised states (as shown schematically in Figure 2.6 (b) for small polarons), whereas this barrier has been argued to be effectively zero in one-dimensional systems [154]. Such effects are evident from Equation 2.4: in one or two dimensions the exponent of interaction terms will be different [152], altering the dependence of energy on L and removing the barrier between the free electron and small polaron states displayed in Figure 2.6 (b). Experiments have provided some confirmation of this dependence, with 3-dimensional RbI showing self-trapped state formation over a few ns [155], whereas 1-dimensional systems display much faster small polaron formation [156, 157], on picosecond timescales, implying the presence of low to no energetic barriers.

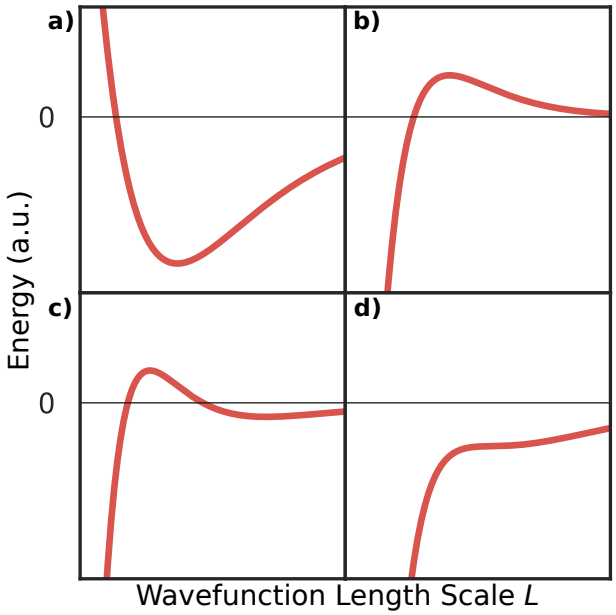


Figure 2.6: Energy potentials for the formation of small and large polarons. Schematic plots of energy against length scale L of the electronic wavefunction, adapted from Emin et al. [152] The figures describe the energy of a polaron in a three-dimensional polar material where a charge can interact with the potential of a defect, and with the lattice *via* long- and short-range interactions, as described in the main text. In case (a) the charge interacts only with the lattice *via* a long-range interaction, leading to a stably bound large polaron forming at finite L. When the charge interacts only with the lattice through a short-range potential, a small polaron can form at $L = 0$ or charge carriers are free as L tends towards infinity, as in case (b). When the charge interacts with a defect potential and with the lattice *via* a short-range potential, a small polaron will always form at $L = 0$, and the large polaron state is metastable, as in (c), or unstable, as in (d). Adapted figure with permission from Ref. [152]. Copyright (1976) American Physical Society.

2.2.1.5 Applying polaron theory to metal-halide semiconductors

Both the Fröhlich and Holstein Hamiltonians are simplified models, and there are inherent difficulties in calculating polaronic effects, especially long-range interactions, when computational methods are based on small systems that often cover only a handful of unit cells [134, 158, 159]. However, they provide useful frameworks within which to discuss interactions between charges and phonons, and can be expanded upon and adapted to specific cases, as discussed below.

Approaches to describe large and small polarons have been attempted across a variety of metal-halide semiconductors, with varying degrees of success. Theoretical descriptions

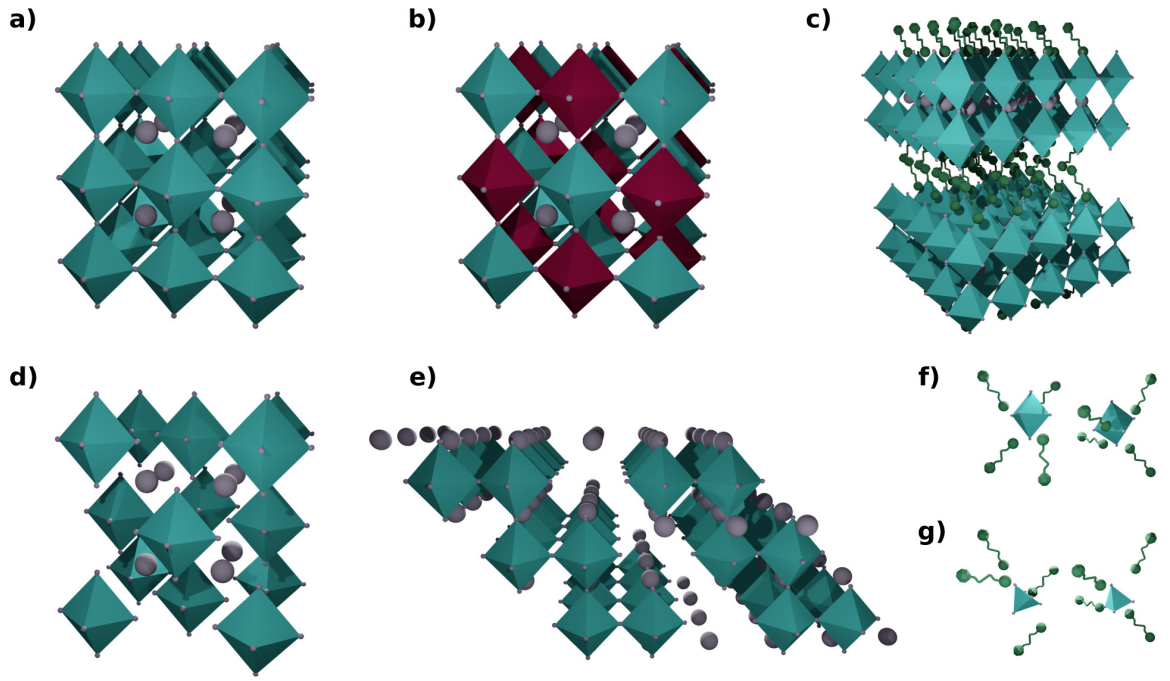


Figure 2.7: Example schematic structures for metal-halide materials. (a) Bulk 3D perovskites with composition ABX_3, with characteristic corner-sharing octahedra for which the halide ions are located at the octahedral corners and the metal ions are located in the centre of the octahedra. The A-site cation is located at the centre between octahedra. (b) Double perovskites, for which alternating metal ions are located at the centre of adjacent octahedra (shown by different colours). (c) A $p = 2$ Ruddlesden-Popper perovskite, for which the larger organic cations (in green) separate planes of corner-sharing octahedra. (d) 2-1-6 Vacancy-ordered perovskites, where metal ions have been removed from alternating sites in a chequered pattern. (e) 3-2-9 Vacancy-ordered perovskites, for which every third metal ion has been removed along the <111> directions. Finally, two different types of quasi zero-dimensional metal-halides, with (f) $[MX_6]$ octahedra and g) $[MX_5]$ pyramids.

of polarons in typical bulk 3D metal-halide perovskites (used to describe materials with formula ABX_3 such as $MAPbI_3$, shown in Figure 2.7 (a)) have focused on Fröhlich-type couplings, and these have been developed with constant input from experimental results across the field [111, 112, 135, 138]. As is discussed below, calculations of the Fröhlich coupling parameter α_F have yielded values between $1 - 2$ for bulk 3D lead-halide perovskites [112, 139, 140], comfortably within the weaker coupling regime of large polarons. Theoretical descriptions of less investigated metal-halide semiconductors, such as double perovskites or low-dimensional metal-halides, are more difficult because of their more heavily disordered crystal structures [35, 102], although attempts have

been made to describe how small polarons and self trapping can lead to emission in layered Ruddlesden-Popper perovskites [160–162], and calculations of the influence of lattice anharmonicity on Feynman/Hellwarth polarons in vacancy-ordered perovskites have also been carried out [163, 164]. Further, as outlined in Section 2.1.4 there have been suggestions that it is the electronic dimension of a material [91], as opposed to its structural dimension, that is the more important feature in determining suitability for different optoelectronic applications [91, 92, 165, 166]. Thus, materials with a high electronic dimension are more likely to have lower charge-carrier effective masses, isotropic charge-carrier transport and shallower defect states [91], making them ideally suited for solar cell devices, whereas the converse case of low electronic dimension might be more applicable to broadband, white-light emitting diodes [92].

2.2.2 Polarons in metal-halide semiconductors

2.2.2.1 Bulk three-dimensional metal-halide perovskites

The nature and impact of polarons in bulk 3D metal-halide perovskites (such as $MAPbI_3$ or $FASnI_3$, see Figure 2.7 (a)) has undergone significant debate, with both theoretical and experimental contributions seeking to clarify current understanding of MHPs [98, 113, 114, 135]. Whereas scattering in the classic inorganic semiconductor silicon is dominated by couplings to acoustic phonon modes [167], as it is a non-polar material, MHPs are ionic materials with a highly polarisable lattice that leads to much stronger interactions between charge carriers and longitudinal optical phonon modes, more similar to the case of the polar semiconductor GaAs [111, 118, 135]. As such, there was some initial discussion around whether charge-carrier interactions with the lattice in 3D bulk MHPs were dominated by acoustic deformation potential scattering [103, 168], but these approaches struggled to accurately replicate measured charge-carrier mobilities or their temperature dependence. Instead, there is now broad acceptance that interactions are dominated

by Fröhlich-type interactions of charge carriers with the electric fields generated by LO phonons of the polar ionic sub-lattice [59, 111, 118]. Frost applied the Fröhlich/Feynman polaron model to MHPs, and although the results produced good qualitative agreement with experimental results, they failed to replicate the experimentally observed $T^{-1.5}$ temperature dependence for the charge-carrier mobility [111]. More recently, attempts have been made to expand upon the simplified Fröhlich model by extending the coupling to three distinct groups of LO phonons [118, 119], or by developing new *ab initio* theories that encompass both Fröhlich polar couplings and non-Fröhlich couplings to acoustic and optical phonons [151, 159]: both approaches appear to replicate measured trends in charge-carrier mobility with temperature better than previous attempts.

Fröhlich coupling strengths and phonon anharmonicity

Various attempts at quantifying the polaron coupling strength α_F in $MAPbI_3$ have been made [111, 112, 119], and a summary of values across a range of MHPs is provided in Table 2.1. Values tend to lie in the range of $\alpha_F = 1 - 2$, with renormalisation of carrier effective masses limited to between 20 - 50 % of the band effective mass, indicating that polaronic effects in MHPs are limited to the weak-to-intermediate coupling range, i.e. behaviour that is well described by Fröhlich-type large polarons. These couplings do serve to limit charge-carrier mobilities at room temperature, with the effect varying between different halide and metal anions [49], as discussed below and as can be seen in Figure 2.8. Further, Munson et al. carried out mid-IR measurements on $MAPbI_3$, from which they calculated a polaron delocalisation length of 9 – 13 nm [169], much larger than the unit cell lengths on the order of approximately 1 nm for tetragonal $MAPbI_3$ [170, 171], clearly placing polarons in this material in the 'large' regime.

There has been discussion around the suitability of the simple Fröhlich model to bulk 3D MHPs, given that it is based upon a harmonic approximation for lattice potentials [89, 119], with some arguing that lattice anharmonicity plays a more substantial role

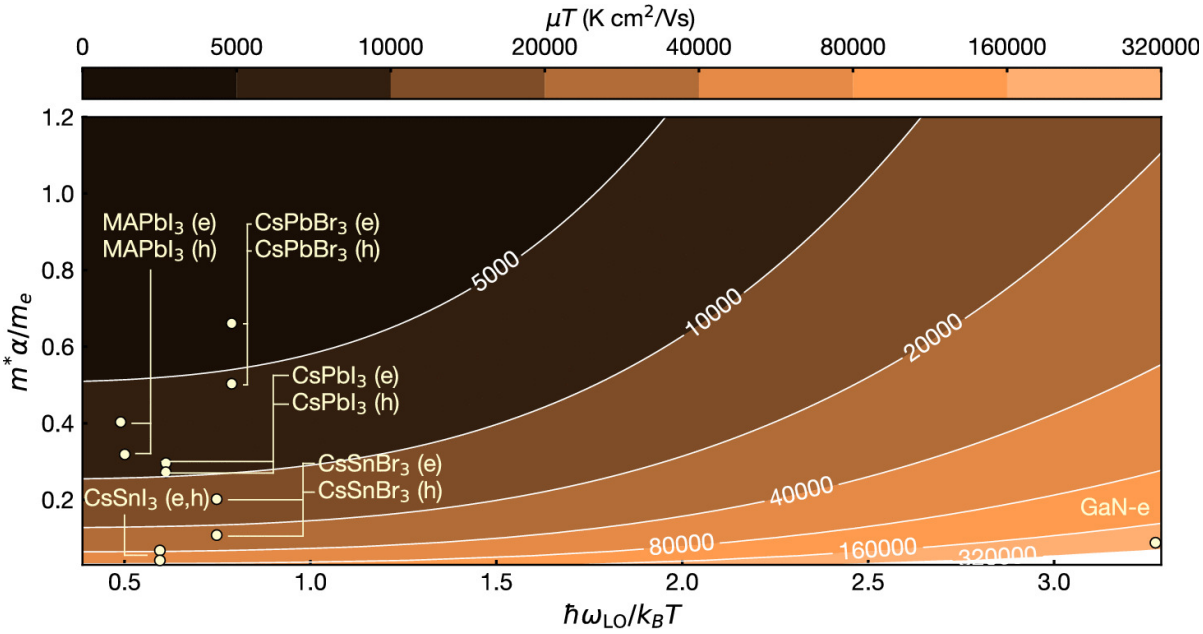


Figure 2.8: Charge-carrier mobilities in MHPs. Figure taken from Poncé et al. [119] showing the dependence of charge-carrier mobility on Fröhlich coupling strength α_F, band effective mass m^* and LO phonon frequency ω_{LO} for a variety of semiconducting materials, calculated using a model that includes Fröhlich-type electron-phonon coupling. In this model, the mobility only depends on two dimensionless parameters: $\alpha_F m^*/m_e$, referred to as the 'polar mass', and the ratio of LO phonon and thermal energies, $\frac{\hbar\omega_{LO}}{k_B T}$. The x-axis values are calculated for $T = 300$ K ($k_b T = 25.9$ meV), and the labels e, h correspond to electron and hole mobilities, respectively. Materials with higher LO-phonon frequencies or smaller 'polar masses', at a given fixed temperature, have higher charge-carrier mobilities. Reprinted with permission from Ref. [119]. Copyright (2019) American Chemical Society.

in soft 3D bulk MHPs than in most polar inorganic semiconductors [90, 137, 172]. A recent study by Mayers et al. [138] applied a molecular dynamics approach to account for large-scale, low-frequency anharmonic lattice motion; this approach replicated the temperature dependence of both the charge-carrier mobility and band gap in $MAPbI_3$ reasonably well [138].

The influence of compositional variation on electron-phonon coupling in MHPs

Compositional variation does allow for some tuning of electron-phonon interactions in 3D bulk MHPs. Both computational and experimental studies show that replacing iodine with bromine at the X-site leads to stronger polaronic couplings [59, 173], and $MAPbI_3$ and $MAPbBr_3$ exhibit different temperature dependence of charge-carrier mobilities

[174, 175], potentially indicating further variations in electron-phonon couplings in each material. Wright et al. investigated the temperature-dependent photoluminescence of (MA/FA)Pb(I/Br)$_3$ to obtain LO phonon energies of $\hbar\omega_{LO} = 11.5, 15.3$ meV and LO phonon coupling strengths of $\gamma_{LO} = 40, 60$ meV in the iodide and bromide MHPs, respectively [59]. (They also provided a very informative list of phonon coupling strengths across a wide range of inorganic semiconductors in their Supplementary Information.) Further, Sendner et al. used far-IR measurements on MAPb(I/Br/Cl)$_3$ (see Figure 2.9) to derive polaron effective masses and electron-phonon coupling constants for each material, placing upper limits on the charge-carrier mobility in single-crystal MAPb(I/Br/Cl)$_3$ of $\mu \sim 200, 160, 60$ cm^{2}V^{-1}s^{-1} respectively [112]. As outlined in Equation 2.3, the Fröhlich coupling strength depends on the inverse of the effective dielectric constant of the material, defined as $\frac{1}{\epsilon_{eff}} = \frac{1}{\epsilon_\infty} - \frac{1}{\epsilon_{static}}$. Given that lead-bromide MHPs have more ionic metal-halide bonds, leading to a lower value for ϵ_{eff}, the observed stronger couplings can be easily explained within the Fröhlich polaron picture [59]. This effect is also apparent from calculations carried out by Poncé et al. for charge-carrier mobilities in MHPs, shown in Figure 2.8, which reveal that stronger lattice couplings for bromide MHPs lead to a larger 'polaronic mass' and thus lower charge-carrier mobilities [119].

There has been significant debate around the role of the A-site cation [114], notably on whether the replacement of dipolar organic cations (MA/FA) with inorganic Cs may lead to changes in polaron binding energy or formation dynamics [173, 176, 177]. Swapping MA with FA or Cs does not appear to affect ultrafast polaron formation dynamics, although there may be a difference between iodide and bromide MHPs: Bretschneider et al. reported polaron formation times of approximately 400 fs in (FA/MA/Cs)PbI$_3$ [178], whereas Munson et al. reported timescales below 150 fs in (FA/MA/Cs)PbBr$_3$ [179]. Further, mid-IR absorption measurements found no variation in energetics or lattice extent of large polarons when swapping between the three cations [179], and

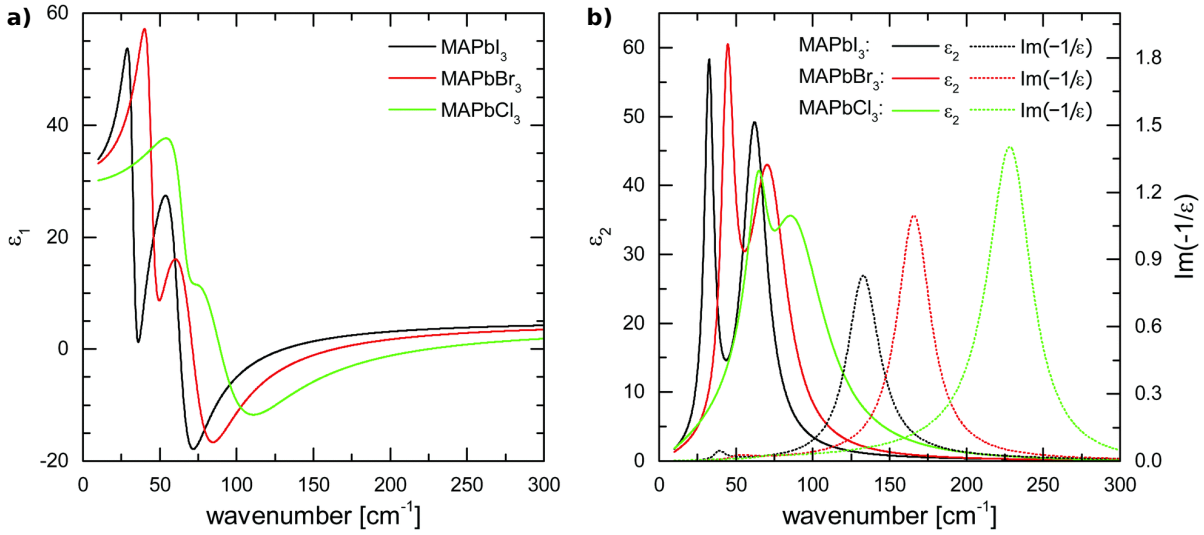


Figure 2.9: Infared measurements of the dielectric function in MAPb(Cl/Br/I)$_3$. (a) Real part of the dielectric function ϵ_1 in solid lines. (b) Imaginary part of the dielectric function ϵ_2 in solid lines, and the loss function Im$[-1/\epsilon(\omega)]$ in dashed lines. Peaks in ϵ_2 correspond to transverse optical phonons, and peaks in the loss function correspond to longitudinal optical phonons. The frequencies of the phonons can be used to calculate the value of ϵ_{static}, and then also the Fröhlich coupling parameter α_F and polaron mass [112, 128, 129]. Reproduced from Ref. [112] with permission from the The Royal Society of Chemistry.

temperature-dependent PL also showed little variation in Fröhlich couplings between FA and MA [59]. Molecular dynamics simulations, combined with Raman measurements, have also been used to argue that replacement of polar MA with Cs does not change the polar, anharmonic fluctuations in lead-halide perovskites [137]. These findings are in good agreement with the notion that Fröhlich coupling is associated with LO phonon modes of the inorganic metal-halide sublattice in 3D bulk MHPs, with the A-cation having little influence [118, 180, 181].

There have been contradictory claims regarding the effect of replacement of lead with tin at the B-site: Neukirch et al. argue that $MASnI_3$ has lower polaron binding energies than present in $MAPbI_3$ for electrons and holes, whereas Mahata et al. argue the opposite and find polaron binding energies to be largest for low Sn content in mixed-cation $MAPb_{0.75}Sn_{0.25}I_3$. Although replacement of lead with lighter tin indeed leads to higher phonon frequencies [182], much of the deterioration in various optoelectronic

properties for low tin content can be traced back to higher defect densities and increased non-radiative recombination pathways [182, 183], without polaronic effects necessarily playing a role. Purely tin-based MHPs have consistently shown higher charge-carrier mobilities than their lead-based counterparts [31, 43, 49], which can be linked to the higher optical phonon frequencies in these materials [182, 184], as well as the lower effective charge-carrier masses in tin-based MHPs [119]. Kahmann et al. analysed the FWHM of PL spectra as a function of temperature for $FASnI_3$ [184], following Wright et al. [59], and obtained a value of 68 meV for the relevant LO phonon energy, a factor of six higher than that reported for (MA/FA)PbI_3 [59]. However, this seems somewhat too high: an approximate model considering the reduced mass of either Sn-I or Pb-I diatomic chains would predict a factor of approximately 1.1 between the resulting phonon frequencies, and this has indeed been measured for the transverse optical modes in mixed tin-lead iodide perovskites [182]. In any case, given that the Fröhlich coupling scales as $\alpha_F \propto \omega_{LO}^{-\frac{1}{2}}$, tin-based MHPs would be expected to exhibit lower polaron couplings and higher charge-carrier mobilities compared to their lead-based counterparts - as reported in both theoretical [119] and experimental work [31, 49, 182] (see also Figure 2.8).

2.2.2.2 Perovskite nanocrystals

The study of perovskite nanocrystals has allowed for comparisons of charge-carrier properties between bulk MHPs and their nano-scale counterparts, with the majority of work focusing on all-inorganic $CsPbBr_3$ nanocrystals. Early-time photoconductivity studies of $CsPbBr_3$ nanocrystals, large enough ($\sim$ 30 nm) to be considered as analogues of single crystals, clearly demonstrate the formation of large polarons in this material [185]. OPTPS measurements have also shown that smaller nanocrystals, exhibiting stronger electronic confinement, have broadened, blue-shifted phonon modes that absorb more strongly in the THz frequency domain relative to bulk $CsPbBr_3$, which is proposed to

be caused by a stronger coupling between the THz radiation and optical phonon modes in the nanocrystals [186]. The broadening of the phonons is associated with shorter phonon lifetimes and is typical of nanoparticles; the blue shift of the modes, however, does not appear to be dependent on size over the studied range (6 – 10nm), indicating that phonon confinement is not the sole responsible factor [186]. These changes in the phonon spectra compared to the bulk perovskite are likely related to structural differences in the lattice, evidenced by XRD studies revealing increasing lattice parameters with decreasing particle size [186, 187]. Such differences in the lattice properties are expected to impact the coupling between phonons and charge carriers, although further studies are needed to confirm and quantify such effects. A study based on TA and molecular dynamics simulations also found strong coupling between charge carriers and phonons in $CsPbBr_3$ nanocrystals across a range of strong-to-weak confinement (0.8 – 12 nm) [188]. Further, a study that combined optical and X-ray transient absorption spectroscopy of moderately-confined ($\sim$ 8 nm) $MAPbBr_3$ nanocrystals argued that structural distortions around the Pb^{2+} cation may lead to the formation of small electron polarons [189].

Recent work has highlighted the importance of structural distortions in inducing polaron formation across MHPs [114, 190, 191], and a crucial question with regards nanocrystals is whether such structural distortions, and thus polaron formation, are facilitated or inhibited by nano-scale structures, as is the case for quasi-zero dimensional metal halides (discussed below). Given that temperature-dependent PL studies have found LO-phonon energies between $\hbar\omega_{LO} = 14 - 33$ meV for (FA/Cs)$PbBr_3$ nanocrystals [192–194], similar to the value of 15 meV obtained for bulk $FAPbBr_3$ by Wright et al. [59], as well as a similar LO-phonon couplings (45 meV in nanocrystal $FAPbBr_3$ [193], as opposed to 60 meV in bulk [59]), it is not fully clear how much fundamental change is caused by the formation of nanocrystals. Although polaron formation and electron-phonon interactions are present in MHP nanocrystals, further clarification is needed in

order to distinguish the extent to which polaronic behaviour is affected by the increased presences of boundaries and surfaces in nanocrystals and the resulting ease of structural distortions, from the effects of electronic confinement that vary with nanocrystal size. Interestingly, intrinsic quantum confinement in nominally bulk $FAPbI_3$ has recently been shown to be associated with lowered electron-phonon coupling [195], suggesting that in the absence of clear material boundaries, such as those present in MHP nanocrystals, electronic confinement may lead to polaronic effects being reduced, rather than enhanced.

2.2.2.3 Double perovskites

By swapping the B-site cation in MHPs with two heterovalent cations of charge 1^+ and 3^+, double perovskites can be formed with composition $A_2B'B"X_6$, opening up a new class of materials for investigation (see Figure 2.7 (b)) [35, 78, 94]. Given the wide variety of compositions that can be studied, it is difficult to draw any fundamental conclusions with regards the origin of charge-lattice interactions that are valid across all double perovskites.

As outlined above in Section 2.1.4, double perovskites can be classified into three classes depending on whether the ions at the B' and B" sites contribute a lone-pair electron to states at the band edge, which in turn influences the electronic dimension of such materials. Given that lower electronic dimension leads to low- or zero-energy barriers between free and self-trapped states [152, 153], one would expect a higher likelihood of polaron formation in $Cs_2AgBiBr_6$ and $Cs_2AgInCl_6$, and in other double perovskites electronically analogous to these. Zelewski et al. [74] combined low-temperature emission, PL excitation and Raman measurements to argue for the presence of a colour centre as the source of the emission peak at 2 eV in $Cs_2AgBiBr_6$ (see Figure 2.10 (a)), and they were able to successfully replicate the PL and PLE spectra based on a Franck-Condon model with Huang-Rhys factor of $S = 11.7$ and a phonon energy of 22.4 meV (obtained

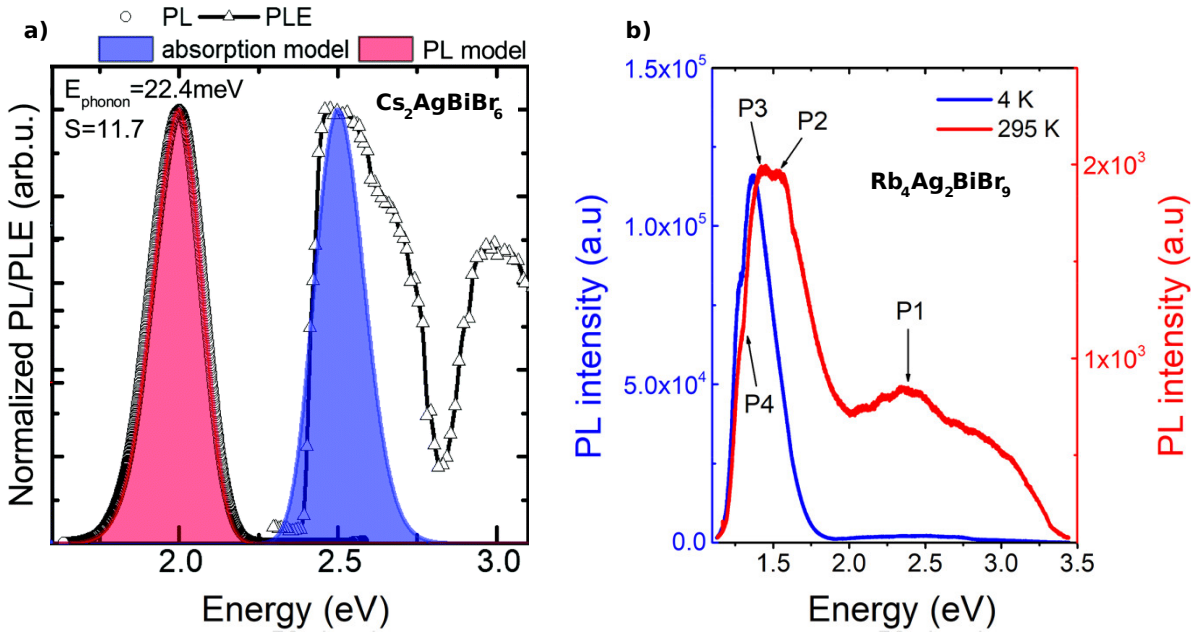


Figure 2.10: Photoluminescence characteristics of small polarons. Typical behaviour of photoluminescence that arises from strongly localised charges, notably exhibiting large Stokes shifts, broadband emission and significantly increased PL intensity at lower temperatures. (a) Photoluminescence and photoluminescence excitation spectra, with their respective Huang-Rhys model fits, for $Cs_2AgBiBr_6$.[74] The large phonon energy, high Huang-Rhys parameter value and large Stokes shift, as well as Raman measurements, led Zelewski et al. [74] to attribute the emission at 2 eV to a colour centre. Reproduced from Ref. [74] with permission from the The Royal Society of Chemistry. (b) Photoluminescence spectra of $Rb_4Ag_2BiBr_9$ at 4 and 295 K, with four separate emission peaks P1 – P4 identified [197]. The sharp increase in emission intensity of peaks P2 – P4 as temperature decreases is part of the evidence used to argue that emission bands arise from distinct self-trapped states located on $[BiBr_6]$ structural units [197]. Reprinted with permission from Ref. [197]. Copyright (2019) American Chemical Society.

from Raman spectroscopy) [74]. Another study carried out fitting of the temperature-dependent PL linewidth for $Cs_2AgBiBr_6$ [145], obtaining $\hbar\omega_{LO} = 22$ meV, slightly above the equivalent values found for $(FA/MA)Pb(I/Br)_3$ [59], as well as a much stronger coupling of charge carriers to LO phonons, with a coupling parameter of $\gamma_{LO} = 226$ meV (compared to 40 and 60 meV for $FAPbI_3$ and $FAPbBr_3$, respectively) [59, 145]. The stronger coupling of electrons to the LO phonons is also consistent with the lower charge-carrier mobilities measured for $Cs_2AgBiBr_6$ [196].

Studies of $Cs_2AgInCl_6$ have shown confinement of holes on $[AgCl_6]$ octahedra, leading to the formation of self-trapped excitons that result in broadband white-light emission [98,

198]. Strong blue emission, with a large Stokes shift, from antimony-doped $Cs_2NaInCl_6$ has also been attributed to self-trapped exciton states [199], and calculations of the band structure of $Cs_2NaInBr_6$ have been used to argue that small hole-polarons and self-trapped excitons form easily in this material [95]. Raman measurements of $Cs_2AgSb_{1-y}Bi_yX_6$ (X = Br, Cl) nanocrystals indicated very strong charge-phonon interactions that lead to intrinsic self-trapping of charges within a few ps, as measured by ultrafast TA [200]. Work by Manna et al. [144] combined Raman measurements with density functional theory (DFT) calculations, finding Fröhlich coupling constants in the range $\alpha_F = 2 - 5$ for $Cs_2AgIn_{1-x}Bi_xCl_6$ nanocrystals, and calculations of charge-carrier mobilities using the Feynman/Hellwarth polaron model suggested upper limits of $2 - 52 cm^2V^{-1}s^{-1}$ in nanocrystals across the range of x [144].

One recent study reported a reduction in the structural dimension of the double perovskite $Cs_2AgBiBr_6$ into $p = 1$, 2 octahedral layers, analogous to the case of Ruddlesden-Popper perovskites (discussed below) [201]. This work found that reduction of structural dimension can modify the electronic band structure of $Cs_2AgBiBr_6$, especially in the case of a single octahedral layer, and demonstrated the ease of structural distortion as the number of octahedral layers is reduced, which enhances the likelihood of charge-carrier localisation [201]. Overall, double perovskites appear to show good correlation between their electronic dimension and the likelihood of charge localisation, making them promising model systems for further experimental studies.

2.2.2.4 Ruddlesden-Popper layered perovskites

Ruddlesden-Popper perovskites include large organic cations that cannot be incorporated at the A-site [100, 202], leading to two-dimensional layers of corner-sharing octahedra, separated by two layers of large organic cations. The variation of type and concentration

of the large organic cation allows for close control over the number of connected two-dimensional octahedral planes, and the materials are often referred to by the (*hkl*) direction in which a three-dimensional MHP lattice has been sliced in order to achieve the layering. An example structure for an $p = 2$ Ruddlesden-Popper perovskite, with stacking direction perpendicular to the (100) direction (as opposed to other directions e.g. (110) or (111)), such as $(PEA)_2(MA)Pb_2I_7$ (PEA = phenylethylammonium), is shown in Figure 2.7 (c)). As outlined above, polaron formation depends on the dimension of the system being studied, and layered Ruddlesden-Popper perovskites appear to be at the threshold for an energetic barrier forming between localised and free states [152, 153, 162, 203].

The additional electronic confinement present in Ruddlesden-Popper perovskites, as well as stronger dielectric screening caused by alternating layers with high and low dielectric constants, lead to strong excitonic effects in these materials [99, 167, 205]. Indeed, narrow, efficient radiative recombination at low Stokes shift has been observed for several Ruddlesden-Popper perovskites [99, 100, 205]. However, in some cases PL from layered perovskites is highly Stokes-shifted, exhibiting a broadband emission spectrum [121, 206–208], typical of emission from self-trapped states [72, 160]. Ultrafast TA and OPTPS of the (110) material ($N-$MEDA)[$PbBr_4$] (N-MEDA = N^1-methylethane-1,2-diammonium) showed fast self-trapping of photoexcited carriers, leading to broadband emission from a distribution of self-trapped excitonic states [203]. Temperature-dependent PL combined with TA and DFT calculations also confirmed the presence of emissive self-trapped small polarons in (EDBE)PbX_4 (X = Br, Cl, and EDBE = 2,2-(ethylenedioxy)bis(ethylammonium)) [209], a corrugated two-dimensional lead-halide perovskite. A study of a new cadmium-based single-layer perovskite, $(F_2CHCH_2NH_3)_2Cd_xPb_{1-x}Br_4$, demonstrated the importance of structural deformation in enabling emission from self-trapped states, with alloyed Cd-Pb materials emitting much more strongly than either purely Cd- or Pb-based materials because of

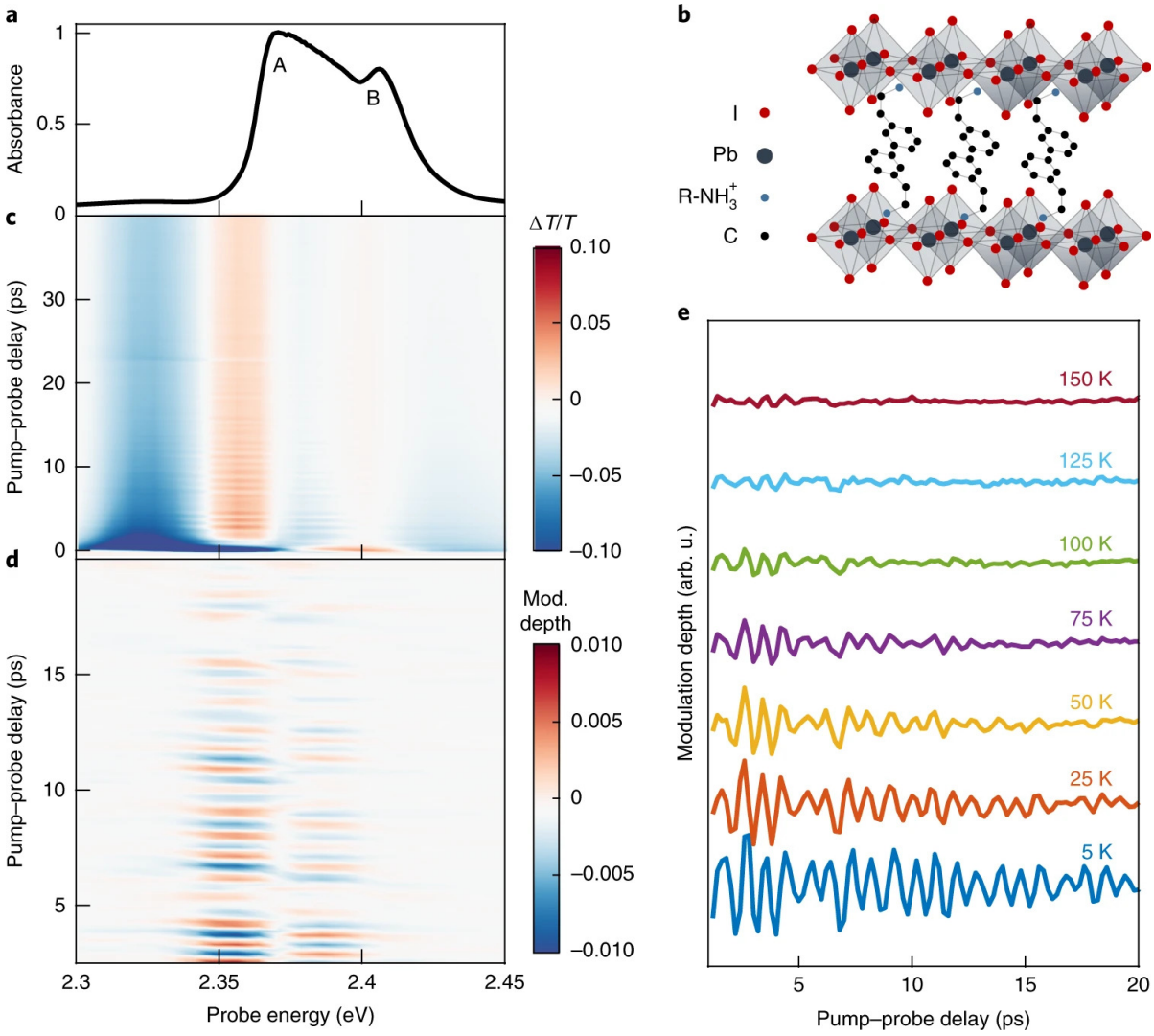


Figure 2.11: Direct evidence of electron-phonon coupling in $(PEA)_2PbI_4$. (a) Exciton absorption spectrum measured at 5 K. (b) Schematic of crystal structure of $(PEA)_2PbI_4$. (c) Time-resolved differential transmission $\Delta T/T$, measured at 5 K with a pump energy of 3.06 eV. (d) Oscillatory components from (c), obtained by subtracting the population dynamics. (e) Temperature dependence of the oscillatory response, taken from slices at 2.35 eV. The oscillations are short-lived and weak at 150 K, mainly because of dynamic disorder [204]. As temperature decreases, clear coherent oscillations on a picosecond timescale are visible due to phonon modulations. The Fourier Transform of the oscillations shows the presence of six low-energy ($< 50 cm^{-1}$) phonon modes, which match well with the calculated phonon modes, and which contribute to the formation of electron and hole polarons in $(PEA)_2PbI_4$ [204]. Reprinted with permission from Springer Nature: Nature Materials, Ref. [204] Copyright (2019).

increased octahedral distortions [210]. Further, swapping the organic spacer cations between BA to PEA has a significant effect on the intensity and energy of Raman modes [211] and can alter the charge-carrier effective mass [212], thus varying the strength of the electron-phonon interaction. This has been linked to the fact that swapping organic spacer cations modifies the stiffness or 'corrugation' of the octahedral layers in Ruddlesden-Popper perovskites, aiding structural distortion and thus impacting on the likelihood of charge-carrier localisation in these materials [211, 212].

Computational studies have tried to describe small polaron formation in single-layer Ruddlesden-Popper perovskites, finding substantial polaron binding energies of several hundred meVs [161], as well as strong exciton couplings to Raman modes [204]. Temperature-dependent TA and time-resolved PL measurements have also been used to argue that phonon couplings in $(PEA)_2PbI_4$ lead to the formation of electron and hole polarons, and drive transitions between different excitonic states and influence exciton dynamics and diffusion (see Figure 2.11) [143, 204, 213, 214]. Further, it also appears that variations in exciton binding energies have an effect on the energies of the polaronic state formed in the case of Coulombically bound electron-hole pairs [215, 216]. For example, a recent study has argued that two excitonic states are present in $(BA)_2PbI_4$ (BA = butylammonium), and that the different binding energies of the two excitons lead to different couplings with the lattice, with a weak exciton binding energy leading to the formation of large polarons [215].

There has been some debate around whether closely-spaced features in low-temperature optical absorption spectra of Ruddlesden-Popper perovskites arise from the presence of multiple excitonic states [143, 204, 215] or rather from a single excitonic state that couples to a high-energy ($\sim$ 40 meV) phonon mode, leading to vibronic progressions [211, 217]. However, regardless of the origin of these specific features, there is clear literature consensus that the presence of strong electron-phonon couplings to low-energy

LO phonon modes of the halide sub-lattice plays a key role in polaron formation in Ruddlesden-Popper perovskites [143, 204, 211, 217].

Overall, while several experimental and computational studies have examined the role of polarons in Ruddlesden-Popper perovskites, their role is not yet fully clarified, given that multiple alternate processes have been evoked to explain their absorption and emission features. As highlighted in two recent reviews [121, 218], many different sources of emission are present in layered perovskites including excitons, lattice defects, light-induced defects, self-trapped states, molecular chromophores in the organic layers, and structural distortions [219]. Notably, if the emission is not arising from the metal-halide octahedral planes but from the larger organic cations, this immediately rules out polaronic or self-trapped states as the source of photoluminescence. It is suggested that for these materials identification of specific localisation effects needs to be done with particular care, requiring multiple complementary experimental or theoretical approaches to provide convincing evidence of polaron formation. For example, in certain cases defect states have been found to induce self-trapping (sometimes known as 'extrinsic self-trapping') [72, 99], making it difficult to distinguish emission from an intrinsic self-trapped state to that associated with a radiative trap state [121, 219]; equally, lattice distortions can both aid the formation of self-trapped states [149] and alter the electronic properties of layered perovskites [219, 220], further confusing the impact of structural changes on charge-carrier transport and emission [99]. Given the wide variety of potential applications for Ruddlesden-Popper perovskites, from solar cells to LEDs [100, 207], photodetectors or X-ray sensitisers [221, 222], a better understanding of the fundamental processes governing charge-lattice interactions would be of great value, as has been achieved so far for their 3D analogues. A clearer picture of these couplings would be especially useful with regards to lighting applications, given the interest in achieving efficient, 'sun-like' or broadband white-light emission in LEDs [123, 198, 223].

2.2.2.5 Non-perovskite metal-halide semiconductors

Finally, a wide range of non-perovskite metal-halide semiconducting materials have been investigated for potential optoelectronic applications. Some of these research studies date back to original work involving alkali halides and photographic materials [120, 155, 224], with other more recent investigations focusing on MHP-related materials such as vacancy-ordered perovskites [101]. This discussion focuses on more recent results, and reviews by Stoneham et al. [149] and by Williams and Song [120] are recommended for comprehensive coverage of earlier work including the alkali halides, vacancies in quartz, and metal-oxides.

2.2.2.6 Vacancy-ordered perovskites

Vacancy-ordered perovskites have been investigated as potential all-inorganic, lead-free variations of MHPs [33, 225]. There are two main types of compositions: materials with the formula $A_3\square B_2^{3+}X_9$ ($\square$ indicates a vacancy) [226], where every third B^{3+} site is unoccupied and the structure involves either quasi-zero dimensional dimers of face-sharing octahedra or two-dimensional layers of octahedra [226] (the latter is shown in Figure 2.7 (e)); and vacancy-ordered double perovskites with formula $A_2\square B^{4+}X_6$ [227], where every other B^{4+} site is unoccupied and the structure involves isolated $[BX_6]$ octahedra [33] (shown in Figure 2.7 (d)). McCall et al. combined Raman and temperature-dependent PL measurements to argue that strong electron-phonon couplings in vacancy-ordered $A_3\square M_2I_9$ (A = Cs, Rb; M = Bi, Sb) gave rise to small polaron formation, with broad, highly Stokes-shifted emission arising from self-trapped excitons [101]. Another study combined optical and x-ray transient absorption with DFT calculations to argue for the formation of small polarons in $Cs_3\square Bi_2Br_9$, through the formation of V_k centres (or, Br_2^- dimers) [228]. Doping of $Cs_2\square SnCl_6$ nanocrystals with antimony leads to an additional low-energy emission band, ascribed to triplet-state self-trapped excitons [229], and a combination of Raman spectroscopy and fitting of PL linewidths found intermediate

electron-phonon coupling strengths in $Cs_2\square SnI_6$ [230]. The inclusion of larger cations at the A-site in $A_2\square SnI_6$ (A = Cs, MA, FA) leads to increased lattice anharmonicity and octahedral tilting, caused by changes in the interoctahedral I-I distances, leading to more tightly bound polarons and lower polaron mobilities [163]. Although some of the vacancy-ordered metal halides show quite dispersive band structures, indicative of lower charge-carrier effective masses and higher mobilities [33, 92, 226], the high likelihood of lattice distortion in many vacancy-ordered perovskites is conducive to polaron formation and strong charge localisation [92, 101, 225], making it difficult for these materials to be used in photovoltaic applications where good charge transport is crucial.

2.2.2.7 Quasi-zero dimensional metal-halides

Quasi zero-dimensional metal-halides also tend to display strong localisation effects, which can be traced back to their structures having easily-distorted individual metal-halide octahedra or similar structural units. Electronically one would expect them to behave analogously to very small nanocrystals, i.e. charges are strongly confined and become spatially localised easily [160, 231, 232]. Materials with chemical formula A_4BX_6, where A is a large organic cation, have isolated $[BX_6]$ octahedra (shown in Figure 2.7 (f)) [223, 231]. For example, in single-crystal $(C_8NH_{12})_4Bi_{0.57}Sb_{0.43}Br_7 \cdot H_2O$ the structure has both $[BiBr_6]^{3-}$ and $[SbBr_6]^{3-}$ octahedral units separated by the larger organic cations [233]; in fully-inorganic $Cs_4(Sn/Pb)Br_6$ the $[(Sn/Pb)Br_6]^{4-}$ are separated by Cs^+ cations [102, 117, 234, 235]; and in $(DETA)PbCl_5 \cdot H_2O$ (DETA = diethylenetriammonium) bi-octahedral units of $[Pb_2Cl_{10}]^{6-}$ form [236] (see Figure 2.12). Slightly different structures arise in $(C_9NH_{20})_2SbCl_5$, which has isolated quadrangular $[SbCl_5]^{2-}$ pyramids [232] (shown in Figure 2.7 (g)); $Cs_3Cu_2I_5$, which has tetragonal and trigonal $[Cu_2I_5]^{3-}$ sites [237, 238]; and $(Bmpip)_2MX_4$ (Bmpip = 1-butyl-1-methylpiperidinium; M = Ge, Sn, Pb; X = Br, I), which forms isolated disphenoidal $[MX_4]^{2-}$ anions [239]. Beyond this, a variety

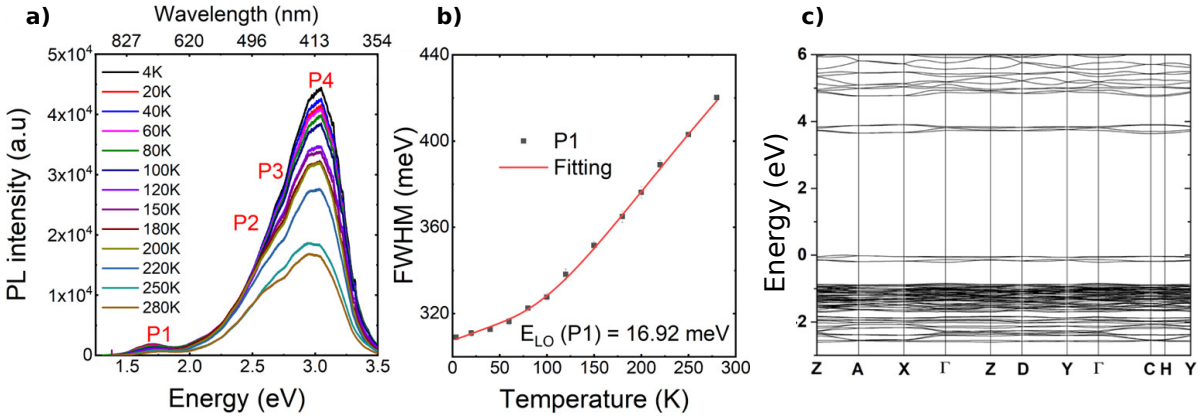


Figure 2.12: Characteristic properties of zero-dimensional metal-halides. Photoluminescence measurements and DFT calculations for the quasi-zero-dimensional metal-halide (DETA)$PbCl_5 \cdot H_2O$ by Yangui et al [236], illustrative of the behaviour observed across many quasi zero-dimensional metal-halide semiconductors. (a) Temperature-dependent spectra between 4 – 280 K, with four emissive species P1 – P4 identified. P1 is attributed to emission from a self-trapped exciton localised on the $[Pb_2Cl_{10}]^{6-}$ bi-octahedra. (b) Fit of the full-width half-maximum of the P1 peak, following the procedure outlined by Wright et al [59]. The fit gives an LO phonon energy of 16.9 meV, matching a measured Raman mode at 137cm^{-1} (17.0 meV), and also gives a very large electron-phonon coupling constant of $\gamma_{LO} = 385$ meVK^{-1} [59, 236]. (c) Band structure calculated for (DETA)$PbCl_5 \cdot H_2O$ using the PBE functional.[236] The bands are highly non-dispersive, which typically indicates a higher likelihood of charge-carrier localisation. Adapted with permission from Ref. [236]. Copyright (2019) American Chemical Society.

of other quasi zero-dimensional materials with a range of compositions and structures have been studied, for which self-trapping or charge localisation has been attributed as the source of photoluminescence [37, 240–243].

A mixture of DFT and photoluminescence-based studies in quasi zero-dimensional materials have been used to argue for emission from polaronic or self-trapped states being prominent, which exhibits typical behaviour including large Stokes shifts [234, 235, 239], and longer-lived, narrower PL at low temperatures (see Figure 2.12 (a) and (c) for a typical example) [102, 236, 237, 240]. However, as highlighted above, a clear distinction of excitonic and polaronic experimental signals, e.g. in ultrafast TA measurements, can be complicated in zero-dimensional systems [244]. The calculated VBM/CBM electronic bands in quasi zero-dimensional metal-halides tend to be highly non-dispersive [117, 241, 243], making charge localisation more likely [91, 152, 153]. Overall, the broadband,

high-efficiency, long-lived PL that is present across many of these materials makes them very promising for applications in lighting or as X-ray scintillators [102, 223, 238]. On the other hand, one would expect their isolated structures to inhibit the efficient charge transport and extraction that is crucial for solar cells [47].

2.2.2.8 Other metal-halide semiconductors

Finally, studies of other metal-halide materials also include $Rb_4Ag_2BiBr_9$, which has a quasi-3D structure involving $[BiBr_6]$ octahedra and $[AgBr_5]$ square pyramids [197], and one-dimensional chains of corner-sharing metal-halide octahedra [245, 246]. Sharma et al. used temperature-dependent PL measurements to argue for the presence of multiple self-trapped states contributing to broadband emission in $Rb_4Ag_2BiBr_9$ [197] (see Figure 2.10 (b)), whereas studies of $(C_4N_2H_{14})PbBr_4$ and $CsCu_2X_3$ (X = Cl, Br, I) have identified multiple distinct self-trapped exciton states along one-dimensional chains [245, 246], leading to broadband light emission in the case of $(C_4N_2H_{14})PbBr_4$ [245].

2.2.2.9 The role of structural distortion and low dimension in non-perovskite metal-halides

The unifying theme for all of the novel non-perovskite metal-halide materials that are discussed here appears to be that, notwithstanding a wide variety of chemical compositions and crystal structures, these materials often have easily deformable lattices and low-dimensional electronic structures [91, 93, 160], greatly enhancing the likelihood of both structural distortions and charge-carrier localisation [152, 153]. This scenario is particularly relevant to quasi-zero dimensional metal-halides, as they lack the cohesive crystal structure that stabilises against distortions [102, 223]. However, so far most studies have relied solely on computational and PL-based measurements for proof of charge-carrier localisation; although these materials are more likely to exhibit strong charge-carrier localisation effects, further experimental evidence from IR/Raman spectroscopy,

ultrafast spectroscopy and charge-carrier mobility measurements would be of great value in identifying the precise origins of these processes.

2.3 Conclusions

An overview of current understanding of polarons and localisation effects across a wide variety of metal-halide semiconductors has been provided in this chapter. In the case of ubiquitous three-dimensional metal-halide perovskites, there is widespread consensus around the dominant role of Fröhlich couplings leading to the formation of large polarons [59, 135]. Polaron formation is fast, occurring within hundreds of fs, and the organic cation plays little to no role in this process [178, 179]. Compositional tuning of the halide alters polaronic effects, with bromide giving much stronger couplings than iodide [59, 177]. Replacement of lead with tin might lead to changes in charge-lattice couplings, although the full impact is not yet clear, given that some of the fundamental changes in optoelectronic properties may still be obscured by extrinsic effects deriving from high defect densities and poor crystallinity in tin-based MHPs [31, 182, 183]. The role of lattice anharmonicity in MHPs is still the subject of some debate [89, 118, 151], and detailed experimental studies, for example using magneto-absorption spectroscopy, which can provide valuable insights into polaron energy levels, transport and interactions with the local lattice structure [134, 247–249], could help to clarify which modelling approach is more suitable for understanding the fundamental properties of MHPs. Overall, polarons in metal-halide perovskites have little detrimental impact, and thus high-performance solar cell devices have indeed been developed based on these materials.

Ruddlesden-Popper layered perovskites are the ‘edge case’ of small polaron behaviour, with several experimental studies of these materials indicating the presence of strong charge-lattice interactions [99, 209], although there are several other competing processes that might play a role in these materials including defect-mediated recombination, exciton

formation and structural distortions [121, 218]. Understanding clearly why certain types of Ruddlesden-Popper perovskites have sharp, efficient emission at low Stokes shift whereas others exhibit broadband PL at large Stokes shifts, and which compositional or structural parameters can be tuned to alter this, will be valuable in developing their application, especially for LEDs.

Studies of non-perovskite metal-halide materials, from vacancy-ordered semiconductors through to zero-dimensional metal-halides, have to date mainly made use of DFT calculations and photoluminescence-based experiments to indicate the presence of strong charge-carrier localisation [101, 102, 160]. These materials tend to show highly non-dispersive electronic bands [33, 243] and highly efficient, broad emission at large Stokes shifts [102, 223], which point towards polaron formation and charge-carrier self-trapping.

3

Experimental Theory and Methods

Contents

3.1 Absorption Spectroscopy 52
3.1.1 Fitting of Absorption Spectra According to Elliott's Theory . . 54
3.2 Photoluminescence Spectroscopy 55
3.2.1 Steady-State PL Measurements 56
3.2.2 Time-Correlated Single Photon Counting 57
3.2.2.1 Fitting to TCSPC Data 58
3.3 Terahertz Spectroscopy 59
3.3.1 Time-Domain Terahertz Spectroscopy (TDTS) 61
3.3.2 Optical-Pump Terahertz-Probe Spectroscopy (OPTPS) 61
3.3.2.1 Time resolution and instrument response of OPTPS . 62
3.3.3 Details of experimental system 63
3.3.4 Calculation and modelling of dielectric function in the THz frequency range 65
3.3.5 Direct calculation of the charge-carrier mobility 67
3.3.6 Fitting to OPTP transient decays 69
3.3.6.1 Long-time (nanosecond) fitting 69
3.3.6.2 Early-time fitting in cases of charge-carrier localisation 71
3.3.7 Drude factor calculation for photoconductivity 74
3.4 X-Ray Diffraction 74
3.4.1 Pawley Fitting 75
3.5 Sample Fabrication 76
3.5.1 $BA_x(FA_{0.83}Cs_{0.17})_{1-x}Pb(I_{0.6}Br_{0.4})_3$ Thin Films used in Chapter 4 76
3.5.2 Cu_2AgBiI_6 Thin Films used in Chapter 5 77
3.5.3 $Cs_2AgBiBr_6$ Thin Films used in Chapter 5 77
3.5.4 $Cu_{4x}(AgBi)_{1-x}I_4$ Thin Films used in Chapter 6 78

In this chapter the experimental methods used for the results presented in Chapters 4, 5, and 6 are outlined. This includes a discussion of the underlying theory of each experimental technique and its link to optoelectronic properties that are crucial for understanding the fundamentals of semiconducting materials. The techniques presented here are all applied to thin-film samples of metal-halide semiconductors, typically with thicknesses of hundreds of nanometres, deposited on 2 mm-thick substrates of z-cut quartz.

3.1 Absorption Spectroscopy

Absorption spectroscopy in the ultraviolet, visible and near-infrared wavelength ranges gives an insight into the electronic states available within a material. If the valence and conduction bands in a semiconductor are approximated as a two-level energy system, then optical absorption corresponds to the process of stimulated absorption. The probability of absorption of a photon with a specific energy will then be determined by the landscape of electronic energy states within the given material. Thus, by measuring how the probability of photon absorption depends on the photon energy, absorption spectroscopy in the visible range can uncover information about the electronic energy states within a semiconductor, including the band gap, exciton binding energy and intra-band defect states.

Throughout this thesis, values of the absorption coefficient are calculated from the reflectance (R) and transmittance (T) of a material. This follows from the fact that any light incident on the material that does not transmit through the sample or reflect off it must be absorbed (to a first-order approximation). The absorption coefficient of a material, α, is calculated from the Optical Density (OD), following Beer's law [66], as:

$$\alpha(E) = -\frac{1}{d_{\text{sam}}} \log\left(\frac{T(E)}{1 - R(E)}\right). \tag{3.1}$$

Here d_{sam} is the thickness of the measured thin-film sample, and the absorption coefficient, transmittance, and reflectance of the material are all functions of the energy of the incident light. It should be noted that Equation 3.1 represents a first approximation of the absorption coefficient of a material, which does not account for e.g. scattering from a rough sample surface, or multiple internal reflections within the sample.

The transmittance and reflectance of a sample are calculated with respect to reference spectra for transmission and reflection, which are typically measured for highly transmittive and reflective materials such as (for the visible range) a blank quartz substrate and a silver mirror, respectively. The transmittance and reflectance of the sample are then calculated as follows:

$$T = \frac{t_{\text{sam}}}{t_{\text{sub}}} \tag{3.2}$$

$$R = \frac{r_{\text{sam}}}{r_{\text{mirr}}} \tag{3.3}$$

where t_{sam}, t_{sub} are the transmission spectra measured from the sample and quartz substrate, respectively, and r_{sam}, r_{mirr} are the corresponding reflection spectra measured from the sample and mirror.

The transmission and reflection spectra are measured with one of two instruments. For Chapters 4 and 5, a Bruker Vertex 80v Fourier-Transform Infrared (FTIR) spectrometer fitted with a transmission/reflection accessory, with a tungsten halogen source and a silicon diode detector was used. For Chapter 6, a Perkin Elmer Lambda 1050 spectrometer with an integrating sphere accessory was used. Deuterium and halogen lamps were used for the UV, and visible and near-infrared spectral ranges, respectively. A photomultiplier tube and lead sulfide detector were used for the UV and visible, and near-infrared ranges, respectively.

Sample thicknesses were determined by scratching thin film samples off of the substrate and measuring the depth of the scratches with a a Veeco Dektak 150 profilometer.

3.1.1 Fitting of Absorption Spectra According to Elliott's Theory

The optical absorption spectrum of a semiconductor has two main contributions: band-to-band absorption, where a valence-band electron is excited into a state in the conduction band, and absorption from bound electron-hole states (referred to as excitons). The excitonic contribution takes the form of a (broadened) series of lines at energies $-E_B/n^2$ below the band gap, where E_B is the excitonic binding energy, following the hydrogenic model for a bound electron-hole pair [167, 250]. A typical three-dimensional direct-gap semiconductor would be expected to have a square-root onset for the optical absorption spectrum [167]; however, this is altered somewhat by the Coulombic interaction between electrons and holes, which enhances the absorption coefficient [67, 251].

These contributions to the optical absorption are captured by Elliott's theory of optical absorption [251]. This theory can be used to describe the energy (E) dependent absorption coefficient $\alpha(E, E_G, E_B)$ arising from a semiconductor with a band gap E_G and with excitons with a binding energy E_B, and has previously been applied to both MHPs and silver-bismuth-halide materials [67, 73]. The overall absorption coefficient is described as:

$$\alpha(E, E_G, E_B) = \frac{b_0}{E}\sum_{n=1}^{\infty}\frac{4\pi E_B^{3/2}}{n^3}\delta\left(E - \left[E_G - \frac{E_B}{n^2}\right]\right) + \frac{b_0}{E}\left[\frac{2\pi\sqrt{\frac{E_B}{E-E_G}}}{1-\exp\left(-2\pi\sqrt{\frac{E_B}{E-E_G}}\right)}\right] c_0^{-1}\mathrm{JDoS}(E) \tag{3.4}$$

where the joint density of states is given by $\mathrm{JDoS}(E) = c_0\sqrt{E - E_g}$ for $E > E_G$ and 0 otherwise, and the joint density of states constant $c_0 = \frac{1}{(2\pi)^2}\left(\frac{2\mu}{\hbar^2}\right)^{\frac{3}{2}} \times 2$, where μ is the reduced effective mass of the electron-hole system. The first term in Equation 3.4 contains the contribution from bound excitonic states, while the second term contains the contributions from the continuum states. Broadening caused by electron-phonon interactions, local fluctuations in the stoichiometry of the material, and energetic disorder

is represented by convolution of $\alpha(E)$ with a normal distribution $\mathcal{N}(0, \Gamma^2)$ which has a mean 0 and standard deviation Γ.

3.2 Photoluminescence Spectroscopy

Photoluminescence (PL) measurements are the natural complement to absorption measurements when building a picture of the electronic states in a semiconducting material. The process of PL emission from a material can be broken down into three key steps. First, as outlined in Section 2.1.2, stimulated absorption takes place when a photon with energy above the band gap is incident on a semiconducting material, leading to the generation of an electron-hole pair. Second, photoexcited charge carriers will then relax, thermalise, localise, scatter off of defects, or undergo a variety of other processes that lead to a change in the energetics of these charge carriers [66, 250]. Third, eventually charge carriers will recombine back to the ground state through radiative or non-radiative processes. The range of photon energies emitted from the material, measured as a photoluminescence spectrum, then reveals valuable information about the behaviour of the charge carriers within the material and the energetic distribution of states near and below the band gap. The details of such steady-state PL spectroscopy are presented in Section 3.2.1.

Further, by measuring how PL emission with a specific photon energy decays over time, the dynamics of specific electronic states within a material can be studied. By observing how PL dynamics change with emission energy, and how emission spectra vary across different time delays, a time-resolved picture of the occupancy of electronic states in a material can be built up. Such time-resolved PL measurements can be carried out using time-correlated single-photon counting, which is detailed below in Section 3.2.2.

3.2.1 Steady-State PL Measurements

Steady-state PL refers to the measurement of the energy-dependent spectrum of photons emitted from a photoexcited sample that is in equilibrium with an illumination source, such as a continuous-wave laser. The experimental setup used to measure steady-state PL consists of a photoexcitation source, collection optics to gather the emitted PL spectrum, and a detector to measure the PL spectrum. For all steady-state PL measurements presented in this thesis, a 398 nm wavelength diode laser (Picoharp, LDH-D-C-405M) operated under continuous wave conditions was used as an illumination source. The intensity of the incoming laser illumination was adjusted using neutral-density filters along the incoming beam path. Apertures and lenses along the beam path were used to control the beam spot size and shape. The collection optics for all of the PL measurements carried out in this thesis consisted of an achromatic doublet, a linear polariser, and a 450 nm long-pass filter. The collimated PL was then focused onto the entrance slit of a grating spectrometer (Princeton Instruments, SP-2558), which then internally re-collimated the light onto a diffraction grating. The diffraction grating separated the light spatially according to its wavelength, and the separated light was then focused onto an intensified charge-coupled device (iCCD) camera for detection. A schematic of the setup is shown in Figure 3.1.

Charge-coupled devices (CCDs) are widely used in commercially-available digital cameras, but tend to have fairly low frame rates ($< 10^6$ frames per second). Intensified CCDs (ICCDs) make use of an image intensifier tube to amplify the light signal, thus reducing the acquisition time, and can also be operated with an optical or electronic (rather than mechanical) shutter, overcoming the time limit imposed by the read-out time of the CCD [252]. These allow for highly sensitive PL measurements, detecting individual photons, thanks to the amplification of the light signal and use of fast ($\sim$ns) electronic or optical gating, greatly enhancing the signal-to-noise ratio of the measured spectrum [252].

3.2.2 Time-Correlated Single Photon Counting

Time-correlated single-photon counting (TCSPC) is a technique used to measure time-resolved PL dynamics for a given material, and is used for the results presented in all three experimental chapters of this thesis to uncover information about the charge-carrier dynamics in metal-halide materials. For such time-resolved measurements, a repeating electronic signal is split in two: one signal generates a photoexcitation pulse from a laser, which photoexcites the material; the other signal triggers a highly precise electronic clock that is based on a time-dependent, linearly-increasing voltage. When a photon emitted by the material is registered by a detector (in this case a Single-Photon Avalanche Diode, SPAD), the voltage is read out, which will be proportional to the time t elapsed since photoexcitation. By measuring repeatedly over many excitation cycles, a histogram can be constructed of emitted photons across multiple delay times, allowing for a determination of the overall PL decay.

Photoexcitation from a 398 nm diode laser (Picoharp, LDH-D-C-405M) was used for

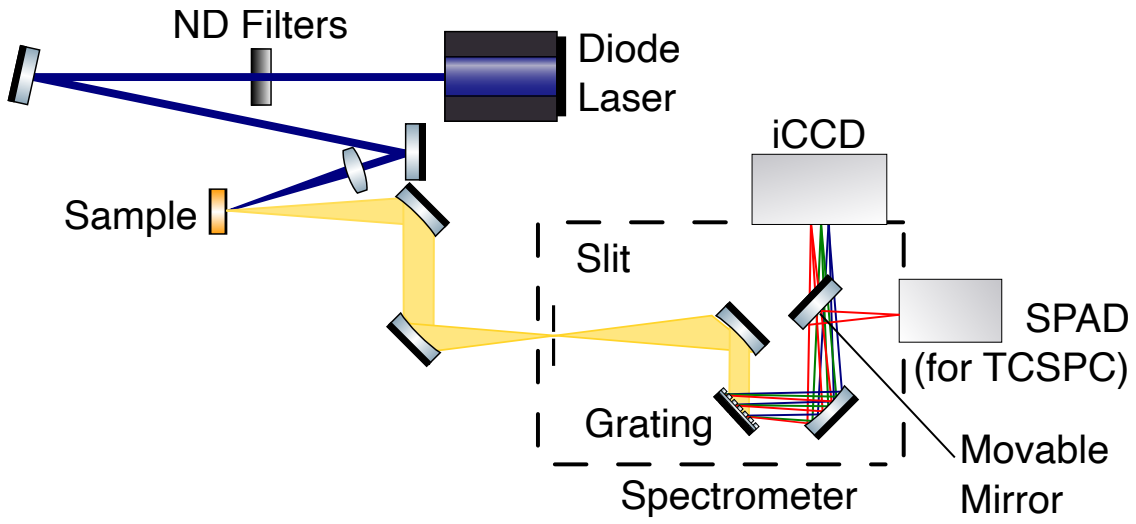


Figure 3.1: Schematic diagram of the experimental setup used for steady-state and time-resolved photoluminescence measurements. The PL is collimated and focused by lenses into the spectrometer, which makes use of a diffraction grating to separate the wavelengths present in the PL spectrum. The wavelength-separated PL is then directed onto the iCCD or Single-Photon Avalanche Diode (SPAD), depending on the position of the movable mirror.

all of the TCSPC measurements presented in Chapters 4, 5 and 6, operated under pulsed excitation, and the collection of the emitted PL photons was done as described in Section 3.2.1. An adjustable mirror within the spectrometer (Princeton Instruments, SP-2558) was used to direct the measured PL onto a single-photon avalanche diode (SPAD, PDM series from MPD) for TCSPC measurements. Signal timing in the TCSPC setup was controlled by a PicoHarp 300 TCSPC Event Timer.

3.2.2.1 Fitting to TCSPC Data

As outlined Section 2.1.2, the rate of radiative recombination in semiconductors is equal to $k_2 n(t)^2$, where k_2 is the bimolecular recombination rate constant, n is the photoexcited charge-carrier density, and t is time. Given that TCSPC measurements record photons emitted following photoexcitation, this technique only measures photons arising from radiative recombination, which should follow a time dependence proportional to $k_2 n(t)^2$ [253]. Thus, a functional expression for the PL intensity is used to fit to the TCSPC data, for which two alternative approaches can be used.

In the case where the charge-carrier density is very low, the overall recombination rate in Equation 2.2 is dominated by contributions from the monomolecular recombination rate $k_1 n$, and so the charge-carrier dynamics can be approximated as:

$$\frac{\mathrm{d}n}{\mathrm{d}t} = -k_1 n. \tag{3.5}$$

Solving Equation 3.5 yields $n(t) = n_0 e^{-k_1 t}$, where n_0 is the initial photoexcited charge carrier density. Then, given that the PL intensity is proportional to $k_2 n(t)^2$, the overall intensity can be described by:

$$\mathrm{PL} \propto k_2 n(t)^2 = k_2 n_0^2 e^{-2k_1 t}. \tag{3.6}$$

In order to minimise the number of free parameters, the initial amplitude of TCSPC is typically normalised to a value of 1. By taking the natural logarithm of Equation

3.6, the overall PL decay can then be described by:

$$\ln\left(\mathrm{PL}\right) \propto -2k_1 t. \tag{3.7}$$

Thus, by fitting the gradient of the logarithm of TCSPC data plotted against time, measured with a low excitation fluence or at long times (> tens of nanoseconds) following photoexcitation, the value of k_1 can be obtained.

Alternatively, in situations where there may be a distribution of monomolecular (trap-mediated) recombination rates, such as when there are a variety of traps with different depths and associated trapping rates, the charge-carrier population can be better described using a stretched exponential [254]. In this case, the charge-carrier density $n(t)$ can be described by:

$$n(t) = n_0 e^{-\left(\frac{t}{\tau_{\mathrm{char}}}\right)^{\beta}}. \tag{3.8}$$

Here τ_{char} is the characteristic lifetime of the decay, and β is the stretching exponent, which can take a value between 0 and 1. In the case of $\beta = 1$, the decay is simply monoexponential; deviations from this value indicate increasingly heterogeneous decays. Given that the measured PL intensity is still proportional to $k_2 n(t)^2$, the logarithm of the PL intensity is now proportional to:

$$\ln\left(\mathrm{PL}\right) \propto -\left(\frac{2t}{\tau_{\mathrm{char}}}\right)^{\beta}. \tag{3.9}$$

As above, by plotting and fitting to the TCSPC data on a log-linear scale, the characteristic lifetime and stretching parameter can be extracted. The weighted 'average' lifetime for the decay can then be calculated as $\tau_{\mathrm{av}} = \frac{\tau_{\mathrm{char}}}{\beta}\Gamma\left(\frac{1}{\beta}\right)$ [254], where Γ is the gamma function.

3.3 Terahertz Spectroscopy

Terahertz spectroscopy enables non-contact investigations of a material in the frequency range 0.1 – 10 THz (3.3 – 333 cm^{-1} or 0.4 – 40 meV) using THz radiation pulses generated

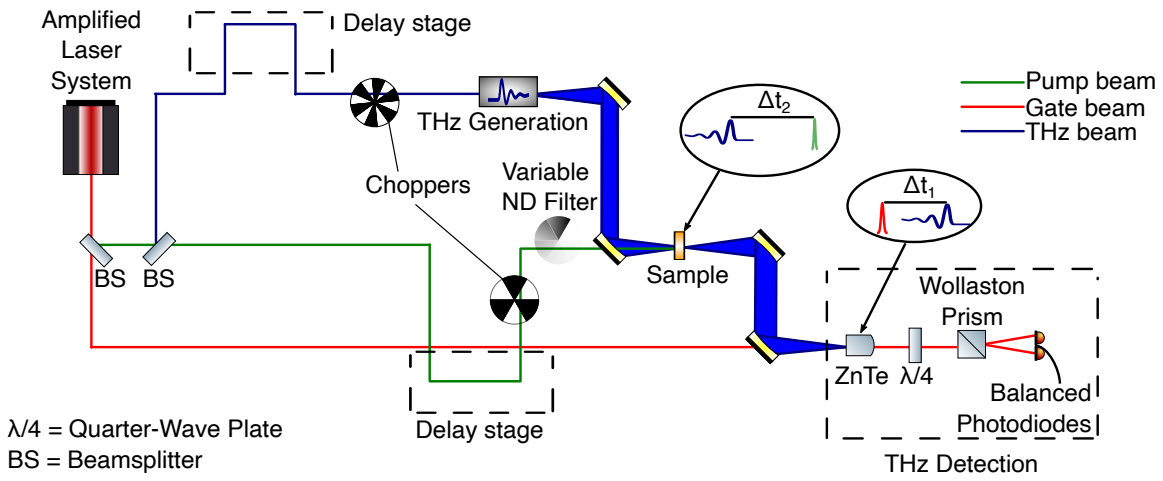


Figure 3.2: Schematic diagram of the experimental setup used for THz spectroscopy measurements. The green, red and blue lines correspond to the pump, gate and THz beam paths, respectively.

with amplified laser systems with pulse widths on the order of tens of femtoseconds [255]. These characteristics make terahertz spectroscopy ideal for investigating the frequency dependence of a material's absorption, dielectric function and photoconductivity in the far-infrared range. Terahertz spectroscopy can be done as simple Time-Domain THz Spectroscopy (TDTS), to investigate properties of the material at equilibrium, or in a time-dependent multi-pulse Optical-Pump Terahertz-Probe (OPTP) measurement, which gives information on charge-carrier dynamics on ultrafast (sub-picosecond) timescales - much faster than what is typically available using PL-based spectroscopy, outlined above, due to the exploitation of optical gating methods for THz detection that provide sub-picosecond time resolution. When applied to metal-halide perovskites, THz spectroscopy has been used to investigate charge-carrier mobilities [50, 256] and recombination dynamics [97], and the phonon modes [175] and background doping densities [31, 182] present in semiconductors, demonstrating the wide range of uses for this experimental technique. A schematic of a typical THz spectroscopy system is shown in Figure 3.2.

3.3.1 Time-Domain Terahertz Spectroscopy (TDTS)

In TDTS a sample is probed by a short pulse $E(t)$ of THz radiation, with the electric field detected as a function of time (spectral information can then be obtained *via* a Fourier transform of the time-dependent electric field strength). Two femtosecond-duration laser pulses are used for TDTS: one is used to generate THz radiation, and the other is used as a 'gate' or detection pulse. The THz pulse is sent through the thin-film sample before being focused onto a detection crystal, where it is spatially and temporally overlapped with the gate beam. Detection occurs via free space electro-optic sampling [255, 257], allowing for high temporal resolution that is limited by the width of the gate pulse ($\sim 35\,\text{fs}$). By varying the time delay Δt_1 between the THz and gate beams (done using a motorised optical delay stage along the THz generation line), different temporal 'slices' of the THz pulse can be detected, allowing for detection of the full THz pulse $E(t)$ lasting $\sim 1\,\text{ps}$.

3.3.2 Optical-Pump Terahertz-Probe Spectroscopy (OPTPS)

OPTP spectroscopy measures the differential change in transmitted THz field, $-\Delta T/T$, when a thin film sample is photoexcited by a pulsed laser beam. Thus, the sample is photoexcited using an optical 'pump' pulse, before being 'probed' with a THz pulse, so that THz transmission through the photoexcited sample can be measured. By varying the time delay Δt_2 between the pump and probe beams, done using a motorised delay stage along the pump beam line, information about the sample can be obtained at different times following photoexcitation, up to a maximum delay of approximately 1 nanosecond, limited by the length of the delay stage.

Two types of scans are typical for OPTP spectroscopy. 'Pump' scans fix THz delay stage to the point of maximum amplitude of the THz field, and then vary the delay time between the optical pump and THz probe beams, enabling the measurement of decays in THz photoconductivity. By varying the excitation fluence for a pump scan, using a variable

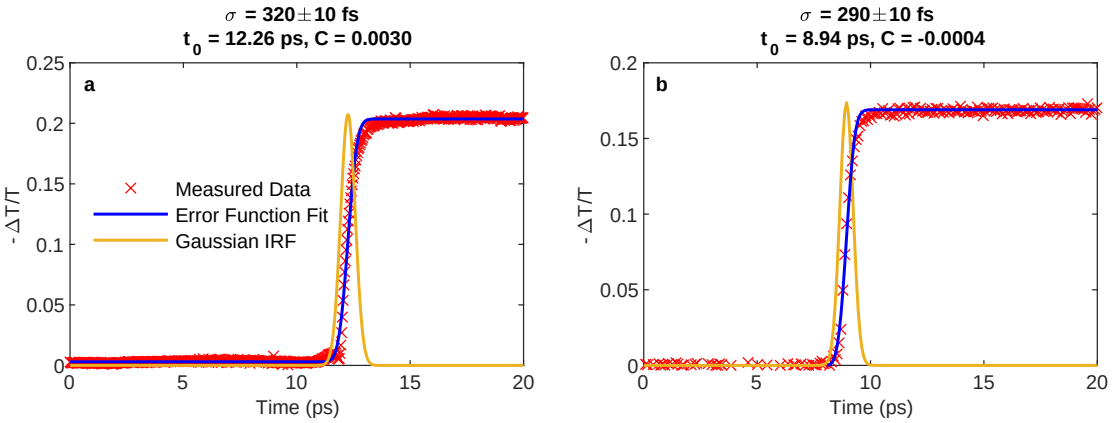


Figure 3.3: Measurement of IRF for OPTPS. Early-time OPTPS onsets for a 2 mm-thick wafer of high-resistivity silicon, pumped at 800 nm at fluences of 17.7 (a) and 14.7 μJcm^{-2} (b), for the two OPTP experimental systems used in this thesis. The data are fitted with an error function in order to extract an estimate of the instrument response function of our OPTP system. The resulting Gaussian IRFs have spreads of 320 and 290 fs, much shorter than the dynamics observed in the thin films measured in all experimental chapters.

neutral-density filter wheel, charge-carrier dynamics in a thin film can be investigated at different excitation intensities, giving insights into bi- and tri-molecular charge-carrier recombination processes. Alternatively, the pump-probe delay time can be fixed at a specific delay, and then the delay time between the gate and probe beams is varied. As in TDTS this allows for the measurements of a spectrum in the THz frequency range, but in this case at a specific time following photoexcitation, yielding a photoconductivity spectrum that gives insights into the nature of photoexcited species within a material.

3.3.2.1 Time resolution and instrument response of OPTPS

The time resolution of an OPTPS system will depend on both the duration of the laser pulses and their temporal stretching, introduced by components along the beam paths (mirrors, lenses, conversion crystals). An estimation of the time resolution (or instrument response function, IRF) of an OPTP system can be obtained by measuring the rise time at low fluences for a highly conductive sample with very high precision, where the increase in photoconductivity upon photoexcitation should be similar to the pulse duration of the pump pulse ($\sim$ 35 fs) and can therefore be regarded as near-instantaneous.

This was carried out for both OPTP systems used in this thesis using a substrate of high-resistivity silicon. These data were then fitted with an error function, via an equation of the form:

$$\mathrm{F}(x) = A\left(1 - \mathrm{Erf}(B(x - C))\right) + D \tag{3.10}$$

where A, B, C and D are fitting constants and the error function is defined as:

$$\mathrm{Erf}(x) = \frac{2}{\sqrt{\pi}} \int_0^x e^{-t^2} dt. \tag{3.11}$$

This timing is then converted into a Gaussian temporal broadening to simulate the IRF of the experimental systems:

$$\mathrm{G}(x) = \alpha e^{-\left(\frac{(x-\beta)}{\sqrt{2}\sigma_{\mathrm{IRF}}}\right)^2}. \tag{3.12}$$

where the broadening constant σ_{IRF} is related to the fitted value B by $\sigma_{\mathrm{IRF}} = 1/\left(\sqrt{2}B\right)$, α is the amplitude and β is the offset in time (equivalent to C).

This approach yields the IRFs shown in Figure 3.3, with $\sigma_{\mathrm{IRF}} = 320$ and 290 fs for the two experimental systems used in the presented studies. Although these values are slower than the laser pulse duration of the amplified laser systems used (~ 35 fs), this is still much faster than all of the charge-carrier dynamics investigated in this thesis.

3.3.3 Details of experimental system

A schematic version of the experimental systems used to measure the THz spectroscopy data presented in this thesis is shown in Figure 3.2. The systems both made use of a spintronic emitter, which relies on the inverse spin Hall effect [258], to generate THz pulses. The emitter was composed of 2 nm of tungsten / 1.8 nm of $Co_{40}Fe_{40}B_{20}$ / 2 nm of platinum, supported by a quartz substrate and magnetically biased by two permanent magnets. The cobalt-iron-boron layer is ferromagnetic, whereas the metal layers are not. When the tri-layer structure is illuminated by a femtosecond excitation pulse, the

differences in charge-carrier lifetimes and transport properties lead to a current through the emitter which has a net spin [258]. When this current enters the non-ferromagnetic layer, spin-orbit coupling leads to a spatial separation of spin-up and spin-down charge carriers in the direction of the external magnetic field, creating an ultrafast transverse current density that gives rise to THz radiation [258].

Detection of the THz pulses transmitted through the sample took place through free-space electro-optic sampling [255, 257]. The detection system is made up of a detection crystal (in this case a 1 mm thick crystal of ZnTe cut along the (110) axis), a quarter-wave plate, a polarising beamsplitter and a pair of balanced photodiodes. The electro-optic effect in the ZnTe crystal is a linear process, therefore the refractive index of the crystal along one axis will vary linearly when a THz electric field is applied. Thus, when the femtosecond 'gate' pulse passes through at the same time as the THz pulse, the polarisation of the gate pulse is altered in proportion to the electric field strength of the THz pulse.

The gate pulse then passes through a quarter-wave plate, which allows for control over the relative polarisation of the gate pulse, and a Wollaston prism, which separates out the gate pulse into two beams with orthogonal linear polarisations. The two linearly-polarised beams are then directed onto a pair of balanced photodiodes, and the quarter-wave plate is used to ensure that the photodiodes are balanced when the THz electric field strength is zero. Changes in the THz electric field within the ZnTe detection crystal lead to a deviation from equilibrium, registered as a positive or negative voltage on the photodiodes, allowing for for full time dependence of the electric field strength (and therefore, of both the phase and amplitude information) of the THz pulse to be obtained.

The voltage produced by the balanced photodiodes is a periodic signal with a frequency equivalent to that of the gate beam and overall amplified laser system f, in this case 5 kHz. The THz beam is mechanically chopped at a frequency $f/2$, allowing for a differential measurements with the THz beam 'on' or 'off' to be taken, calculated as

Chapter	Amplified Laser System	Central Wavelength	Pulse Duration	Repetition Rate	Optical Pump Wavelength and Generation Method
Chapter 4	Spectra Physics, MaiTai, Ascend, Spitfire	800 nm	35 fs	5 kHz	400 nm, obtained by frequency doubling using a β-barium-borate crystal.
Chapter 5	Spectra Physics, MaiTai, Empower, Spitfire	800 nm	35 fs	5 kHz	400 nm, obtained by frequency doubling using a β-barium-borate crystal.
Chapter 6	Spectra Physics, MaiTai, Ascend, Spitfire	800 nm	35 fs	5 kHz	400 nm, obtained by frequency doubling using a β-barium-borate crystal. 500, 585 nm, obtained as output from an optical parametric amplifier (Light Conversion: TOPAS-C), pumped with 800 nm-wavelength excitation from the amplified laser system.

Table 3.1: Summary of THz spectroscopy systems used for the three experimental chapters of this thesis.

$T = T_{\mathrm{THzOn}} - T_{\mathrm{THzOff}}$. In addition, the optical pump beam is mechanically chopped at a frequency $f/4$, giving a modulation for every pair of THz pulses and allowing for the calculation of $\Delta T = (T^{\mathrm{PumpOn}}_{\mathrm{THzOn}} - T^{\mathrm{PumpOn}}_{\mathrm{THzOff}}) - (T^{\mathrm{PumpOff}}_{\mathrm{THzOn}} - T^{\mathrm{PumpOff}}_{\mathrm{THzOff}})$. This signal is measured using box-car averaging [259], which integrates the signal over a defined time-window and can be varied in order to maximise the signal-to-noise ratio.

Measurements were carried out in an evacuated box held at a pressure below 10^{-2} mbar. Summaries of the experimental systems used in Chapters 4, 5 and 6 are outlined in Table 3.1.

3.3.4 Calculation and modelling of dielectric function in the THz frequency range

By comparing the frequency-dependent THz field transmitted through a thin film sample ($E_{\mathrm{sam}}(\omega)$) to that transmitted through a blank z-cut quartz substrate ($E_{\mathrm{ref}}(\omega)$), the relative

transmitted THz amplitude can be calculated as $T(\omega) = E_{\text{sam}}(\omega)/E_{\text{ref}}(\omega)$. Further, in order to account for variations in the thickness of the z-cut quartz substrates, a phase factor can be included, giving the following final expression for $T(\omega)$:

$$T(\omega) = \frac{E_{\text{sam}}(\omega)}{E_{\text{ref}}(\omega)} e^{\frac{-i\Delta d(n_s-1)\omega}{c}}, \tag{3.13}$$

where $\Delta d = d_{\text{sam}} - d_{\text{ref}}$ is the difference of the thickness of the two substrates, $n_s = 2.13$ is the refractive index of quartz in the THz frequency regime [260], and c is the speed of light.

Typically, thin films of the metal-halide materials studied in this thesis have a thickness much less than the wavelength in the THz range (i.e. $d_{\text{sam}} << \lambda_{\text{THz}}$) and the underlying quartz substrate is thicker than the wavelength in the THz range (i.e. $d_{ref} > \lambda_{\text{THz}}$). The dielectric function in vacuum can then be calculated as [261]:

$$\epsilon(\omega) = \frac{ic(1+n_s)}{\omega d_{\text{sample}}} \left(\frac{1}{T(\omega)} - 1 \right) + 1. \tag{3.14}$$

The dielectric response of a material can be modelled through Lorentzian fitting of the spectra as the sum of contributions from n phonon modes that are present in the measured spectral range, and the high-frequency response ϵ_∞:

$$\epsilon\left(\omega\right) = \sum_{i=1}^{n} \epsilon_{\text{ph}}^{(i)}\left(\omega\right) + \epsilon_\infty. \tag{3.15}$$

Here the contribution from each phonon mode can be modelled as a Lorentzian oscillator, which results in the following expression for the Drude-Lorentz dielectric response [250]:

$$\epsilon_{\text{ph}}(\omega) = -\Delta\epsilon_s \frac{\omega_0^2}{\omega^2 - \omega_0^2 + i\gamma\omega}, \tag{3.16}$$

where $\Delta\epsilon_s$ is the contribution of the phonon mode to the static (zero-frequency) value of the dielectric function, ω_0 is its (angular) resonance frequency, and γ is its broadening parameter (half line width). The overall static value of the dielectric function, with two phonon modes present (as used in Chapter 6), can thus be calculated as:

$$\epsilon_s = \epsilon_\infty + \Delta\epsilon_s^1 + \Delta\epsilon_s^2. \tag{3.17}$$

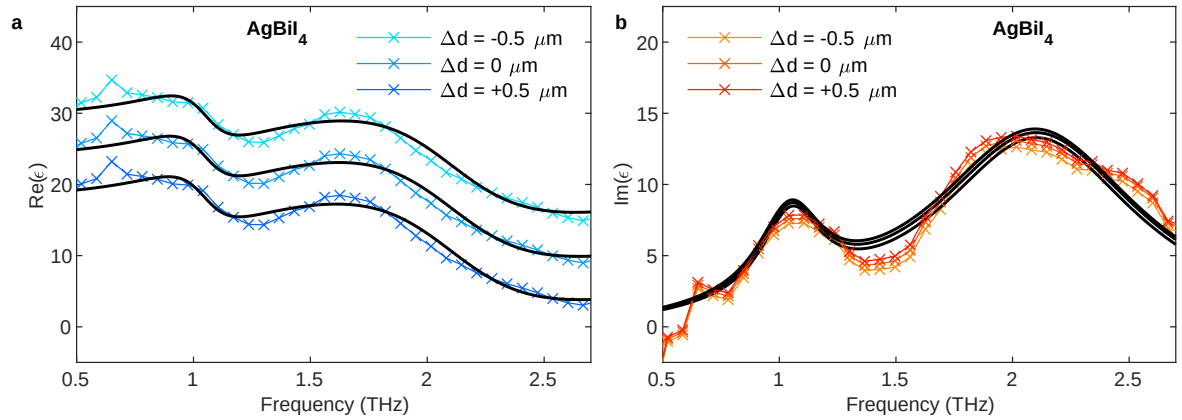


Figure 3.4: Impact of difference in substrate thickness, Δd, on dielectric function calculations. (a) Real part of the dielectric function in the THz frequency range for a thin film of $AgBiI_4$, calculated using values of $\Delta d = -0.5, 0, +0.5\,\mu m$ for the variations in substrate thickness (lighter to darker shades of blue, fits in black). Changing the value of Δd leads to substantial vertical offsets in the real part of the dielectric function, influencing the values of ϵ_∞^{THz} and ϵ_s^{THz}. (b) Imaginary part of the dielectric function in the THz frequency range, calculated using values of $\Delta d = -0.5, 0, +0.5\,\mu m$ (lighter to darker shades of red, fits in black). Variations in Δd do not lead to substantial variations in phonon peak frequencies or broadenings.

It should be noted that the correction to account for the difference in substrate thickness, Δd, leads to variations in the final shape of the real and imaginary parts of the dielectric function, and thus to the values obtained from the fits. As has been shown by La-O-Vorakiat et al. [262], variations in the value of Δd lead to very minor changes in the imaginary part of the dielectric function (and thus in the values of phonon peak frequencies and broadenings), but influence the real part of the dielectric function more substantially (and thus the extracted values of ϵ_∞ and ϵ_s). Figure 3.4 shows an example plot of the real and imaginary parts of the THz dielectric function for $AgBiI_4$ for the three values of Δd, with the corresponding fits. The variations in Δd lead to substantial variations in ϵ_∞^{THz} and ϵ_s^{THz} (apparent in the real part of the dielectric function), whereas the peak positions and broadenings vary little (as shown in the imaginary part of the dielectric function).

3.3.5 Direct calculation of the charge-carrier mobility

OPTP measurements can be used to calculate the charge-carrier mobility in a thin film, using a process outlined by Wehrenfennig et al. [97] The charge-carrier sum mobility

is linked to the photoconductivity of a thin film by:

$$\mu = \frac{\Delta S A_{\text{Eff}}}{Ne}. \tag{3.18}$$

Here ΔS is the sheet conductivity of the film, A_{Eff} is the effective overlap area of the optical pump and THz probe beams, N is the number of photoexcited free charge carriers, and e is the elementary charge.

Given that THz wavelengths are both much longer than the thickness of typical thin film samples ($\lambda_{THz} >> d_{sam}$), and also shorter than the quartz substrate thickness ($\lambda_{THz} < d_{sub}$), the following approximation for the sheet photoconductivity of a thin film between two media with refractive indeces n_A and n_B can be used [263]:

$$\Delta S = -\epsilon_0 c(n_A + n_B)\left(\frac{\Delta T}{T}\right). \tag{3.19}$$

Here $\Delta T = (T^{\text{PumpOn}}_{\text{THzOn}} - T^{\text{PumpOn}}_{\text{THzOff}}) - (T^{\text{PumpOff}}_{\text{THzOn}} - T^{\text{PumpOff}}_{\text{THzOff}})$ is the photoinduced change in the transmitted THz electric field, as outlined above, and the refractive indeces of the media on either side of the thin film are $n_A = 1$ for vacuum and $n_B = 2.13$ for a z-cut quartz substrate.

The number of photoexcited charge-carrier pairs can be determined as:

$$N = \phi \frac{E\lambda}{hc}\left(1 - R_{\text{pump}}(\lambda) - T_{\text{pump}}(\lambda)\right), \tag{3.20}$$

where E is the energy contained in an optical excitation pulse of wavelength λ, R_{pump} and T_{pump} are the sample reflectance and transmittance at the pump wavelength, and ϕ is the branching ratio of photons-to-free-charges.

Equations 3.19 and 3.20 can be substituted into 3.18 in order to obtain:

$$\phi\mu = -\epsilon_0 c(n_A + n_B)\frac{A_{\text{Eff}} hc}{Ee\lambda\left(1 - R_{\text{pump}}(\lambda) - T_{\text{pump}}(\lambda)\right)}\left(\frac{\Delta T}{T}\right). \tag{3.21}$$

Given that the branching ratio $0 \leq \phi \leq 1$, the calculated effective charge-carrier mobility is always a lower bound of the actual value; it is only identical to the true free-carrier

mobility when there is full conversion of photons to charges. Further, the determined charge-carrier mobility arises from contributions to the conductivity from both free electrons and free holes, and these cannot be separated, meaning that all reported values of charge-carrier mobilities in this thesis are the sum of electron and hole mobilities.

For very high excitation fluences ($> 50\,\mu\text{Jcm}^{-2}$) the proportionality between $\Delta T/T$ and μ no longer holds, due to both non-linear processes such as two-photon absorption, and also as the build-up of charge carriers in their respective bands leads to a probing of the non-parabolic elements of the band structure [97]. Mobilities are thus calculated from the initial photoconductivity value (just after photoexcitation) for fluences below this value.

3.3.6 Fitting to OPTP transient decays

3.3.6.1 Long-time (nanosecond) fitting

This section describes the method used to analyse and fit OPTP transient decays over long timescales, out to several hundred picoseconds. This approach is used for data analysis in Chapters 4 and 6. As outlined in Section 2.1.2, the overall charge-carrier dynamics in a metal-halide semiconductor can be approximately described by the following differential equation:

$$\frac{\mathrm{d}n}{\mathrm{d}t} = -k_1 n - k_2 n^2 - k_3 n^3. \tag{3.22}$$

Here n is the number of charge-carrier pairs and k_1, k_2 and k_3 are the recombination rate constants for mono-, bi-, and tri-molecular processes, respectively. For the studies presented in this thesis, the density of photoexcited charge carriers is always low enough that trimolecular Auger recombination can be neglected. Thus, setting $k_3 = 0$ yields the following differential equation:

$$\frac{\mathrm{d}n}{\mathrm{d}t} = -k_1 n - k_2 n^2. \tag{3.23}$$

This equation has an analytical solution given by:

$$n(t) = \frac{k_1 A}{e^{k_1 t} - k_2 A} \tag{3.24}$$

where A can be related to the initial charge-carrier density n_0 as:

$$\frac{1}{A} = \frac{k_1}{n_0} + k_2. \tag{3.25}$$

Thus, at $t = 0$, one obtains the value $n(t = 0) = n_0$.

The change in transmitted THz radiation, $\frac{\Delta T}{T}(t) \equiv x(t)$ is proportional to the free charge-carrier density in the thin film:

$$n(t) = \phi C x(t). \tag{3.26}$$

Here ϕ indicated the number of free charge-carriers per photon, and $C = \tilde{n}_0/x(0)$ is the proportionality factor between the initial THz response $x(0)$ and the absorbed photon density $\tilde{n}_0$, given by:

$$\tilde{n}_0 = \frac{E\lambda\alpha(\lambda)}{hcA_{\text{Eff}}} \left(1 - R_{\text{pump}}(\lambda)\right). \tag{3.27}$$

Here $\alpha(\lambda)$ is the absorption coefficient at the photoexcitation wavelength λ, which along with the reflection coefficient can measured for each sample. The effective overlap area A_{Eff} can be calculated from the pump and probe beam parameters as $A_{\text{Eff}} = 2\pi \left(\sigma^2_{\text{Pump}} + \sigma^2_{\text{THz}}\right)$, where $\sigma_{\text{Pump/THz}}$ are the broadening parameters for the pump and THz probe beams. For very high excitation fluences ($> 50\,\mu\text{Jcm}^{-2}$) the proportionality in 3.26 no longer holds; C is therefore determined based on the initial response for fluences below this.

Substituting 3.26 into 3.23 gives:

$$\frac{\mathrm{d}x}{\mathrm{d}t} = -C\phi k_2 x^2 - k_1 x \tag{3.28}$$

$$= -B_2 x^2 - B_1 x. \tag{3.29}$$

Analytical solutions to this ODE are fitted globally to the decays across all fluences in order to extract the rate constants B_i. Given the influence of the photon-to-free-charge conversion ratio ϕ, only the apparent bimolecular recombination rate ϕk_2 can be determined. Just as for the charge-carrier mobility, given that $0 \leq \phi \leq 1$ the values presented for k_2 in the results chapters are thus underestimates of the true values.

Finally, in order to account for an initial spatially varying charge-carrier density (due to absorption following the Beer-Lambert law), the fitting algorithm takes into account an exponentially decaying charge-carrier density. This is done by dividing the sample into 30 equally thick slices and computing the decay function for each of these individually.

3.3.6.2 Early-time fitting in cases of charge-carrier localisation

This section describes the method used to analyse and fit OPTP transient decays over very short timescales, corresponding to the first few picoseconds following photoexcitation, for a system where an ultrafast decrease in photoconductivity (corresponding to charge-carrier localisation) is observed. This approach is used for data analysis for the temperature-dependent OPTP data presented in Chapter 5 and for the fluence-dependent OPTP data presented in Chapter 6.

The simple model used to describe charge-carrier localisation is outlined schematically in Figure 3.5. Charge carriers are initially photoexcited into the conduction band into a free-carrier state with mobility μ_{deloc} and population n_{deloc}. Charge carriers then localise into a state with lowered mobility μ_{loc} and population n_{loc}, with the localisation rate given by k_{loc}. In general, such a three-level system that includes bi- and tri-molecular recombination processes must be solved numerically, but in this case several simplifying assumptions are made in order to fit analytical solutions to the data. There is not a 'delocalization' rate that would allow charges to go from n_{loc} back to n_{deloc}, and it is also assumed that there is no recombination from the delocalized carrier state down to the

ground state. Further, the rate of charge-carrier recombination from the localized state back to the ground state is assumed to be limited by monomolecular recombination, with no higher-order contributions. Finally, it is assumed that all photoexcited carriers begin in the free state, such that $n_{\mathrm{deloc}}(t=0) = n_0$ and $n_{\mathrm{loc}}(t=0) = 0$.

The simplified model outlined above can be described using a set of coupled rate equations:

$$\frac{\mathrm{d}n_{\mathrm{deloc}}}{\mathrm{d}t} = -k_{\mathrm{loc}} n_{\mathrm{deloc}} \tag{3.30}$$

$$\frac{\mathrm{d}n_{\mathrm{loc}}}{\mathrm{d}t} = -k_1 n_{\mathrm{loc}} + k_{\mathrm{loc}} n_{\mathrm{deloc}}. \tag{3.31}$$

These are straightforward to solve analytically, with the solutions given by:

$$n_{\mathrm{deloc}}(t) = n_0 e^{-k_{\mathrm{loc}} t} \tag{3.32}$$

$$n_{\mathrm{loc}}(t) = n_0 \frac{k_{\mathrm{loc}}}{k_{\mathrm{loc}} - k_1} \left(e^{-k_1 t} - e^{-k_{\mathrm{loc}} t} \right). \tag{3.33}$$

These solutions yield a charge-carrier density (per unit volume), which must be converted into a sheet photoconductivity to then be fitted to the $\Delta T/T$ transient decays measured using OPTP spectroscopy.

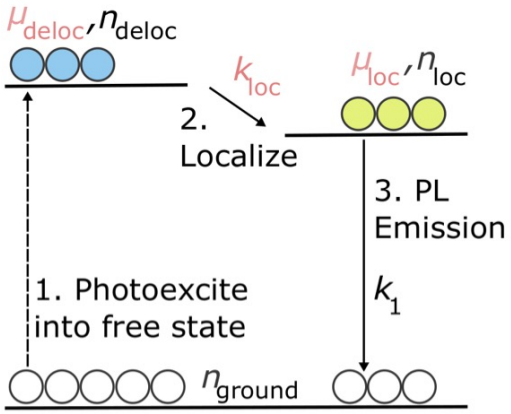


Figure 3.5: Schematic of the two-level mobility model used to fit the OPTP decays Chapters 5 and 6. The dotted line indicates the initial photoexcitation of charges, in this case due to pulsed laser excitation.

The photoconductivity of a material with n photoexcited charge-carriers per unit volume, with charge q and mobility μ, is given by:

$$\Delta\sigma = nq\mu. \tag{3.34}$$

In this case, where there are contributions from two different states, the overall photoconductivity is given by:

$$\Delta\sigma = e\left(n_{\text{deloc}}\mu_{\text{deloc}} + n_{\text{loc}}\mu_{\text{loc}}\right). \tag{3.35}$$

In order to calculate our initial number of photoexcited charge-carriers, the expression in Equation 3.20 can be used. To convert this into a charge-carrier density per unit volume, this was divided by the effective overlap area of the optical pump and THz probe beams, and the thickness of the sample, such that:

$$n_0 = \frac{N}{d_{\text{film}}A_{\text{Eff}}}. \tag{3.36}$$

As outlined above, for a thin film on a thick quartz substrate, the expression in Equation 3.19 can be used to relate the sheet photoconductivity in the thin film to the measured $\Delta T/T$ signal. Thus, the overall $\Delta T/T$ signal can be described using the following analytical form:

$$\frac{\Delta T}{T} = \frac{-n_0 ed}{\epsilon_0 c\left(n_A + n_B\right)}\left(\left(\mu_{\text{deloc}} - \frac{\mu_{\text{loc}}k_{\text{loc}}}{k_{\text{loc}} - k_1}\right)e^{-k_{\text{loc}}t} + \frac{\mu_{\text{loc}}k_{\text{loc}}}{k_{\text{loc}} - k_1}e^{-k_1 t}\right). \tag{3.37}$$

In order to account for the Instrument Response Function of the OPTP system used here (see Section 3.3.2.1), the expression in Equation 3.37 is convolved with a normalised Gaussian pulse with a fixed broadening parameter (or width) of σ_{IRF}, depending on the experimental system used. Accounting for an offset in time t_0, the overall expression used to fit the OPTP data is thus:

$$\frac{\Delta T}{T}(t-t_0) = \frac{-en_0 d_{\text{film}}}{2\epsilon_0 c(n_A + n_B)}\left\{\left(\mu_{\text{deloc}} - \frac{\mu_{\text{loc}}k_{\text{loc}}}{k_{\text{loc}} - k_1}\right)e^{-k_{\text{loc}}(t-t_0)+\frac{k_{\text{loc}}^2\sigma_{\text{IRF}}^2}{2}}\,\text{Erfc}\left(\frac{k_{\text{loc}}\sigma_{\text{IRF}}^2 - (t-t_0)}{\sqrt{2}\sigma_{\text{IRF}}}\right)\right.$$
$$\left. + \frac{\mu_{\text{loc}}k_{\text{loc}}}{k_{\text{loc}} - k_1}e^{-k_1(t-t_0)+\frac{k_1^2\sigma^2}{2}}\,\text{Erfc}\left(\frac{k_1\sigma_{\text{IRF}}^2 - (t-t_0)}{\sqrt{2}\sigma_{\text{IRF}}}\right)\right\}. \tag{3.38}$$

Here Erfc(x) is the complementary error function, defined as:

$$\mathrm{Erfc}(x) = \frac{2}{\sqrt{\pi}} \int_x^\infty e^{-t^2} dt. \tag{3.39}$$

3.3.7 Drude factor calculation for photoconductivity

The Drude model for the photoconductivity of free carriers with short momentum scattering time in a solid yields a flat, zero-valued imaginary part of the photoconductivity in the THz regime [250, 261, 263]. In order to quantify deviations from this model, a 'Drude Factor' can be calculated as [174]:

$$f_{\mathrm{Drude}} = \frac{1}{x} \sum_1^x \frac{\sqrt{\mathrm{Re}\left(\Delta T/T\right)^2}}{\sqrt{\mathrm{Re}\left(\Delta T/T\right)^2 + \mathrm{Im}\left(\Delta T/T\right)^2}}. \tag{3.40}$$

Here $\Delta T/T = \frac{T_{\mathrm{On}} - T_{\mathrm{Off}}}{T_{\mathrm{Off}}}$ is the change in THz transmission at each frequency point, and x is the total number of points in frequency space across which the 'Drude Factor' is calculated. In the case of ideal Drude-like conductivity, $f_{\mathrm{Drude}} = 1$, and deviations indicate other contributions e.g. from localized charge-carrier states [263]. This parameter is calculated for the silver-bismuth-halide materials studied in Chapters 5.

3.4 X-Ray Diffraction

X-ray diffraction experiments involve the measurement of elastically scattered X-rays off a thin film of material with a crystalline structure. X-rays have a wavelength on the order of 0.1 – 10 nm, very similar to the length scales associated with the lattice spacings in perovskite and metal-halide materials. This similarity in length scales mean that the scattering of X-rays off a crystalline material will lead to interference patterns. In the simplest possible case, where layers of atoms in a material are separated by a distance d, then Bragg's Law dictates that the scattering angle 2θ between the incoming and scattered beams obeys the following relationship [264]:

$$2d \sin\theta = p\lambda. \tag{3.41}$$

Here p is an integer and λ is the wavelength of the incident X-ray beam. Thus, by carrying out experiments where λ is known and fixed, and varying θ, information about the crystal structure of a material can be obtained. For real-life materials there are several additional complicating factors: the precise dimensions of the unit cell, location of atoms within the unit cell and the symmetry of the crystal lattice will all influence the measured interference pattern of the X-rays [264]. Thus, careful measurement and analysis of XRD patterns can yield valuable insights into the crystal structure of new materials.

When considering the crystal structure of MHPs, often links are drawn between the crystallinity of a material, the level of energetic disorder present within the states available to photoexcited charge carriers, and various optoelectronic properties of MHPs. In such cases, crystallinity should be thought of as the fraction of a material that possesses long-range order and is not amorphous. Thus, materials with low crystallinity will have a high proportion of amorphous material, and correspondingly weak intensities on a measured XRD pattern, whereas highly crystalline materials will have strong diffraction peaks indicating a large degree of long-range order in the material.

For all XRD measurements presented in this thesis, a PANalytical X'Pert powder X-ray diffractometer was used, with a Cu-$K_{\alpha 1}$ source. In order to correct against sample tilt, a relevant z-cut quartz peak in the data, present for all of the samples deposited on z-cut quartz substrates, was used as a reference and fixed to 2θ =16.43°.

3.4.1 Pawley Fitting

Pawley fitting is a process in which observed peaks in a powder pattern are fitted at 2θ values that are constrained by the unit cell and symmetry of the lattice [265–267]. A unit cell is first used to generate the initial set of reflections expected in a measured XRD pattern, and the peak positions are then adjusted by refining the lattice parameters that define the unit cell. Following this, the heights of individual peaks are

individually refined, and the background, peak shapes and instrument response/correction parameters are also refined, to allow for a full description of the measured XRD pattern. Pawley fitting is a useful precursor to Rietveld fitting [268, 269], which requires a full structural model of a material, and gives an indication of the 'best fit possible' from an eventual full structural refinement.

3.5 Sample Fabrication

3.5.1 $BA_x(FA_{0.83}Cs_{0.17})_{1-x}Pb(I_{0.6}Br_{0.4})_3$ Thin Films used in Chapter 4

Z. Wang (Department of Physics, University of Oxford) carried out the fabrication of $BA_x(FA_{0.83}Cs_{0.17})_{1-x}Pb(I_{0.6}Br_{0.4})_3$ thin films outlined in this section.

First, a $(FA_{0.83}Cs_{0.17})Pb(I_{0.6}Br_{0.4})_3$ precursor solution was prepared by dissolving formamidinium iodide (FAI; Dyesol), caesium iodide (CsI; Alfa Aesar), lead iodide (PbI_2; TCI) and lead bromide ($PbBr_2$; TCI) in anhydrous N,N-dimethylformamide (DMF; Sigma-Aldrich) to obtain a stoichiometric solution. The solution was then stirred overnight in a nitrogen-filled glovebox.

Then, 69 µl of hydroiodic acid (HI; Sigma-Aldrich), 57 wt% in H_2O and 34.6 µl of hydrobromic acid (HBr; Sigma-Aldrich), 48 wt% in H_2O was added into 1 ml of 1.2 M $(FA_{0.83}Cs_{0.17})Pb(I_{0.6}Br_{0.4})_3$ precursor solution, and aged for approximately 48 hours under a nitrogen atmosphere without stirring.

In parallel, a $BAPb(I_{0.6}Br_{0.4})_3$ precursor solution was generated by dissolving n-butylammonium iodide (BAI; Dyesol), PbI_2 and $PbBr_2$ in DMF to obtain a stoichiometric solution. This solution was also stirred overnight in a nitrogen-filled glovebox.

Prior to film deposition, the $(FA_{0.83}Cs_{0.17})Pb(I_{0.6}Br_{0.4})_3$ and $BAPb(I_{0.6}Br_{0.4})_3$ precursor solutions were mixed to achieve $BA_x(FA_{0.83}Cs_{0.17})_{1-x}Pb(I_{0.6}Br_{0.4})_3$ with desired BA contents.

The precursor perovskite solution was spin-coated in a nitrogen-filled glovebox at 2000 rpm for 45 s, on a z-cut quartz substrate pre-heated at 80 °C [260]. The films were dried inside the glovebox on a hot plate at a temperature of 70 °C for 60 s. The films were then immediately transferred into an oven and annealed in air at 175 °C for 80 minutes.

3.5.2 Cu_2AgBiI_6 Thin Films used in Chapter 5

G. Longo (Department of Physics, University of Oxford) carried out the fabrication of Cu_2AgBiI_6 thin films outlined in this section.

1.03 mmol of AgI, 1.25 mmol of CuI and 0.877 mmol of BiI_3 were dissolved in 2 ml of a mixture of DMSO and DMF with a 3:1 volume ratio. The BiI_3 was synthesised by H. Sansom, in order to avoid impurities found in commercially available BiI_3 [80]. This non-stoichiometric composition was used as it has experimentally been observed (through X-ray diffraction measurements) to be the only one leading to thin films with the expected composition [84]. The solution was stirred at 150 °C for 30 minutes. The hot solution was filtered with a PTFE syringe filter with 0.22 µm pore size.

The filtered solution was then kept at 75 °C during the entire spin-coating process. The solution was spin-coated on z-cut quartz substrates in a nitrogen-filled drybox, with a speed of 4000 rpm for 60 seconds with 4000 $rpms^{-1}$ acceleration. The spin-coated films were then annealed at 50 °C in air for 45 minutes, and, after this, at 150 °C for 3 minutes.

3.5.3 $Cs_2AgBiBr_6$ Thin Films used in Chapter 5

G. Longo (Department of Physics, University of Oxford) carried out the fabrication of Cu_2AgBiI_6 thin films outlined in this section.

$Cs_2AgBiBr_6$ thin films were prepared through sequential vapour deposition onto z-cut quartz substrates, as reported in Ref. [270]. The precursors were AgBr (99% purity, purchased from Fluka), $BiBr_3$ ($\geq$ 98% purity, purchased from Sigma Aldrich) and CsBr (99.9% purity, purchased from Sigma Aldrich). These precursors were placed in separate

crucibles within a sealed vacuum chamber, and sequentially thermally evaporated onto the substrates. The optimized procedure involved the evaporation of 90 nm of AgBr, 120 nm of $BiBr_3$ and 150 nm of CsBr to obtain $Cs_2AgBiBr_6$ films of 290 nm thickness. The deposited films were annealed on a hotplate in air at 250 °C for 15 minutes to form the desired double perovskite phase of $Cs_2AgBiBr_6$. The successful formation of $Cs_2AgBiBr_6$ thin films by this procedure was confirmed by X-ray diffraction (XRD) of thin films deposited on FTO. The XRD pattern [270] exhibited sharp peaks (indicating high crystallinity) and confirmed the absence of any additional phases or unreacted precursors.

3.5.4 $Cu_{4x}(AgBi)_{1-x}I_4$ Thin Films used in Chapter 6

H. Sansom (Department of Physics, University of Oxford) carried out the fabrication of $Cu_{4x}(AgBi)_{1-x}I_4$ thin films outlined in this section.

AgI, Bi and I_2 powders (Table 3.2) were dissolved in 0.8 ml DMSO by stirring at 140 °C for 15 minutes. In a separate vial CuI powders were dissolved in pyridine by stirring at 140 °C for 15 minutes. The CuI in pyridine solution was quickly filtered through a 0.22 µm pore-size, 13 mm diameter PTFE filter and added to the AgBiI in DMSO solution. The Cu-Ag-Bi-I in DMSO and pyridine solution was stirred for another 15 minutes at 140 °C. The solution was filtered through a 0.22 µm pore-size, 13 mm diameter PTFE filter and left to kept stirring at 100 °C during deposition.

Glass microscope slides cut to size (approx. 24 × 24 mm) and z-cut quartz substrates were sonicated in soap and de-ionised (DI) water for 15 minutes, rinsed with DI water, sonicated in acetone for 15 minutes, sonicated in IPA for 15 minutes, dried using an N_2 gun, and then further cleaned in a UV-Ozone generator for 10 minutes. Following this, the substrates were quickly transferred to a N_2-filled dry box and kept at 150 °C for deposition. 100 µl of the 100 °C Cu-Ag-Bi-I solution was deposited dynamically on to the 150 °C substrate and spun at 4000 rpm for 45 seconds on a spincoater, with the

Nominal x and composition	Solution 1				Solution 2	
	AgI (mg)	**Bi (mg)**	**I_2 (mg)**	**DMSO (ml)**	**CuI (mg)**	**Pyridine (ml)**
0, $AgBiI_4$	157	139	254	0.8	0	0.22
0.09, $Cu_{0.4}AgBiI_{4.4}$	157	139	254	0.8	51	0.32
0.2, $CuAgBiI_5$	157	139	254	0.8	127	0.48
0.33, Cu_2AgBiI_6	157	139	254	0.8	254	0.74
0.6, Cu_6AgBiI_{10}	157	139	254	0.8	762	1.77

Table 3.2: Summary of material and solvent amounts used to create solutions for each of the five compositions investigated in Chapter 6.

amounts of each solution used for each composition outlined in Table 3.2. The films were then annealed at 50 °C for 30 minutes in air, during which the films turned from a clear orange film to a dark red-brown film. The film was then annealed at 150 °C for 5 minutes in air. Films were kept in a nitrogen-filled glovebox until needed for measurements.

4

Interplay of Composition and Optoelectronic Properties of 2D-3D Hybrid Lead-Halide Perovskites

Contents

4.1 Introduction and Background 81
4.2 Experimental Details 83
4.3 Understanding of Butylammonium Inclusion 84
4.4 Main Experimental Results and Discussion 86
4.4.1 Structural changes occuring with increasing BA content 86
4.4.2 Trends in emission and absorption with increasing BA content 88
4.4.3 Material aging and stability against light-induced halide segregation 92
4.4.4 Trap-mediated charge-carrier recombination 97
4.4.5 Bimolecular (band-to-band) charge-carrier recombination . . . 100
4.4.6 Effective charge-carrier mobility and diffusion lengths 106
4.5 Summary and Conclusion 108

Work in this chapter was initially published as: L. R. V. Buizza, T. W. Crothers, Z. Wang, J. B. Patel, R. L. Milot, H. J. Snaith, M. B. Johnston, L. M. Herz. 'Charge-Carrier Dynamics, Mobilities and Diffusion Lengths of 2D-3D Hybrid Butylammonium-Caesium-Formamidinium Lead Halide Perovskites', *Advanced Functional Materials*, **2019**, *29*

(35), 1902656 (Ref. [55]).

4.1 Introduction and Background

The first experimental chapter of this thesis focuses on understanding how the crystal structure and composition of conventional bulk 3D perovskites can be adapted to improve optoelectronic properties, enhancing device performance and stability. As outlined in Chapter 2, MHPs have an excellent mix of optoelectronic properties for applications in solar panel devices, and the most commonly investigated MHP, $MAPbI_3$, has been shown to exhibit shallow trap states [56, 57], low Urbach energies [58], and small phonon energies [59, 60]. Notwithstanding these impressive characteristics, MHP-based solar cells still struggle with stable performance over hundreds to thousands of hours, degrading due to interactions with light and moisture, as well as suffering from thermal instability and light-induced ion migration effects [28, 29, 271]. Attempts at altering the A-site cation by replacing MA with FA, caesium, or their mixtures have led to improved thermal stability and performance of solar cells [42, 272, 273].

A recent innovative step towards materials with higher environmental stability has been the inclusion of two-dimensional (2D) Ruddlesden-Popper phases inside the perovskite films. Here, the addition of larger, hydrophobic organic cations, such as 2-phenylethylammonium (PEA) or butylammonium (BA) to the precursors, leads to the formation of 2D layered structures, whose corner-sharing octahedral planes are separated by bilayers of monovalent organic cations that are too large to be directly incorporated into the ABX_3 perovskite crystal structure [274, 275]. These 2D structures improve moisture-related stability substantially, producing devices that are stable over thousands of hours [100, 276]. However, reduced light absorption and lower charge-carrier mobilities and diffusion lengths, especially in low-p materials (where p is the number of planes of corner-sharing octahedra, separated by large organic cations), can lead

to decreased power conversion efficiencies for Ruddlesden-Popper perovskites, relative to their 3D counterparts [205, 277].

To address these drawbacks, there have been several attempts to combine the beneficial features of 2D and 3D perovskite structures through 2D-3D hybrid structures, which have yielded solar cells achieving high PCEs and excellent stability over thousands of hours [110, 278, 279]. The first attempt at a hybrid structure involved a typical heterojunction device structure, combining $MAPbI_3$ with a Ruddlesden-Popper perovskite top layer that acts as a charge extraction layer and moisture barrier [279]. In another approach the combination of small amounts of aminovaleric acid iodide ($HOOC(CH_2)_4NH_3I$) with the usual MAI and PbI_2 precursors led to the formation of films comprising a thin layer of 2D perovskite, followed by a 2D-3D interface and then a bulk 3D phase [278]. In a third study, the substitution of mixed formamidinium-caesium with butylammonium has been shown to result in a 3D bulk structure interspersed with smaller crystallites that contain a mixture of different 2D Ruddlesden-Popper phases (i.e. with varying p-values), referred to as a 2D-3D heterostructure [110].

In all of these cases, the formation of a 2D-3D hybrid structure leads to some alteration of optoelectronic properties, such as changes in photoluminescence intensity and peak position, as well as longer PL decay lifetimes. It should be noted that there is a clear distinction between uniformly layered Ruddlesden-Popper systems with a well-defined, low value of p, which exhibit relatively strong electronic and dielectric confinement, and such hybrid 2D-3D systems that involve a phase-segregated mixture of mainly 3D perovskite with some small amounts of 2D phase interspersed within or at the boundary of the 3D bulk. Such hybrid 2D-3D systems are targeting the best of both worlds – the enhanced environmental stability of 2D Ruddlesden-Popper phases combined with the favourable electronic properties of 3D bulk MHPs.

To elucidate the influence of electronic confinement on optoelectronic properties, initial studies have investigated the charge-carrier dynamics in layered lead-halide perovskite Ruddlesden-Popper structures with varying p [205, 280]. For such materials with low p values, confinement leads to the enhancement of excitonic peaks observed in absorption spectra and increases in monomolecular recombination rates as p decreases [205]. Further, transient absorption (TA) measurements display a broadening of spectral features with increasing value of p [280]. In both cases, as p increases the optoelectronic behaviour tends towards that of standard bulk 3D lead iodide perovskite. There has also been an initial reporting of TA measurements for 2D-3D heterostructures, with similar features observed for both 2D-3D materials and the associated pure 3D phase [281].

In this thesis chapter an investigation of charge-carrier dynamics, notably recombination rates and mobilities, is presented for the system of 2D-3D hybrid perovskites $BA_x(FA_{0.83}Cs_{0.17})_{1-x}Pb(I_{0.6}Br_{0.4})_3$ with varying BA content ($0 \leq x \leq 0.8$, where x is the molar fraction in the precursor solutions, as described in Chapter 3 Section 3.5). This work provides a systematic investigation of the impact of the 2D-3D hybrid structure on optoelectronic properties across a broad compositional range. The results presented in this chapter help to define a compositional boundary at which hybrid 2D-3D systems approach the behaviour of purely 3D perovskites, which is essential information for the successful implementation of these materials in photovoltaic devices. In particular, knowledge of optimal compositions for large charge-carrier mobilities and reduced charge-carrier recombination rates will allow for an enhanced understanding of how best to tune these 2D-3D hybrid materials for optimized devices.

4.2 Experimental Details

Sample preparation was carried out by Z. Wang, Department of Physics, University of Oxford, as outlined in Section 3.5.

Optical absorption, X-ray diffraction, steady-state and time-resolved photoluminescence, and OPTPS measurements were carried out as described in Chapter 3.

Infrared absorption measurements were taken using the same FTIR spectrometer as outlined in Chapter 3, fitted with a attenuated total reflection (ATR) accessory. A globar light source was used with a nitrogen-cooled photovoltaic HgCdTe (MCT) detector. Measurements were taken with samples placed in air. ATR measurements were carried out by J. B. Patel and L. R. V. Buizza. Analysis of the ATR spectra was carried out by J. B. Patel.

4.3 Understanding of Butylammonium Inclusion

Inclusion of BA in the films was verified through infrared absorption spectra which are able to track the fingerprint of a BA-specific C-N stretching mode near 1090 cm^{-1} (see Figure 4.1). The infrared absorption for the C-N stretching frequency associated with *n*-butylammonium iodide is shifted compared to the formamidinium iodide, as shown in Figure 4.1. The shift in frequency is due to the R-groups attached to the primary ammonium ion or amine ($BA^+ = R{-}^+NH_3$, $FA^+ = R{-}NH_2$) [282–284]. The R-group in BA^+ consists of an aliphatic chain (C_4H_9) whereas the R-group in FA^+ consists of an imino group ($CHNH_2$). The result of the different R-groups is a change in the C-N bond length and bond angle, and will result in a difference in the C-N stretching frequency between the BA^+ and FA^+ [282, 285]. Using the assigned peaks in the precursor powder, it can be clearly observed that the C-N stretching frequency in the butylammonium cation (BA^+) is 1092 cm^{-1}. The broad peak of the C-N stretching frequency associated with the formamidinium (FA^+) cation is masked by the strong absorption of quartz. Therefore, by tracking the C-N stretching frequency the addition of BA^+ in the perovskite thin film can be monitored. Further, the vibrational frequencies of

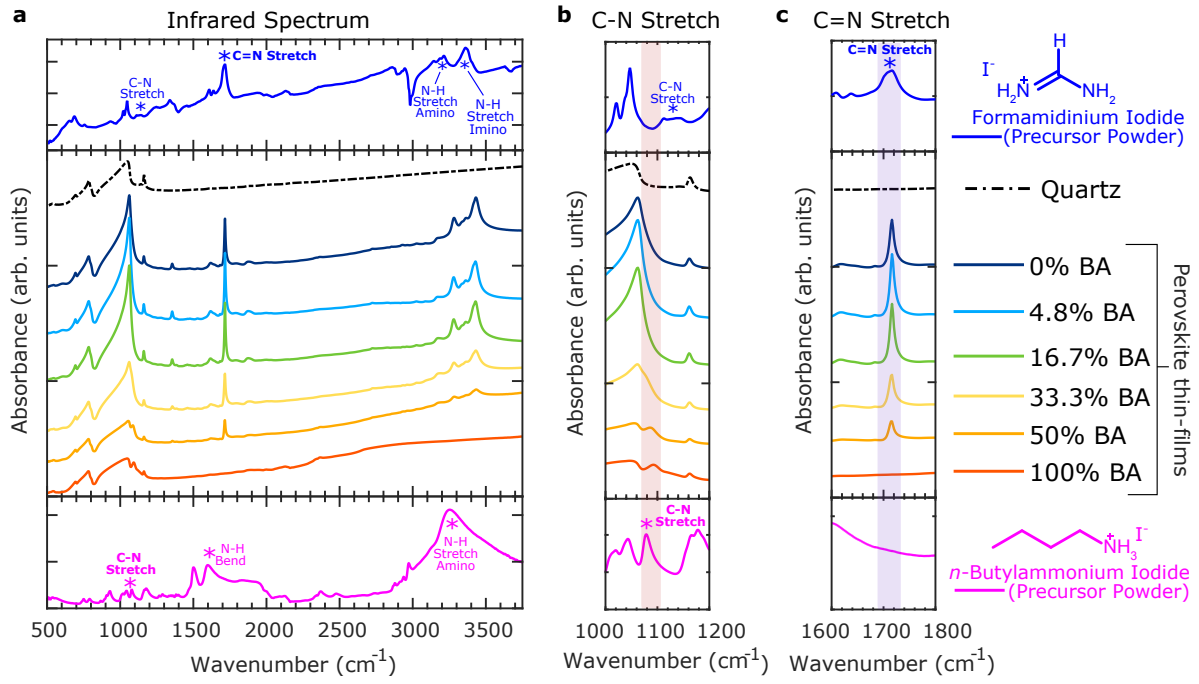


Figure 4.1: Infrared absorption spectra. (a) Infrared absorption spectra of $BA_x(FA_{0.83}Cs_{0.17})_{1-x}Pb(I_{0.6}Br_{0.4})_3$ thin films. Also shown are the IR spectra of the precursor powders, formamidinium iodide and n-butylammonium iodide (blue and pink lines, respectively). The peaks were assigned according to relevant references [285–287]. (b) Spectral zoom showing the infrared spectra of the perovskite thin films between 1000 cm^{-1} and 1200 cm^{-1}. The rise in absorption of the C-N stretching mode from the butylammonium cation (BA^+) highlight the increasing BA^+ fraction in the perovskite thin-films. (c) The infrared spectra of the perovskite thin films between 1600 cm^{-1} and 1800 cm^{-1}. The decrease in absorption of the C=N stretching mode (from the formamdinium) highlight the decrease in FA^+ fraction in the perovskite thin films. Infared absorption measurements were carried out by J. B. Patel and L. R. V. Buizza. Analysis of the spectra was carried out by J. B. Patel.

bonds associated with the imino group (-C=N-) in the FA^+ at 1716 cm^{-1} and 3433 cm^{-1} are shown to decrease in absorption as the BA^+ fraction is increased in the perovskite. The N-H stretching frequency in the BA^+ is broad, hence it is masked by the increased absorption of the quartz above 3000 cm^{-1}.

Note that the method of sample preparation outlined above in Section 4.2 was optimised with the aim of achieving smooth films that incorporate a high density of 2D crystallites at the boundaries of 3D grains. This approach had previously been shown to result in the thin films containing plate-like 2D-phase crystallites standing up between 3D perovskite grains, as indicated by a combination of scanning electron

microscopy images and 2D X-ray diffraction measurements [110]. Crucially, for optimised stoichiometries such materials may be able to exhibit the advantageous combination of 3D-like charge transport and environmental stability, while also limiting pin-hole formation in devices that can arise from surface roughness, which will be explored here. In contrast to the methods typically employed to yield well-defined Ruddlesden-Popper phases, where increasing the value of p leads to more octahedral corner-sharing layers, the addition of BA in the manner employed here will ultimately lead to non-stoichiometries at very high BA composition. However, the experimental observations below show that the alternative of addition of BA as part of Ruddlesden-Popper phases in solution can lead to very high surface roughness. Thus, the method outlined for synthesis in Chapter 3 Section 3.5 is optimized to strike a careful balance to yield a combination of optimized proportion and location of 2D crystallites, while also maintaining a smooth surface over a sufficiently large range of BA content.

4.4 Main Experimental Results and Discussion

4.4.1 Structural changes occuring with increasing BA content

Figure 4.2 shows the variation of several optoelectronic and crystallographic properties with BA content for thin films of $BA_x(FA_{0.83}Cs_{0.17})_{1-x}Pb(I_{0.6}Br_{0.4})_3$. Figures 4.2 (a), (b) confirm that the addition of small amounts of BA greatly enhances the intensity of the (100) and (200) reflections in X-Ray Diffraction (XRD) measurements, and reduces any other (hkl) reflections (Figure 4.2 (a)) [110]. Similarly, the (200) reflection angle increases with BA content, and additional peaks appear that are not present in the $x = 0$ spectrum, for compositions with $x \geq 0.333$ (see Figure 4.2 (b), Figure 4.3 (e) – (i)). The enhanced intensity of the (100) and (200) peaks relative to other reflections is indicative of improved crystallinity throughout the film, with full-width half-maximum (FWHM) values lowest for

$x = 0.167$ and rising beyond this to a value of FWHM = 0.25°for $x = 0.8$ (see Figure 4.4). The increase in (200) reflection angle with BA content has two potential explanations.

As the BA content increases, the volume fraction of 2D crystallites increases, leading to additional strain on the 3D bulk, thus giving altered interplanar spacing associated with larger reflection angles. Alternatively, these shifts with BA content could be caused by a variation in halide composition in the 3D bulk, with the iodide:bromide ratio

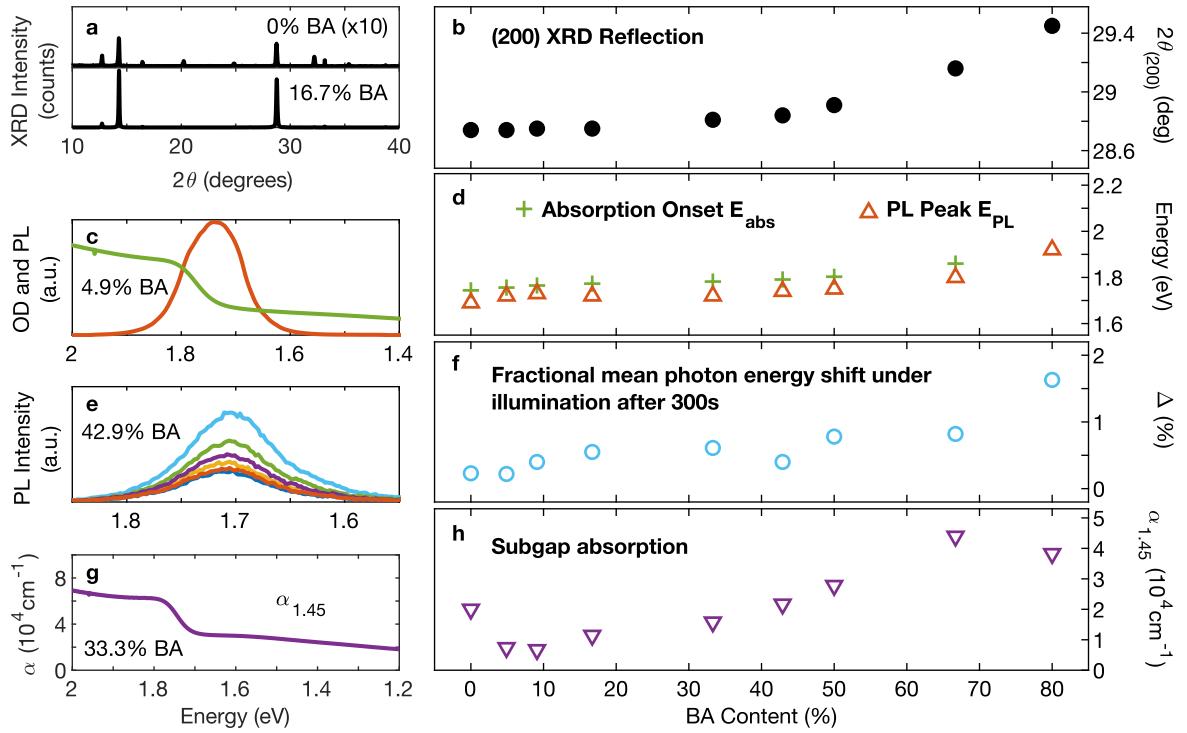


Figure 4.2: Variation of crystallographic and optoelectronic properties of $BA_x(FA_{0.83}Cs_{0.17})_{1-x}Pb(I_{0.6}Br_{0.4})_3$. (a) X-Ray Diffraction reflection patterns for x = 0, 0.167. (b) Shift in (200) reflection peak position, increasing monotonically as BA content increases. (c) Absorption and PL spectra for $x = 0.049$. Absorption was measured using a Bruker Vertex 80v Fourier-Transform Infrared spectrometer, and PL was measured immediately following continuous wave excitation at 398 nm at an intensity of 122 $mWcm^{-2}$. (d) Absorption onset energy, calculated from the inflection point of the absorption spectrum, and PL peak emission energy. Both increase monotonically with BA content. (e) PL spectra over time for x = 0.429. Samples were under sustained illumination using a continuous wave 398 nm beam at an intensity of 95 $mWcm^{-2}$ and measured after 1, 10, 30, 60, 120, 300 s. (f) Percentage shift in mean photon energy over 300 s of continuous illumination, defined as parameter Δ (see 4.2), for films that had been aged for three months under nitrogen atmosphere. For films with BA content of 0.67 and 0.8 significant spectral shifts had already occurred during aging, meaning that Δ could be even higher for un-aged films. (g) Absorption spectrum for $x = 0.333$, including below-bandgap scattering. (h) Absorption coefficient at 1.45 eV, as a proxy for scattering from samples. Scattering is substantial above $x = 0.5$.

increasing from 60:40 towards closer to 50:50 in the bulk material. Such variation may result from a need for improved lattice matching at the 2D-3D grain boundaries with increased BA content. In this case, the higher measured reflection angles signify a decreased interatomic spacing resulting from the incorporation of a larger fraction of the smaller bromide anions in the 3D bulk. The distinction between these two mechanisms is discussed in more detail below.

4.4.2 Trends in emission and absorption with increasing BA content

Both the absorption onset and peak PL emission energy blue-shift with increasing BA content (Figure 4.2 (d)), with the $x = 0$ sample displaying an absorption onset at 1.74 eV (711 nm) and values increasing monotonically across the series, to 1.86 eV (667 nm) for $x = 0.667$. The change in PL and absorption spectra is continuous across the composition range, although for samples with very high BA content ($x = 0.667$, 0.8) it is clear that some inhomogeneity or phase-segregation is present, with a lack of clearly-defined 3D bulk and 2D crystallite regions, as the absorption spectra are very broad and no longer exhibit clear onsets (see Figure 4.5). Similar trends have been observed in 2D Ruddlesden-Popper systems, with both the absorption onset and PL peak blue-shifting with decreasing n-value [205]. However, here it is proposed that the PL originates from the 3D bulk phase, rather than a confined Ruddlesden-Popper phase. This argument is supported by the lack of excitonic peaks that are typically observed in the absorption spectra of 2D systems. In addition, the absorption and PL spectra of these samples, even for high BA content, have very similar shapes to those of bulk 3D systems, in agreement with other reports on hybrid 2D-3D systems [278, 281]. This observation, together with the inhomogeneity of the absorption spectra at high BA content, is the result of the way in which the BA content in the series has been increased, leading to an absence of clearer confinement effects at high BA content. However, it should also be noted that, given that all of the samples

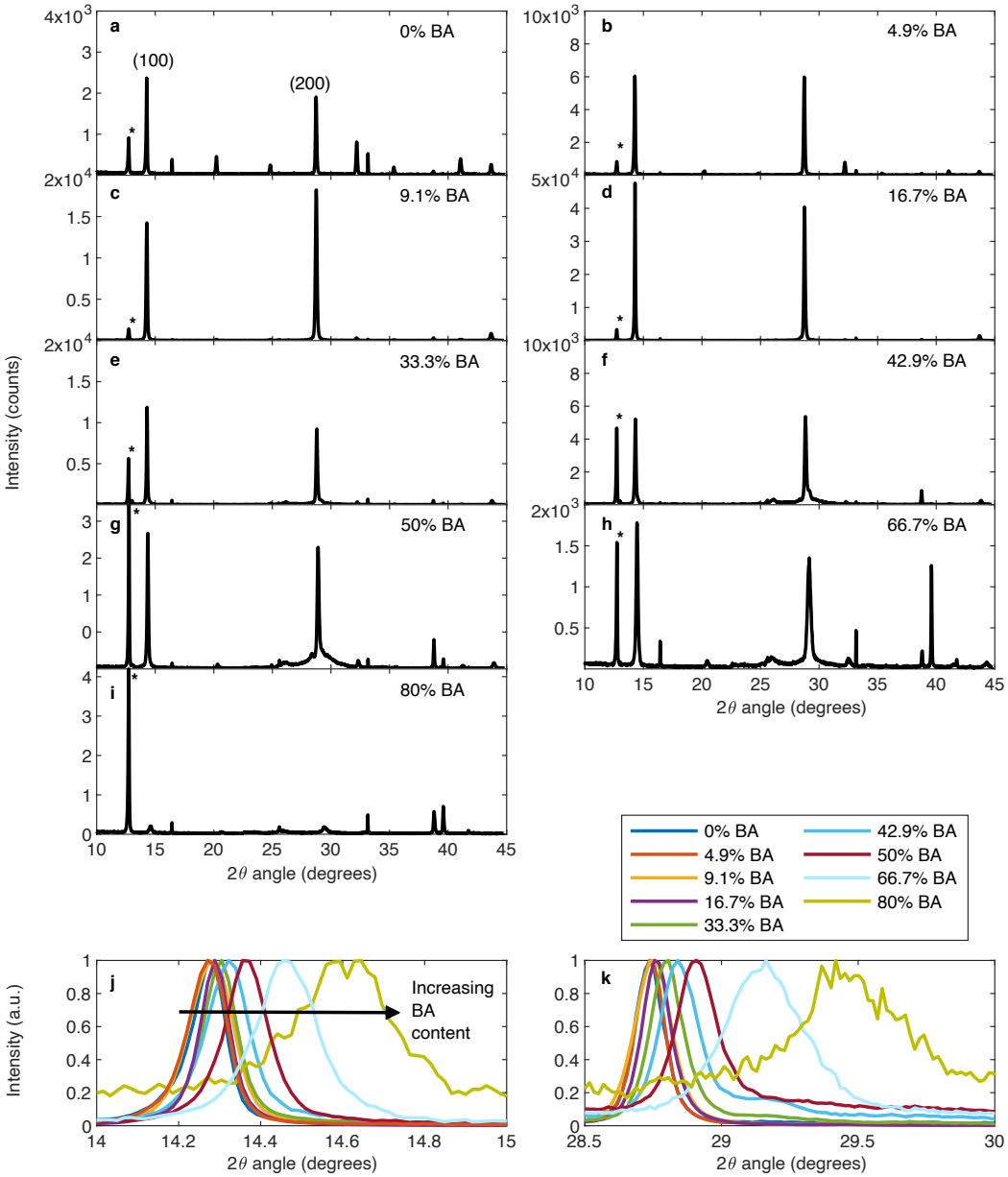


Figure 4.3: XRD spectra across compositional range. (a) – (i) X-Ray Diffraction spectra for thin films of $BA_x(FA_{0.83}Cs_{0.17})_{1-x}Pb(I_{0.6}Br_{0.4})_3$, for $x = 0 - 0.8$. Peaks marked with an asterisk (*) are identified as PbI_2 peaks at 12.7°. (k) The main (100) reflection is found at $\sim 14.3°$and (l) the (200) reflection is found at $\sim 28.7°$. Both peak positions shift to larger angles with increasing BA content.

were very thick (> 700 nm) it is also possible that additional features in the absorption spectra below 550 nm were not fully resolved due to low light transmission (Figure 4.5).

The blue-shift in band gap that is observed via absorption and PL measurements with increasing BA content must also be married with the above-mentioned explanations for

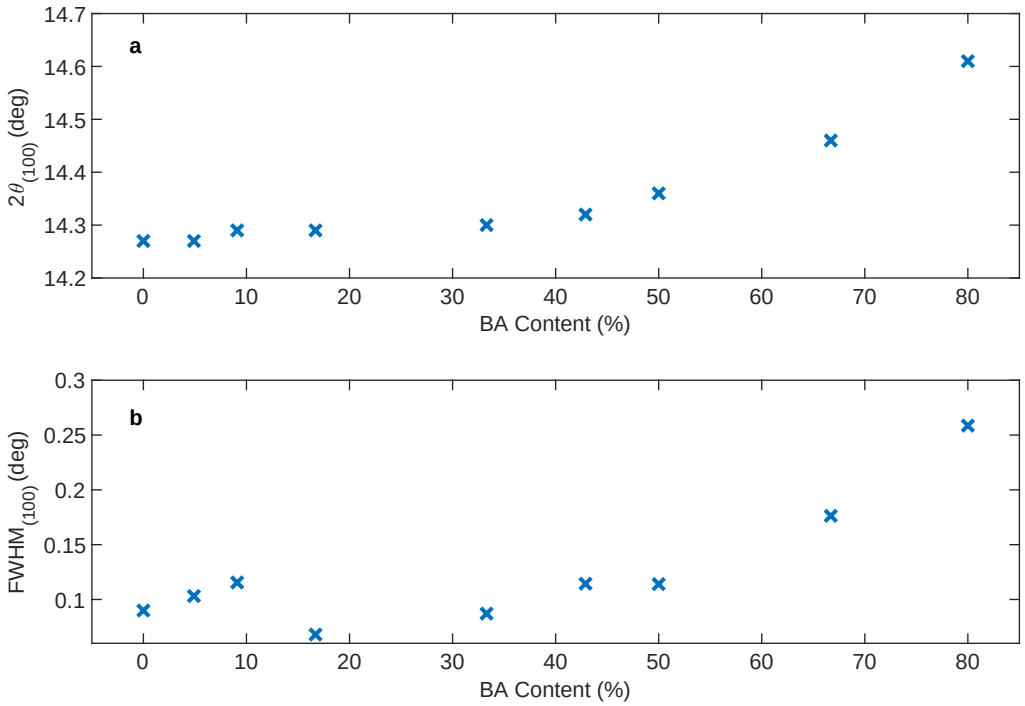


Figure 4.4: XRD (200) peak position and broadening. X-Ray Diffraction peak positions for (100) reflections (a) and full-width half-maximum (FWHM) values of the (100) peaks (b). Peak positions and FWHM values both increase with BA content.

the corresponding increases in XRD reflection angles. The dependence of band gap energy on lattice spacing is not trivial, with several contributing factors. As outlined in Chapter 2, the electronic structure of MHPs is inverted relative to classical inorganic semiconductors, such as GaAs, leading to lead-halide perovskites having a positive deformation potential [288–290]. This has been confirmed by pressure-dependent measurements in $MAPbBr_3$, where increasing pressure in the cubic phase leads to shorter Pb-Br bond lengths, raising the VBM and leaving the CBM unchanged, giving a smaller band gap [291]. However, if the A-site cation is varied, there is a non-obvious relationship between the size of the cation and the band gap. One would expect smaller cations to lead to decreased interatomic spacing, thus giving smaller band gaps. However, a crucial factor is the metal-halide bond angle, meaning that larger ionic radii give larger angles, lining up the metal-halide bonds, giving lower band gaps [65, 220]. Thus, for example, swapping MA

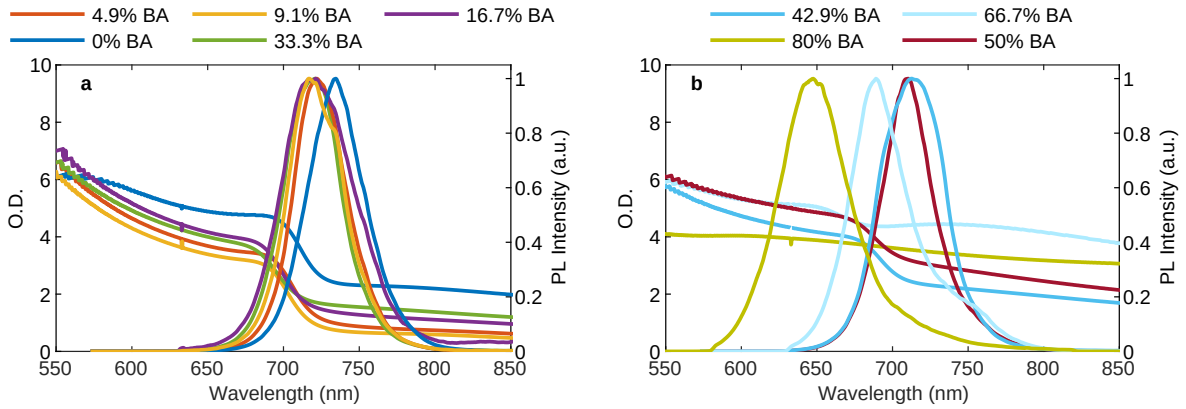


Figure 4.5: Steady-state photoluminescence and absorption spectra. Spectra are shown for $x = 0 - 0.333$ (a) and $x = 0.429 - 0.8$ (b). PL was measured following continuous-wave excitation at 398 nm at an intensity of 122 mWcm^{-2} on the front of the samples. The absorption onset and PL peak both blue-shift with increasing BA content.

for FA leads to a lower band gap in $FAPbI_3$ than in $MAPbI_3$ [59, 272].

Temperature-dependent measurements have further probed this relationship, with previous studies showing that the band gap of MHPs blue-shifts with increasing temperature, and this effect has been found in conventional $MAPbI_3$ as well as mixed-halide and mixed lead-tin perovskites [30, 59, 174, 292]. When considering the effect of temperature, there are contributions from both lattice deformation and electron-phonon coupling [293]. There is debate as to the dominance of the contributions: early work suggested that the electron-phonon couplings might cancel each other out, leaving just the lattice expansion contribution [293]. However, more recent work has found a large anharmonicity in electron-phonon couplings [90], and theoretical calculations have found the dominant increase in band gap to arise from the electron-phonon couplings [294, 295].

Finally, by tuning the halide content the orbital overlap can be changed, altering the energy of the VBM whilst leaving the CBM unchanged, due to the large contribution from the halide p-orbital to the VBM [296]. One thus obtains a varying band gap energy with halide content, with E_g decreasing in order of chlorine / bromine / iodine, with mixtures of two halides confirming this trend [44, 296, 297].

The addition of BA to the materials under investigation here leads to lower interatomic spacing [110], and if this were the only effect, would result in corresponding decrease in the band gap due to the positive deformation potential of MHPs [288, 296]. However, since the PL and absorption show a blue-shift with increasing BA content it is thus suggested that the more convincing explanation is of a slight variation in halide content within the 3D bulk region. The presence of a higher bromide fraction within the 3D bulk region of samples with a greater BA content will thus increase the band gap whilst reducing the lattice spacing, which is consistent with the observed trends in both XRD peaks and band gaps. Alternatively, the increased stress on the 3D bulk, caused by the higher proportion of 2D crystallites, could lead to an increase in octahedral tilting, which has been shown to alter the band gap of MHPs [65]. It should be noted that the Br-I content stated in the compositions reflects the halide composition in the starting solution; the final composition in the films after spin-coating and annealing may vary slightly from this ratio.

Accompanying these morphological changes is a broad feature in the absorption spectra below the bandgap (Figure 4.2 (g), (h)), which becomes significant at high BA contents. This subgap "absorption", which is really a reduction in light transmission, is attributed to scattering caused by surface roughness. The lower scattering intensity observed for films with low BA content can be attributed to the improved crystal growth that is observed in the XRD data, leading to better grain alignment and thus giving smoother surfaces and lower light scattering at long wavelengths.

4.4.3 Material aging and stability against light-induced halide segregation

To investigate the long-term stability of the materials, the thin films of $BA_x(FA_{0.83}Cs_{0.17})_{1-x}Pb(I_{0.6}Br_{0.4})_3$ were aged for three months in an inert nitrogen glovebox (as an approximation of the effect of encapsulation for devices) and subsequently the PL spectra were re-measured to probe for any potential changes in halide distribution. Figure

4.5 shows the PL spectra as they were originally measured for freshly prepared samples (with extracted peak positions given in Figure 4.2 (d)) while Figure 4.6 shows the PL spectra after the aging process. For all compositions, the spectra had shifted somewhat relative to the original PL spectra, indicating that some amount of halide segregation or redistribution in material morphology may have taken place. For samples with BA content $x \leq 0.5$ this shift is relatively small, on the order of tens of nanometers. However, the shift becomes significant for $x = 0.667$, 0.8 (see Figure 4.6 (h), (i)), where the main peaks at 690 and 646 nm now only appear as a secondary peak/shoulder, with the dominant peak in the spectra now at much longer wavelengths. Thus, at these very high BA fractions the presence of excess BA decreases long-term material compositional stability, even when the samples are stored in an inert atmosphere. For lower BA fractions, however, materials are stable, in agreement with a recent study that demonstrated a clear enhancement of long-term solar cell performance stability when BA content of $x = 0.09$ was included in devices based on $BA_x(FA_{0.83}Cs_{0.17})_{1-x}Pb(I_{0.6}Br_{0.4})_3$, compared to BA-free ($x = 0$) devices [110].

These aged films were further examined in terms of their stability against halide segregation under illumination. The issue of reversible light-induced shifts in PL spectra in lead mixed iodide-bromide perovskites has been known for several years and is commonly believed to derive from halide segregation, first proposed by Hoke et al. [27]. For example, the constant illumination of $MAPb(Br_yI_{1-y})_3$ films with intermediate values of y leads to the gradual appearance and growth of a lower-energy secondary PL peak at 740 nm, which has been attributed to emission from an iodide-enriched phase. The proposed mechanism is that photoexcitation leads to the migration of halide ions, resulting in the phase segregation of the perovskite film into iodide- and bromide-rich regions [27, 271]. This process has been shown to depend on the film crystallinity and morphology, bromide content y, intensity of illumination, and the environment in which the film is illuminated, with studies suggesting a link with the propensity of the material to trap

charge-carriers [28, 51, 298]. Modification of the A-cation site, e.g. by introduction of particular ratios of FA and caesium, has also been shown to stabilise the material against photoinduced halide segregation by improving crystallinity [51, 256].

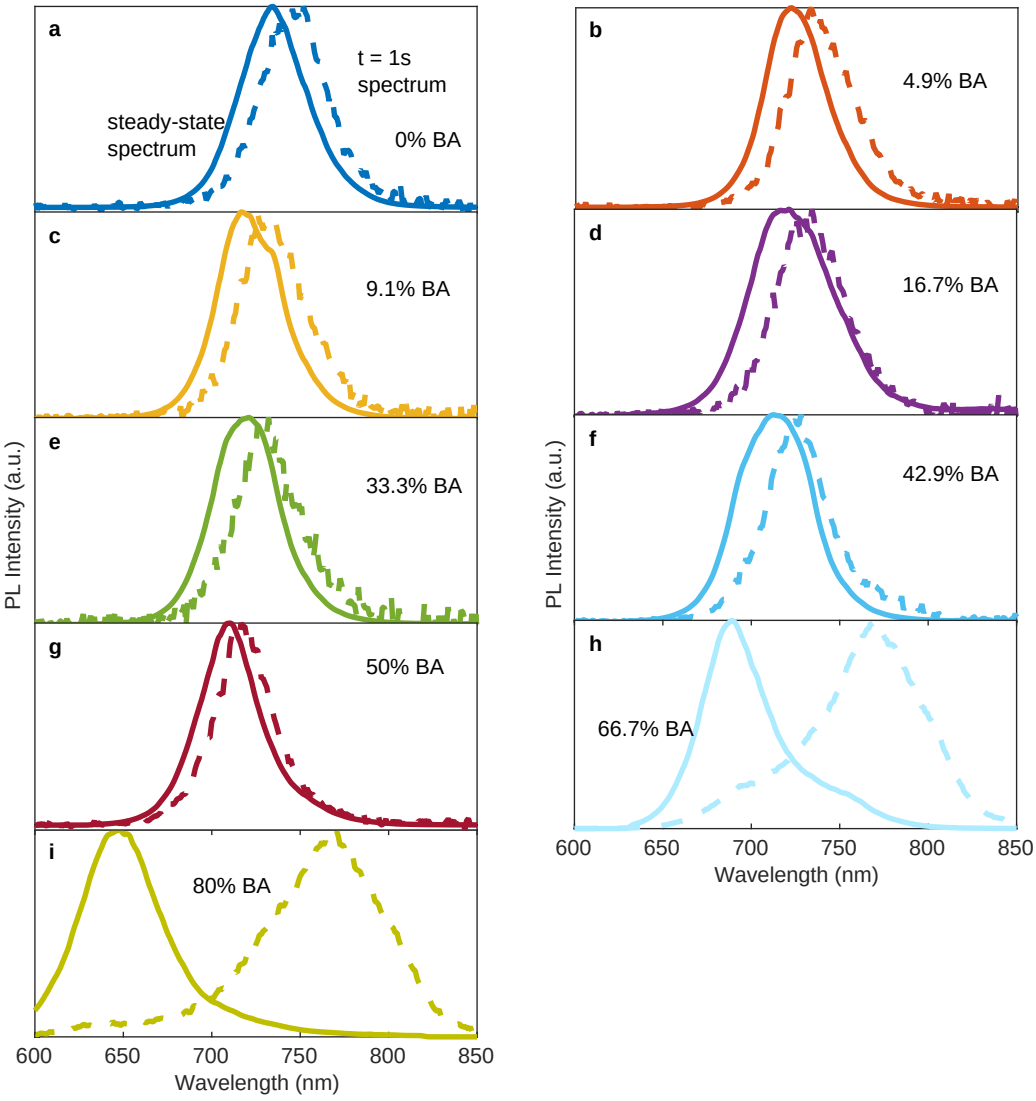


Figure 4.6: Long-term stability of PL emission. (a) – (i) Photoluminescence spectrum shift between original steady-state PL spectra (solid lines), and spectra measured for thin films of $BA_x(FA_{0.83}Cs_{0.17})_{1-x}Pb(I_{0.6}Br_{0.4})_3$ following aging in a nitrogen glovebox for three months (dashed lines), for $0 \leq x \leq 0.8$ content (the latter spectra also forming the spectra measured after 1 second of illumination as explained below and shown in Figure 4.7).

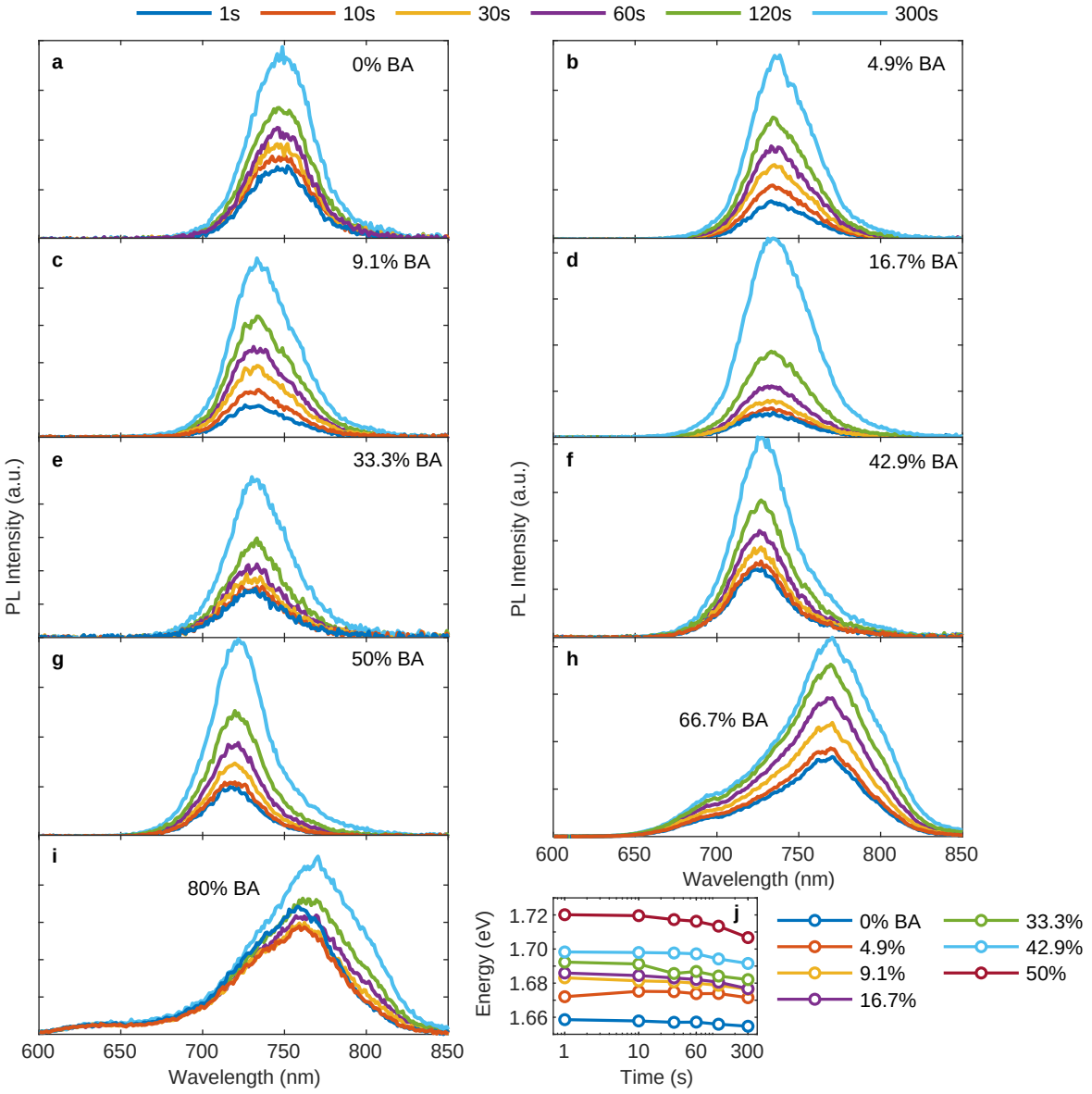


Figure 4.7: Halide segregation observed through PL measurements. (a) – (i) PL spectra for thin films of $BA_x(FA_{0.83}Cs_{0.17})_{1-x}Pb(I_{0.6}Br_{0.4})_3$ for $x = 0 - 0.8$ under constant 398 nm continuous-wave illumination at approximately one sun intensity (95 $mWcm^{-2}$). (j) Shift in mean photon energy over 1 – 300 s (see 4.1 for details).

For this study, the aged $BA_x(FA_{0.83}Cs_{0.17})_{1-x}Pb(I_{0.6}Br_{0.4})_3$ films were excited using 398 nm continuous-wave illumination at 95 $mWcm^{-2}$, with PL spectra measured after 1, 10, 30, 60, 120 and 300 seconds. It was found that for all samples the PL increases in intensity over time when under continuous illumination at approximately one-sun intensity, as has been previously observed in other mixed-halide systems (Figure 4.7) [27, 28]. In order to quantify the amount of segregation undergone by each sample, the mean photon energy of each spectrum was calculated and plotted over time (see Figure 4.7 (j)). The PL spectra are measured in units of intensity per unit wavelength, and thus the mean photon energy is calculated as:

$$< E_{\text{phot}} >= \frac{\text{Total Energy}}{N_{\text{phot}}} = \frac{\sum_{i=1}^{N} I_i}{\sum_{i=1}^{N} N_i} = hc\frac{\sum_{i=1}^{N} I_i}{\sum_{i=1}^{N} I_i\lambda_i} \tag{4.1}$$

where I_i are the intensities and λ_i are the wavelengths at which they are recorded. The measure of halide segregation, Δ, is then defined as:

$$\Delta = \frac{(E_0 - E)}{E_0} \tag{4.2}$$

where E_0 is the initial mean photon energy and E is the mean photon energy at some later time.

For compositions with $x \leq 0.33$ the amount of segregation is negligible: Δ is less than one percent (Figure 4.2 F). Such improved stability, relative to $MAPb(Br_yI_{1-y})_3$, observed here for $BA_x(FA_{0.83}Cs_{0.17})_{1-x}Pb(I_{0.6}Br_{0.4})_3$ with $x \leq 0.5$ is in good agreement with measurements of similar mixed-cation, mixed-halide systems [42, 51], in the absence of BA. For higher BA content ($x = 0.667, 0.8$) the broad absorption spectra and significantly weaker XRD reflections measured for these samples indicate inhomogeneity and poor crystallinity of the films. Given the links between halide segregation and poor material crystallinity [28, 51, 299, 300], as well as high trap-mediated charge-carrier recombination (observed for samples with high BA content, as discussed further below), it is therefore

not surprising that for x =0.667, 0.8, films not only show morphological changes with aging time, but also stronger PL spectral shifts Δ under illumination (Figure 4.2 (f)).

Overall, the observed trends in the structural and optical properties of $BA_x(FA_{0.83}Cs_{0.17})_{1-x}Pb(I_{0.6}Br_{0.4})_3$ thin films illustrate the behaviour of the hybrid 2D-3D system: for compositions up to $x = 0.5$, the materials behave analogously to typical 3D lead-halide perovskites, whilst for high quantities of BA ($x \geq 0.667$) there is increased inhomogeneity, poor crystal structure, low long-term stability and increased halide segregation under illumination.

4.4.4 Trap-mediated charge-carrier recombination

Charge-carrier dynamics are then investigated (of freshly prepared films), first by measuring PL transient decays using time-correlated single-photon counting (TCSPC). As has been shown across multiple perovskite compositions [48, 50, 54, 56, 97, 256], at the low excitation fluences employed, PL decays will mostly be dominated by trap-mediated (monomolecular) charge-carrier recombination. Previous reports for 2D-3D hybrid systems have noted that, relative to neat 3D systems, the introduction of large hydrophobic cations often reduces trap-mediated charge-carrier recombination [110, 278, 281]. For the $BA_x(FA_{0.83}Cs_{0.17})_{1-x}Pb(I_{0.6}Br_{0.4})_3$ thin films under investigation here, PL decay lifetimes across the series of materials are found to be long, on the order of hundreds of nanoseconds, although the beneficial passivating characteristics of the hybrid systems begin to disappear above $x \geq 0.33$.

Figure 4.8 displays the impact of the addition of BA on monomolecular recombination rates for a select number of films (transients for all BA fractions and excitation fluences are shown in 4.10). Films were photoexcited at a wavelength of 398 nm with fluences ranging from 3 – 280 $nJcm^{-2}$, and PL decays measured over 1000 ns. Figure 4.8 (a) shows the highly monoexponential behaviour of the PL transients at low excitation fluence —

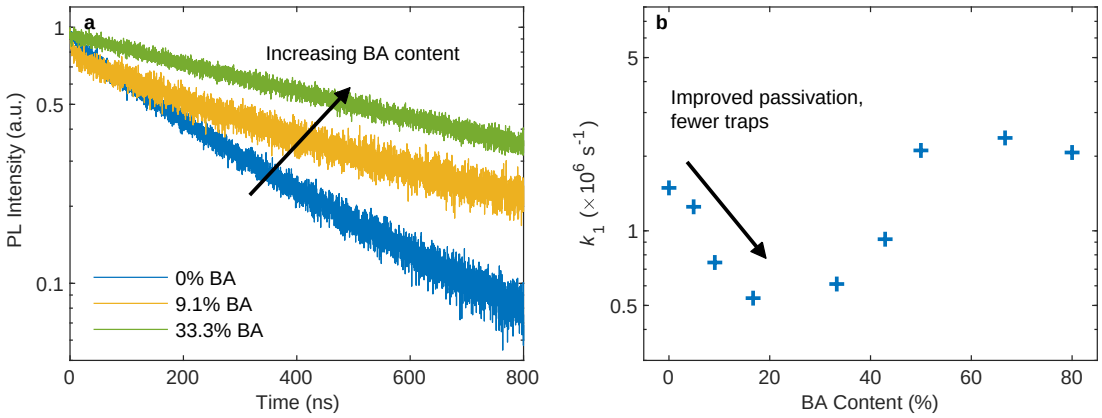


Figure 4.8: Impact of BA on trap-mediated recombination. (a) PL transients for three hybrid perovskite films of composition $BA_x(FA_{0.83}Cs_{0.17})_{1-x}Pb(I_{0.6}Br_{0.4})_3$ with $x = 0$, 0.091, 0.333 (curves for further compositions and excitation fluences shown in the SI). Samples were measured by time-correlated single-photon counting (TCSPC), following pulsed excitation at 398 nm, with a 1 MHz repetition rate and a fluence of 4.4 nJcm^{-2}. (b) Monomolecular charge-carrier recombination rate (k_1) of $BA_x(FA_{0.83}Cs_{0.17})_{1-x}Pb(I_{0.6}Br_{0.4})_3$ across the composition range $x = 0 - 0.8$, determined by fitting monoexponential decays to PL decays (shown in Figure 4.9).

this trend is observed across all samples up to $x = 0.429$. Given that the instrument response function for the system used is short (of the order of 100 ps), and in order to make a consistent comparison across the composition series, a monoexponential expression was fitted to the transients taken at the lowest fluence, such that the time-dependent PL intensity $I(t) = I_0 e^{-t/\tau_1}$. The fits begin at t = 100 ns, beyond which the decays are clearly mono-exponential in the majority of compositions (Figure 4.9). As outlined in Section 3.2.2.1, because the radiative charge-carrier recombination component originates from band-to-band transitions [253], the monomolecular recombination rate of charge carriers is then taken to be $k_1 = 1/(2\tau_1)$. (It should be noted that the factor of two is not always included in derivations of charge-carrier diffusion lengths derived from PL measurements, which should be kept in mind when values stated for charge-carrier recombination rates or diffusion lengths are compared across reports in the literature.)

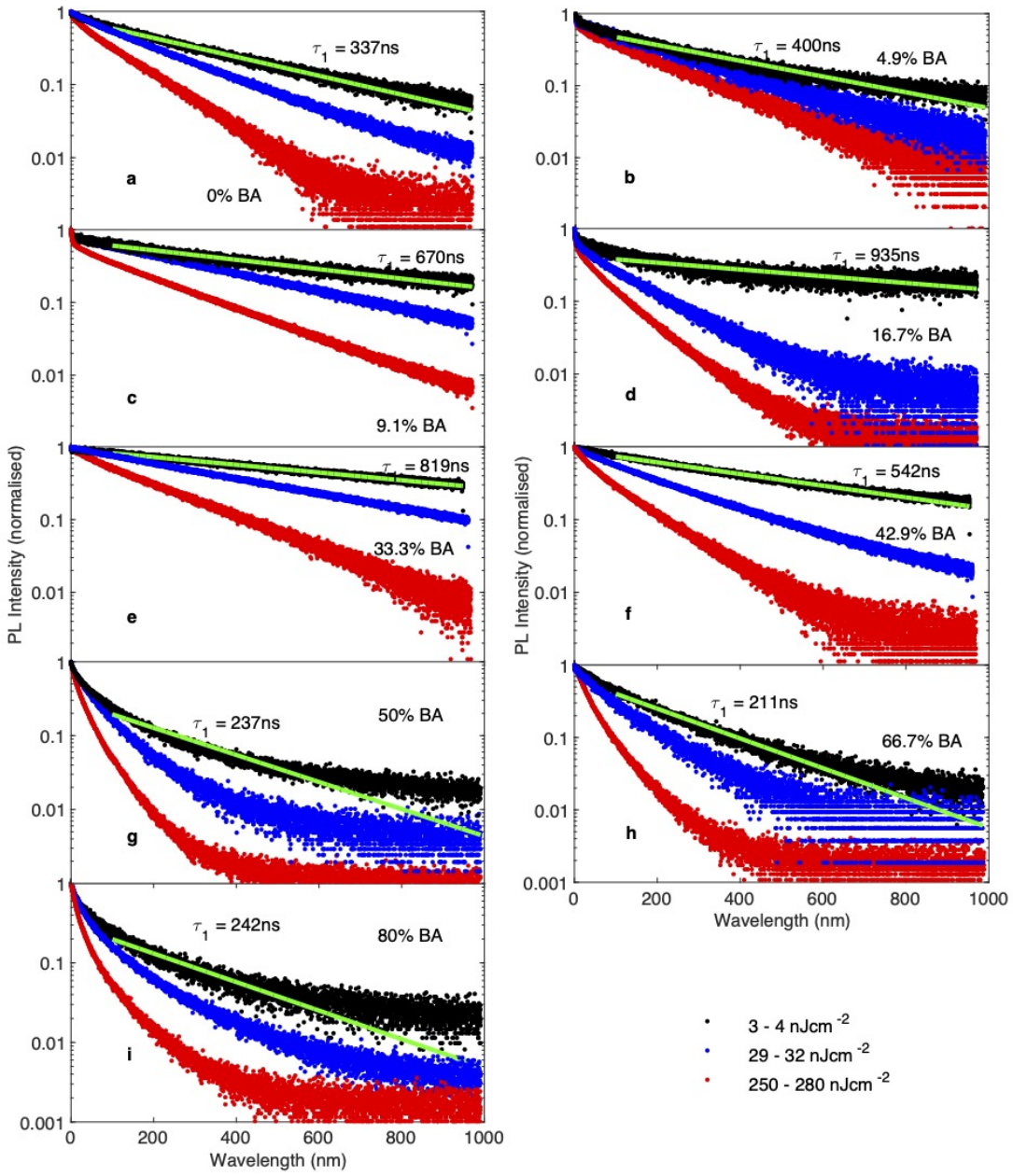


Figure 4.9: Time-resolved PL measurements. (a) – (i) Transient PL decay curves for a range of excitation fluences for thin films of $BA_x(FA_{0.83}Cs_{0.17})_{1-x}Pb(I_{0.6}Br_{0.4})_3$ for $x = 0$ – 0.8. Samples were excited at 398 nm using fluences of ~ 4, ~ 30, $\sim 250\,\mathrm{nJcm^{-2}}$. Decay lifetimes decreased with decreasing fluence, and traces at the lowest fluence were fitted with a monoexponential curve (green) to extract a lifetime τ_1.

The variation of k_1 with BA content is displayed in Figure 4.8 (b). A clear passivating impact from the addition of BA is observed, with lifetimes increasing substantially between $x = 0 - 0.167$, from $\tau_1 = 337\,\text{ns}$ to $\tau_1 = 935\,\text{ns}$ (see also Figure 4.9). As was recently shown through a combination of scanning electron microscopy images and 2D x-ray diffraction measurements [110], the material fabrication protocol employed here will lead to 2D perovskite crystallites accumulating at the boundary of large 3D perovskite grains. Therefore, the reduction in trap-mediated charge-carrier recombination rates at low BA content is most likely associated with the passivation of traps at the grain boundary, or the formation of an electronic barrier suppressing charge-carrier diffusion into traps.

Above the lower end of the composition range the addition of BA leads to increased charge-carrier recombination, with rates rising to above $2 \times 10^6\,\text{s}^{-1}$ for $x \geq 0.5$. As has previously been reported, 2D Ruddlesden-Popper phase perovskites display highly excitonic recombination, especially for low p-values [205, 275]. However, given the inhomogeneity, poor crystallinity and higher scattering of the films with high BA content, as well as the lack of any excitonic features in both the PL and absorption spectra in Figure 4.5, it is likely that the observed increased in monomolecular recombination rates derive from a significant rise in the trap-state density for the fabrication procedure adopted here, rather than any excitonic effects [174, 301, 302].

4.4.5 Bimolecular (band-to-band) charge-carrier recombination

To assess the dependence of apparent band-to-band (bimolecular) charge-carrier recombination on the BA content in the materials, photoconductivity transients were measured at early times after excitation with elevated fluences, using optical-pump terahertz-probe spectroscopy (OPTPS). The samples were excited at a wavelength of 400 nm through the front of the films, and the fractional change in transmitted terahertz signal ($-\Delta T/T$) was measured. Variation of the delay between the pump and probe beams allows for

transient decays such as those shown in Figure 4.10 to be recorded. The initial $\frac{\Delta T}{T}$ signal can be converted into photoinduced conductivity, which is proportional to the product of charge-carrier density n and effective mobility $\phi\mu$, as outlined in Chapter 3. Hence, the initial value (immediate after photoexcitation) of the photoconductivity can be used to deduce the sum over the electron and hole mobilities in the material, if the density of initially created charge-carriers is known.

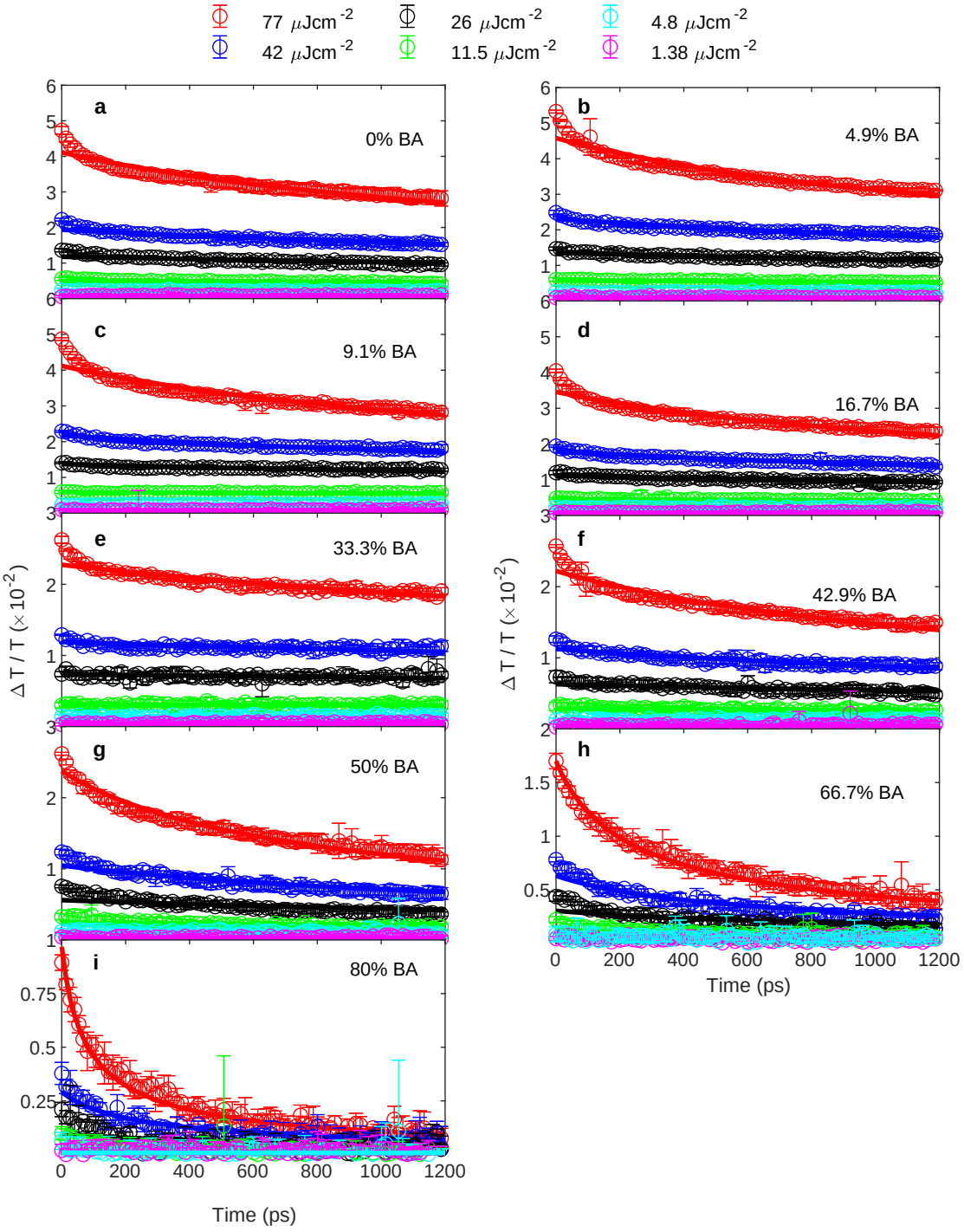


Figure 4.10: OPTPS decays across comopsitional range. (a) – (i) OPTPS transient decay traces for thin films of $BA_x(FA_{0.83}Cs_{0.17})_{1-x}Pb(I_{0.6}Br_{0.4})_3$, measured following excitation at 400 nm at a range of fluences for $x = 0 - 0.8$ BA content. Data are in open circles with error bars, and fits according to Equation 4.4 describe the photoconductivity decay, shown as solid lines.

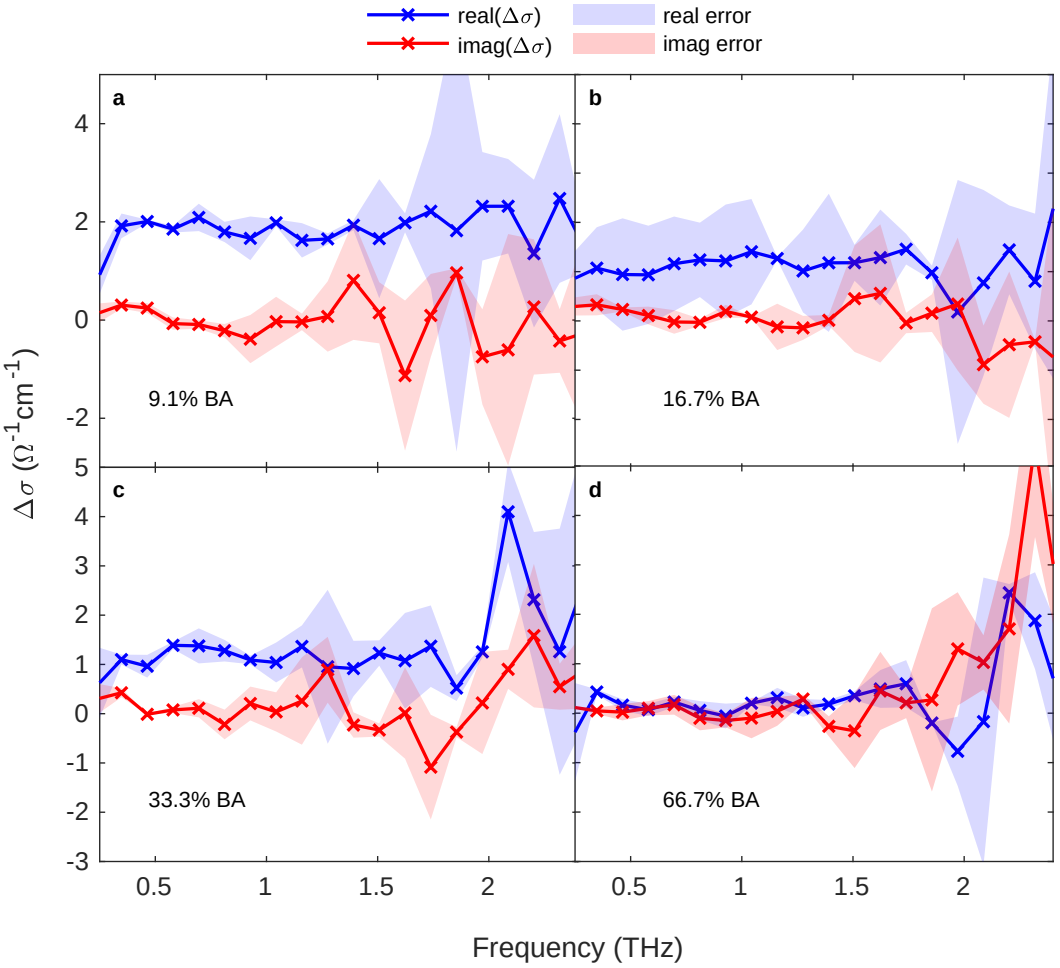


Figure 4.11: THz photoconductivity spectra. Terahertz photoconductivity spectra measured for thin films of $BA_x(FA_{0.83}Cs_{0.17})_{1-x}Pb(I_{0.6}Br_{0.4})_3$, after 1 ns following excitation at 400 nm at a fluence of 1.38 μJcm^{-2}, across four different compositions. Solid lines with crosses are the mean value of two scans, with the shaded area representing the statistical error.

An important point to note is that the fraction of absorbed photons that is converted into free charge carriers, the photon-to-free-charge branching ratio ϕ, is not determined in this experiment. Thus, for clarity and consistency the values are presented in terms of the apparent bimolecular recombination rate constants ϕk_2 and effective charge-carrier mobilities $\phi\mu$. For 3D lead-halide perovskites ϕ =1 can be assumed, given that excitonic effects at room temperature are negligible as a result of the low exciton binding energy [135]. For Ruddlesden-Popper systems with low n-values, greater electronic confinement effects and larger exciton binding energies are present [48], meaning that ϕ could potentially be

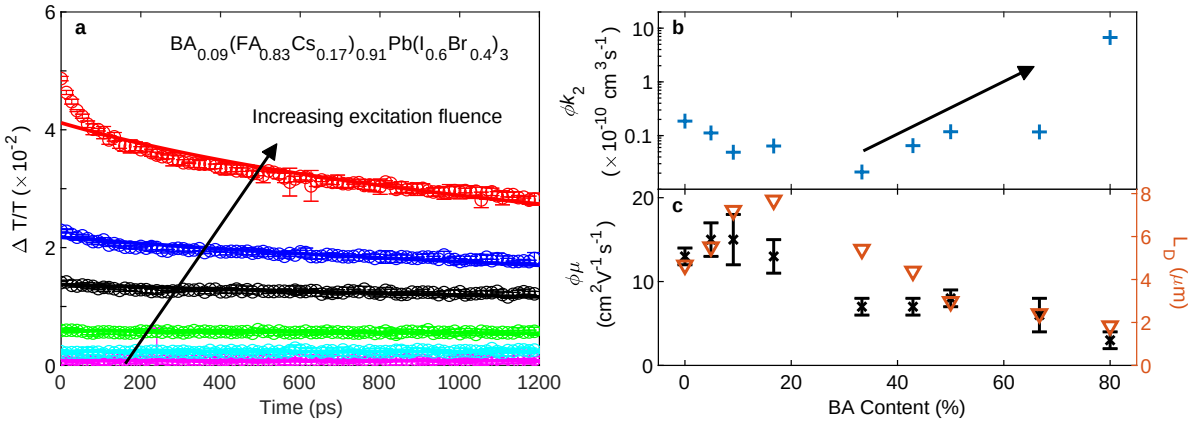


Figure 4.12: Charge-carrier dynamics and mobilities from OPTPS. (a) Example OPTPS transient decays for excitation at fluences of $1.38, 4.8, 11.5, 26, 42, 77\,\mu\mathrm{Jcm}^{-2}$ for a thin film of composition $\mathrm{BA}_{0.09}(\mathrm{FA}_{0.83}\mathrm{Cs}_{0.17})_{0.91}\mathrm{Pb}(\mathrm{I}_{0.6}\mathrm{Br}_{0.4})_3$ (curves for other compositions shown in Figure 4.10). Data are given as open circles with error bars, and solid lines are fits to the decays according to Equation 4.4. (b) Apparent bimolecular recombination rate ϕk_2 across the composition range $x = 0 - 0.8$, extracted by fitting of the OPTPS transient decays. (c) Values of the effective charge-carrier sum mobility $\phi\mu$ and diffusion length across the composition range. Diffusion length values are calculated at a charge-carrier density of $n = 10^{14}\,\mathrm{cm}^{-3}$, similar to charge-carrier densities obtained for MHPs under solar illumination [47].

smaller than one. In the 2D-3D hybrid system that are presented here, 3D perovskite domains are interspersed with 2D crystallites near the grain boundaries [110], and it might therefore be expected that the majority of photoexcited species would be free charge carriers. Terahertz photoconductivity spectra, presented in Figure 4.11, indeed show a Drude-like free carrier response (positive flat real part, zero imaginary part, as expected for free carriers with short momentum relaxation time) across a range of compositions, indicating that the photoconductivity transients are dominated by the response of free charge carriers in these materials. Given that $0 \leq \phi \leq 1$, the presented values are thus underestimates of the true physical values.

The time dependence of the charge-carrier density n may be described by the following rate equation:

$$\frac{\partial n}{\partial t} = -k_1 n - k_2 n^2 - k^3 n^3 \tag{4.3}$$

where k_1 is the monomolecular recombination rate, k_2 is the bimolecular and k_3 the Auger recombination rate constant. In order to separate out competing charge-carrier

recombination mechanisms, the solutions to this rate equation are used to carry out global fits to the data across multiple fluences, adjusting to account for the excitation density profile [47, 48, 97]. Typical values of k_3 near $2 \times 10^{-29}\,\mathrm{cm^6 s^{-1}}$ mean that [48, 174], at the fluences employed here, Auger recombination makes an insignificant contribution, and thus k_3 is set to zero. In this case, the following analytical solution to Equation 4.3 is used to fit the data:

$$n(t) = \frac{k_1 \alpha}{e^{k_1 t} - \alpha k_2} \quad \text{for} \quad \frac{1}{\alpha} = \frac{k_1}{n_0} + k_2 \tag{4.4}$$

where n_0 is the initial amplitude of the transient decay. Values of k_1 are fixed to those extracted from the TCSPC measurements that were taken over much longer time scales, but it should be noted that given the measurement window of $\sim 1\,\mathrm{ns}$ for the photoconductivity transients, all of the monomolecular recombination lifetimes are too long to have any significant impact on the fit results. The dominant contribution therefore is from radiative bimolecular charge-carrier recombination. This process has been shown to be the inverse of photon absorption [67], and is mediated by photon reabsorption, which masks the intrinsic recombination rates in a material, in particular for thicker films [303].

Figure 4.12 (b) shows the values extracted for the apparent bimolecular recombination rate constant as a function of BA content. For most films, ϕk_2 is close to $0.1 \times 10^{-10}\,\mathrm{cm^3 s^{-1}}$, similar to previously measured values for $(FA_{0.83}Cs_{0.17})Pb(I_{0.6}Br_{0.4})_3$ [51], however, samples with higher BA content appear to have higher rate constants, rising up to $6.7 \times 10^{-10}\,\mathrm{cm^3 s^{-1}}$. The variability of bimolecular recombination rate constants reported for prototypical $MAPbI_3$ in the literature ($0.6 - 23 \times 10^{-10}\,\mathrm{cm^3 s^{-1}}$) has been addressed in work by Crothers et al. [303], who proposed that the re-absorption of emitted photons within a thin film may reduce the apparent, externally measured values of the bi-molecular charge-carrier recombination constants [48, 303]. Since photon reabsorption will be affected by film thickness and light scattering, these effects can lead

to a large variation of the determined values of k_2. The samples used were relatively thick ($> 700\,\text{nm}$), meaning that both photon reabsorption and charge-carrier diffusion will play a significant role. Hence the apparent bimolecular recombination rate constants determined here will be lower than the true intrinsic values expected from the principle of detailed balance [67]. The rise in values of ϕk_2 with BA content is thus attributed mostly to poorer photon retention and increased photon out-coupling from the thin films, with an increase in the intrinsic rate playing a more minor role. The increased outcoupling for higher BA content should be expected, given that a reduction in the light transmitted through the films at photon energies below the bandgap was observed (see Figure 4.2 (h) and Figure 4.5), indicative of higher surface roughness that will scatter light near the emission energy of recombining charge carriers. Therefore, while for low BA content the films are smooth and have improved photon-retention capability, leading to the observed low values of ϕk_2 [303], at high BA content increased scattering and light outcoupling results in a higher value of $6.7 \times 10^{-10}\,\text{cm}^3\text{s}^{-1}$ for $x = 0.8$, which is close to the intrinsic limit recently determined for $MAPbI_3$ [303].

4.4.6 Effective charge-carrier mobility and diffusion lengths

Figure 4.12 (c) displays the effective charge-carrier mobility values extracted from OPTPS measurements for films of $BA_x(FA_{0.83}Cs_{0.17})_{1-x}Pb(I_{0.6}Br_{0.4})_3$, with values ranging from $13 - 15\,\text{cm}^2\text{V}^{-1}\text{s}^{-1}$ for $x \leq 0.167$, which are well within the range required for efficient photovoltaic device performance [47]. However, as the BA content is further increased, charge-carrier mobilities rapidly decline down to $3 \pm 1\,\text{cm}^2\text{V}^{-1}\text{s}^{-1}$ for $BA_{0.8}(FA_{0.83}Cs_{0.17})_{0.2}Pb(I_{0.6}Br_{0.4})_3$ ($x = 0.8$). The measured value of $13 \pm 2\,\text{cm}^2\text{V}^{-1}\text{s}^{-1}$ for the BA-free $(FA_{0.83}Cs_{0.17})Pb(I_{0.6}Br_{0.4})_3$ is also in excellent agreement with previously reported values [51]. While there have been reports of charge-carrier mobilities in Ruddlesden-Popper perovskite systems declining with decreasing number of layers p, as

electronic confinement is increased [205, 304], the lack of sharp absorption features in the films with high BA content means that this explanation is unlikely to hold here. Instead, it is proposed that the decline in effective charge-carrier mobility for high BA content is associated with a deterioration in material crystallinity, as supported by the increase in the width and decrease in intensity of the XRD diffraction peaks (see Figures 4.3 and 4.4).

Finally, the measured charge-carrier recombination constants and mobilities are combined in order to extract charge-carrier diffusion lengths across the composition range, using the following equation:

$$L_D = \sqrt{\frac{D}{R_{tot}(n)}} = \sqrt{\frac{\mu k_B T}{e R_{tot}(n)}} \tag{4.5}$$

where the total charge-carrier recombination rate is $R_{\mathrm{Tot}} = -\frac{1}{n}\frac{\mathrm{d}n}{\mathrm{d}t} = nk_2 + k_1$, and $k_3 = 0$ as discussed above (meaning that the equation approximately holds for $n < 10^{16}\,\mathrm{cm}^{-3}$). Because of the dependence of the charge-carrier recombination rate R_{tot} on the density of charge-carriers n, the charge-carrier diffusion length itself will depend on the absorbed photon density. The diffusion lengths are calculated at a charge-carrier density of $\sim 10^{14}\,\mathrm{cm}^{-3}$, which is close to the expected density generated under AM1.5 solar irradiation for materials with monomolecular (trap-mediated) carrier lifetimes similar to those measured here [47]. The charge-carrier diffusion lengths are found to exceed 1.8 µm across the composition range, with a maximum value of 7.7 µm for $\mathrm{BA}_{0.17}(\mathrm{FA}_{0.83}\mathrm{Cs}_{0.17})_{0.83}\mathrm{Pb}(\mathrm{I}_{0.6}\mathrm{Br}_{0.4})_3$. These values are well above the film thickness required in order for most of the light with photon energies above the band gap to be absorbed, according to absorption depths of between 100 — 1000 nm across the above-gap solar spectrum (see Figure 4.5). The peak in diffusion lengths at compositions with $x = 0.091$ and 0.167 correlates well with previous device studies that find excellent solar cell performance for low BA content, as well as other reports of improved device performance for low amounts of 2D-3D hybridization [110, 278, 281]. This study therefore

demonstrates that the reason for such excellent performance is the combination of a reduction in trap-mediated charge-carrier recombination coupled with maintained good effective charge-carrier mobility for low BA content.

4.5 Summary and Conclusion

In summary, in this chapter the optoelectronic properties of 2D-3D hybrid perovskites $BA_x(FA_{0.83}Cs_{0.17})_{1-x}Pb(I_{0.6}Br_{0.4})_3$ have been investigated across a wide range of BA contents $x = 0 - 0.8$. Small amounts of BA are found to markedly improve charge-carrier lifetimes, with trap-mediated recombination rates decreasing by a factor of three between compositions with $x = 0$ and $x = 0.167$. However, when excessive amounts of BA are added, film formation is inhomogeneous and of low crystallinity, resulting in enhanced trap state densities, worsened photon retention and significantly lower charge-carrier mobilities. A sweet spot is demonstrated for the addition of small amounts of BA ($x = 0.091 - 0.167$) where enhanced crystallinity and passivation of trap states at grain boundaries lead to much longer monomolecular lifetimes, and slightly enhanced charge-carrier mobilities relative to the BA-free 3D perovskite $(FA_{0.83}Cs_{0.17})Pb(I_{0.6}Br_{0.4})_3$, yielding charge diffusion lengths in excess of 7 µm, comfortably beyond requirements for efficient thin-film solar cells. Thus for this range, the materials exhibit beneficial properties of both 3D and 2D materials, i.e. a combination of excellent charge transporting properties with enhanced stability, including stability toward light induced halide segregation. This study thus provides an explanation, based on the underlying optoelectronic properties of the $BA_x(FA_{0.83}Cs_{0.17})_{1-x}Pb(I_{0.6}Br_{0.4})_3$ hybrid system, for the excellent performance of hybrid 2D-3D perovskite systems that enables the fabrication of efficient and highly stable photovoltaic solar cells.

5

Temperature-Dependent Studies of Charge-Carrier Localisation and Transport in Cu_2AgBiI_6 and $Cs_2AgBiBr_6$

Contents

5.1 Introduction and Background 110
5.2 Experimental Details 113
5.3 Materials Synthesis and Understanding of Crystal Structure 113
5.4 Main Experimental Results and Discussion 118
5.4.1 Understanding the steady-state optoelectronic properties of Cu_2AgBiI_6 118
5.4.2 Charge-carrier dynamics: photoexcitation, localisation and emission 122
5.4.3 Temperature-dependent OPTPS investigation of charge-carrier localisation and transport 127
5.4.4 Comparison with charge-carrier localisation in $Cs_2AgBiBr_6$ . . 138
5.5 Summary and Conclusion 143

Work in this chapter was initially published as: L. R. V. Buizza, A. D. Wright, G. Longo, H. C. Sansom, C. Q. Xia, M. J. Rosseinsky, M. B. Johnston, H. J. Snaith, L. M. Herz. 'Charge-Carrier Mobility and Localization in Semiconducting Cu_2AgBiI_6 for Photovoltaic Ap-

plications', *ACS Energy Letters*, **2021**, *6* (5), 1729-1739 (Ref. [86]) and A. D. Wright, L. R. V. Buizza, K. J. Savill, G. Longo, H. J. Snaith, M. B. Johnston, L. M. Herz. 'Ultrafast Excited-State Localization in $Cs_2AgBiBr_6$ Double Perovskite', *The Journal of Physical Chemistry Letters*, **2021**, *12* (13), 3352-3360 (Ref. [73]).

5.1 Introduction and Background

The second experimental chapter of this thesis moves on to study the fundamental charge-carrier dynamics and transport properties in the lead-free silver-bismuth semiconducting materials Cu_2AgBiI_6 and $Cs_2AgBiBr_6$. Whereas Chapter 4 focused on the interplay between composition and optoelectronic properties in hybrid 2D-3D perovskites, in this chapter the attention moves to understanding how charge carriers interact with the lattice in silver-bismuth-halide semiconductors, and how this affects their potential performance in optoelectronic devices. Specifically, temperature-dependent measurements allow for great insights into both the steady-state electronic structure and charge-carrier transport of these materials. The main focus of the discussion is a detailed temperature-dependent study of Cu_2AgBiI_6 to assess its suitability for photovoltaic applications, and then a comparison is made, using temperature-dependent OPTPS measurements, with $Cs_2AgBiBr_6$.

As outlined in Chapter 2, in recent years substantial interest has emerged around so-called 'double perovskites' [33], a vast class of over 90,000 materials, some of which can be lead-free [35]. The most frequently investigated material in this class is the all-inorganic double perovskite $Cs_2AgBiBr_6$, which is highly thermodynamically stable and has an indirect band gap with weak absorption onset around 2 eV as well as a strong direct gap near 3.1 eV [73, 74, 76, 78, 305]. Spectroscopic and theoretical studies of this material have pointed towards low charge-carrier mobilities and long fundamental charge-carrier lifetimes [73, 75, 196, 305–307], and work by Zelewski et al. has suggested the existence

of a colour centre as the source of photoluminescence in $Cs_2AgBiBr_6$ [74], which would be indicative of strong electron-phonon coupling in this material. Relaxing the constraints of single- or double-perovskite structures allows for an even wider variety of materials to be explored for optoelectronic applications. These have ranged from all-inorganic materials such as quasi zero-dimensional tin halides $Cs_{4-x}A_xSn(Br_{1-y}I_y)_6$ (A = Rb, K) [102], bismuth-based $AgBiI_4$ [80], $CuBiI_4$ [308], $Cs_3Bi_2Br_9$ [228] and $Rb_4Ag_2BiBr_9$ [197], the 'hollow' tin perovskite {en}$FASnI_3$ (en = ethylenediammonium) [309], and (100) and (110) layered perovskites [203, 206–209].

The exploration of such wide material space has raised the question of how coupling between charge carriers and the lattice is affected, given this varies substantially as material structure is altered or as dimension is decreased, for example by the creation of layered materials [91, 153, 201]. The nature of electron-phonon coupling and charge localisation plays a fundamental role in determining any intrinsic limits to the optoelectronic properties of materials and their suitability for photovoltaic applications. As discussed in Chapter 2, the strength of charge-carrier localisation in a given material depends on its chemical composition, ease of structural distortion, and structural and electronic dimension. Further, it appears that in double perovskite or silver-bismuth materials, although the crystal structure can be three-dimensional, the electronic band structure is of lower dimension [92], making charge-carrier localisation more likely [73, 74, 152, 307]. Studies across a variety of material classes demonstrate the general dependence of self-trapping on dimension: higher-dimension systems exhibit potential barriers between free and self-trapped states, meaning that self-trapping may occur only above certain temperatures and self-trapping rates display clear temperature dependence [72, 107, 152]. In contrast, there appears to be little to no barrier for one- or zero-dimensional systems — a result that has been borne out both theoretically and experimentally [153, 156, 310]. Given that charge-lattice interactions lower charge-carrier mobilities, the extent of their strength in

any given semiconductor has an important bearing on photovoltaic performance. Because all charges interact with the surrounding lattice to some extent, an accurate assessment of the strength of such interactions and the resulting mobilities is therefore of central importance for any new light-harvesting material for photovoltaic applications.

In this thesis chapter, the optoelectronic properties of a novel silver-bismuth based semiconductor, the recently reported Cu_2AgBiI_6 [84], are investigated. The nature of charge-carrier excited states in Cu_2AgBiI_6 is explored, based on temperature-dependent photoluminescence (PL), UV-visible absorption, time-correlated single-photon counting (TCSPC) and optical-pump terahertz-probe spectroscopy (OPTPS) measurements. These experiments reveal several complementary pieces of evidence that together paint a picture of charge-carrier self-trapping and small-polaron formation in this material. The increase in intensity of long-lived, highly Stokes-shifted PL emission as temperatures are lowered, the discovery of an ultrafast decrease in photoconductivity that results in a long-lived localised charge-carrier population with lowered mobility, and the increasing mobility of this localised state with rising temperature all point towards a strong influence of the lattice on charge carriers in Cu_2AgBiI_6. This leads to the conclusion that upon photoexcitation, self-trapped charge carriers or small polarons form rapidly within picoseconds in Cu_2AgBiI_6. However, the temperature-activated mobility of such small polaron states still allows for sufficiently high charge-carrier mobilities at room temperature which, together with strong direct absorption near 2.1 eV and low exciton binding energy of 29 meV, make this material highly suitable for use in optoelectronic devices. Further, an OPTPS-based investigation of $Cs_2AgBiBr_6$ is also presented, revealing very similar temperature-dependent behaviour for both the charge-carrier dynamics and mobility. Together with the results for Cu_2AgBiI_6, this points towards the presence of silver and bismuth as the underlying cause of charge-carrier localisation, and this topic is investigated in more detail in Chapter 6.

5.2 Experimental Details

Sample preparation of both Cu_2AgBiI_6 and $Cs_2AgBiBr_6$ thin films was carried out by G. Longo, Department of Physics, University of Oxford, as outlined in Section 3.5. The samples were deposited on 2 mm z-cut quartz substrates, which have excellent thermal conductivity and transparency over the THz bandwidth and temperature ranges used in the studies discussed in this chapter [260].

The X-ray diffraction measurements were carried out as described in Chapter 3. The Pawley fitting and analysis of XRD data in this chapter was carried out by H. Sansom, Department of Physics, University of Oxford. The temperature-dependent optical absorption measurements and fits according to Elliott's theory, and the temperature-dependent photoluminescence measurements, presented for Cu_2AgBiI_6 in this chapter were carried out by A. D. Wright, Department of Physics, University of Oxford.

The temperature-dependent OPTPS measurements of both Cu_2AgBiI_6 and $Cs_2AgBiBr_6$ were carried out as described in Chapter 3 and using liquid helium, with samples mounted in a cold-finger cryostat (Oxford Instruments, MicrostatHe). The temperature was regulated via a temperature controller (Oxford Instruments, MercuryiTC) connected to a resistive heater and temperature sensors mounted both on the cryostat heat exchanger and at the end of the sample holder.

5.3 Materials Synthesis and Understanding of Crystal Structure

An initial investigation of Cu_2AgBiI_6 focused on its synthesis, structural and compositional properties, stability and basic optoelectronic properties [84]. This early investigation revealed that Cu_2AgBiI_6 constitutes a heavily-disordered network in which alternating layers of octahedral sites facilitated by the cubic close-packed iodide sub-lattice are partially occupied by Ag^+ or Bi^{3+} [84]. This structure is shown in Figure 5.1 (a),

with the unit cell enclosed by the black line, and the edge-sharing octahedral sites highlighted in purple.

An alternative description is that the octahedral network can be considered as a cation-disordered $CdCl_2$ structure. The heavy cation disorder is apparent in the partial occupancy of each cation site, indicated by the fractional filling of the circles at each ionic site in Figure 5.1 (a). The Cu^+ partially occupies all of the tetrahedral sites facilitated by the cubic close-packed iodide sub-lattice. The structure shows a much higher level of cation disorder than the standard 3D corner-sharing octahedral networks present in (double) perovskites (i.e. it has a higher configurational entropy) [84]. For a more detailed outline of the structure, readers are pointed to the original structural characterisation by Sansom et al. [84]. The structure and chemical composition of Cu_2AgBiI_6 (including the presence of Ag^+ and Bi^{3+}, layered ordering and significant cation disorder) are likely to reduce the electronic dimension of the material [91] and facilitate interactions of charge carriers with the lattice, making charge-carrier localisation more likely to occur.

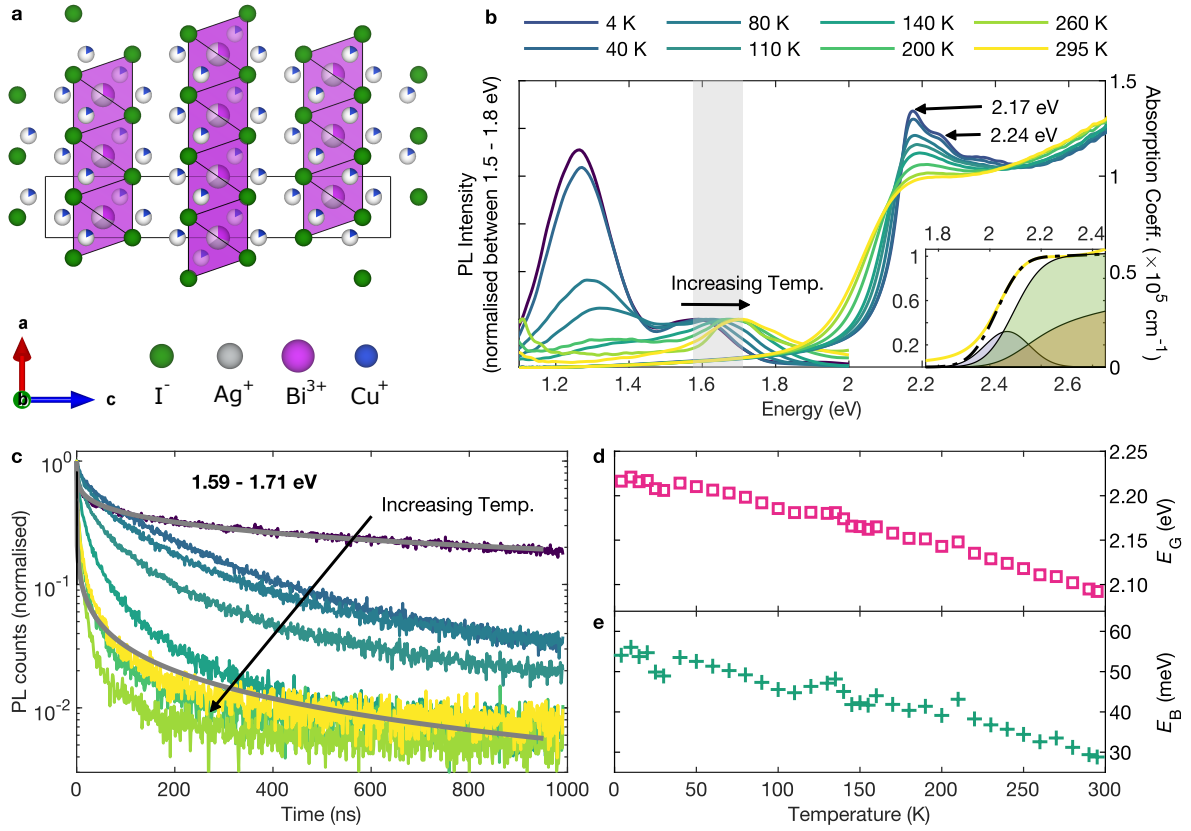


Figure 5.1: Temperature-dependent photoluminescence and absorption. (a) Crystal structure of Cu_2AgBiI_6, with the edge-sharing octahedral layers highlighted in purple. The partial occupancy of the Ag^+, Bi^{3+} and Cu^+ sites is shown by the fractional filling of the circles at each ionic site. (b) Temperature-dependent photoluminescence and UV-visible absorption measurements of Cu_2AgBiI_6 thin films between 4 – 295 K. The PL peak blue-shifts with increasing temperature. The shaded region between 1.59 – 1.71 eV indicates the high-energy region from which TCSPC measurements were taken (shown in (c)) and from which peak counts were measured (shown in Figure 5.4 (c)). The inset shows the fit to the spectrum at 295 K using Elliott's theory (black dashed line) [251], with the shaded areas indicating the excitonic (blue) and continuum contributions without (brown) and with (green) Coulombic enhancement. (c) Time-resolved PL decays measured using TCSPC at a fluence of 200 nJcm^{-2}. The decays are very heterogeneous (non-exponential) at high temperatures, and become much longer-lived at low temperatures. The grey solid lines are fits to a stretched exponential at 4 and 295 K. (d) Value of the band gap energy E_G extracted at each temperature using the Elliott fits. (e) Value of the exciton binding energy E_B extracted at each temperature using the Elliott fits. Temperature-dependent PL and absorption measurements were carried out by A. D. Wright.

To confirm the composition and structure of the specific samples investigated in this chapter, X-ray diffraction (XRD) measurements were carried out on thin films of Cu_2AgBiI_6 on z-cut quartz substrates, giving the diffraction intensities shown in Figure 5.2. A Pawley fit was performed on the XRD patterns of the individual films used for the spectroscopic measurements. All the peaks in the XRD patterns could be fitted to a mixture of two rhombohedral phases each with a trigonal unit cell and space group $R\bar{3}m$, or to the z-cut quartz peaks of the substrate. This is consistent with the phases found by X-ray diffraction and transmission electron microscopy energy dispersive X-ray (TEM EDX) analysis in films processed using the same method by Sansom et al. [84]. In that original study, TEM EDX showed that the phases were a mixture of the targeted quaternary phase with a non-stoichiometric composition close to Cu_2AgBiI_6, and an impurity ternary phase with a non-stoichiometric composition close to Cu_2BiI_5 [84, 311]. The peak at 25° is mainly attributable to the Cu_2AgBiI_6 film, whilst the peaks at 12.8° , 29.3° and 41.5° are a combination of reflections from the Cu_2AgBiI_6 as well as some small amount of impurities, likely to be Cu_2BiI_5. These assignments are in agreement with the original investigation of Cu_2AgBiI_6 [84], and the above-mentioned impurities have also been examined in the original study and previous work [84, 311]. It is worth noting that the original study of Cu_2AgBiI_6 solved the crystal structure at 100 K [84], raising the possibility of a phase transition arising below this temperature, as the measurements here and below were carried out to temperatures as low as 4 K. However, there are no clear discontinuities or sudden changes in behaviour of the absorption and PL spectra or in the charge-carrier dynamics below 100 K (see below), making it unlikely that a structural phase transition has occurred as the temperature is varied.

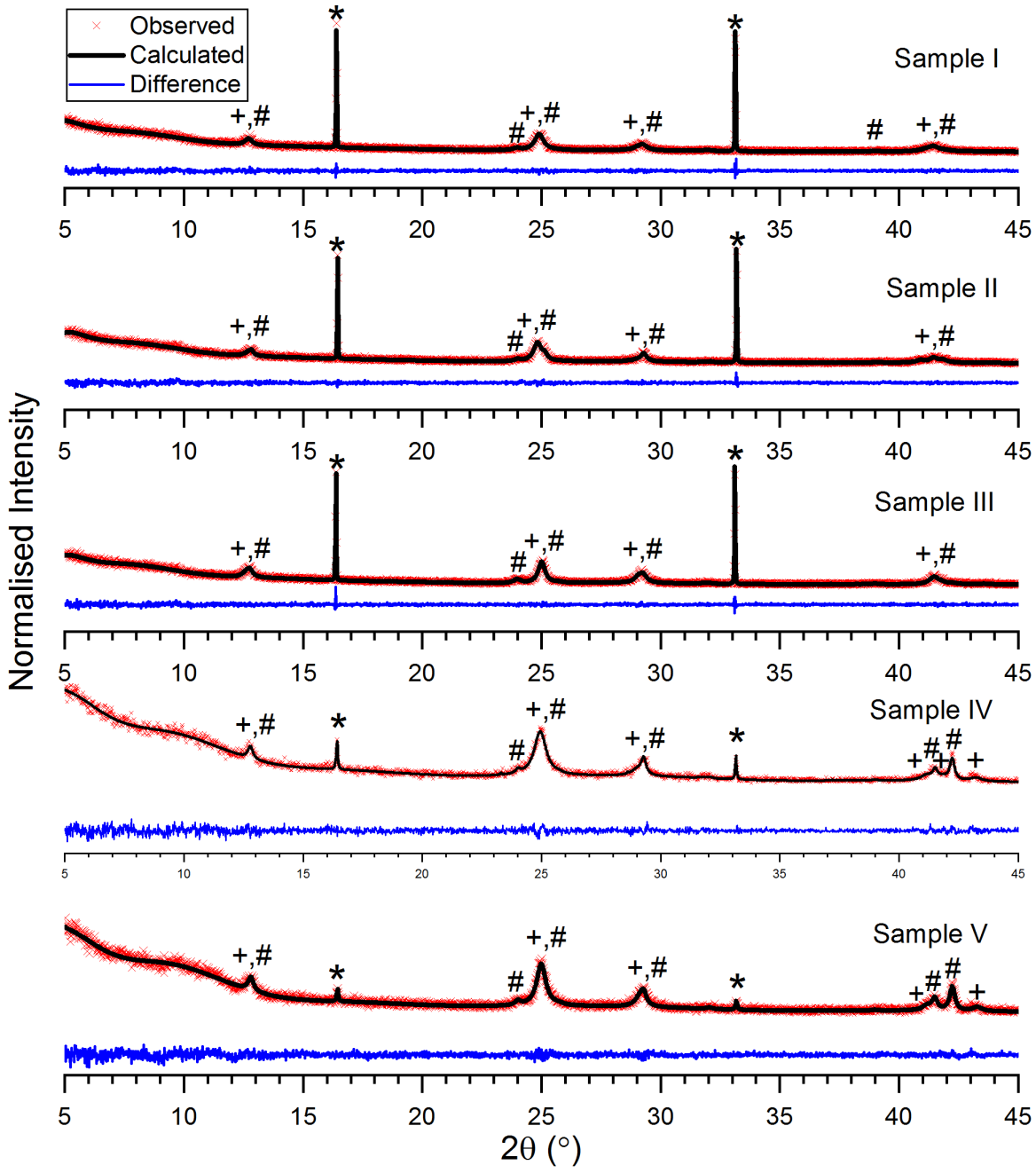


Figure 5.2: X-ray diffraction measurements of the Cu_2AgBiI_6 thin films. XRD spectra are shown as red crosses, measured using a Panalytical X'Pert powder diffractometer using the Cu−Kα_1 line as incident radiation. Pawley fits are the thick black lines, with the difference between the data and fits below in blue. The peaks highlighted with (+) are due to Cu_2AgBiI_6, whereas those highlighted with (#) are due to Cu_2BiI_5 impurities. The peaks highlighted with (*) at 16.3° and 33.2° are due to the quartz substrate. XRD measurements were carried out by L. R. V. Buizza, and the fitting and analysis were carried out by H. Sansom.

5.4 Main Experimental Results and Discussion

5.4.1 Understanding the steady-state optoelectronic properties of Cu_2AgBiI_6

In order to establish the energetic distribution of electronic states in Cu_2AgBiI_6, temperature-dependent measurements of UV-visible absorption and photoluminescence spectra between 4 – 295 K were carried out (see Figure 5.1 (b)). At 4 K the absorption onset of Cu_2AgBiI_6 occurs at approximately 2 eV, which red-shifts to lower energies as the temperature is raised to 295 K. Further, the absorption spectrum of Cu_2AgBiI_6 at 4 K displays a clear excitonic feature with some fine structure, with two peaks visible at 2.174 and 2.235 eV (see Figure 5.1 (b)). The trends in absorption with temperature are examined through fits to the spectra based on Elliott's theory [251], accounting for both free electron and hole states and bound exciton contributions to the absorption, which are enhanced by Coulombic interactions, with bound excitonic contributions featuring prominently just below the band gap (see inset in Figure 5.1 (b) and Figure 5.3) [67]. The resulting direct band gap energy E_G and exciton binding energy E_B for temperatures between 4 – 295 K are shown in Figure 5.1 (d) and (e), respectively. The excellent fit of Elliott's theory near the band edge and strong absorption coefficient values suggest a direct nature of this absorption onset.

Although the Elliott fits deviate slightly from the fine structure in the absorption spectra measured at low temperatures (see Figure 5.3), they are in good qualitative and quantitative agreement with the measured data. The fits confirm that the band gap shifts from 2.22 eV at 4 K down to 2.09 eV at 295 K, a trend that is opposite to that observed for conventional metal-halide perovskites such as $MAPbI_3$, $FAPbI_3$ or $FASnI_3$ [30, 59, 174, 175], for which increasing temperatures lead to a blue-shift in band gap, owing to a combination of trends in electron-phonon coupling and the positive deformation potential of these materials [90, 294, 295]. However, the temperature dependence of the band gap of Cu_2AgBiI_6 matches that observed for the well-studied silver-bismuth material

$Cs_2AgBiBr_6$ [73, 305], and it is also similar to what is typically found in conventional inorganic semiconductors such as Si and GaAs, which obey Varshni's rule of increasing band gaps with decreasing temperature [312, 313].

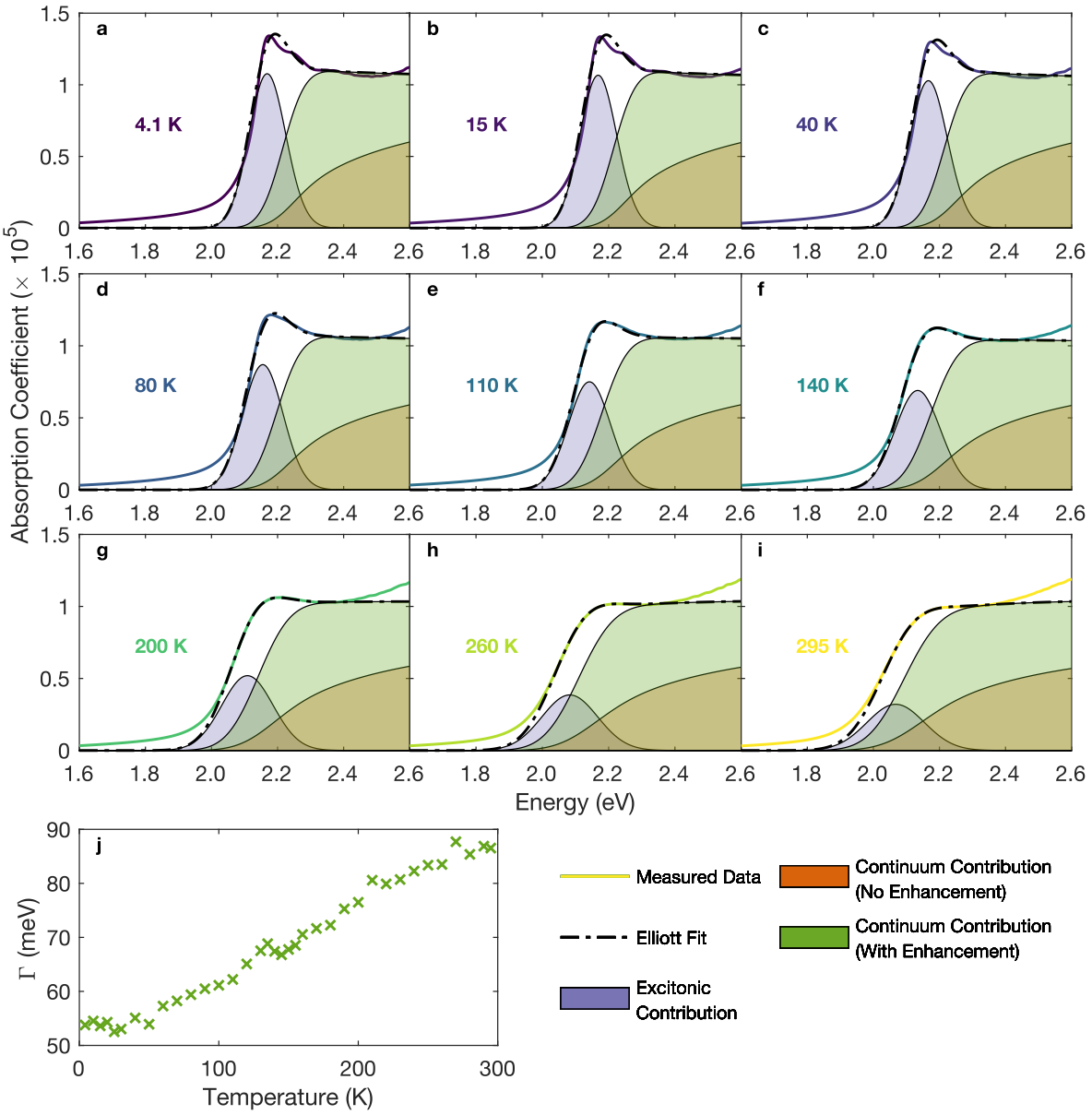


Figure 5.3: Temperature-dependent Elliott fitting of optical absorption spectra. (a) - (i) Fits (dashed black lines) to the steady-state optical absorption spectra (solid coloured lines), across the temperature range 4 – 295 K using Elliott's theory.[251] The excitonic (blue) and free carrier contributions, without (orange) and with (green) Coulombic enhancement are shown as the filled areas. (j) Broadening parameter Γ obtained from the Elliott fits. Measurement and fitting of the optical absorption spectra was carried out by A. D. Wright.

The exciton binding energy extracted from such Elliott fits falls from 54.1 meV to 28.8 meV between 4 K and room temperature. A simpler determination of a binding energy by inspection of the fine structure observed near the absorption onset at 4 K, assuming that the adjacent peaks can be assigned to the $n = 1, 2$ Wannier excitonic states [314], gives $E_B \sim 80$ meV. Such a low exciton binding energy of ~ 29 meV at room temperature is exciting, given that excitonic features near the direct gap of the related semiconducting double perovskite $Cs_2AgBiBr_6$ are commensurate with much higher exciton binding energies nearer several hundred meV [73, 77], and may partly derive from the lower direct band gap of Cu_2AgBiI_6 compared with $Cs_2AgBiBr_6$ [167]. It should be noted that the temperature-dependent values of the exciton binding energy determined for Cu_2AgBiI_6 fall in between those measured for three-dimensional lead-halide perovskites [48, 67, 175], which are on the order of a few or a few tens of meVs, and those derived for two-dimensional Ruddlesden-Popper perovskites [315] or for $Cs_2AgBiBr_6$ [73, 77, 316], of several hundred meVs. The layered structure of Cu_2AgBiI_6 likely supports some electronic confinement [167], leading to increased binding energies relative to three-dimensional metal-halide perovskites. However, this effect is somewhat mitigated by the fully three-dimensional iodine network, and unlike in layered Ruddlesden-Popper perovskites, there is no dielectric confinement effect that enhances exciton binding energies further [315]. These factors, together with possible variations in charge-carrier effective masses, likely explain why the value of E_B found for Cu_2AgBiI_6 sits in between three-dimensional metal-halide perovskites and two-dimensional Ruddlesden-Popper perovskites. However, the general trend of lower exciton binding energy with rising temperature is in line with estimates made using Elliot theory for both $MAPbI_3$ and $FAPbI_3$ [67, 175], where the exciton binding energy falls by a factor of 2 – 3 between 4 – 295 K. This reduction is mainly attributed to changes in the dielectric function with temperature, given the quadratic dependence of binding energy on dielectric permittivity for Wannier

excitons [48, 67, 175]. Overall, the room temperature exciton binding energy of ~ 29 meV observed here for Cu_2AgBiI_6 compares with thermal energies (26 meV), meaning that the formation of uncorrelated electrons and holes should be highly effective, which will aid charge extraction in solar cell architectures.

To complement the information on electronic states provided by optical absorption measurements and to allow for insights into the energetics of localised states, steady-state photoluminescence measurements of a thin film of Cu_2AgBiI_6 were carried out. The photoluminescence spectra of Cu_2AgBiI_6 (see Figure 5.1 (b)) exhibit weak and fairly broad emission peaking at 1.71 eV at room temperature, and display a large Stokes shift from the band gap of several hundred meV. As the temperature is lowered, this peak red-shifts slightly, down to 1.59 eV at 4 K, opposite to the trend observed for the absorption onset. It is therefore unlikely that this emission band is associated with radiative band-to-band recombination of free charge carriers. Instead, based on the observations here and further investigations detailed below, this emission band is assigned to a self-trapped state, for which a large Stokes shift and broad emission peak are highly characteristic [72]. Studies of other silver-bismuth compounds, such as Cs_2AgBiX_6 [74, 76] and $Rb_4Ag_2BiBr_9$ [197], quasi-zero dimensional tin-halides [102], and layered perovskites [203, 208] have similarly observed highly red-shifted emission from self-trapped states. Given the large cation disorder and edge-sharing octahedra in Cu_2AgBiI_6 [84], strong charge-lattice interactions should be present, resulting in highly Stokes-shifted emission, as has recently been suggested for a colour centre in $Cs_2AgBiBr_6$ [74]. In addition, a narrowing of the emission spectra (see Fig 5.1 (b)) and increase in intensity is observed as the temperature is lowered (see Figure 5.4 (c)), analogous to what has been observed for the emission attributed to a self-trapped state in both $Rb_4Ag_2BiBr_9$ [197] and $(EDBE)PbBr_4$ (EDBE = 2,2'-(ethylenedioxy)bis(ethylammonium)) [208]. As Figure 5.4 (c) shows, the emission intensity around 1.59 – 1.71 eV in Cu_2AgBiI_6 increases by over a factor of ten as the

temperature is lowered, similar to previous observations of self-trapped states [72, 197, 208]. However, it should be noted that as the temperature is lowered, alternative non-radiative decay pathways mediated by lattice vibrations are significantly suppressed, which would lead to an enhancement of the emission from any radiative transition.

When the temperature is lowered below 200 K a second emission peak emerges in the near infrared around 1.35 eV, shifting down to 1.26 eV at 4 K and growing in intensity to surpass that of the higher-energy peak below 120 K (see Figure 5.1 (b) and Figure 5.4 (a)), and which could have multiple potential explanations. Given that this energy scale is very similar to the absorption at 1.24 eV observed through photo-thermal deflection spectroscopy (PDS) in the original investigation by Sansom et al. [84], it most likely arises from a mid-gap defect state, similar to what is observed with Bi-doped $CsAg_{1-x}Na_xInCl_6$ nanocrystals [317]. Alternatively, the emission could be associated with an impurity, for example the small quantities of Cu_2BiI_5 that were identified in the XRD measurements. However, this impurity is unlikely to be BiI_3, since this has been shown to absorb only weakly at the excitation wavelength near 398 nm and luminesce near 1.8 eV [318–320], where no significant intensity was observed. Finally, an alternative explanation for the lower-energy emission band of Cu_2AgBiI_6 between 1.26 – 1.35 eV at low temperatures could be the disordered geometry of the structure supporting sites of distinctly different energies at different points in the lattice. Such effects have been proposed for $Rb_4Ag_2BiBr_9$ [197], for which self-trapped excitons on $BiBr_6$ units give rise to three distinct peaks in the measured PL spectra that are separated by up to 240 meV.

5.4.2 Charge-carrier dynamics: photoexcitation, localisation and emission

To elucidate the dynamics relating to the charge-lattice interactions, time-resolved spectroscopy on femtosecond through to microsecond timescales was performed, using both nanosecond time-resolved PL and sub-picosecond time-resolved THz photoconductivity

techniques (as discussed in Chapter 3). The time-resolved photoluminescence transients, measured using time-correlated single photon counting with $\sim$ 100-ps time resolution, are discussed first (see Figure 5.1 (c)). Such transients therefore allow for an examination of the timescales involved in the recombination of the higher-energy self-trapped emitting state. At high temperatures the PL decays associated with the 1.59 –1.71 eV emission band are very heterogeneous, exhibiting both very fast early components within the first few ns after excitation, as well as a tail with longer-lived dynamics. As the temperature is decreased, the initial fast component becomes much less dominant and the longer-lived tail increases significantly in lifetime. Given the heterogeneity of these dynamics, stretched-exponential functions of the form $I = I_0 e^{-(t/\tau_{\text{char}})^{\beta}}$ were fitted to these data in order to extract PL lifetimes [254], which are presented in Figure 5.4 (d) of the SI. These fits yield an average PL lifetime of tens of nanoseconds at room temperature, rising to 4.1 µs at 4 K, for the high-energy PL band between 1.59 –1.71 eV. Similar dynamics were measured for the low-energy emission, and these are shown in Figure 5.4 (b). Finally, time-resolved PL spectra were recorded at 4 K over the first 100 ns after excitation, which exhibit no energetic shifts over these timescales (see Figure 5.4 (e)).

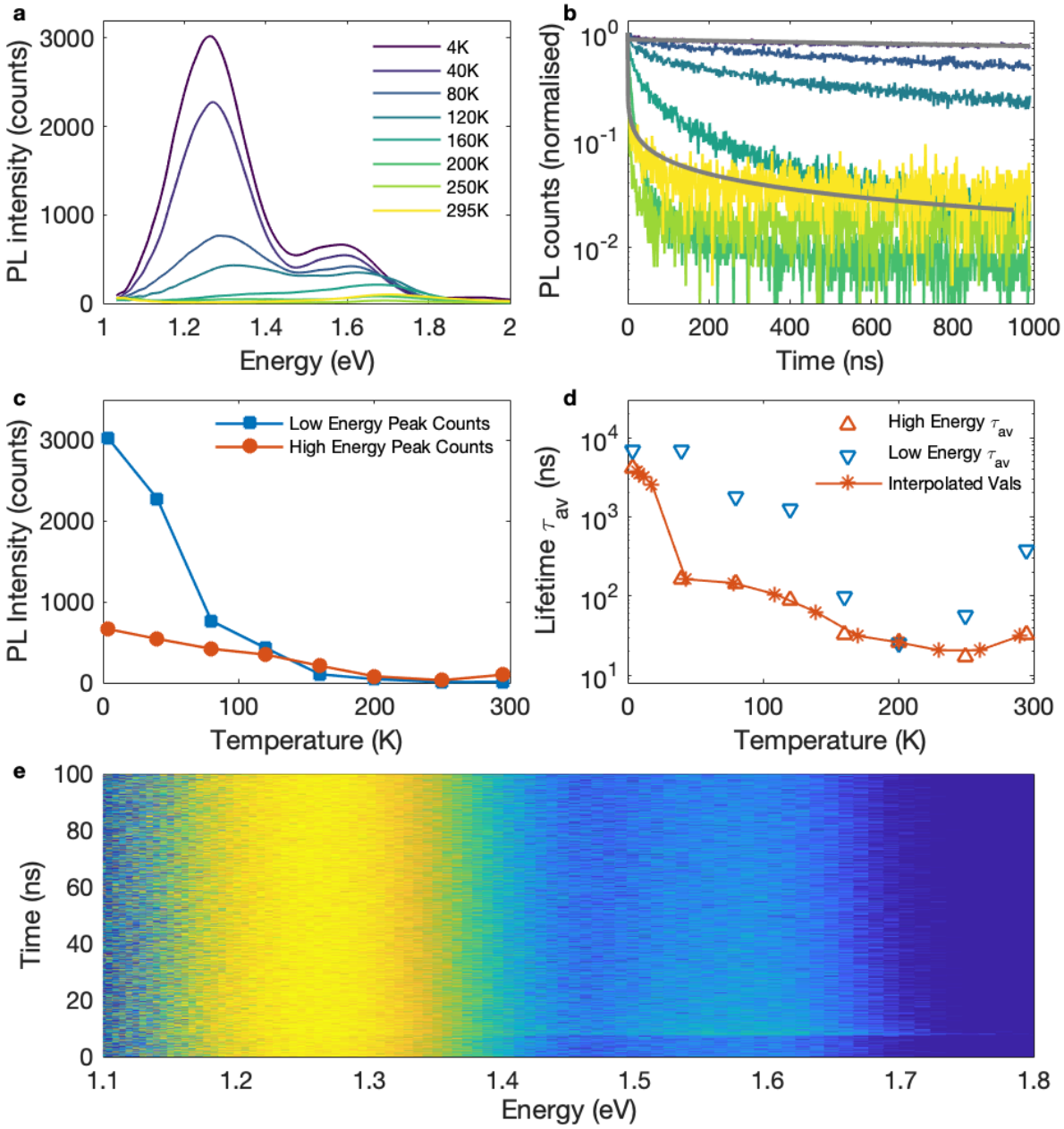


Figure 5.4: Temperature-dependent photoluminescence. (a) Un-normalised photoluminescence spectra between 4 – 295 K. As the temperature is lowered, a peak in the near infrared emerges at around 1.35 eV, and below 120 K this peak has a higher intensity than the high-energy emission. (b) Time-resolved PL decays of the low-energy emission between 1.26 – 1.31 eV, measured between 4 – 295 K. The solid grey lines at 4 K and 295 K are fits to the PL decays. (c) Intensity of photoluminescence peaks at high (1.59 – 1.71 eV) and low (1.26 – 1.31 eV) energy, plotted at each measured temperature. (d) PL lifetimes of high and low energy peaks, extracted from fits to TCSPC measurements, as discussed in the main text and above (shown as empty triangles). The stars joined by lines show the linearly-interpolated values used to obtain k_1 as an input to the two-level mobility model. (e) Time-resolved PL spectrum of Cu_2AgBiI_6 at 4 K over 100 ns, measured at an excitation fluence of 200 nJcm^{-2}, showing both high- and low-energy peaks present throughout the measurement window. Temperature-dependent PL measurements were carried out by A. D. Wright.

To interpret the observed PL dynamics, it should be noted that self-trapped states have often been found to exhibit an increased lifetime as the temperature is lowered, as for example in zero-dimensional Cs_4SnBr_6 [102] and across the alkali halides [321], and by several orders of magnitude in the case of KBr, KI and RbI [120, 321], similar to what is reported here. However, trap-mediated recombination pathways may also be facilitated by lattice vibrations with increasing temperature, as seen in $MAPbI_3$ [174] and mixed lead-tin $FAPb_{1-x}Sn_xI_3$ perovskites [30], which may also partly explain the faster PL dynamics at higher temperatures. The observed heterogeneity of the PL decay from Cu_2AgBiI_6 (in particular at high temperature) is also in good agreement with the structural disorder deduced from XRD and the measured sizeable Stokes shifts. However, the lack of shifts in the emission spectra over time evident in Figure 5.4 (e) suggests that energetic relaxation either within electronic bands (e.g. from a direct to an indirect gap region) [314], into the self-trapped state, or through charge migration to lattice locations with different emission energies, does not occur to a significant extent within the time window of 100 ps to 100 ns following excitation. Higher temporal resolution is therefore required in order to examine such effects.

As mentioned earlier, an additional infrared PL emission emerges at lower temperatures, dominating the emission spectra below 120 K (see Figure 5.4 (a)). This emission is between 1.26 – 1.35 eV, and blue-shifts and narrows slightly as the temperature is lowered. The PL decays for this lower-energy peak were also measured using TCSPC at a fluence of 200 $nJcm^{-2}$, with the decays shown in 5.4 (b). At room temperature the decays are very heterogeneous, but as the temperature is lowered they become homogeneous and the lifetime is much longer. The fits to the low-energy PL decays also give lifetimes that increase by several orders of magnitude as the temperature decreases, as has been found for emission from self-trapped states in $Rb_4AgBiBr_9$ [102][72][321]. However, it cannot be

Temp (K)	High-Energy τ_{av} (ns)	High-Energy β	Low-Energy τ_{av} (ns)	Low-Energy β
4	4100	0.24	7000*	N/A
40	164	0.53	7000*	N/A
80	145	0.45	1800*	N/A
120	90	0.37	1260	0.39
160	33	0.28	97	0.36
200	26	0.18	25	0.18
250	17	0.19	57	0.17
295	33	0.18	373	0.15

Table 5.1: Values of parameters extracted from the fits to the PL decays. Values of τ_{av} and β are shown for the stretched-exponential fits, and the values marked with '*' are from the monoexponential fits.

ruled out that this increase in lifetime simply arises due to the shutting off of non-radiative decay pathways, especially due to the significant disorder present in Cu_2AgBiI_6.

In order to gain further insights into the dynamics of charge carriers and the potential formation of any self-trapped states, ultrafast optical-pump terahertz-probe spectroscopy was carried out using an amplified laser system (Spectra Physics, MaiTai – Empower – Spitfire) with a 400-nm pump pulse train (as outlined in Chapter 3). This technique provides insights into the fractional change in transmitted THz-field amplitude $-\Delta T/T$, which is proportional to the transient photoconductivity of a material, with sub-picosecond time resolution (as outlined in Section 3.3.2.1), making it ideal for the study of charge-carrier localisation effects. Optical excitation at approximately 400 nm (3.1 eV) was used in both the PL and OPTPS measurements, well above the band gap, meaning that free carriers, rather than excitons, predominantly form immediately following photoexcitation in Cu_2AgBiI_6. Measurements at room temperature across several excitation fluences, shown in Figure 5.5 (a), reveal an ultrafast decay: the photoconductivity (proportional to the charge-carrier sum mobility μ and number of photoexcited charge-carriers n) decreases by a factor of two within a few ps, in a process that is fluence-independent (see Figure 5.5 (b) inset). It should be noted that the THz field probing Cu_2AgBiI_6 lies in the plane of the thin film: although there are clear 2D layers of octahedra in Cu_2AgBiI_6, the random lattice

orientation across different grains in the thin film means that results from the OPTPS measurements can be interpreted as a bulk average across all directions in the material.

Previously reported timescales for the formation of self-trapped states in layered metal-halide perovskites are similar to those measured here, varying between hundreds of fs [203, 209, 233], through to tens of ps, [228] and self-trapped exciton formation in other systems such as KI, NaCl or Argon clusters has also been observed to occur on picosecond timescales [322–324]. The lack of fluence dependence and presence of this ultrafast decay even at low excitation fluences ($\leq 10\,\mu\mathrm{Jcm}^{-2}$) rules out any bimolecular or Auger contributions, or exciton formation, as the origin of this component, once more indicating the likelihood of self-trapping processes leading to the observed ultrafast decay in charge-carrier conductivity.

5.4.3 Temperature-dependent OPTPS investigation of charge-carrier localisation and transport

To gain insights into the mechanisms limiting the charge-carrier mobility, and to reveal any thermally-activated processes, temperature-dependent THz photoconductivity (OPTPS) measurements were conducted on Cu_2AgBiI_6 with the resulting transients shown in Figure 5.5 (b) and (c). Transient OPTPS decays were measured out to 25 ps after excitation, and the temperature was varied between 7 – 290 K using a liquid-helium cryostat. Longer, fluence-dependent decays out to 1000 ps using logarithmically-spaced points in time were also recorded at 7 K, and THz photoconductivity spectra were taken at several time delays for temperatures of 7 K and 295 K (see Figure 5.6). The transient decays across all temperatures exhibit an initial fast decay component, followed by a long-lived decay. Through visual inspection and data fitting described in more detail below, the decay time of the initial ultrafast component is found to be temperature-invariant. However, at lower temperatures, the ultrafast component plays a more substantial

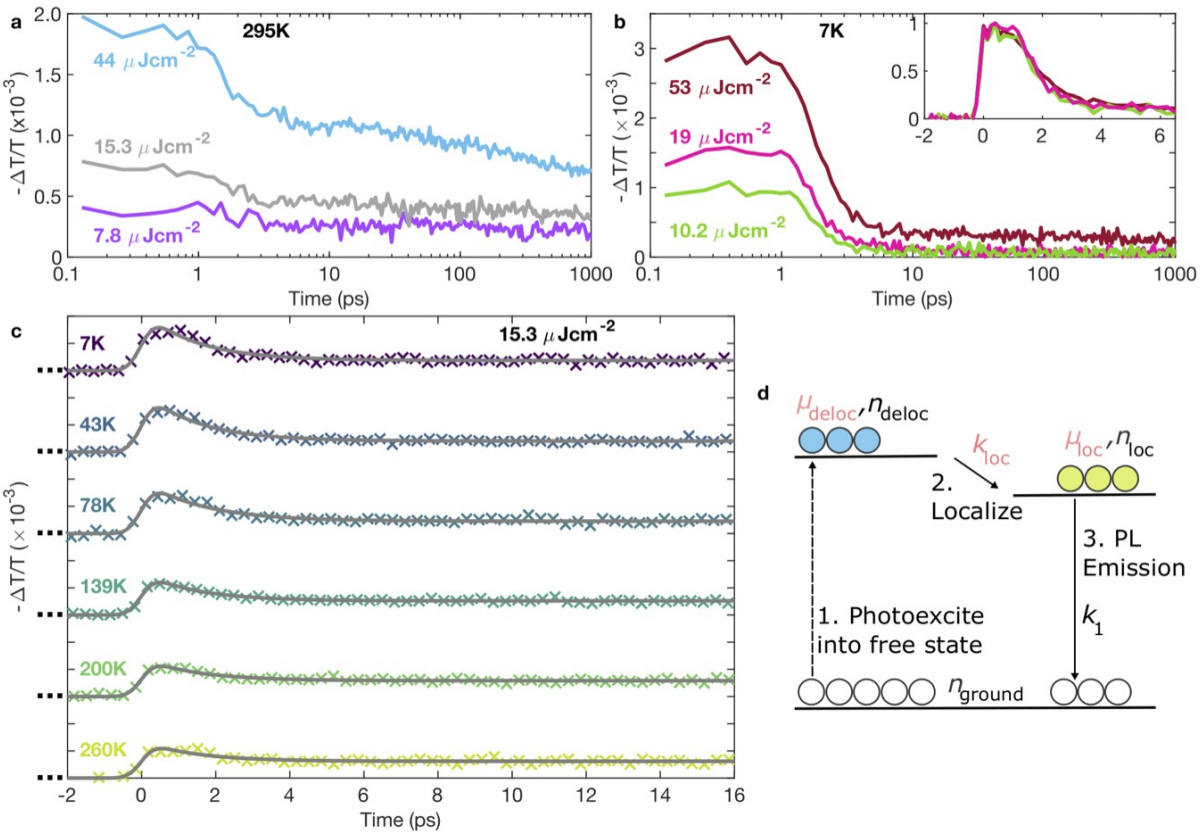


Figure 5.5: Temperature-dependent photoconductivity decays for Cu_2AgBiI_6. Such OPTPS transients are shown for a range of different excitation fluences for (a) 295 K and (b) 7 K. The inset in (b) shows the normalised traces at 7 K over the first 6 ps, indicating a lack of fluence dependence to the charge-carrier dynamics. (c) Early-time temperature-dependent OPTPS data measured at a fluence of 15.3 μJcm^{-2} and fitted with a two-level mobility model, with the fits shown as grey solid lines. The two-level mobility model is explained schematically in (d), with fixed parameters shown in black and parameters that are fitted and extracted from the model in pink. The dotted line indicates the initial photoexcitation of charges, in this case due to pulsed laser excitation. See Section 3.3.6.2 for a full explanation of the model and corresponding differential equations.

role, i.e. the contribution of the longer-lived component to the photoconductivity decreases as the temperature is reduced.

In order to verify the origin of the photoinduced conductivity response, spectra were recorded across the range of 0.4 – 2.5 THz at temperatures of 7 and 295 K and time delays of 0.2 ps, 2 and 92 ps (see Figure 5.6 (d) – (i)). The photoconductivity spectra exhibit very flat real and imaginary parts, with the latter being near-zero, indicative of Drude-like conductivity with short momentum scattering times [261]. No sharp resonances were

observed, suggesting the absence of discrete optically allowed transitions in the energy range 2 – 10 meV (0.5 – 2.5 THz). These observations thus suggest that inter-excitonic transitions do not fall into this range, in good agreement with the estimate of the binding energy obtained from the absorption measurements. Further, optical phonon modes are also absent in this energy region, and therefore it is safe to assume that the measured photoconductivity simply arises from photoinduced charge carriers and exhibits a linear dependence on charge-carrier mobility and population. A 'Drude Factor' is calculated, following the method presented by Milot et al. [174], in order to assess the extent to which photoconductivity spectra follow a free-carrier response with short scattering times (zero imaginary part, constant real part). This analysis yields values above 0.8 at all time delays for low (7 K) and room (295 K), indicating that Drude-like free-carrier conduction prevails (see Figure 5.6 (c)) However, it should be noted that at 7 K an interesting decrease in the Drude factor occurs over time, from 0.97 to 0.82 between 0.2 and 92 ps after excitation, which may be indicative of a stronger deviation from free-carrier like transport as charge carriers localise over time.

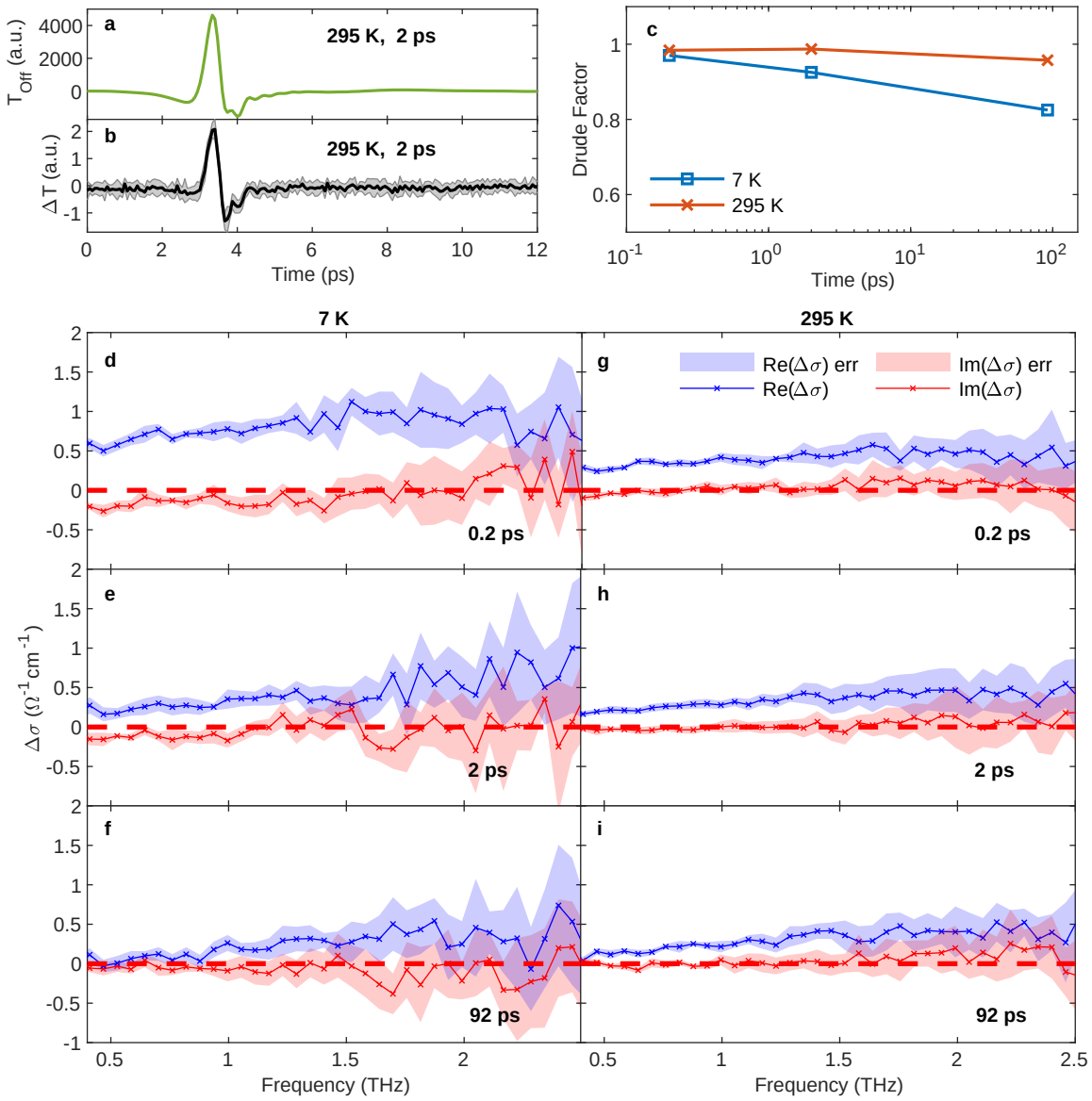


Figure 5.6: Temperature- and delay-dependent photoconductivity spectra. (a) Transmitted THz field amplitude with no photoexcitation T_{Off} for the photoconductivity spectrum measured at 295 K and a delay of 2 ps. (b) Differential THz field amplitude $\Delta T = T_{\mathrm{On}} - T_{\mathrm{Off}}$ for the photoconductivity spectrum measured at 295 K and a delay of 2 ps. (c) Calculated Drude Factor (see above for details) for each of the photoconductivity spectra shown in (d-i). Terahertz photoconductivity spectra measured on a thin film of Cu_2AgBiI_6 at delays of 0.2, 2, 92 ps at 7 K (d-f) and 295 K (g-i). Spectra were measured at a fluence of 10.2 μJcm^{-2}.

To assess the mobility of charge-carriers before and after the ultrafast charge-carrier localisation, the early-time transient decays in Figure 5.5 (c) were fitted with a simple two-level model, shown schematically in Figure 5.5 (d) and discussed in detail in Section 3.3.6.2. The model assumes carriers are initially photoexcited high into the conduction band into a free-carrier state associated with a high mobility μ_{deloc} and a population n_{deloc}, which determine the initial photoconductivity response at t = 0 ps. Following this, the mobility of charge carriers is reduced through the formation of a 'localised' state, with mobility μ_{loc} and population n_{loc}, with the localisation rate given by k_{loc}. From the localised state, charges will subsequently recombine down to the ground state over longer timescales, as observed in the time-resolved PL. This recombination is thus described using long-time recombination rates k_1, which are extracted from the lifetimes obtained from the fits to the low-energy PL decays recorded with TSCPC at each temperature. While the initial free-carrier state could in principle also contribute photoluminescence through band-to-band recombination, no PL could actually be observed at energies close to the absorption onset, presumably because the free state depopulated too rapidly to contribute significantly and to be resolved in the TCSPC measurements. Both the free and the localised charge-carrier populations then contribute to the total recorded photoconductivity, given by $\Delta\sigma = e\,(n_{\mathrm{deloc}}\mu_{\mathrm{deloc}} + n_{\mathrm{loc}}\mu_{\mathrm{loc}})$. Through knowledge of the initial density of photons absorbed ($n_0 = 1.59 \times 10^{18}\,\mathrm{cm}^{-3}$, calculated as outlined in Equation 3.20 in Section 3.3.5) the localisation rate k_{loc} and effective charge-carrier mobilities μ_{deloc} and μ_{loc} can be extracted at each temperature. Although this is a highly simplified schematic description of the charge-carrier dynamics (e.g. it does not account for the subsequent diffusion and recombination dynamics of charge carriers that, for example, give rise to the lower-energy emission around 1.25 eV), it allows us to focus on the key processes that dominate the charge-carrier dynamics over the first 25 ps: namely, charge-carrier localisation from a high-mobility state into a low-mobility state.

In order to examine the charge transport mechanisms both before and after charge-carrier localisation, the respective mobility values extracted through the model and presented in Figure 5.7 (a) are examined. The value of μ_{deloc} describes the mobility of charge carriers that have been initially excited; these charges then can localise with a rate k_{loc} into a state with charge-carrier mobility μ_{loc}. The two species exhibit distinctly different temperature-dependencies in their mobilities; while μ_{deloc} decreases with increasing temperature, μ_{loc} is found to increase. To describe these trends, a power-law dependence $\mu \propto T^p$ is fitted to both trends, yielding negative values of the exponent $p = -0.33 \pm 0.07$ for μ_{deloc}, and a positive $p = 0.16 \pm 0.05$ for μ_{loc}. Further, following Holstein and Emin [107, 325], an expression reflecting the thermally-activated nature of the localised mobility, i.e. $\mu_{loc} \propto e^{\frac{-E_{\text{A}}}{k_B T}}$, is fitted to obtain an activation energy of $E_{\text{A}} = 0.4 \pm 0.2\,\text{meV}$.

In general, the temperature dependence of charge-carrier mobility depends strongly on the type of scattering or lattice coupling experienced by charge carriers, with the overall charge-carrier interactions potentially having several contributions at any given temperature [119, 135, 167]. The negative temperature trend of the mobility of the free charge carriers is in accordance with relatively weak charge-lattice interactions (large polarons) dominating transport, while the positive trend for the localised state is a signature of a self-trapped or small-polaron state, as discussed further below. The localisation rate k_{loc} appears to be largely temperature independent (see Figure 5.7 (b)) with an average value of $k_{\text{loc}} = 0.65 \pm 0.05\,\text{ps}^{-1}$, indicating that the localisation process itself is not temperature activated and therefore most likely barrier-free [152], suggesting that it may be caused by the low-dimensional electronic nature of Cu_2AgBiI_6 deriving from its structure and chemical composition [91, 93, 153]. This would also be in accordance with recent reports of ultrafast self-trapping in $Cs_2AgBiBr_6$ [73, 307], which also has a

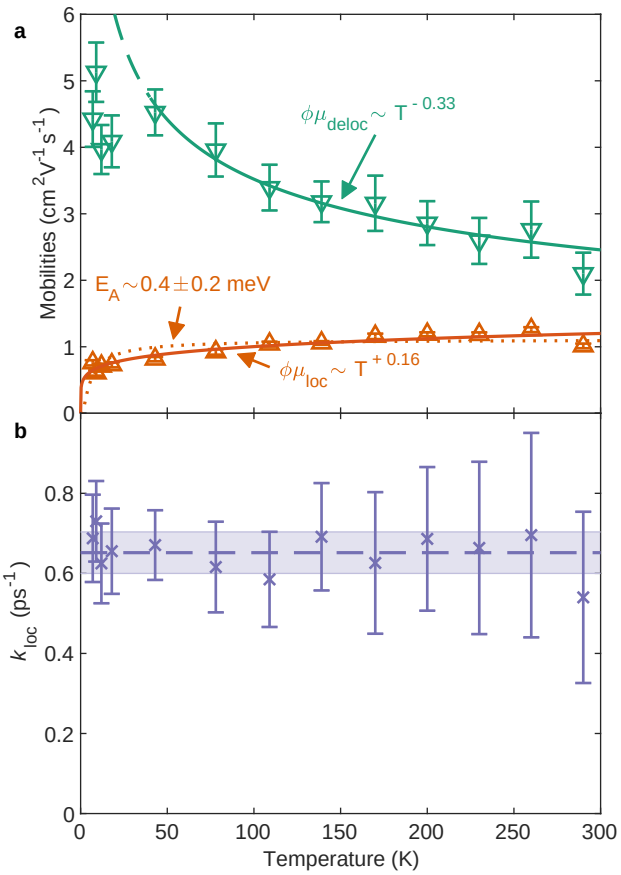


Figure 5.7: Charge-carrier mobilities and localisation rates. Temperature-dependence of (a) effective THz charge-carrier mobilities and (b) charge-carrier localisation rates extracted from the two-level mobility model discussed in the main text. The values of μ_{deloc} for the lowest four temperatures were not included in the power-law fit, as this relation diverges unphysically as $T \to 0$. The dashed line in (b) indicates the mean value of $k_{\text{loc}} = 0.65 \pm 0.05\,\text{ps}^{-1}$ across all temperatures, showing the lack of temperature dependence of the self-trapping process.

zero-dimensional electronic structure [91][93], raising the question of the importance of the presence of silver and bismuth for charge-carrier localisation to occur [36].

In order for us to understand the temperature dependence of the mobility μ_{deloc} of free charge carriers in Cu_2AgBiI_6 prior to charge localisation, i.e. that of the initially formed large polarons, the findings presented here are contrasted against those made for the related hybrid metal-halide perovskites. The mobility of free charge carriers in metal-halide perovskites is governed by fundamentally similar mechanisms to those operating in classical inorganic semiconductors such as GaAs [49]; however, some subtle differences may arise from metal-halide perovskites being mechanically soft and exhibiting

temperature-dependent dielectric constants and anharmonic lattice vibrations [90, 119, 326]. For the simple case of $MAPbI_3$, Fröhlich coupling to longitudinal optical phonons has been shown to be the dominant mechanism affecting carrier mobilities, as expected for a polar semiconductor [49, 59]. However, there have been some discussions in the literature about the exact temperature dependence of the mobility expected for $MAPbI_3$. While experiments mostly agree that mobilities vary with temperature with an exponent of $p \approx -1.5$ in the tetragonal phase [49, 174, 327], theoretical calculations have somewhat struggled to reproduce the observed trends conclusively. A simple application of Fröhlich's theory incorporating experimental parameters yielded a $p = -0.46$ dependency [111], while closer attention to the way in which couplings were distributed across the many longitudinal optical modes in $MAPbI_3$ yielded much more negative values of p [119], closer to experiment, and even more negative values in the low-temperature orthorhombic phase where acoustic phonon scattering begins to dominate. In addition, recent microscopic models accounting for lattice fluctuations have suggested that anharmonicity in $MAPbI_3$ may give rise to negative exponents near $p = -2$ [138]. Other metal-halide perovskites, including $FAPbI_3$ [175], $FASnI_3$ [31] and $Cs_2AgBiBr_6$ [73, 196], have exhibited mobility exponents different from $p \approx -1.5$, implying a variety of charge-lattice interactions and scattering mechanisms that need to be taken into account across different materials. The low value of $p = -0.33$ measured here for Cu_2AgBiI_6 may therefore derive from the presence of multiple scattering mechanisms, some of which may relate to intrinsic electron-phonon coupling, while others derive from extrinsic effects correlating with the partially-layered ordering in the structure and high cation disorder of this material [84]. High charge-carrier mobilities are crucial for photovoltaic applications [47], and the values of $\mu_{\text{deloc}} = 2.1 - 5.1\,\text{cm}^2\text{V}^{-1}\text{s}^{-1}$ presented here are a promising initial measurement. Further, the flatter temperature dependence of the delocalised charge-carrier mobility, relative to conventional metal-halide perovskites [49, 174], suggests that extrinsic factors,

such as poor crystallinity, still play a significant role, meaning that suitable improvements in processing protocols may still improve charge-carrier mobilities substantially [49].

Following the initial localisation step, charge carriers exhibit a positive temperature dependence of increasing μ_{loc} with increasing temperature. Such behaviour is highly indicative of temperature-activated 'hopping' transport typical of localised charge carriers [107, 325]. Theoretical studies of such small polarons in crystal lattices have predicted a positive temperature dependence of the carrier mobility [107, 310], confirmed by experiments across material classes such as chalcogenide glasses or perovskite-oxides [325, 328, 329], whilst contributions from polarons and energetic disorder to charge transport in organic semiconductors have been studied extensively, with mobilities of charges or neutral excitons in some organic semiconductors also rising with increasing temperature [330, 331]. The formation of a self-trapped state or small polaron agrees well with the measurement of positive temperature dependence for μ_{loc}, and the very low value for the activation energy of $0.4 \pm 0.2\,\mathrm{meV}$ is in excellent agreement with the invariance of the localisation rate k_{loc} with temperature.

The measurement of positive temperature dependence for μ_{loc} in Cu_2AgBiI_6 thus supports the notion that a self-trapped state or small polaron forms soon after photoexcitation. The fast localisation timescales (see Figure 5.7 (b)) that have little temperature dependence imply a small barrier to the formation of a self-trapped state [152, 156], as observed in lower-dimensional perovskites such as ($N-$MEDA)[$PbBr_4$] [203] ($N-$MEDA = N1-methylethane-1,2-diammonium), and are in accordance with the structure of Cu_2AgBiI_6, with edge-sharing octahedra and octahedral layering. Thus, the values measured for μ_{loc} are likely to result from a combination of hopping transport of a self-trapped state, as well as any remaining free-carrier contribution, for example from either free electrons or holes that do not undergo self trapping, as it is not certain at this point which carrier types are subject to self-trapping. As discussed in a recent review

article [36], this reduction in charge-carrier mobility can be qualitatively interpreted as a reduction in charge-carrier scattering time or an increase in charge-carrier effective mass. There may be slight changes in carrier scattering times when charge carriers localise in Cu_2AgBiI_6, as quantified by changes in the calculated 'Drude Factor' above, but these are likely to be quite small and would not lead to substantial changes in charge-carrier mobility. Instead, given that charge carriers are observed localising into small polarons which then carry a local lattice deformation with them as they 'hop' between lattice sites, it is argued that this localisation translates to a substantial increase in carrier effective mass, which leads to the observed reduction in charge-carrier mobility.

Overall, photoexcitation therefore initially creates a number of free electrons and holes forming large polarons, which contribute to the initial photoconductivity with an overall electron-hole sum mobility given by μ_{deloc}. These free charges rapidly localise on a picosecond time scale into a self-trapped or small polaron state, reducing the measured photoconductivity, with the long-time signal comprising contributions from remaining free charges and hopping transport of the localised state, described overall as μ_{loc}. The delocalised state can be considered to describe the band-edge free carriers identified with the band gap energy of $\sim 2\,\mathrm{eV}$ observed in the optical absorption measurements, whereas the localised state is associated with the energy of the main PL band around $\sim 1.7\,\mathrm{eV}$. The variation in charge-carrier mobility of both localised and free states with temperature then gives rise to the variations in observed OPTPS transients shown in Figure 5.5 (c). As a guide for the suitability of Cu_2AgBiI_6 for optoelectronic devices, the measured values for μ_{loc} and k_1 at room temperature are used to calculate an estimate of the charge-carrier diffusion length $L_D = \sqrt{\frac{\mu k_B T}{e k_1}}$ as $\sim 400\,\mathrm{nm}$. This value is similar to the typical layer thickness implemented in many thin-film photovoltaic and optoelectronic devices [16], suggesting that this material has good promise for use in these architectures. In addition, further improvements are likely achievable through

optimization of materials processing, defect passivation and device-based optimisation, as has been the case for conventional metal-halide perovskites.

It should be noted that in principle, the presence of an initial high-mobility electronic state and a longer-time low-mobility state could alternatively derive from the relaxation of charges from a direct band into an indirect band. Studies of other bismuth-halide based materials such as $Cs_2AgBiBr_6$, $Cs_2AgBiCl_6$ and $Rb_4Ag_2BiBr_9$ have revealed indirect band gaps [94, 197], with higher-lying direct gaps contributing more prominently to absorption. This has been shown to be a general property of silver-bismuth double perovskites for which both Ag and Bi orbitals contribute to the band structure at the valence band minimum or conduction band maximum [332]. Further, theoretical calculations of the band structure of silver-bismuth Cs_2AgBiX_6 (X = Br, Cl) show that the direct bands at the Γ point are more strongly curved than the lower-lying indirect bands at the L and X points [94]. Given that higher curvature implies lower charge-carrier effective masses and thus higher charge-carrier mobilities, charge-carrier relaxation from the direct gap to the indirect gap would lead to lower mobilities, and thus decreased photoconductivity. Although, as explained above, Cu_2AgBiI_6 is not a double perovskite, it could have similar contributions to the band structure, making it plausible that the measured OPTPS transients are caused by ultrafast relaxation of charge carriers into an indirect gap following initial excitation across the direct gap. However, this explanation cannot easily support the observed switch in temperature-dependent behaviour of the charge-carrier mobility between the delocalised and localised states, as it is unlikely for charge-carrier scattering mechanisms to change so profoundly simply because of relaxation into an indirect gap. Indeed, charge-carrier mobilities in Si and GaP, which are indirect semiconductors with a higher-lying direct gap, decrease as temperature increases due to increased phonon scattering - the opposite of what is observed here [333–336]. If charge

carriers in Cu_2AgBiI_6 relaxed into an indirect band within a few ps, then μ_{loc} would be expected to display a similar temperature dependence to what is observed for μ_{deloc}.

A similar argument is valid to exclude charge-carrier cooling as the potential source of the early-time reduction in photoconductivity: given that higher-lying bands in metal-halide perovskites have lower curvature (higher effective mass), charge-carrier relaxation into the more curved (lower effective mass) band extrema should lead to a rise in charge-carrier mobility, and thus photoconductivity. This has been observed in excess-energy dependent OPTPS in conventional metal-halide perovskites [178, 337], but is the opposite to what is observed here for Cu_2AgBiI_6. Given this, the thermally-activated hopping mobility μ_{loc} indicates the formation of small polarons or self-trapped carriers in Cu_2AgBiI_6, as outlined above, at the lowest point of the bandstructure [72, 107, 325].

5.4.4 Comparison with charge-carrier localisation in $Cs_2AgBiBr_6$

There is a striking similarity between the charge-carrier dynamics observed for Cu_2AgBiI_6, described above, and those measured for the double perovskite $Cs_2AgBiBr_6$. This is seen clearly in Figure 5.8, which shows a series of temperature-dependent OPTPS measurements and fits as described above, but for a thin film of $Cs_2AgBiBr_6$, using the same experimental setup and photoexciting at a fluence of fluence of 10.1 μJcm^{-2}.

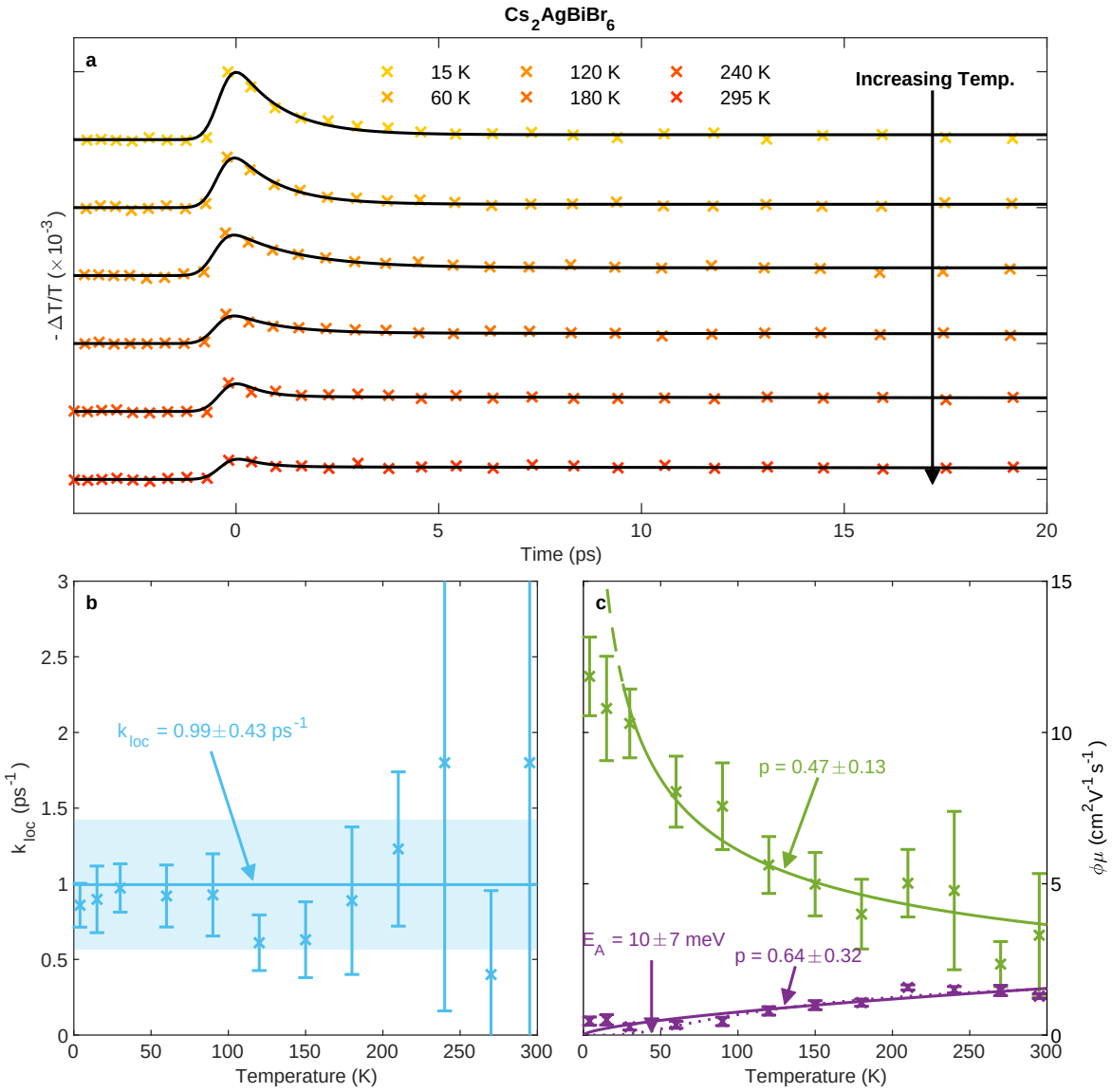


Figure 5.8: Temperature-dependent OPTPS measurements and fit outputs for $Cs_2AgBiBr_6$. (a) Early-time temperature-dependent OPTPS data measured for $Cs_2AgBiBr_6$ at a fluence of $10.1\,\mu Jcm^{-2}$ and fitted with the same two-level mobility model as discussed above, with the fits shown as black solid lines. (b) Extracted values of k_{loc} for $Cs_2AgBiBr_6$, which has a temperature-independent average value of $k_{loc} = 0.99 \pm 0.43 ps^{-1}$. (c) Extracted values of μ_{deloc} and μ_{loc} for $Cs_2AgBiBr_6$. Both show very similar behaviour to Cu_2AgBiI_6, discussed above, with the localised 'small polaron' mobility rising with temperature to a value above $1\,cm^2V^{-1}s^{-1}$, albeit with a larger activation energy of $E_A = 10 \pm 7\,meV$.

The interpretation of these results, specifically for $Cs_2AgBiBr_6$, have been discussed in detail elsewhere [73], and have been reported in a separate investigation as well [307]. This discussion instead focuses on the similarities and differences between the results obtained for the two silver-bismuth based materials investigated here. The most striking aspect of the two sets of measurements is the near-identical qualitative behaviour: both reveal reasonably high delocalised (or 'large polaron') charge-carrier mobilities, fast localisation on picosecond timescales, and hopping-type transport for a 'small polaron' state. This immediately points towards the presence of silver and bismuth as the underlying source of the charge-carrier localisation that takes place, rather than the presence of Cs^+/Cu^+ at the A-site or the halide at the X-site. This is discussed in more detail in Chapter 6, and is a significant issue when considering the application of silver-bismuth-halide materials to optoelectronic devices [36].

Charge-carrier localisation has two distinct aspects: the initial localisation from a free to a localised state, and then the 'hopping' transport between different ionic sites in the crystal. The charge-carrier localisation rate k_{loc} is indicative of the energy barrier between free and localised states, and this is slightly higher in the double perovskite $Cs_2AgBiBr_6$ ($k_{\mathrm{loc}} = 0.99\,\mathrm{ps}^{-1}$, $\tau_{\mathrm{loc}} \sim 1$ps), relative to Cu_2AgBiI_6 ($k_{\mathrm{loc}} = 0.65\,\mathrm{ps}^{-1}$, $\tau_{\mathrm{loc}} \sim 1.5$ps). The picosecond-scale localisation present in both materials implies a very low energetic barrier between localised and free states, as would be expected for a low-dimensional system [152], and in good agreement with the description of silver-bismuth materials as having low electronic dimension [91–93] (notwithstanding their high structural dimension). Further, the slightly higher value of k_{loc} implies that the energetics of the initial localisation 'step' are slightly more favourable in $Cs_2AgBiBr_6$.

The second process, of small polaron hopping, is temperature-activated [130, 136] and the results here show that small polaron motion is not inhibited at room temperature in either material. By fitting the values of μ_{loc} with an activation-energy expression, which

gives values of 10 ± 7 meV and 0.4 ± 0.2 meV for $Cs_2AgBiBr_6$ and Cu_2AgBiI_6, respectively, it is also evident that the barrier to hopping is somewhat larger in $Cs_2AgBiBr_6$, although the fit to the data is less good for this material. The barrier between distinct localised states on an ionic lattice depends on the local energy landscape experienced by a photoexcited charge, and is highly influenced by the dimension of a material [152, 310]. Although both materials, given their silver- and bismuth-based octahedral structures, are expected to have low electronic dimension [92, 93], the presence of tetrahedrally-faciliated Cu^+ in Cu_2AgBiI_6, which improves general electronic connectivity (as discussed in Chapter 6) may make the hopping transport step more energetically favourable, leading to the lower value of E_A. This issue is discussed in more detail in Chapter 6, where the ratio of Cu^+ to Ag^+ and Bi^{3+} content is varied and investigated.

Figure 5.8 also shows clearly that the double perovskite $Cs_2AgBiBr_6$ has a higher charge-carrier mobility for the free state, whereas the mobility of the localised state is broadly similar across the two materials (on the order of $\mu_{\text{loc}} \sim 1\,\text{cm}^2\text{V}^{-1}\text{s}^{-1}$). The majority of electronic states at the band extrema in silver-bismuth based materials are due to contributions from Ag^+ and Bi^{3+} states to the CBM and VBM [94, 316, 332], implying that there should be greater similarities than differences between $Cs_2AgBiBr_6$ and Cu_2AgBiI_6. It has been found that Cs^+ contributes little to the electronic states at the band extrema in $Cs_2AgBiBr_6$,[94, 316], whereas Cu^+ d-states do contribute somewhat to the VBM in Cu_2AgBiI_6 [84]. However, as discussed below in Chapter 6, increasing the contribution of Cu^+, relative to Ag^+ and Bi^{3+} states, leads to much improved charge-carrier mobilities, ruling this out as the source of the improved charge transport. Further, the replacement of bromine with iodine has been found to lead to reduced charge-carrier mobilities in conventional MHPs [51, 256], reflecting an underlying increase in electron-phonon coupling [59, 119], ruling out this other compositional replacement as the source of the improved charge-carrier mobilities.

Given that compositional replacement does not explain the higher mobilities found in $Cs_2AgBiBr_6$, another potential explanation is that differences in crystal structure or extrinsic properties lead to the differences measured here [49]. As discussed above, Cu_2AgBiI_6 is made up of a close-packed iodide sublattice together with a partially-layered network of edge-sharing octahedra, along with partial cation occupancy and some cation disorder (mainly for Cu^+). Instead $Cs_2AgBiBr_6$ has a close-packed bromide sublattice together with a network of corner-sharing octahedra, centred on alternating Ag^+ and Bi^{3+} cation sites. The partial layering present in Cu_2AgBiI_6 likely reduces electronic connectivity somewhat, relative to $Cs_2AgBiBr_6$, thus inhibiting charge-carrier transport. Further, the substantial cation disorder and energetic disorder described above for Cu_2AgBiI_6 will also lead to a reduction in charge-carrier mobility [49]. Together, these two factors might explain the variation in charge-carrier mobilities between these two materials.

An alternative explanation for these observations is that the simplified two-level mobility model, and underlying OPTPS measurements, is unable to capture differences between the charge-carrier dynamics and transport of electrons and holes. Thus, if the localisation of one photoexcited species took place preferentially (e.g. holes at Ag^+ sites [338]), this would be measured as a reduction in the photoconductivity signal measured *via* OPTPS. The localised mobility μ_{loc} would then reflect the sum of the 'small polaron' mobility for the localised species, as well as the delocalised mobility for the remaining free species. The differences between $Cs_2AgBiBr_6$ and Cu_2AgBiI_6 could then be explained as differences in the transport properties of one specific species. For example, if holes became localised in both materials, the difference in values of both μ_{deloc} and μ_{loc} could arise from free holes becaming substantially more mobile in $Cs_2AgBiBr_6$ due to alterations in the VBM (leading to a larger value for μ_{deloc}), and following localisation the remaining mobility μ_{loc} (made up of the free electron mobility together with the small polaron mobility) remains low and fairly similar in both materials.

Finally, it should be noted that the charge-carrier localisation rate is temperature-independent in both materials, indicating a very low barrier to localisation in silver-bismuth materials. This is in excellent agreement with theoretical predictions that silver-bismuth materials have a low electronic dimension due to the electronic isolation of distinct Ag^+ and Bi^{3+} sites, as discussed in Chapter 2 [91–93], and holds notwithstanding the difference in crystal structure between the two materials investigated here.

5.5 Summary and Conclusion

In conclusion, in this chapter clear evidence for strong charge-lattice coupling leading to self-trapping processes in the recently discovered semiconductor Cu_2AgBiI_6, as well as in the double perovskite $Cs_2AgBiBr_6$, has been presented. For Cu_2AgBiI_6, self-trapping of charge carriers is apparent in the temperature-dependent PL and leads to highly Stokes-shifted emission. The self-trapping process is also prominent in the charge-carrier dynamics: at low temperatures the photoluminescence exhibits a very long lifetime, on the order of microseconds, whilst there is an ultrafast decay in photoconductivity that is visible at all temperatures. Overall, the small polaron mobility together with an attractive bandgap near 2.1 eV for large-gap sub-cells in multi-layer photovoltaic architectures or visible light emission, and low exciton binding energies comparable to thermal energies at room temperature, therefore make Cu_2AgBiI_6 an attractive new semiconductor for optoelectronic applications.

Across both silver-bismuth materials, localised charge carriers have lower mobilities, leading to decreased photoconductivity on a picosecond timescale. Further, the lack of temperature dependence of the localisation rate and very low activation energy obtained for the 'hopping' transport imply a low energetic barrier to self-trapping, which may derive from the lowered electronic dimension of these materials. These findings thus allow connections to be made between order, electronic and lattice structure design and the

extent to which such localisation tends to occur. Overall, it should be noted that while the presence of a self-trapped state and ultrafast localisation somewhat lowers charge-carrier transport, this effect is not substantial at room temperature, partly because the small-polaron motion is temperature-activated. At room temperature, this process therefore only reduces the measured photoconductivity in either material by a factor of two or so, still leaving sufficiently high values above $1\,\mathrm{cm^2V^{-1}s^{-1}}$ to enable efficient photovoltaic devices.

6

Interplay of Structure, Charge-Carrier Localisation and Dynamics in Copper-Silver-Bismuth-Halide Semiconductors

Contents

6.1 Introduction and Background 146
6.2 Experimental Details 148
6.3 Main Experimental Results and Discussion 149
6.3.1 Structural discontinuity and enhanced electronic connectivity with increasing copper content 149
6.3.2 Influence of copper on the electronic structure 153
6.3.3 Charge-carrier localisation and energetics are intrinsically linked to the presence of Ag and Bi 157
6.3.4 Observation of ultrafast charge-carrier localization and small-polaron formation 161
6.3.5 Unravelling the sequence of charge-carrier relaxation, localisation and recombination 163
6.3.6 Influence of Cu^+ on charge-carrier mobility and transport . . . 172
6.3.7 Understanding, mitigating and tailoring charge-carrier localisation 176
6.4 Summary and Conclusion 179

Work in this chapter was initially published as: L. R. V. Buizza,

H. C. Sansom, A. D. Wright, A. M. Ulatowski, M. B. Johnston, H. J. Snaith, L. M. Herz. 'Interplay of Structure, Charge-Carrier Localisation and Dynamics in Silver-Bismuth-Halide Semiconductors', *Advanced Functional Materials*, **2021**, *32*, 2108392 (Ref. [87]).

6.1 Introduction and Background

The third and final experimental chapter of this thesis builds on the results presented in Chapter 5 and discusses the factors influencing charge-carrier localisation and transport across a range of quaternary copper-silver-bismuth-iodide materials. By understanding how variations in composition and structure alter the underlying optoelectronic properties of these materials, wider conclusions can be drawn about silver-bismuth-halide based semiconductors. The fact that charge-carrier localisation is found to be intrinsically linked to the presence of silver and bismuth raises questions about the potential future applications for such materials, and potential options for mitigating and tuning such localisation are outlined at the end of this chapter.

Given the results presented in Chapter 6, and the wider context discussed in Chapter 2, it must be suspected that the presence of strong charge-carrier localisation effects may be a key reason behind the underperformance of silver-bismuth semiconductors to date: recent studies have shown the formation of small polarons localised within a few picoseconds in both $Cs_2AgBiBr_6$ [73, 74, 145, 307, 338] and Cu_2AgBiI_6 [86]. In their study of $Cs_2AgBiBr_6$, Wu et al. [307] draw attention to two key factors contributing to strong self-trapping in this material: the structural instability and strong acoustic-phonon deformation potentials present in bismuth [339, 340] and Bi-based compounds such as Bi_2Te_3 [341, 342] or BiI_3 [343], and the soft nature of silver-halide bonds that are easily distorted, which together lead to charge-carrier localisation [146]. At a fundamental level, such ease of structural distortion can be interpreted in terms of the greater ionicity (i.e. a greater difference in electronegativities) of silver-halide and bismuth-halide bonds in such

materials, relative to lead-halide bonds, which imparts larger electron-phonon couplings in silver-bismuth semiconductors [73, 74, 77, 86, 145]. In the work on $Cs_2AgBiBr_6$ and Cu_2AgBiI_6 presented in the previous chapter [73, 86], the localisation of charge carriers was further linked to the low electronic dimension of such silver-bismuth materials [91, 92], which leads to individual structural units (such as octahedra) to be electronically isolated from each other, acting as a barrier to efficient charge-carrier transport. Taken together, these works point towards two potential causes for charge-carrier localisation in silver-bismuth materials: first, the easy structural distortion of bismuth-based systems and 'soft' silver-halide bonds; second, the low electronic dimension that prevails in materials with alternating silver and bismuth structural units. Although similar charge-carrier localisation effects have been observed across these and other materials [77, 197, 228, 344–346], an holistic understanding of the interplay between crystal structure, electronic structure and optoelectronic properties in silver-bismuth materials, and how such effects may be tuned through stoichiometric engineering, has remained lacking thus far.

Here, five materials along the $AgBiI_4$ – CuI solid solution line ($Cu_{4x}(AgBi)_{1-x}I_4$ with $x = 0, 0.09, 0.2, 0.33, 0.6$) are investigated to reveal how changes in crystal structure and composition influence charge-carrier dynamics, localisation and transport. A combination of X-ray diffraction (XRD), photoluminescence (PL) and optical absorption measurements demonstrate that these silver-bismuth semiconductors display a promising mix of the optoelectronic properties found in $MAPbI_3$, notably of strong optical absorption, low exciton binding energies, bandgaps in the visible range and charge-carrier mobilities well above $1\,cm^2V^{-1}s^{-1}$. Further, ultrafast optical-pump terahertz-probe spectroscopy (OPTPS) with a variable pump fluence and photon energy allows us to probe small polaron motion and reveals how charge-carrier relaxation, localisation and recombination interact following photoexcitation. The addition of Cu^+ is found to improve the photoluminescence intensity and charge-carrier mobility substantially, although this is accompanied by a

slight decrease in optical absorption strength and a faster charge-carrier localisation rate. Further, it is found that reduced exciton binding energies and increased charge-carrier mobilities with rising Cu^+ content can be well-explained by a reduction in charge-carrier effective mass, which is attributed to increased contributions from copper states at the valence band minimum that lead to increased band curvature. Interestingly, the measurements reveal that bimolecular (radiative) recombination is not well-described by a band-to-band radiative-balance model, as it exhibits inverse trends in optical absorption strength and bimolecular recombination rate constants. Instead small-polaron recombination rate constants appear to increase with rising charge-carrier mobilities, similar to the Langevin-type recombination found in organic semiconductors. Finally, the results presented here are used to draw wider conclusions around charge-lattice interactions in silver-bismuth semiconductors, including how these effects can be tailored or mitigated according to the potential target application of such materials.

6.2 Experimental Details

Sample preparation of the materials with composition $Cu_{4x}(AgBi)_{1-x}I_4$ was carried out by H. C. Sansom, Department of Physics, University of Oxford, as outlined in Section 3.5. Pawley fitting and analysis of the XRD spectra, SEM images and SEM-EDX analysis were carried out by H. C. Sansom.

X-ray diffraction, optical absorption, steady-state and time-resolved photoluminescence, TDTS and OPTPS were carried out as described in Chapter 3. Elliott fitting of the absorption spectra was carried out by A. D. Wright.

In order to calculate the values of the dielectric function in the infrared region, ϵ^{IR}, the measured values of R, T between 1200 – 1300 nm from the UV-Visible absorption measurements were fitted with values of R and T calculated from Fresnel coefficients, accounting for Fabry-Perot interference inside the thin film sample [250], of the stack

of layers vacuum-sample-quartz-vacuum. This approach allows for the extraction of the values of the refractive index and dielectric function in the infrared frequency range.

6.3 Main Experimental Results and Discussion

6.3.1 Structural discontinuity and enhanced electronic connectivity with increasing copper content

Replacement of equimolar amounts of Ag^+ and Bi^{3+} with Cu^+ will lead to changes in the composition of the materials investigated here, which are investigated using scanning electron microscopy (SEM) imaging and energy-dispersive X-ray (SEM-EDX) analysis. Thin films of $Cu_{4x}(AgBi)_{1-x}I_4$ with nominal (aimed-for) compositions of $x = 0$ ($AgBiI_4$), 0.09 ($Cu_{0.4}AgBiI_{4.4}$), 0.2 ($CuAgBiI_5$), 0.33 (Cu_2AgBiI_6) and 0.6 (Cu_6AgBiI_{10}) were deposited onto glass microscopy slides and z-cut quartz substrates.

The exact compositions measured *via* SEM-EDX for these films show good agreement with the nominal (expected) compositions across the whole range (see Figure 6.5 (a) and Figure 6.1), albeit with a slight iodine deficiency present. The SEM images (Figure 6.2) also show less uniform surface coverage with increasing x, indicating a rise in surface roughness. Previous studies of $AgBiI_4$ [80], $CuAgBiI_5$ [85] and Cu_2AgBiI_6 [84] ($x = 0$, 0.2, 0.33) have found the crystal structure of these materials to have high levels of atomic disorder, notably with low Cu^+ occupancy on tetrahedral sites, and to contain octahedral networks of varying dimension that form depending on the amount of Ag^+ and Bi^{3+}.

Fitting of the a and c lattice parameters for the five compositions studied here, derived from XRD measurements, show an interesting discontinuity moving from $x \leq 0.2$ to $x \geq 0.33$, which is also reflected in the calculated unit cell volumes (see Figure 6.3). It is argued that this discontinuity corresponds to a change in the crystal structure where the octahedral network transitions from three dimensional (3D) in $CuAgBiI_5$ to two dimensional (2D) in Cu_2AgBiI_6 following substitution of octahedral site occupancy (Ag^+ and

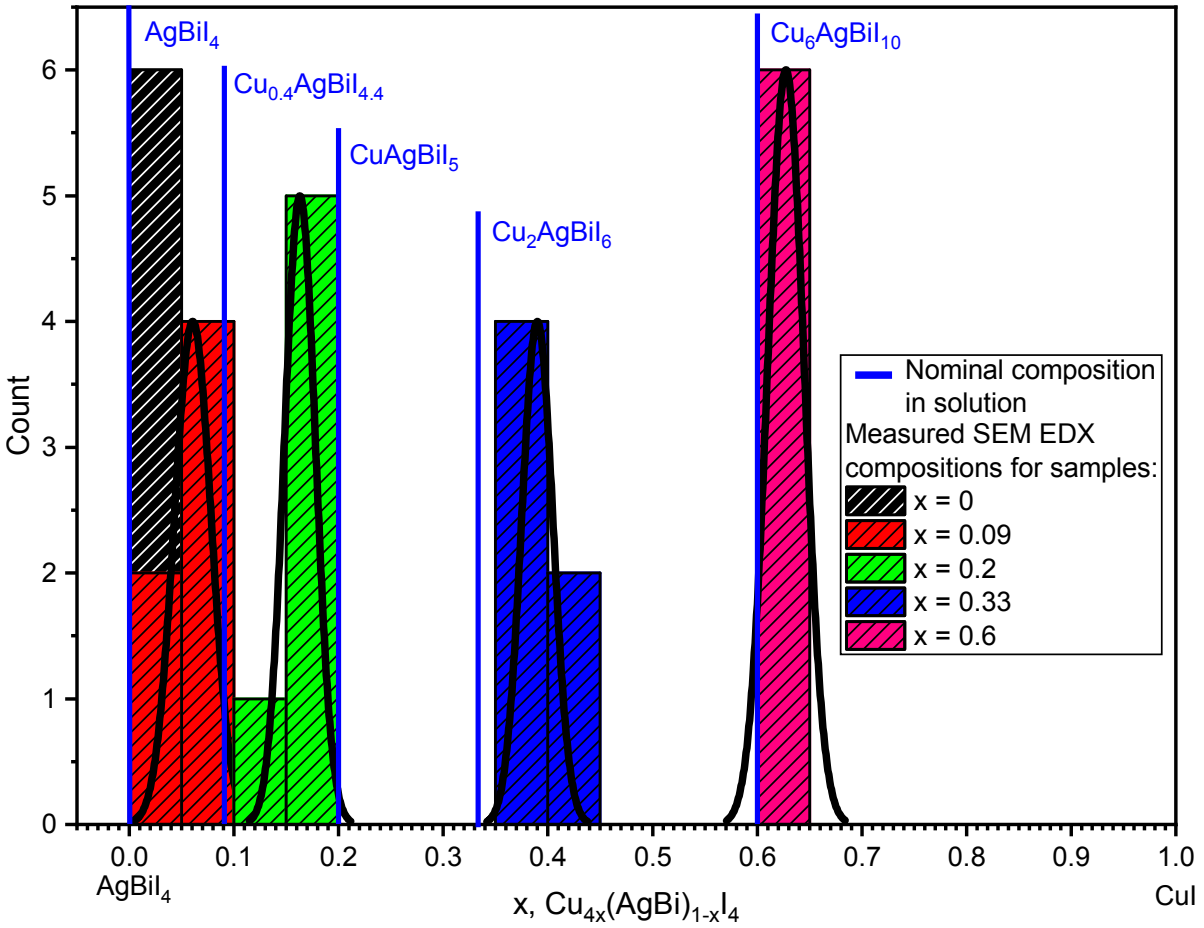


Figure 6.1: Histogram of compositions measured using SEM-EDX. These values were measured for films deposited on microscope slides. There is no Gaussian distribution for $x = 0$ as there was no copper included in this material, giving no variation along the $AgBiI_4$ – CuI solid solution line. Variations in silver and bismuth content for this composition are shown in Figure 6.5. Compositional analysis using SEM-EDX was carried out by H. Sansom.

Bi^{3+}) with tetrahedrally-coordinated Cu^+ [80, 84], as is shown schematically in Figure 6.4.

Further, it is proposed that the addition of Cu^+ leads to a general increase in electronic connectivity, although the significant disorder present in these materials complicate the verification of this *via* density-functional-theory (DFT) approaches [80, 84]. Crystallographic and DFT-based studies of $AgBiI_4$ [80] and $CuBiI_4$ [308, 347] have shown that the conduction band minimum (CBM) of these materials consists of bismuth and iodine electronic *p*-states, and the valence band maximum (VBM) comprises mainly iodine *p*-states, with some contributions from silver or copper electronic states, respectively. Notably, this result holds across all of the multiple potential crystal structures that these

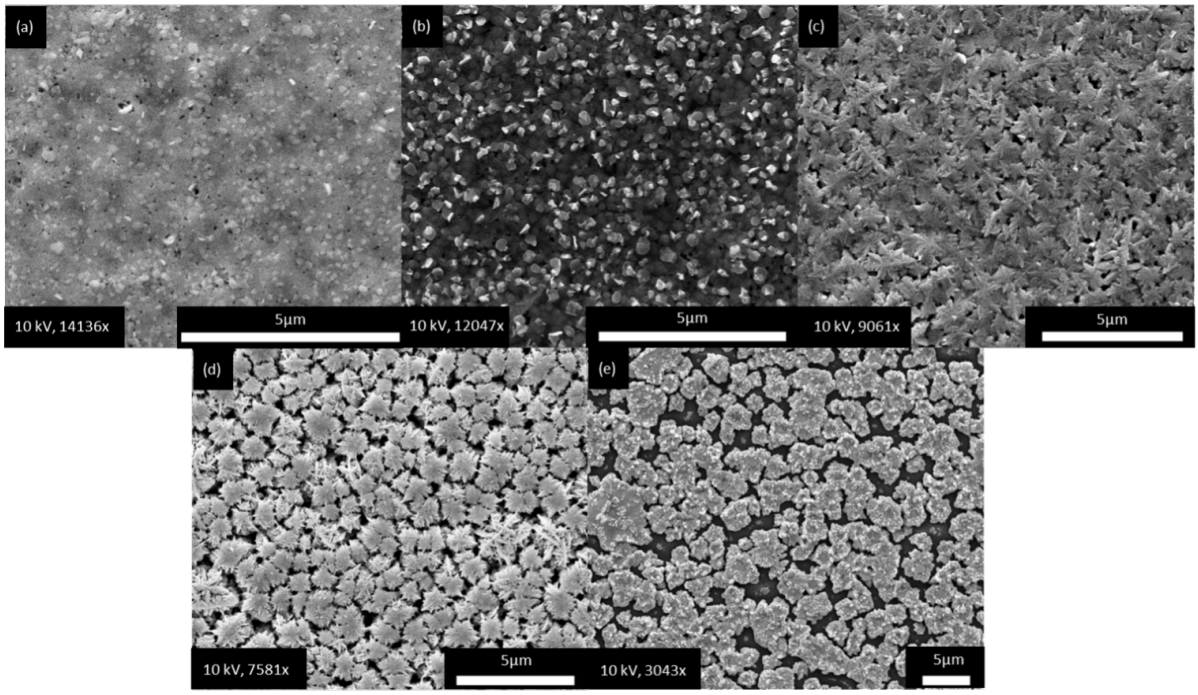


Figure 6.2: SEM images of $Cu_{4x}(AgBi)_{1-x}I_4$ films. Images are for nominal compositions $x = 0$ ($AgBiI_4$, (a)), 0.09 ($Cu_{0.4}AgBiI_{4.4}$, (b)), 0.2 ($CuAgBiI_5$, (c)), 0.33 (Cu_2AgBiI_6, (d)), 0.6 (Cu_6AgBiI_{10}, (e)) deposited on microscope slides. SEM images taken by H. Sansom.

materials can take as the lowest-energy configuration [80, 347].

Although the exact crystal structure of the Cu-Ag-Bi-I materials investigated here will also vary (namely, 2D vs. 3D octahedral networks), it is suggested that an increase in proportion of tetrahedrally-coordinated Cu^+ should lead to two effects: changes in the electronic structure of the VBM, and increased electronic connectivity. The former arises from copper mainly contributing to electronic states in the valence band, as has been shown for Cu_2AgBiI_6 [84]. The latter point follows from the increased availability of tetrahedrally-coordinated sites facilitated by the cubic close-packed iodide sublattice, relative to octahedrally-coordinated sites. This point is of great importance to silver-bismuth based materials, given that neighbouring silver- and bismuth-based octahedra have been shown to be electronically near-isolated [91–93] owing to the non-optimal spatial overlap of contributions from the silver and bismuth electronic states. Thus, as the octahedral network changes with reduced Ag-Bi content, the increased presence of

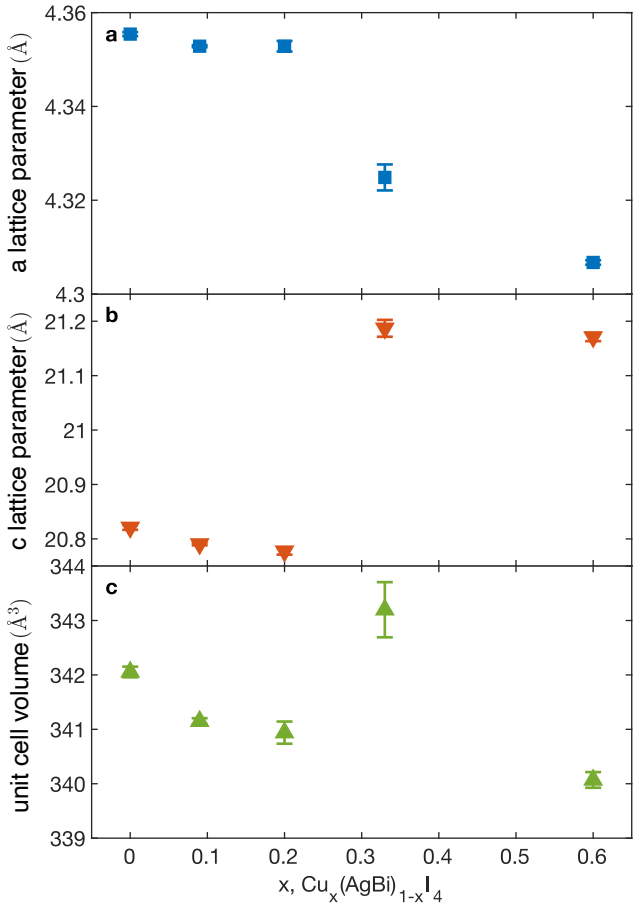


Figure 6.3: Variation of lattice parameters with compositions. (a) – (c) Extracted a- and c-lattice parameters, as well as the unit cell volume, from Pawley fits to XRD patterns of $Cu_{4x}(AgBi)_{1-x}I_4$ films for nominal compositions $x = 0$ ($AgBiI_4$), 0.09 ($Cu_{0.4}AgBiI_{4.4}$), 0.2 ($CuAgBiI_5$), 0.33 (Cu_2AgBiI_6), 0.6 (Cu_6AgBiI_{10}). The lattice parameters were extracted from the XRD measurements taken for films on quartz substrates, as outlined above. Analysis of XRD spectra and extraction of lattice parameters was carried out by H. Sansom.

tetrahedral copper leads to increased spatial and electronic overlap between different crystallographic sub-structures, improving the electronic connectivity across the material.

Overall, an increase of x in the thin films of $Cu_{4x}(AgBi)_{1-x}I_4$ is expected to yield two significant changes in the composition and crystal structure: a change in the octahedral network from 3D to 2D with decreasing presence of octahedral Ag^+ and Bi^{3+}, and an increased tetrahedral occupancy and increase in tetrahedral connectivity of Cu^+, with the iodide sublattice remaining largely unchanged. Both changes influence the electronic band structure of the materials as well as the strength of interactions between charge carriers and the lattice. The discussion now moves on to the influence of Cu^+

content and structural changes on the optoelectronic properties and formation of small polarons across the silver-bismuth materials investigated here, based on results from a variety of spectroscopic measurements.

6.3.2 Influence of copper on the electronic structure

In order to probe the viability of these proposed concepts, and to understand how the addition of copper alters the electronic band structure in these silver-bismuth materials, UV-visible absorption measurements were carried out on spin-coated thin films, deposited on z-cut quartz substrates. To extract values for band gap energies and exciton binding energies, fits to the absorption spectra near their onsets according to Elliott's theory [251], which describes the electronic transitions between parabolic bands of a semiconductor in the presence of Coulomb interactions, were carried out. It is found that the band gap energy decreases slightly from 2.05 eV for $x = 0$ ($AgBiI_4$) down to 2.00 eV for $x = 0.6$ (Cu_6AgBiI_{10}), accompanied by a corresponding reduction in the exciton binding energy from 27 meV to 19 meV. (See Figure 6.5 (b) for the steady-state optical absorption of $CuAgBiI_5$ ($x = 0.2$, black line), as well as a fit to the spectrum according to Elliott's theory

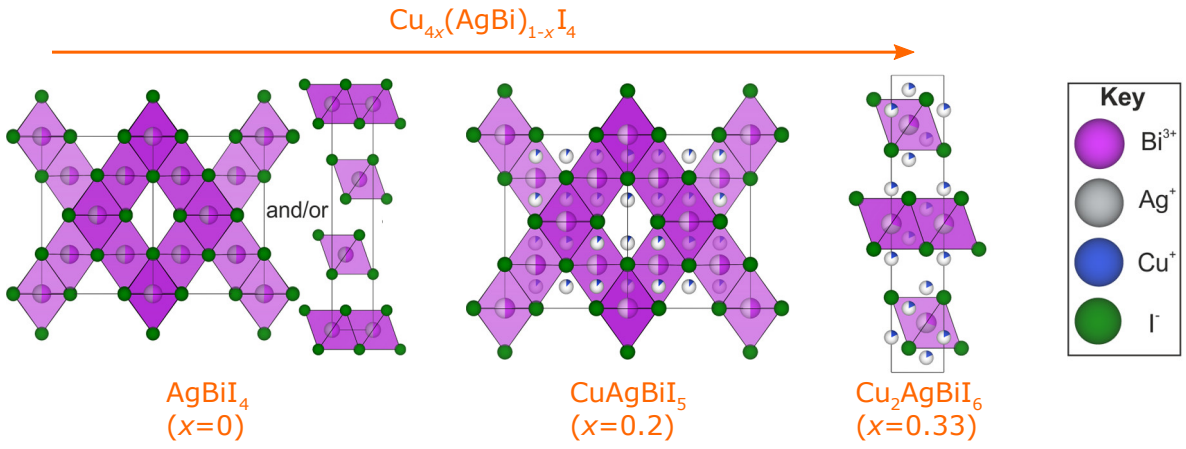


Figure 6.4: Crystal structures of $Cu_{4x}(AgBi)_{1-x}I_4$ materials Crystal structure of $Cu_{4x}(AgBi)_{1-x}I_4$ for x = 0, 0.2, 0.33 (structures for x = 0.09 and 0.6 have not yet been solved). As x increases there is a transition from a 3D octahedral network to a 2D octahedral network. Adapted with permission from Ref. [85]. Copyright (2021) American Chemical Society.

(pink dashed line), and see Figure 6.6 (a) – (d) for fits to the remaining compositions). Further, the magnitude of the absorption coefficient at 2.3 eV, $\alpha_{2.3}$, is used as a proxy for the overall above-band gap absorption strength; this takes a high value for $AgBiI_4$ ($x = 0$), above $8 \times 10^4 cm^{-1}$, but falls with increasing x, markedly so in the case of Cu_6AgBiI_{10} ($x = 0.6$). As the relative proportion of Bi^{3+} and Ag^+ is diluted upon increasing x content (addition of Cu^+), the strength of the above-band gap absorption decreases correspondingly, which is attributed to much stronger contributions to the above-gap electronic transitions from silver and bismuth, relative to copper. Indeed, previous studies have shown that at an energy of 2.3 eV, BiI_3 ($9.7 - 16.5 \times 10^4\,cm^{-1}$ [318]) and AgI ($6.9 - 11.2 \times 10^4\,cm^{-1}$ [348, 349]) have a much larger absorption coefficient than CuI ($0.5 - 0.9 \times 10^4\,cm^{-1}$ [350]), in excellent agreement with the trend observed here.

The exciton binding energies extracted from the Elliott fits are comparable to thermal energies at room temperature (~ 26 meV), and somewhat higher than that in $MAPbI_3$ of 12 ± 7 meV [135], indicating that excitons likely do not play a substantial role in the charge-carrier dynamics in the silver-bismuth materials studied here. Further, the measured values are much lower than the several hundred meV reported for Cs_2AgBiX_6 (X = Br, Cl) [73, 77, 316], which is likely associated with the somewhat lower direct band gaps in the materials investigated here [250], as well as differences in charge-carrier effective masses, discussed in more detail below.

The exciton binding energy depends generally on the dielectric screening and electron-hole reduced mass M as $E_B \propto \frac{M}{\epsilon_r^2}$. An insight into the origin of such suitably low exciton binding energies must therefore centre on these two parameters. The dielectric screening, ϵ, in these silver-bismuth materials can be determined from fits to the reflectance and transmittance between 1200 – 1300 nm (ϵ^{IR}), and also from THz absorption spectroscopy (which yields ϵ_∞^{THz} and ϵ_s^{THz}). For all of the silver-bismuth materials studied here, E_B lies at energies in between the range probed using the THz absorption measurements

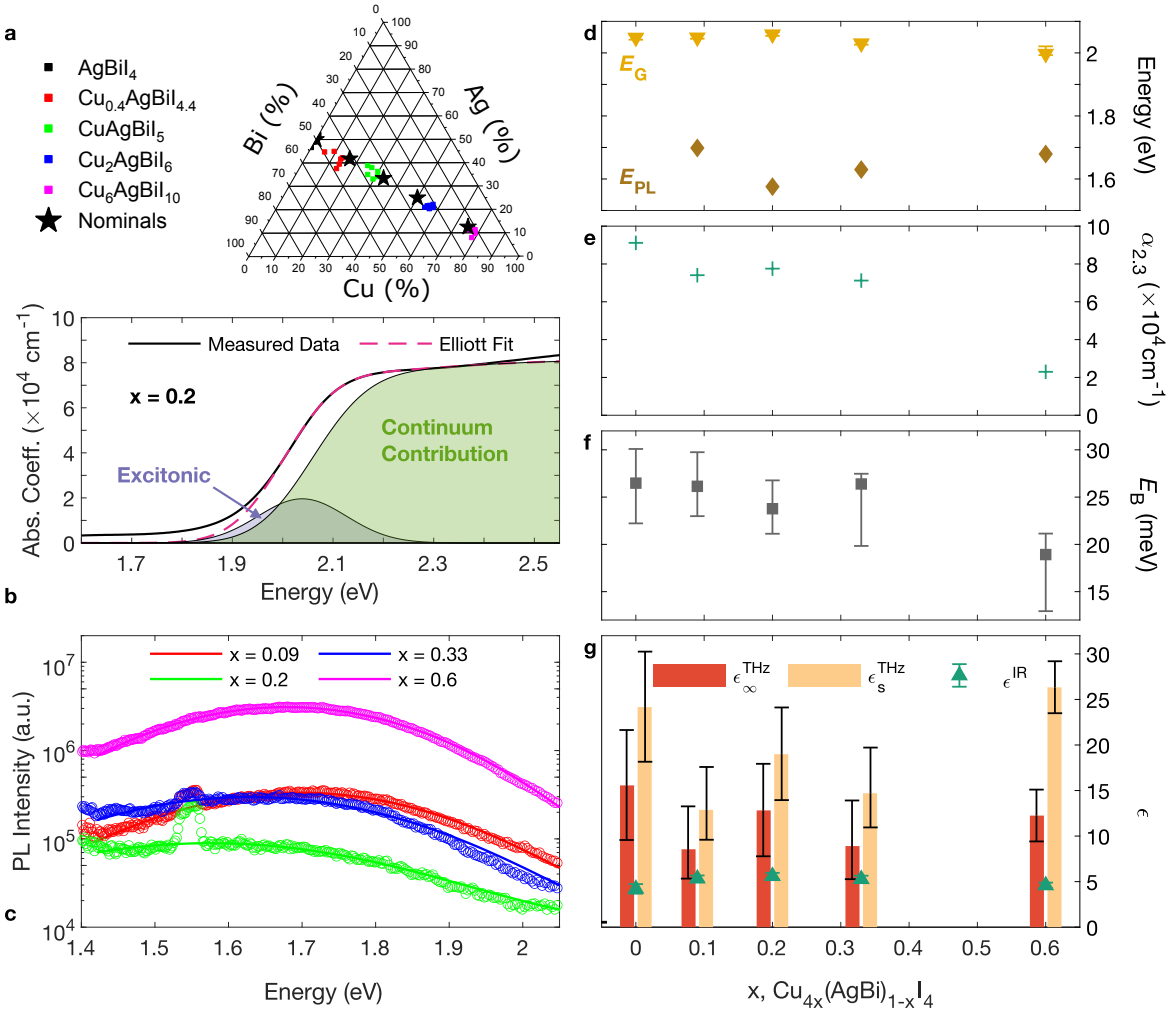


Figure 6.5: Influence of copper on electronic structure and energetics. (a) Nominal (black stars) and measured (coloured squares) chemical compositions, measured using SEM EDX, of the five $Cu_{4x}(AgBi)_{1-x}I_4$ compositions investigated in this work. (b) UV-visible absorption spectrum of $CuAgBiI_5$ ($x = 0.2$) (black line), and fit according to Elliott's theory [251] (pink dashed line). (c) Steady-state photoluminescence from thin films of four compositions (shown as open circles), following photoexcitation at 398 nm at an intensity of 265 Wcm^{-2}. The spectra are fitted with Gaussian lineshapes, with the fits shown as solid lines. (The peak around 1.55 eV present in some of the spectra is caused by the second-order diffraction peak of the 3.1 eV excitation light.) (d) Band gap energy E_G (yellow triangles) extracted from the Elliott fits and peak PL energy E_{PL} (brown diamonds) extracted from the Gaussian fits, for each composition. (e) Optical absorption coefficient at 2.3 eV, used as an indication of the overall optical absorption strength for each composition. (f) Exciton binding energy E_B extracted from the Elliott fits, for each composition. Error bars were obtained by varying the range of energies to which the fits were applied. (g) Measured values of the dielectric function ϵ. Values of the THz high-frequency (red bars) and static (cream bars) values of the dielectric function $\epsilon_{\infty/s}^{THz}$ were extracted from THz absorption measurements. Values of the dielectric function in the infrared ϵ^{IR}, were calculated from reflection and transmission spectra between 1200 – 1300 nm. Fitting of the optical absorption spectra was carried out by A. D. Wright.

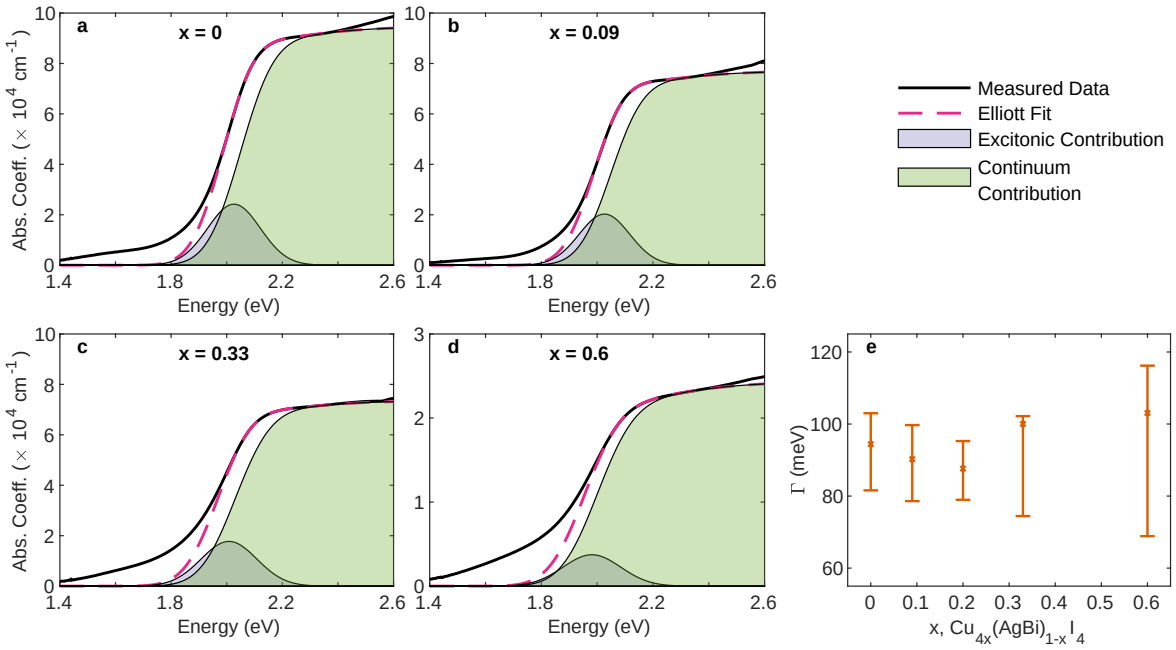


Figure 6.6: Elliott fitting of optical absorption spectra. (a) – (d) Fits (dashed pink lines) to the steady-state optical absorption spectra (solid black lines) of $Cu_{4x}(AgBi)_{1-x}I_4$ films using Elliott's theory [251], for thin films of the compositions shown in each figure. The excitonic (blue) and free-carrier contribution with Coulombic enhancement (green) are shown as the filled areas. The equivalent plot for the composition with $x = 0.2$ is shown in the main text. (e) Broadening parameter Γ obtained from the Elliott fits. Fitting of the optical absorption spectra was carried out by A. D. Wright.

(2 – 11 meV) and the infrared limit of the optical absorption measurements carried out ($\sim$ 0.95 eV). The appropriate value for estimating E_B is thus somewhere between the values of ϵ^{IR} obtained in the infrared and the high-frequency constant in the THz range ϵ_∞^{THz} [135], and the measured values are shown in Figure 6.5 (g).

Overall, the dielectric screening across the compositional range studied here is found to be similar to that encountered in $MAPbI_3$: all values lie close to or above the value for $MAPbI_3$ at frequencies corresponding to its exciton binding energy (approximately equal to $\epsilon_\infty^{THz} = 5.4$ [135]). This finding implies that the higher exciton binding energies found here, roughly twice the value encountered in $MAPbI_3$, are caused by enhanced charge-carrier effective masses, rather than reduced dielectric screening [135, 167], a result which is in good agreement with the lower charge-carrier mobilities obtained here (given

that $\mu \propto \frac{1}{m^*}$, as discussed below). Further, there is no trend in dielectric screening with composition, but the reduction in exciton binding energy with x (from 27 meV to 19 meV) correlates very well with the increased charge-carrier mobilities (reduced effective mass) with x discussed below, suggesting that the significant consequence of the addition of copper is the alteration of the curvature of the electronic bands around the VBM.

Overall, the optical absorption spectra and dielectric values of the silver-bismuth materials investigated here seem to combine the best of $MAPbI_3$ and $Cs_2AgBiBr_6$, in that they have direct band gaps in the optical range with strong absorption above the absorption onset, exciton binding energies similar to thermal energies and middling dielectric screening, whilst remaining fully inorganic and lead free. Further, the substitution of Ag^+ and Bi^{3+} with Cu^+ is found not to alter the band gap energy of these materials substantially, but to cause a reduction in exciton binding energy, which is attributed to decreased charge-carrier effective masses resulting from an increased curvature around the band extrema.

6.3.3 Charge-carrier localisation and energetics are intrinsically linked to the presence of Ag and Bi

Charge-carrier localisation can lead to photoexcited carriers losing energy by causing or interacting with structural distortions, leading to changes in the energetic distribution of states experienced by the charge carriers [36, 72] which can be studied through spectroscopic measurements. In order to understand such changes, measurements of the steady-state photoluminescence were carried out, which reveal highly Stokes-shifted PL spectra with large full-width half-maxima (FWHM, see Figure 6.5 (c) and Figure 6.7). The spectra were measured for thin films following photoexcitation at 398 nm at an excitation intensity of 265 Wcm^{-2} (the PL was too faint to be distinguished from background noise for $AgBiI_4$). All of the spectra peak between 1.58 – 1.70 eV, at

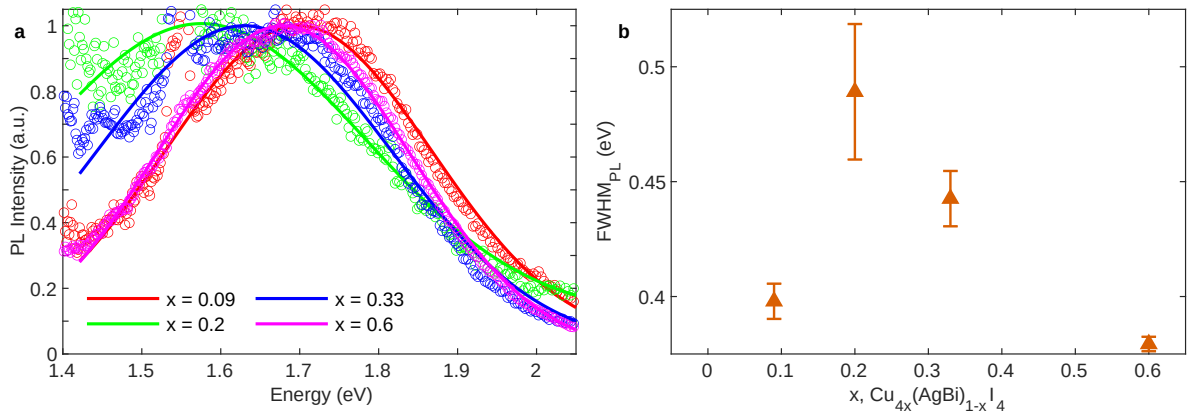


Figure 6.7: Steady-state photoluminescence. (a) Normalised photoluminescence spectra of $Cu_{4x}(AgBi)_{1-x}I_4$ films. Measured spectra are shown as open circles, Gaussian fits as solid lines. (b) Full-width half-maxima extracted from the Gaussian fits to the photoluminescence spectra.

substantial Stokes shifts of 300 – 400 meV from the band gap energy, with values of the full-width half-maxima all above 350 meV (see Figure 6.7 (b)).

The large Stokes shifts and FWHM observed for the PL are characteristic of strong electron-phonon couplings [36, 72], as has been observed for localised states in other silver-bismuth materials such as $Cs_2AgBiBr_6$ [73, 74], Cu_2AgBiI_6 [84, 86] and $Rb_4Ag_2BiBr_9$ [197]. Further, the PL band around 1.6 – 1.7 eV has been previously attributed to emission from a localised (small polaron) state in Cu_2AgBiI_6 [86], and the PL measured here is attributed to the emission from a similar state. It should be noted that the energy of this band does not follow any clear trend with composition, indicating that the energetics of the localised state are independent of copper content, in good agreement with the small variation in band gap discussed above. The constant energy of this PL band serves as confirmation that the emission, and underlying localised state, is intrinsically associated with the presence of silver and bismuth in a close-packed iodide sublattice in these materials, and that the energy level of this state does not vary substantially, relative to the band structure, with composition.

To understand whether any variations in the energetics of the localised state occur over the first few nanoseconds of the PL decays, time-resolved emission spectra (TRES) were

also measured for the two most emissive compositions, Cu_2AgBiI_6 and Cu_6AgBiI_{10}, shown in Figure 6.8. The measurements reveal slightly differing behaviour that provides insight into the trade-off between high-energy band-edge emission, around 2 eV ($\sim$ 620 nm), and the localised-state emission around 1.7 eV ($\sim$ 730 nm). For Cu_2AgBiI_6 (Figure 6.8 (a) – (c)) a band-edge (low Stokes shift) contribution to the PL was measured between 600 – 650 nm over the first few nanoseconds, which decays more quickly than the main peak of the PL at around 730 nm. This is observed more clearly in the transient decays (Figure 6.8 (b)), where the decays at 600 and 650 nm over the first $\sim$ 8 ns are somewhat faster than that at 730 nm, and also in the spectral slices shown in Figure 6.8 (c), where the high-energy band-edge PL disappears after the first $\sim$ 2 ns. In the case of Cu_6AgBiI_{10} (Figure 6.8 (d) – (f)), such band-edge emission is not observed, with transient decays at 600, 650 and 750 nm being generally very similar (Figure 6.8 (e)) and little change apparent in the spectral slices taken over the first 10 ns (Figure 6.8 (f)). Such change in the early-time PL spectra reveals that the ratio of band-edge PL to the highly Stokes-shifted PL arising from the small polaron is variable, and can be tuned by changing the quantity of Cu^+ vs. Ag^+ and Bi^{3+}.

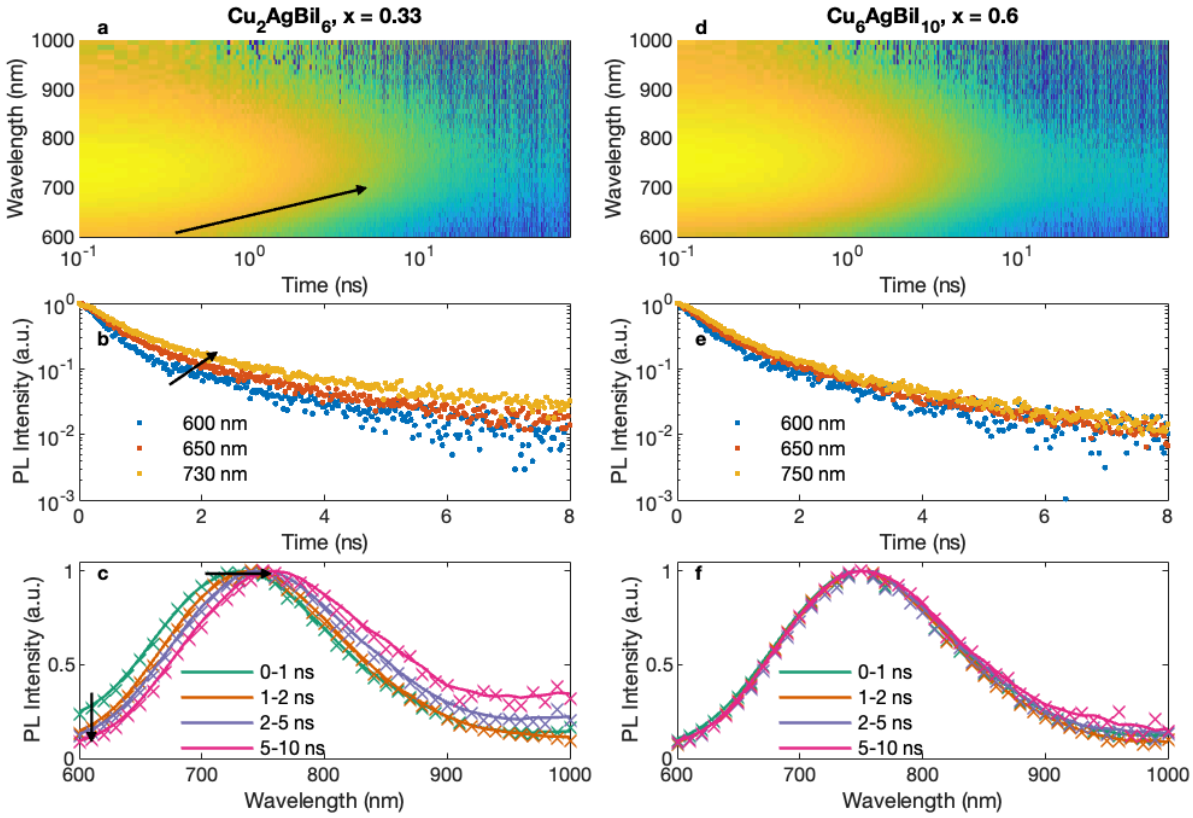


Figure 6.8: Time-resolved emission spectroscopy. (a) Time-resolved emission spectrum for a thin film of Cu_2AgBiI_6 ($x = 0.33$), measured at a fluence of 1610 nJcm^{-2}. (b) Time-resolved PL decays at wavelengths of 550, 600 and 730 nm for Cu_2AgBiI_6 ($x = 0.33$), showing that the decay at higher energies (shorter wavelengths) is slightly faster than at the main PL peak at 730 nm. (c) Time-resolved PL spectra for Cu_2AgBiI_6 ($x = 0.33$), integrated over different periods after photoexcitation, showing a red-shift in peak PL energy, as well as a drop in intensity of the high-energy PL over the first 10 ns. (d) Time-resolved emission spectrum for a thin film of Cu_6AgBiI_{10} ($x = 0.6$), measured at a fluence of 1610 nJcm^{-2}. (e) Time-resolved PL decays at wavelengths of 550, 600 and 750 nm for Cu_6AgBiI_{10} ($x = 0.6$), showing that the decay at higher energies (shorter wavelengths) is slightly faster than at the main PL peak at 750 nm, although less so than in the case of Cu_2AgBiI_6 ($x = 0.33$). (f) Time-resolved PL spectra for Cu_6AgBiI_{10} ($x = 0.6$), showing very little change in PL spectral shape or peak energy over the first 10 ns.

6.3.4 Observation of ultrafast charge-carrier localization and small-polaron formation

To complete the understanding of the interactions between charges and the lattice in these silver-bismuth-halide materials, pump photon energy-dependent OPTPS was carried out. The OPTPS photoconductivity transients, shown in Figure 6.9, outline the dynamics of the charge-carrier localisation that takes place in the silver-bismuth materials. The transients display an ultrafast decay in the photoconductivity over the first few picoseconds, with the signal decaying to close to zero for low x, whereas a substantial long-time conductivity remains for mid-to-high x values, in some cases over half of the initial peak in photoconductivity. These early-time dynamics over the first $\sim 6\,\mathrm{ps}$ show no dependence on fluence (as shown in Figure 6.10), ruling out any influence from bi- or tri-molecular recombination processes, such as exciton formation or Auger recombination. Instead, ultrafast photoconductivity decays similar to those observed in $Cu_{4x}(AgBi)_{1-x}I_4$ here, have previously been attributed to charge-carrier localisation (i.e. the formation of small polarons) through temperature-dependent OPTPS measurements for both $Cs_2AgBiBr_6$ [73] and Cu_2AgBiI_6 [86]. The fact that this decay is clearly present across all compositions investigated here, including for $x = 0$ (i.e. a composition with no copper), and also has been reported for the bromide-based double perovskite $Cs_2AgBiBr_6$, means that the charge-carrier localisation must derive from the presence of silver and/or bismuth in all of these materials.

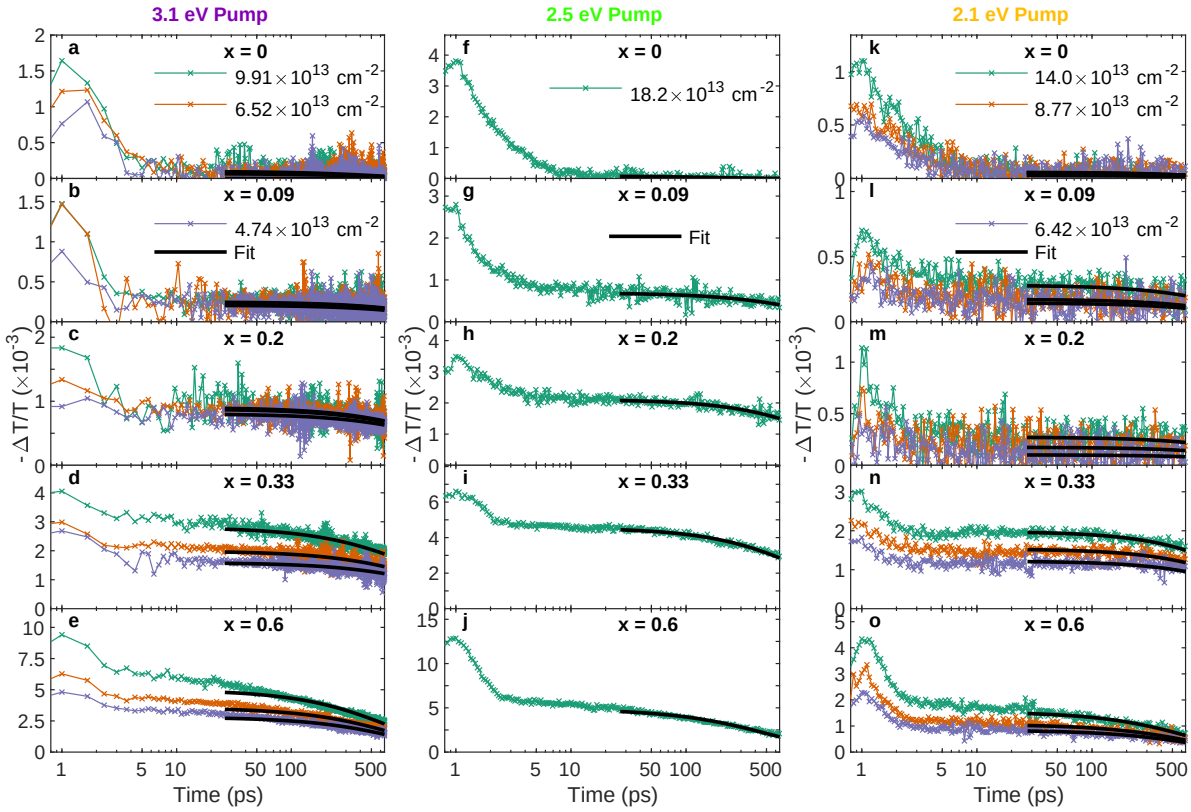


Figure 6.9: Long-time OPTPS transient decays. (a) – (e) OPTPS transient decays covering the first 600 ps, for thin films with the five $Cu_{4x}(AgBi)_{1-x}I_4$ compositions shown, following photoexcitation at 3.1 eV with incident photon fluxes of $N_A = 9.91, 6.52, 4.74 \times 10^{13}\,cm^{-2}$. The solid black lines are fits to the decays as outlined above. (f) – (j) OPTPS transient decays out to 600 ps for thin films with the five compositions shown, using photoexcitation at 2.5 eV with incident photon flux of $N_A = 18.2 \times 10^{13}\,cm^{-2}$. The solid black lines are fits to the decays as outlined above. (k) – (o) OPTPS transient decays out to 600 ps for thin films with the five compositions shown, using photoexcitation at 2.1 eV with incident photon fluxes of $N_A = 14.0, 8.77, 6.42 \times 10^{13} cm^{-2}$. The solid black lines are fits to the decays as outlined above. For ease of comparison, all decays have been shifted along the time axis such that their peak values are at $t = 1$ ps. Photoexcited charge carriers localise over the first few picoseconds, leading to the sharp drop in measured terahertz transmission $-\Delta T/T$, before recombining back to the ground state over longer timescales. For $AgBiI_4$ ($x = 0$) the photoconductivity decays to near-zero values within ~ 10 ps, and the recombination over long timescales is fluence-independent. For larger x the photoconductivity after the first ~ 5 ps remains substantial, and the long-time decays show a clear fluence dependence, indicating the presence of bimolecular (radiative) recombination.

6.3.5 Unravelling the sequence of charge-carrier relaxation, localisation and recombination

Having examined the early-time charge-carrier localization process, the full charge-carrier dynamics are now examined, separating the OPTPS photoconductivity transients into early- and long-time components in order to distinguish between different processes such as charge-carrier localization, trap-mediated and band-to-band recombination. Figure 6.11 (f) schematically represents these processes, captured through fits to the early- and long-time dynamics that were carried out separately, given the distinctly different timescales for localization and recombination.

The early-time dynamics were fitted with the two-level mobility model outlined in Chapter 3 Section 3.3.6.2: charge carriers are initially photoexcited into the conduction band into a free-carrier (large polaron) state with mobility μ_{deloc} and population n_{deloc}. Charge carriers then localise into a state with lowered mobility μ_{loc} and population n_{loc}, with the localisation rate given by k_{loc}. These early-time fits were carried out between -2 and 8 ps globally across all fluences, for each composition and excitation wavelength. This approach allows for the extraction of values of k_{loc}, μ_{deloc} and μ_{loc} for each composition at excitation energies of 3.1, 2.5 and 2.1 eV.

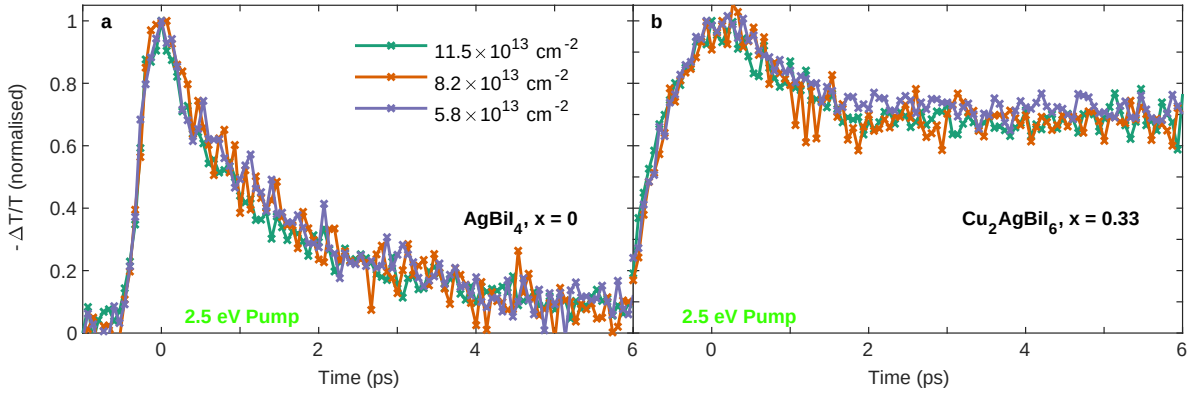


Figure 6.10: Normalised OPTPS transient decays. Decays between -1 – 6 ps for thin films of $AgBiI_4$ (a) and Cu_2AgBiI_6 (b), following photoexcitation at 2.5 eV with incident photon fluxes of $N_{\mathrm{A}} = 11.5, 8.2, 5.8 \times 10^{13}\,\mathrm{cm}^{-2}$. The transients show very little difference, implying a lack of fluence dependence to the dynamics at early times.

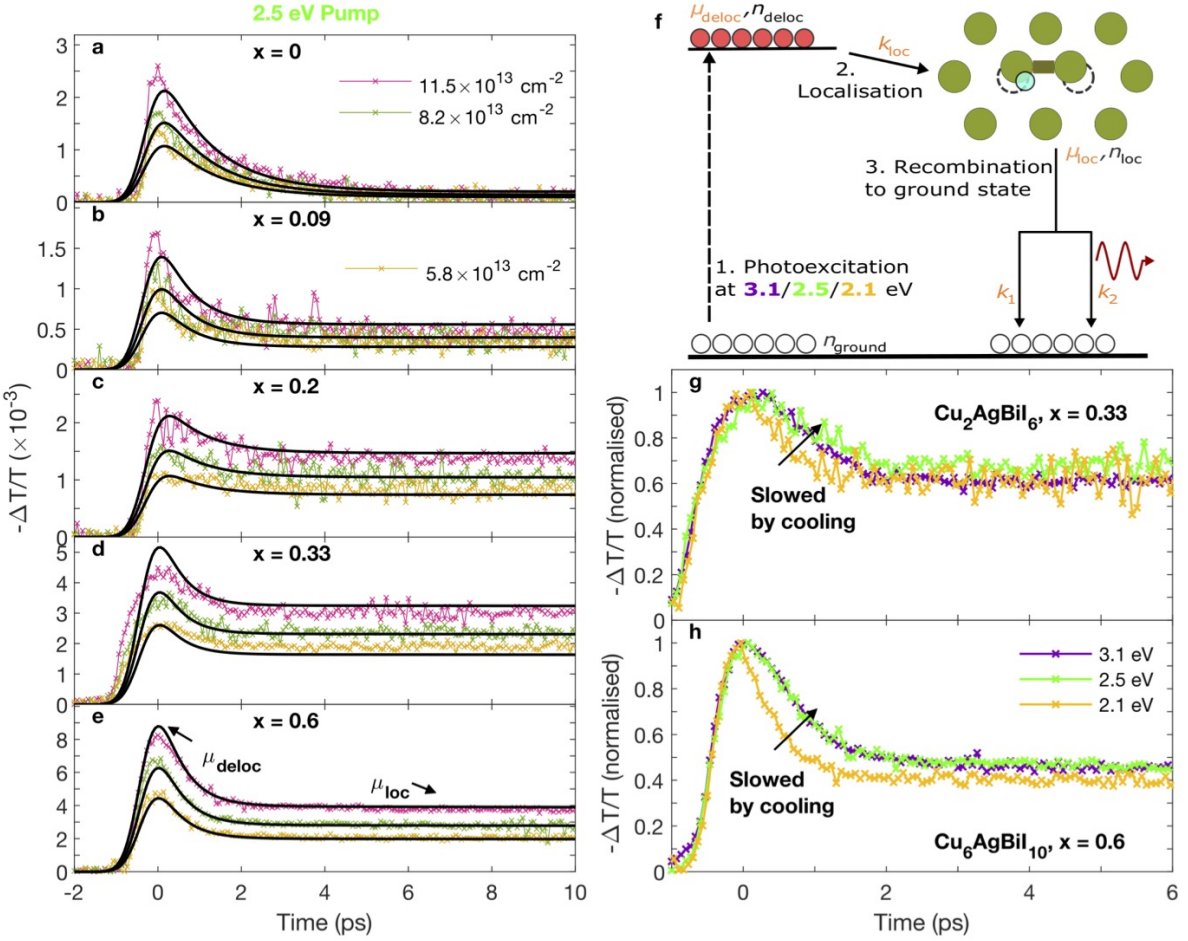


Figure 6.11: Early-time OPTPS transient decays. (a) – (e) Fluence-dependent early-time photoconductivity transients for $Cu_{4x}(AgBi)_{1-x}I_4$, measured using OPTPS with excitation at an energy of 2.5 eV (500 nm, excess energy of 0.45 eV above the bandgap). The black lines are fits to the decays between -2 and 8 ps using a two-level charge-carrier mobility model, explained in the main text. The initial peak amplitude determines the mobility μ_{deloc} of delocalized charge carriers, whereas the longer-time response is determined by the mobility μ_{loc} of localized charge carriers.Measurements were carried out with incident photon flux of $N_A = 11.5, 8.2, 5.8 \times 10^{13}\,\text{cm}^{-2}$. (f) Schematic of the charge-carrier dynamic processes present across $Cu_{4x}(AgBi)_{1-x}I_4$. (g,h) Normalised OPTPS photoconductivity transients at times between -1 – 6 ps with respect to photoexcitation for thin films of (g) $Cu_2(AgBi)I_6$ ($x = 0.2$) and (h) $Cu_6(AgBi)I_{10}$ ($x = 0.6$), for photoexcitation at 3.1, 2.5 and 2.1 eV which generates charge-carrier densities of $n_0 = 1.50, 2.63, 1.96 \times 10^{18}\text{cm}^{-3}$ and $n_0 = 1.15, 1.26, 1.46 \times 10^{18}\text{cm}^{-3}$ for the two compositions, respectively. Transients obtained for excitation at photon energies of 3.1 and 2.5 eV decay more slowly over the first 1 ps than for excitation at 2.1 eV, indicating additional charge-carrier relaxing to the bottom of the band through thermalisation and cooling. (Early-time transient decays following photoexcitation at 3.1 and 2.1 eV (excess energies of 1.05 and 0.05 eV) are shown for all five compositions in Figure S13.)

Following localisation, the photoconductivity dynamics are dominated by radiative and trap-mediated charge-carrier recombination processes occurring over longer timescales. To analyze these long-time dynamics, transients were fitted from 25 ps onwards with the solution to an ordinary differential equation (ODE) that describes charge carriers recombining to the ground state *via* monomolecular (trap-mediated) and bimolecular (radiative) recombination, described by the following equation:

$$n(t) = \frac{k_1 A}{e^{k_1 t} - A k_2}. \tag{6.1}$$

Here, k_1 is the trap-mediated (monomolecular) recombination rate, k_2 is the radiative (bimolecular) recombination rate constant, and the constant A is defined such that $\frac{1}{A} = \frac{k_1}{n_0} + k_2$. It should be noted that this type of ODE has been previously applied to describe the recombination of charge carriers in conventional metal-halide perovskites [55, 97], where photoexcited charge carriers take the form of large polarons [36, 135], as opposed to the small polarons that are identified with the long-time OPTPS signal. However, given that the small polarons in silver-bismuth materials have reasonable charge-carrier mobilities at room temperature (see below and Refs. [73] and [86]) and very low energy barriers to their temperature-activated motion [73, 86], and that exciton binding energies are relatively small, it is reasonable to assume that the dynamics of the localised state can be well described by the equation above. Fits were carried out for each composition and excitation energy of 3.1, 2.5 and 2.1 eV, globally across all fluences, yielding values of k_1 and k_2. It should be noted that the fluence-dependence in the shape of the transients provides for the accurate extraction of the bimolecular rate constant k_2, as evident in Figure 6.9. However, in the case of $AgBiI_4$ ($x = 0$) the near-zero long-time OPTPS signal and distinct lack of fluence dependence (Figure 6.9 (a), (f) and (k)) meant that a bimolecular recombination rate constant could not be extracted; these decays were therefore fitted with a monoexponential, and only a value of k_1 was obtained.

First, the values of the trap-mediated recombination rate k_1, shown in Figure 6.12 (a), are discussed. Values obtained from fits to OPTPS photoconductivity transients range between $k_1 = 10^8 - 10^{10}\,\mathrm{s}^{-1}$, and are in excellent agreement with those extracted from the time-resolved PL measurements (shown as blue squares). These correspond to lifetimes around 0.1 – 10 ns, which is at the lower end of those typically encountered in lead-halide perovskites, but competitive with those for tin-rich tin-lead halide perovskites [32]. These values indicate a high density of traps and energetic disorder in all of the compositions, and follow no trend with pump excess energy, as would be expected for a monomolecular process: charge carriers relax, form small-polaron states and then diffuse to traps. The highest values of k_1, obtained for $AgBiI_4$ ($x = 0$), also correlate well with the absence of a detectable PL spectrum for that composition. Defect formation may be similar to that for the double perovskite $Cs_2AgBiBr_6$, where silver vacancies form easily and can act as localisation centres for holes [79, 338], whilst a variety of other defect and vacancy states, including Bi vacancies and Bi_{Ag} antisites, can also act as charge-carrier trapping sites [79, 351]. There is some disagreement in the literature on whether processing in a halide-poor, or a Bi-poor/halide-rich, environment would avoid the formation of such trap states [79, 351]. Given the slight iodine deficiency identified in some of the films studied here, processing in a halide-rich environment may yield a reduction in defect density and improved charge-carrier transport, leading to enhanced device performance. By comparison, it has been shown that for metal-halide perovskites, charge-carrier lifetimes above hundreds of nanoseconds are desirable to reduce trap-mediated recombination and yield efficient current extraction and open-circuit voltage in an operating photovoltaic device [47, 352]. Thus, the values of k_1 obtained here suggest that substantial improvements in materials processing and defect passivation may lead to more efficient optoelectronic devices. Such work has shown great results for metal

halide perovskites [14, 41] but has been conducted on silver-bismuth semiconductors, such as $Cs_2AgBiBr_6$ [270], to a much lesser extent to date.

The next point of discussion is the mechanisms for radiative bimolecular (band-to-band) recombination in $Cu_{4x}(AgBi)_{1-x}I_4$. It should be noted that OPTPS yields only an

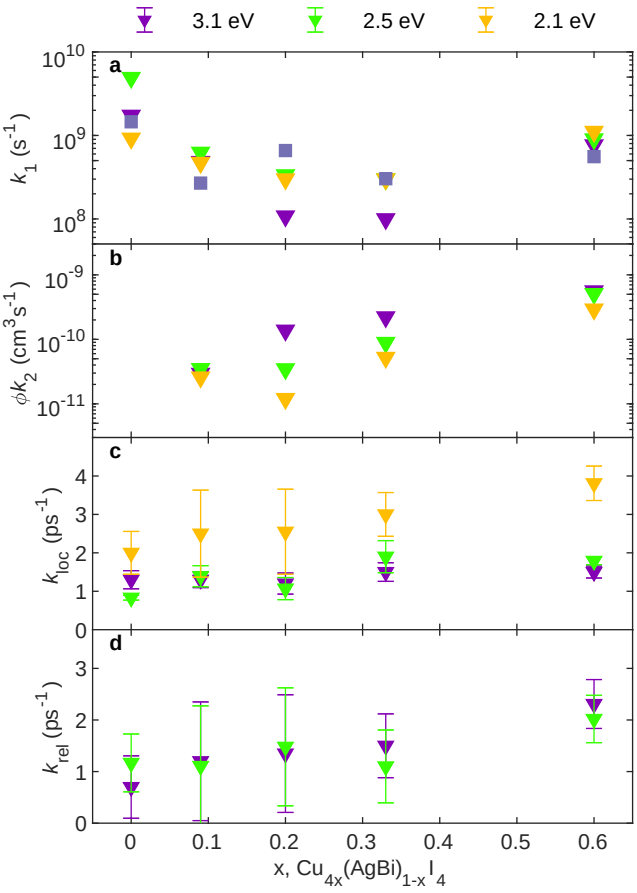


Figure 6.12: Charge-carrier rate constants. Charge-carrier rate constants obtained for $Cu_{4x}(AgBi)_{1-x}I_4$ thin films from fits to the long- and early-time OPTPS photoconductivity transients, plotted versus Cu^+ content x. Parameters are shown in purple, green and yellow according to the used photoexcitation energies of 3.1, 2.5 and 2.1 eV, respectively. (a) Monomolecular (trap-mediated) recombination rate constant k_1 obtained from fits to the long-time OPTPS data. The blue squares are values of k_1 obtained from fits to the PL decays recorded by TCSPC, which are in excellent agreement with those extracted from the OPTPS measurements. (b) Effective bimolecular (radiative) recombination rate constant ϕk_2 obtained from fits to the long-time OPTPS transients. The bimolecular rate constant is enhanced with higher x (increasing Cu^+ content), in good agreement with the increased measured PL intensities. (c) Localisation rate k_{loc} obtained from fits to the early-time OPTPS transients. The localization rate is slightly larger for increasing x, and is also markedly larger when films are photoexcited near resonance at 2.1 eV, as opposed to higher up into the bands at 2.5 or 3.1 eV. (d) Extracted charge-carrier relaxation rate k_{rel}, obtained from the difference between the localization rates at 2.5 and 3.1 eV and the localization rate at 2.1 eV for each composition.

effective bimolecular radiative recombination rate constant, ϕk_2, where ϕ is the branching ratio of absorbed photons to free charge carriers generated. Given that the exciton binding energies are comparable to thermal energies at room temperatures, ϕ may be somewhat smaller than 1, in particularly for compositions with small x. Values of ϕk_2, shown in Figure 6.12 (b), increase markedly with x, rising from a value of $\sim 0.3 \times 10^{-10}\,\mathrm{cm^3 s^{-1}}$ for $x = 0.09$ up to $\sim 6 \times 10^{-10}\,\mathrm{cm^3 s^{-1}}$ for $x = 0.6$, correlating well with the increased intensity observed in the steady-state PL measurements and with the enhanced film roughness, which would increase light out-coupling from the thin films [253, 303]. An increase in value of ϕk_2 with pump excess energy is also observed across all compositions. This is attributed to an increase in the photon-to-charge branching ratio ϕ: as the pump energy increases well above the band gap, fewer excitons are formed following the initial photoexcitation, leading to increased electron-hole radiative recombination.

For conventional lead-halide perovskites, radiative band-to-band recombination has been shown to be the inverse of optical absorption [67]. However, examining correlations between band-edge absorption strength shown in Figure 6.5 (e) and bimolecular recombination rates shown in Figure 6.12 (b), this principle does not appear to apply to the small-polaron localised state in $Cu_{4x}(AgBi)_{1-x}I_4$. Instead, the opposite trend to that expected from the principle of detailed balance is observed: ϕk_2 rises and $\alpha_{2.3}$ falls with increasing x, and the ratio of $\frac{\phi k_2}{\alpha_{2.3}}$ rises by two orders of magnitude across the compositional range, rather than remaining constant. This observation cannot be caused by variations in refractive index, as the dielectric constants show little trend with x (as shown in Figure 6.5 (g)). In addition, given the similarity in exciton binding energies across the compositional range, the photon-to-charge branching ratio ϕ should not change to such an extreme extent, and neither would surface roughness. Instead, it is suggested that some of the assumptions around the principle of detailed balance calculations (which leads to the conclusion that bimolecular recombination is the inverse

of optical absorption [67]) no longer apply to radiative recombination from a small polaron state. Indeed, Wu et al. argue that polaron formation in $Cs_2AgBiBr_6$ allows for much larger bimolecular recombination rate constants than would be expected for this indirect gap semiconductor, as charge-carrier localisation leads to a breakdown of the band-to-band recombination picture [307].

As an alternative description, the Langevin model for radiative recombination can be considered - a model that is often applied to organic semiconductors that typically support small polarons [353]. The Langevin model assumes that electon-hole recombination proceeds through charge capture into the Coulomb potential generated by the opposite charge, making bimolecular recombination rates proportional to the approach velocity and therefore mobility of the charge carrier. In this simple model, the radiative rate constant is therefore determined by $k_2^{\text{Langevin}} = e\mu/\epsilon_0\epsilon_r$. Using an approximate average value determined here for the small polaron mobility $\mu_{\text{loc}} \sim 1\,\text{cm}^2\text{V}^{-1}\text{s}^{-1}$ (see below) and $\epsilon_r = \epsilon_\infty^{\text{THz}} \sim 6$ yields $k_2^{\text{Langevin}} \sim 3 \times 10^{-7}\,\text{cm}^3\text{s}^{-1}$, several orders of magnitude above what is found here across the entire compositional range. Therefore, the Langevin criterion does not appear to be quantitatively satisfied at first sight. However, the strong correlation between the bimolecular recombination rate constants and the charge-carrier mobilities (discussed below) across the compositional series qualitatively support the notion of Langevin-like recombination. One potential explanation for the numeric discrepancy is that the charge-carrier localisation observed here may only affect one species, reducing the charge-carrier mobility for that species but leaving a reasonably high mobility for the remaining free carrier in a large polaron state. In such a scenario, for which the mobility of one species is much larger than that of the other, Monte-Carlo-based simulations of organic polymer blends have shown that bimolecular recombination can be somewhat below the Langevin limit, depending on the precise ratio of charge-carrier mobilities [354]. Although the situation for an inorganic crystalline semiconductor is somewhat

different, with long-range order and higher charge-carrier mobilities, a similar underlying principle may apply. Thus, charge-carrier recombination rates for small polarons in silver-bismuth materials that are qualitatively well-described by a Langevin-type model, whilst remaining numerically somewhat below the Langevin limit.

Next, the charge-carrier localisation rate k_{loc} is analysed in order to understand how compositional variations impact the localisation process, and two interesting trends in the fitted values are found (see Figure 6.12 (c)). First, the localisation rate increases slightly with x (increasing Cu^+ content), for all pump wavelengths. This is attributed to a slight change in the crystal structure of the materials as Cu^+ content increases: as discussed above, materials with high copper content such as Cu_2AgBiI_6 have a layered 2D octahedral network [84], whereas $AgBiI_4$ has been shown to have octahedral networks that are fully connected in all three dimensions [80]. Given that charge-carrier localisation has been shown to depend on the dimension of a system [36, 72, 152, 153], with lower-dimensional systems having faster localisation with lower or non-existent energetic barriers, this finding agrees well with the theoretical predictions. However, this effect is quite small, i.e. an order-of-magnitude change in localisation rate is not observed, and this could be linked to the general low electronic dimension of silver-bismuth materials [36, 91, 355], which might dominate over any changes in structural dimension.

Second, the localisation rate is found to be much larger, nearly doubled, when photoexcitation occurs near resonance at 2.1 eV, as opposed to higher up into the bands at 3.1 or 2.5 eV (excess energies of 1.05 and 0.45 eV, respectively). This is attributed to charge-carrier relaxation preceding localisation, when photoexcitation occurs well above the band gap. Studies of conventional metal-halide perovskites using OPTPS have found slower rises in photoconductivity with increasing pump energy [178, 337], attributed to charge-carrier relaxation occurring within the first hundreds of femtoseconds: as relaxation to the bottom of the band takes place, the charge-carrier mobility increases

because the band extrema are more highly curved, leading to a rise in photoconductivity response over the relaxation timescale. Such a pronounced rise in mobility (and thus photoconductivity) over the first few hundred femtoseconds is not observed in the silver-bismuth materials studied here, most likely because of the very flat band structure found in such materials [76, 94], which would lead to little change in mobility as carriers relax. Thus, the photoconductivity dynamics observed for the silver-bismuth materials in this study suggest that charge-carriers must first relax to the bottom of the band and lose significant energy before effectively being able to localise into a small polaron state. Given this, more accurate values for the rate for localisation are obtained by generating charge carriers close to the band gap at 2.1 eV, leading to negligible initial charge-carrier relaxation, which yields a localisation rate between $2-4\,\mathrm{ps}^{-1}$ ($\tau_{\mathrm{loc}} \sim 0.25-0.5\,\mathrm{ps}$). Instead, when photoexcition occurs above resonance at 3.1 and 2.5 eV, charge carriers must first undergo relaxation via both thermalisation and charge-carrier cooling [178, 356–358] before localising to the small polaron state (as shown in Figure 6.11 (g) and (h)). In order to quantify the timescale of charge-carrier relaxation, a relaxation rate is calculated as $k_{\mathrm{rel}} = k_{\mathrm{loc}}^{2.1\mathrm{eV}} - k_{\mathrm{loc}}^{3.1\,\mathrm{or}\,2.5\mathrm{eV}}$, which yields rough estimates around $1-2\,\mathrm{ps}^{-1}$ ($\tau_{\mathrm{rel}} \sim 0.5-1\,\mathrm{ps}$), in good agreement with timescales between 0.1 – 1 ps for charge-carrier relaxation found in conventional lead-halide perovskites [178, 358].

Overall, this analysis of the photoconductivity transients provides clear insights into the dynamical charge-carrier processes occurring in the silver-bismuth semiconductors $Cu_{4x}(AgBi)_{1-x}I_4$ from sub-picosecond through to nanosecond timescales. When photoexcitation occurs above resonance charge-carriers first relax to the bottom of the conduction band over the first 0.5 – 1 ps. Charge-carriers are photoexcited into a delocalised large-polaron state and, once cooled, localise over the next 0.25 – 0.5 ps into a small polaron state. Such small polarons subsequently recombine, through either trap mediated recombination over a nanosecond time scale, or through fluence-dependent radiative

bimolecular recombination that gives rise to the highly Stokes-shifted photoluminescence at energies around 1.6 – 1.7 eV. An assessment across the compositional series reveals that the replacement of Ag^+ and Bi^{3+} with Cu^+ increases the rates of both charge-carrier relaxation and localisation — a direct consequence of the enhanced curvature at the valence band maximum with increased contributions from copper electronic states, as well as the shift from a 3D to a 2D octahedral network, as discussed above. In addition, the radiative bimolecular recombination rate constants are found to increase with Cu^+ content, in good agreement with the enhanced PL signal. However, the mechanism of bimolecular recombination in these materials is found to deviate from that observed in conventional metal halide perovskites. The anticorrelation between bimolecular rates constants and strength of absorption near the band edge indicate that the detailed-balanced approach described by Davies et al. [67] does not apply to these silver-bismuth materials. Instead the correlation between bimolecular rate constants and charge-carrier mobilities suggests that radiative recombination from the small polaron state may take place *via* a Langevin-style process.

6.3.6 Influence of Cu^+ on charge-carrier mobility and transport

To gain insights into charge-carrier transport in $Cu_{4x}(AgBi)_{1-x}I_4$ semiconductors and how it may be affected by charge-carrier localisation, the values of the effective charge-carrier mobilities extracted from the fits to the early-time OPTPS dynamics are presented in Figure 6.13. Again, these values combine the 'true' mobilities of the large/small polaron states (μ_{deloc} and μ_{loc}, respectively) with the photon-to-charge branching ratio ϕ, which may vary as the pump excess energy is altered. Further, it should be noted that OPTPS is only able to probe directly the sum charge-carrier mobility arising from contributions from both electrons and holes; $\mu_{\text{deloc/loc}}$ thus represent the total sum mobility for the electrons and holes in the large and small polaron states, respectively. The values of the effective

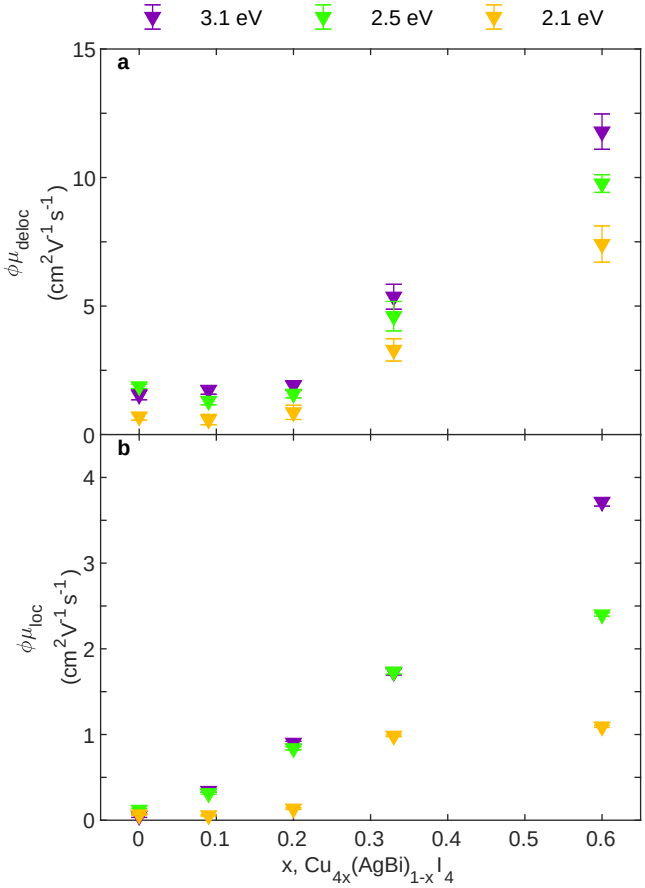


Figure 6.13: Charge-carrier mobilities. Effective electron-hole sum mobilities for $Cu_{4x}(AgBi)_{1-x}I_4$ thin films obtained from fits to the early-time OPTPS photoconductivity transients and plotted versus Cu^+ content x. Values are shown in purple, green and yellow according to the used photoexcitation energies of 3.1, 2.5 and 2.1 eV, respectively. (a) Effective large-polaron mobility $\phi\mu_{\text{deloc}}$ and (b) effective small polaron mobility $\phi\mu_{\text{loc}}$. Values increases markedly with x because of reduced charge-carrier effective masses, and also rise with pump excess energy because of increases in free-charge-to-photon branching ratios by which the mobility values are factored.

large polaron mobility $\phi\mu_{\text{deloc}}$ show two clear trends: a sharp increase in charge-carrier mobility with x, from $1.5\,\text{cm}^2\text{V}^{-1}\text{s}^{-1}$ to $11.7\,\text{cm}^2\text{V}^{-1}\text{s}^{-1}$ (a trend observed across all three photoexcitation energies); and rising values of $\phi\mu_{\text{deloc}}$ with increasing pump excess energy.

The increase in large polaron mobility with x is caused by several complementary effects: charge-carrier mobilities depend on a mix of intrinsic factors, such as charge-lattice couplings or local electronic band structure, and extrinsic factors such as scattering off grain boundaries or local fluctuations in the energy landscape [49, 97]. The steady-state

PL measurements demonstrate that increased Cu^+ presence leads to some reduction in trap density and energetic disorder, reducing scattering from defects and improving charge-carrier mobilities. Further, although a transition from a 3D to a 2D octahedral network occurs with increasing x, this effect is countered by the accompanying increase in tetrahedrally-coordinated Cu^+ improving general electronic connectivity, as argued above, which aids charge transport. Finally, as mentioned above, density functional theory (DFT) calculations carried out on both $CuBiI_4$ [347] and Cu_2AgBiI_6[84] have shown contributions to the valence band maximum from Cu-d electronic states (as opposed to from Ag-d and Bi-s states in $Cs_2AgBiBr_6$ [94, 316, 332]). Thus, it is proposed that increased relative contributions from copper states leads to a more curved valence band maximum [94, 316, 332], and correspondingly higher mobilities and lower effective masses for holes.

The trend of increasing value of $\phi\mu_{\mathrm{deloc}}$ with increasing pump excess energy, for any given composition, is attributed to a rise in photon-to-charge branching ratio ϕ: as the pump excess energy rises well above the band gap, fewer neutral excitons and more free charge carriers are formed [313, 359]. Given that only individual electrons or holes contribute to the measured THz photoconductivity in the energy range studied here, and that neutral excitons do not (as $E_{\mathrm{B}} > 10\,\mathrm{meV}$), an increase in the proportion of free charges being formed, relative to excitons, will be registered as an larger $-\Delta T/T$ signal and subsequently higher charge-carrier mobility. Similar trends have been observed through time-resolved microwave conductivity on $MAPbI_3$ [359]. An alternative explanation for this trend is that the increased charge-carrier mobility with increasing pump excess energy is linked to probing different locations of the band structure. However, given that higher-lying bands in silver-bismuth materials tend to be flatter than the band extrema [93, 94, 332], one would expect the opposite trend to that observed here, i.e. decreased values of μ_{deloc} with increasing pump excess energy and therefore rule out this explanation.

The effective mobility of the small polaron state, $\phi\mu_{\mathrm{loc}}$, follows similar trends to those observed for the large polaron mobility: it increases sharply with x and also increases with pump excess energy, for analogous reasons. The trend of higher mobility values with x implies a reduced 'barrier' to the hopping-type transport typical of small polarons [72, 107]. This may appear contradictory to the observed rise in localisation rate k_{loc} with increasing x, but the two processes are physically distinct: the localisation rate is a proxy for the size of the energetic barrier between delocalised and localised states in a material [152], whereas the small polaron mobility gives an indication of the energetic barrier for movement of a localised charge from one particular lattice site to another [107]. Thus, the enhanced electronic connectivity that follows increased Cu^+ content leads to higher small polaron mobilities; most likely because the spatial separation between electronic states arising from Ag^+ and Bi^{3+} octahedra [91, 92], is lowered, which in turn reduces the barrier to charge motion.

Alternatively, studies of a variety of silver-bismuth materials have argued for selective localisation of holes on Ag^+ sites or electrons on Bi^{3+} sites [338, 346]. Given that the two-level mobility model used here, for simplicity, does not assume contributions from distinct electrons and holes, this observed rise in μ_{loc} could also be interpreted as an increased mobility of the remaining, non-localised, free charges. Thus, one photoexcited species (e.g. electrons) could localise very rapidly, reducing the measured photoconductivity, but the other remains free to move, contributing to the photoconductivity well beyond the first few picoseconds.

An important conclusion is that the substantial rise in charge-carrier mobility with increasing Cu^+ content makes these materials the most promising for implementation in photovoltaic devices. In particular, $Cu_{4x}(AgBi)_{1-x}I_4$ with $x = 0.33$ and above shows good charge-carrier mobilities of $\sim 1\,\mathrm{cm^2V^{-1}s^{-1}}$ or more at long times scales for which small polarons have formed, which are most relevant to charge-carrier extraction. For

$AgBiI_4$, on the other hand, small polaron formation leads to negligible remnant charge-carrier mobility, making such AgBi-rich, Cu-poor materials less suitable for photovoltaic applications, as has been seen in device-based studies thus far [81, 83].

6.3.7 Understanding, mitigating and tailoring charge-carrier localisation

Overall, the results presented thus far show that small polaron formation takes place across the compositional series $Cu_{4x}(AgBi)_{1-x}I_4$, regardless of changes in crystal structure with Cu^+ content, implying such localisation is intrinsically linked to the presence of Ag^+ and Bi^{3+}. Importantly, such localisation effects can be adapted and mitigated by variations in the crystal structure (between a 2D and 3D octahedral network), and by dilution of the amount of Ag^+ and Bi^{3+}, relative to Cu^+, allowing for greater electronic conductivity. As has been shown, Cu^+ addition can tailor charge-carrier dynamics and transport, both of which are crucial for determining suitability across a variety of optoelectronic applications. Further, such charge-carrier localisation is also found to lead to a modification of band-to-band bimolecular recombination mechanisms, typically described by a radiative-balance approach for lead halide perovskites, but for $Cu_{4x}(AgBi)_{1-x}I_4$ more akin to small-polarons recombination *via* Langevin-type similar to processes in organic semiconductors. Overall, the results demonstrate that increased Cu^+ content leads to a reduction in charge-carrier effective masses and enhanced charge-carrier mobilities, linked to the increased contributions of copper electronic states at the valence band maximum. This chapter ends with a discussion of attempted strategies for the alteration of localisation effects across wider material classes, focusing on the influence of chemical composition, electronic dimension and structural distortion [36] with a view of guiding further materials development.

Compositional tuning through use of mono- and tri-valent alternatives to silver and bismuth has been explored for a range of semiconductors,[33, 93] by substitution of Na^+

[360], K^+, Tl^+ or In^+ for Ag^+, and Tl^{3+} [361], Sb^{3+} [196, 316, 362] or In^{3+} [362, 363] for Bi^{3+}. Substitution of Na^+ for Ag^+ in $Cs_2Ag_{1-y}Na_yBiCl_6$ has been shown to lead to local structural distortions deriving from mismatched octahedra for large doping levels ($y > 0.6$) [360]; combined with the predicted low electronic dimension of $Cs_2NaBiCl_6$ [91, 93], this could imply a similar or stronger amount of charge-carrier localisation, relative to the silver-based material.

With regards to substitutions of bismuth, attempted doping of $Cs_2AgBi_{1-y}In_yBr_6$ with In^{3+} has had very limited success in photovoltaic devices [363], and the increased emission with indium content from the highly Stokes-shifted main PL band correlates well with its assignment to a localised state, possibly also implying stronger charge carrier localisation [73, 74, 338]. Further, for the indium-based material $Cs_2AgInCl_6$ it has been suggested that holes localise on [$AgCl_6$] octahedra, leading to the formation of self-trapped excitons that result in broad, highly Stokes-shifted emission [98, 198]. Based on such initial results, it is thus not recommended to apply such substitutions to the series of silver-bismuth materials investigated here. Recent theoretical work on the double perovskites $Cs_2Ag(Bi/Sb)X_6$ (X=Br^-,Cl^-) by Biega et al. [316] has suggested that swapping Bi^{3+} for Sb^{3+} leads to somewhat reduced exciton localisation (without removing it entirely) [316]. Separately, studies of BiI_3 [343], $(MA)_3Bi_2I_9$ [344] and $(MA)_3Sb_2I_9$ [345] by Scholz et al. have found very strong electron-phonon couplings across all of these materials, confirming that the observed charge-carrier localisation is linked intimately to the presence of bismuth or antimony, rather than the specifics of a particular crystal structure. This finding is in excellent agreement with the observation that structural and compositional variations across the solid solution line alter, but do not completely remove, charge-carrier localisation.

To examine the specific impact of crystal structure on charge-carrier localisation, alterations to the structural dimension of silver-bismuth materials can be attempted.

This approach has been pursued for layered Ruddlesden-Popper versions of the double perovskite $Cs_2AgBiBr_6$ [201], where a reduction from two to one octahedral layers facilitated structural distortions that are likely to aid charge-carrier localisation. Another, similar, approach is to design tailored large organic spacer cations that can separate individual sub-units of the crystal sub-structure, which had been implemented for $(AE_2T)_2AgBiI_8$ [346]. Through variation of the length and dipolar nature of such organic cations, the 'stiffness' of the lattice could be reduced or enhanced, depending on the application, allowing for a variation in strength of electron-phonon coupling [36]. However, given that charge-carrier localisation in $Cu_{4x}(AgBi)_{1-x}I_4$ studied here is linked closely to the presence of bismuth and silver, owing to the large electronegativity of the silver- and bismuth-halide bonds and the structural instability of bismuth, such structural variation is likely to provide an avenue for tailoring, rather than entirely removing, charge-carrier localisation in these materials.

Overall, these examples show that compositional substitution can provide an effective tool for removing or reducing charge-carrier localisation in metal halide semiconductors. While replacement of Ag^+ with Na^+ and of Bi^{3+} with Sb^{3+} has not appeared to be fully successful in early studies, it is clear that such investigations are at an incipient stage. Future studies that examine the influence of specific compositional replacements for silver and bismuth, or of structural alterations, on charge-carrier localisation will help to unlock the potential of silver-bismuth semiconductors across a wide range of optoelectronic applications. Given that these materials have to date received significantly less attention and research focus compared to their more prominent lead halide perovskites counterparts, such research is likely to from a highly promising future avenue towards lead-free materials for photovoltaic applications.

6.4 Summary and Conclusion

This chapter has demonstrated the promise of new quaternary Cu-Ag-Bi-I semiconductors, $Cu_{4x}(AgBi)_{1-x}I_4$, that have direct band gaps in the visible range, low exciton binding energies and charge-carrier mobilities rising to above $10\,cm^2V^{-1}s^{-1}$ for high Cu^+ content. The addition of Cu^+ is found to improve general optoelectronic properties by reducing disorder and improving electronic connectivity throughout the lattice, enhancing PL emission and charge-carrier transport, which is favourable for photovoltaic applications. Through excess-energy dependent OPTPS, charge-carrier dynamics are unravelled: relaxation and localisation from large- to small-polaron states on a picosecond time scale, and subsequently recombination through trap-mediated and radiative bimolecular recombination. Further, the OPTPS measurements show that the principle of detailed balance fails to describe band-to-band recombination of small polarons adequately for these silver-bismuth materials. Instead, correlation between charge-carrier mobilities and bimolecular recombination constants across the series suggest that such processes may be better described by the Langevin model. Further, increased Cu^+ content leads to reduced exciton binding energies and enhanced charge-carrier mobilities, which is linked to a reduction in charge-carrier effective masses caused by enhanced contributions from copper states at the VBM. Overall, materials with higher Cu^+ display the most advantageous optoelectronic properties in this series, since, despite their faster localization dynamics, they display the highest small-polaron mobilities and strongest radiative recombination. In conclusion, although charge-carrier localisation takes place across Ag^+ and Bi^{3+} containing compositions across the solid solution line of $AgBiI_4$ – CuI and is most likely linked to the presence of Ag^+ and Bi^{3+}, its impact can be tailored and mitigated by changes in crystal structure and electronic connectivity, opening a new window into material design for optoelectronic applications.

7

Conclusion and Outlook

This thesis has addressed the issue of how changes in the composition and structure of several metal-halide semiconductors influence their underlying optoelectronic properties. The insights gained here are crucial to determine the suitability of new metal-halide materials to applications in semiconductor-based devices, and have addressed the four questions outlined in the Introduction. The investigation of 2D-3D hybrid perovskite materials led to an understanding of why they have achieved excellent performance in solar cell devices, and the range in which such hybridisation provides benefits. The discovery of strong charge-carrier localisation effects in silver-bismuth-halide based materials provided novel insights into this less-studied materials class. As-yet undiscovered Cu-Ag-Bi-I materials were identified as possessing a promising mix of optoelectronic properties for application in photovoltaic devices, notwithstanding the presence of such charge-carrier localisation. Further, temperature-dependent measurements carried out on Cu_2AgBiI_6 and $Cs_2AgBiBr_6$ provided experimental confirmation of theoretical predictions of low electronic dimension and the presence of charge-carrier localisation and poor charge-carrier transport in silver-bismuth based materials. Such insights were predominantly gained through the use of ultrafast optical-pump terahertz-probe spectroscopy, which

allows for an understanding of charge-carrier transport and dynamics on a sub-picosecond timescale, and together with optical absorption and photoluminescence spectroscopies, and X-ray diffraction, these techniques provide an excellent toolkit for understanding the optoelectronic properties of new semiconductors.

Chapter 4 studied hybrid 2D-3D perovskite materials with composition $BA_x(FA_{0.83}Cs_{0.17})_{1-x}Pb(I_{0.6}Br_{0.4})_3$, understanding how the addition of butylammonium impacted upon charge-carrier energetics, recombination and transport. Analysis of the steady-state absorption and photoluminescence showed that addition of butylammonium (BA) led to a blue-shift in the band gap energy, which together with X-ray diffraction measurements revealed a small variation in iodide:bromide content in the 3D bulk of these materials. Time-resolved photoluminescence measurements showed that the addition of small amounts of BA passivated traps and increased monomolecular charge-carrier lifetimes and also led to a slight improvement in charge-carrier mobilities, but that such trends were reversed for excessive amounts of BA ($x > 0.2$), destroying the beneficial optoelectronic properties gained from hybridisation. Together, these results point towards an optimal hybridisation range for BA content of $x = 0.091 - 0.167$, combining the excellent optoelectronic properties of 3D perovskites with the stability of 2D perovskites, and correlating very well with the excellent device performance and stability observed for $x = 0.091$ [110]. This study thus demonstrates that the combined compositional, structural and optoelectronic properties of the $BA_x(FA_{0.83}Cs_{0.17})_{1-x}Pb(I_{0.6}Br_{0.4})_3$ hybrid system yield an excellent candidate for highly efficient and stable solar cell devices. Future work in this area could investigate the different approaches to 2D-3D hybridisation [110, 278, 279] for the same chemical composition, studying how differences in structural variations lead to corresponding variations in charge-carrier energetics and transport in such materials.

The two remaining experimental chapters of this thesis explored a range of novel silver-bismuth-halide semiconductors. The work in Chapter 5 combined temperature-

dependent THz, photoluminescence and optical absorption spectroscopies to provide a fundamental understanding of the novel material Cu_2AgBiI_6. These measurements found a band gap of 2.1 eV, exciton binding energy of only 29 meV and charge-carrier mobilities above 1 $cm^2V^{-1}s^{-1}$ at room temperature for this material, that together make it suitable for applications in the top cell of tandem solar cells. However, intriguingly OPTPS measurements also revealed a picosecond-scale reduction in photoconductivity in Cu_2AgBiI_6, which was attributed to the localisation of charge carriers into a small polaron state. Temperature-dependent OPTPS measurements showed that small polaron motion is characterised by temperature-activated hopping transport, yielding long-time charge-carrier mobilities that rise with increasing temperature. The same localisation and small-polaron hopping was also observed for $Cs_2AgBiBr_6$ *via* temperature-dependent OPTPS measurements, notwithstanding the markedly different crystal structure and composition of this material. Together, these investigations revealed that charge-carrier localisation is linked to the presence of silver and bismuth in these materials, correlating well with the proposed low electronic dimension of such materials [88, 91–93] posing questions for their suitability in optoelectronic devices that require good charge transport properties.

This topic was further addressed by the work in Chapter 6, where the interplay between composition, structure and charge-carrier dynamics was studied across five silver-bismuth-halide materials with composition $Cu_x(AgBi)_{1-x}I_4$. Charge-carrier localisation was observed in ultrafast OPTPS measurements across the entire compositional range, including for $x = 0$, leading to the conclusion that charge-carrier localisation is intrinsically linked to the presence of Ag^+ and Bi^{3+}. Further, the addition of tetrahedrally-coordinated Cu^+ was found to yield enhanced photoluminescence intensity and higher charge-carrier mobilities. The former was attributed to a reduction in trap density and disorder, whereas the latter was ascribed to a combination of increased general electronic connectivity as well as a reduction in charge-carrier effective masses. The latter trend was also observed in the

reduction in exciton binding energies observed with increasing Cu^+ content, which was also found to be due to reduced charge-carrier effective masses. Intriguingly, the bimolecular recombination rate constants in these five materials were found to increase with rising Cu^+ content, accompanied by a decreased optical absorption coefficient, opposite to what has been observed for radiative band-to-band recombination in metal-halide perovskites [67]. This insight led to the suggestion that the formation of small polarons causes a breakdown in the band-to-band recombination picture, and instead radiative recombination is better described by Langevin-type recombination for these silver-bismuth-halide materials.

Together, these two latter chapters provided a comprehensive overview of the charge-carrier dynamics and transport properties of silver-bismuth-halide materials, advancing current understanding of such lead-free semiconductors. This work serves to confirm suggestions, based on theoretical studies of new metal-halide semiconductors [88, 91–93], that the presence of silver and bismuth lead to a low electronic dimension for these materials [91, 92], and that this is linked to the lack of lone pair electrons in both silver and bismuth lattice substructures (i.e. octahedra) [88, 93]. Future studies could systematically compare different compositional replacements to silver and/or bismuth, to verify whether alternatives such as Na^+, $In^{+/3+}$ or Sb^{3+} will also lead to charge-carrier localisation, as is predicted for such materials [88, 91–93], and how this influenced charge-carrier dynamics and transport. Separately, investigations of the impact of crystal structure and structural distortions [201] on charge-carrier localisation would also provide a separate route to understanding and mitigating charge-carrier localisation effects, enabling tailoring of new semiconductors to specific applications in energy and optoelectronics.

Overall, there is still plenty of scope for further experimental studies of new metal-halide semiconductors, ideally using IR, Raman or OPTP spectroscopies to better understand the precise nature of charge-carrier localisation and its influence on opto-electronic properties. Given the wide range of possible materials, focusing research onto

a few 'prototypical' metal-halide systems could be of great help in clarifying common properties of some of these materials, as has been done with $MAPbI_3$ with respect to MHPs. Thus, research could focus on model vacancy-ordered materials with formula $A_3\square B_2^{3+}X_9$ and $A_2\square B^{4+}X_6$, and the zero-dimensional metal-halide A_4BX_6. Ideally, such work would centre around materials that included the same metal and halide elements, allowing for easier comparisons to be made. Alternatively, given the ease of compositional variation across double perovskites, these could be good model systems for continued study of the correlation between electronic dimension, structural dimension, presence of lone-pair electronic states and charge-carrier localisation, building on the work presented here. Further work might also clarify whether structural distortion in a material can be used as an impactful way to tune its optoelectronic properties, which would provide a new window into materials design and selection [163, 211]. Such research would set a clear pathway towards identification of the most promising material systems for future investigation and application in optoelectronic devices.

There is clear demand for new semiconducting materials applied to energy innovation, from efficient white-light emitting LEDs [99, 123] to lead-free, non-toxic solar cells [33, 35] that make use of earth-abundant materials with low environmental footprints [364, 365]. Thus, establishing a rigorous and methodical approach to exploring this wide range of new metal-halide semiconductors will be crucial to ensuring that research can focus on those materials best suited to specific applications. As has been outlined in this thesis, identifying and characterising charge-carrier dynamics and polaronic behaviour is complex, requiring multiple complementary experimental signatures, yet it is also fundamental to understanding the semiconducting properties of a material, and thus judging its effectiveness for a particular optoelectronic device. There are several potential pitfalls in such work. First, multiple processes can lead to similar experimental signals, as in transient absorption decays. Second, carrying out only one kind of steady-state

measurement, such as PL or optical absorption, is often not enough to provide definitive evidence for charge-carrier localisation. Third, disentangling which processes lead to polaron formation can prove fiendishly difficult. Nonetheless, it is clear that there are many varied, fascinating and potentially useful materials that are only at the start of being investigated and understood. Innovative material selection and characterisation, along with careful, strategic approaches across this field of research will be necessary to drive continued exploration of new metal-halide semiconductors for energy applications.

References

[1] Steinberger, J. K.; Lamb, W. F. and Sakai, M. 'Your money or your life? The carbon-development paradox'. *Environmental Research Letters*, 2020, **15**, 044016.

[2] Csereklyei, Z.; Mar Rubio-Varas, M. d. and Stern, D. I. 'Energy and economic growth: The stylized facts'. *The Energy Journal*, 2016, **37**, 223–255.

[3] Sakai, M.; Brockway, P. E.; Barrett, J. R. and Taylor, P. G. 'Thermodynamic efficiency gains and their role as a key 'engine of economic growth''. *Energies 2019, Vol. 12, Page 110*, 2018, **12**, 110.

[4] Smith, N. *Why I'm so excited about solar and batteries.* https://noahpinion.substack.com/p/why-im-so-excited-about-solar-and.

[5] Acemoglu, D. 'Introduction to modern economic growth'. *Introduction to Modern Economic Growth*, 2008.

[6] Cowen, T. and Southwood, B. 'Is the rate of scientific progress slowing down?' *SSRN Electronic Journal*, 2019.

[7] Ritchie, H. and Roser, M. 'Energy'. *Our World in Data*, 2020.

[8] Jorgenson, A. K. 'Economic development and the carbon intensity of human well-being'. *Nature Climate Change 2014 4:3*, 2014, **4**, 186–189.

[9] Masson-Delmotte, V.; Zhai, P.; Pörtner, H. O.; Roberts, D.; Skea, J.; Shukla, P. R.; Pirani, A.; Moufouma-Okia, W.; Péan, C.; Pidcock, R. *et al. Global warming of 1.5°C. An IPCC Special Report on the impacts of global warming of 1.5°C above pre-industrial levels and related global greenhouse gas emission pathways, in the context of strengthening the global response to the threat of climate change, sustainable development, and efforts to eradicate poverty.* Intergovernmental Panel on Climate Change, 2018.

[10] Masson-Delmotte, V.; Zhai, P.; Pirani, A.; Connors, S. L.; Péan, C.; Berger, S.; Caud, N.; Chen, Y.; Goldfarb, L.; Gomis, M. I. *et al. Summary for Policymakers, Climate Change 2021: The Physical Science Basis. Contribution of Working Group I to the Sixth Assessment Report of the Intergovernmental Panel on Climate Change.* IPCC, 2021.

[11] Sun, H.; Edziah, B. K.; Sun, C. and Kporsu, A. K. 'Institutional quality, green innovation and energy efficiency'. *Energy Policy*, 2019, **135**, 111002.

[12] Smil, V. 'Energy (r)evolutions take time'. *World Energy*, 2019, **44**, 10–14.

[13] Hepburn, C.; Pless, J. and Popp, D. 'Encouraging innovation that protects environmental systems: Five policy proposals'. *The Review of Environmental Economics and Policy*, 2018, **12**, 154–169.

[14] Jena, A. K.; Kulkarni, A. and Miyasaka, T. 'Halide perovskite photovoltaics: Background, status, and future prospects'. *Chemical Reviews*, 2019, **119**, 3036–3103.

[15] Sivaram, V. *Taming the sun.* The MIT Press, 2018.

[16] Green, M. A.; Ho-Baillie, A. and Snaith, H. J. 'The emergence of perovskite solar cells'. *Nature Photonics*, 2014, **8**, 506–514.

[17] *Best Research-Cell Efficiency Chart*. Accessed: 2021-09-20. https://www.nrel.gov/pv/cell-efficiency.html.

[18] Extance, A. 'The reality behind solar power's next star material'. *Nature*, 2019, **570**, 429–432.

[19] Richter, A.; Hermle, M. and Glunz, S. W. 'Reassessment of the limiting efficiency for crystalline silicon solar cells'. *IEEE Journal of Photovoltaics*, 2013, **3**, 1184–1191.

[20] BloombergNEF. *BloombergNEF Executive Factbook*. 2020.

[21] Woodhouse, M.; Smith, B.; Ramdas, A. and Margolis, R. *Crystalline silicon photovoltaic module manufacturing costs and sustainable pricing: 1H 2018 benchmark and cost reduction road map*. National Renewable Energy Laboratory, 2019. https://www.nrel.gov/docs/fy19osti/72134.pdf..

[22] Jones-Albertus, R.; Feldman, D.; Fu, R.; Horowitz, K. and Woodhouse, M. 'Technology advances needed for photovoltaics to achieve widespread grid price parity'. *Progress in Photovoltaics: Research and Applications*, 2016, **24**, 1272–1283.

[23] Sofia, S. E.; Wang, H.; Bruno, A.; Cruz-Campa, J. L.; Buonassisi, T. and Peters, I. M. 'Roadmap for cost-effective, commercially-viable perovskite silicon tandems for the current and future PV market'. *Sustainable Energy & Fuels*, 2020, **4**, 852–862.

[24] Liu, X. K.; Xu, W.; Bai, S.; Jin, Y.; Wang, J.; Friend, R. H. and Gao, F. 'Metal halide perovskites for light-emitting diodes'. *Nature Materials*, 2020, 1–12.

[25] Quan, L. N.; Rand, B. P.; Friend, R. H.; Mhaisalkar, S. G.; Lee, T.-W. and Sargent, E. H. 'Perovskites for next-generation optical sources'. *Chemical Reviews*, 2019, **119**, 7444–7477.

[26] Boyd, C. C.; Cheacharoen, R.; Leijtens, T. and McGehee, M. D. 'Understanding degradation mechanisms and improving stability of perovskite photovoltaics'. *Chemical Reviews*, 2019, **119**, 3418–3451.

[27] Hoke, E. T.; Slotcavage, D. J.; Dohner, E. R.; Bowring, A. R.; Karunadasa, H. I. and McGehee, M. D. 'Reversible photo-induced trap formation in mixed-halide hybrid perovskites for photovoltaics'. *Chemical Science*, 2015, **6**, 613–617.

[28] Knight, A. J.; Wright, A. D.; Patel, J. B.; McMeekin, D. P.; Snaith, H. J.; Johnston, M. B. and Herz, L. M. 'Electronic traps and phase segregation in lead mixed-halide perovskite'. *ACS Energy Letters*, 2018, **4**, 75–84.

[29] Conings, B.; Drijkoningen, J.; Gauquelin, N.; Babayigit, A.; D'Haen, J.; D'Olieslaeger, L.; Ethirajan, A.; Verbeeck, J.; Manca, J.; Mosconi, E. *et al.* 'Intrinsic thermal instability of methylammonium lead trihalide perovskite'. *Advanced Energy Materials*, 2015, **5**, 1500477.

[30] Parrott, E. S.; Green, T.; Milot, R. L.; Johnston, M. B.; Snaith, H. J. and Herz, L. M. 'Interplay of structural and optoelectronic properties in formamidinium mixed tin-lead triiodide perovskites'. *Advanced Functional Materials*, 2018, **28**, 1802803.

[31] Milot, R. L.; Klug, M. T.; Davies, C. L.; Wang, Z.; Kraus, H.; Snaith, H. J.; Johnston, M. B. and Herz, L. M. 'The effects of doping density and temperature on the optoelectronic properties of formamidinium tin triiodide thin films'. *Advanced Materials*, 2018, **30**, 1804506.

[32] Savill, K. J.; Ulatowski, A. M. and Herz, L. M. 'Optoelectronic properties of tin–lead halide perovskites'. *ACS Energy Letters*, 2021, **13**, 2413–2426.

[33] Giustino, F. and Snaith, H. J. 'Toward lead-free perovskite solar cells'. *ACS Energy Letters*, 2016, **1**, 1233–1240.

[34] Flora, G.; Gupta, D. and Tiwari, A. 'Toxicity of lead: A review with recent updates'. *Interdisciplinary toxicology*, 2012, **5**, 47–58.

[35] Filip, M. R. and Giustino, F. 'The geometric blueprint of perovskites.' *Proceedings of the National Academy of Sciences of the United States of America*, 2018, **115**, 5397–5402.

[36] Buizza, L. R. V. and Herz, L. M. 'Polarons and charge localisation in metal-halide semiconductors for photovoltaic and light-emitting devices'. *Advanced Materials*, 2021, **33**, 2007057.

[37] Worku, M.; Xu, L. J.; Chaaban, M.; Ben-Akacha, A. and Ma, B. 'Optically pumped white light-emitting diodes based on metal halide perovskites and perovskite-related materials'. *APL Materials*, 2020, **8**, 10902.

[38] Seth, S. and Samanta, A. 'Photoluminescence of zero-dimensional perovskites and perovskite-related materials'. *Journal of Physical Chemistry Letters*, 2017, **9**, 176–183.

[39] Chen, Y.; Sun, Y.; Peng, J.; Tang, J.; Zheng, K. and Liang, Z. '2D Ruddlesden–Popper perovskites for optoelectronics'. *Advanced Materials*, 2018, **30**, 1703487.

[40] Rose, G.; Humboldt., A. von and Ehrenberg, C. G. 'Mineralogischgeognostiche reise nach dem Ural, dem Altai and dem Kaspische Meere, zweiter band'. *Verlag der Sanderschen Buchandlung*, 1842.

[41] Nayak, P. K.; Mahesh, S.; Snaith, H. J. and Cahen, D. 'Photovoltaic solar cell technologies: Analysing the state of the art'. *Nature Reviews Materials*, 2019, **4**, 269–285.

[42] McMeekin, D. P.; Sadoughi, G.; Rehman, W.; Eperon, G. E.; Saliba, M.; Horantner, M. T.; Haghighirad, A.; Sakai, N.; Korte, L.; Rech, B. *et al.* 'A mixed-cation lead halide perovskite absorber for tandem solar cells.' *Science*, 2016, **351**, 151–155.

[43] Noel, N. K.; Stranks, S. D.; Abate, A.; Wehrenfennig, C.; Guarnera, S.; Haghighirad, A.-A.; Sadhanala, A.; Eperon, G. E.; Pathak, S. K.; Johnston, M. B. *et al.* 'Lead-free organic–inorganic tin halide perovskites for photovoltaic applications'. *Energy Environ. Sci.*, 2014, **9**, 3061–3068.

[44] Protesescu, L.; Yakunin, S.; Bodnarchuk, M. I.; Krieg, F.; Caputo, R.; Hendon, C. H.; Yang, R. X.; Walsh, A. and Kovalenko, M. V. 'Nanocrystals of cesium lead halide perovskites ($CsPbX_3$, X = Cl, Br, and I): Novel optoelectronic materials showing bright emission with wide color gamut'. *Nano Letters*, 2015, **15**, 3692–3696.

[45] Goldschmidt, V. M. 'Die gesetze der krystallochemie'. *Naturwissenschaften 1926 14:21*, 1926, **14**, 477–485.

[46] Walsh, A. 'Principles of chemical bonding and band gap engineering in hybrid organic–inorganic halide perovskites'. *Journal of Physical Chemistry C*, 2015, **119**, 5755–5760.

[47] Johnston, M. B. and Herz, L. M. 'Hybrid perovskites for photovoltaics: charge-carrier recombination, diffusion, and radiative efficiencies'. *Accounts of Chemical Research*, 2016, **49**, 146–154.

[48] Herz, L. M. 'Charge-carrier dynamics in organic-inorganic metal halide perovskites'. *Annual Review of Physical Chemistry*, 2016, **67**, 65–89.

[49] Herz, L. M. 'Charge-carrier mobilities in metal halide perovskites: Fundamental mechanisms and limits'. *ACS Energy Letters*, 2017, **2**, 1539–1548.

[50] Wehrenfennig, C.; Eperon, G. E.; Johnston, M. B.; Snaith, H. J. and Herz, L. M. 'High charge carrier mobilities and lifetimes in organolead trihalide perovskites'. *Advanced Materials*, 2014, **26**, 1584–1589.

[51] Rehman, W.; Mcmeekin, D. P.; Patel, J. B.; Milot, R. L.; Johnston, M. B.; Snaith, H. J. and Herz, L. M. 'Photovoltaic mixed-cation lead mixed-halide perovskites: Links between crystallinity, photo-stability and electronic properties'. *Energy Environ. Sci.*, 2017, **10**, 361–369.

[52] Trimpl, M. J.; Wright, A. D.; Schutt, K.; Buizza, L. R. V.; Wang, Z.; Johnston, M. B.; Snaith, H. J.; Müller-Buschbaum, P. and Herz, L. M. 'Charge-carrier trapping and radiative recombination in metal halide perovskite semiconductors'. *Advanced Functional Materials*, 2020, **30**, 2004312.

[53] deQuilettes, D. W.; Frohna, K.; Emin, D.; Kirchartz, T.; Bulovic, V.; Ginger, D. S. and Stranks, S. D. 'Charge-carrier recombination in halide perovskites'. *Chemical Reviews*, 2019, **119**, 11007–11019.

[54] Stranks, S. D.; Eperon, G. E.; Grancini, G.; Menelaou, C.; Alcocer, M. J. P.; Leijtens, T.; Herz, L. M.; Petrozza, A. and Snaith, H. J. 'Electron-hole diffusion lengths exceeding 1 micrometer in an organometal trihalide perovskite absorber'. *Science*, 2013, **342**, 341–344.

[55] Buizza, L.; Crothers, T.; Wang, Z.; Patel, J.; Milot, R.; Snaith, H.; Johnston, M. and Herz, L. 'Charge-carrier dynamics, mobilities, and diffusion lengths of 2D–3D hybrid butylammonium–cesium–formamidinium lead halide perovskites'. *Advanced Functional Materials*, 2019, **29**.

[56] DeQuilettes, D. W.; Vorpahl, S. M.; Stranks, S. D.; Nagaoka, H.; Eperon, G. E.; Ziffer, M. E.; Snaith, H. J. and Ginger, D. S. 'Impact of microstructure on local carrier lifetime in perovskite solar cells.' *Science*, 2015, **348**, 683–6.

[57] De Wolf, S.; Holovsky, J.; Moon, S.-J.; Löper, P.; Niesen, B.; Ledinsky, M.; Haug, F.-J.; Yum, J.-H. and Ballif, C. 'Organometallic halide perovskites: Sharp optical absorption edge and its relation to photovoltaic performance'. *The Journal of Physical Chemistry Letters*, 2014, **5**, 1035–1039.

[58] Sadhanala, A.; Deschler, F.; Thomas, T. H.; Dutton, S. E.; Goedel, K. C.; Hanusch, F. C.; Lai, M. L.; Steiner, U.; Bein, T.; Docampo, P. *et al.* 'Preparation of single-phase films of $CH_3NH_3Pb(I_{1-x}Br_x)_3$ with sharp optical band edges'. *The Journal of Physical Chemistry Letters*, 2014, **5**, 2501–2505.

[59] Wright, A. D.; Verdi, C.; Milot, R. L.; Eperon, G. E.; Pérez-Osorio, M. A.; Snaith, H. J.; Giustino, F.; Johnston, M. B. and Herz, L. M. 'Electron-phonon coupling in hybrid lead halide perovskites'. *Nature Communications*, 2016, **7**, 11755.

[60] Kirchartz, T.; Markvart, T.; Rau, U. and Egger, D. A. 'Impact of small phonon energies on the charge-carrier lifetimes in metal-halide perovskites'. 2018, **9**, 939–946.

[61] Kim, H. S.; Lee, C. R.; Im, J. H.; Lee, K. B.; Moehl, T.; Marchioro, A.; Moon, S. J.; Humphry-Baker, R.; Yum, J. H.; Moser, J. E. *et al.* 'Lead iodide perovskite sensitized all-solid-state submicron thin film mesoscopic solar cell with efficiency exceeding 9%'. *Scientific Reports*, 2012, **2**, 591.

[62] Liu, M.; Johnston, M. B. and Snaith, H. J. 'Efficient planar heterojunction perovskite solar cells by vapour deposition'. *Nature*, 2013, **501**, 395–398.

[63] Brivio, F.; Walker, A. B. and Walsh, A. 'Structural and electronic properties of hybrid perovskites for high-efficiency thin-film photovoltaics from first-principles'. *APL Materials*, 2013, **1**, 042111.

[64] Umebayashi, T.; Asai, K.; Kondo, T. and Nakao, A. 'Electronic structures of lead iodide based low-dimensional crystals'. *Physical Review B*, 2003, **67**, 155405.

[65] Filip, M. R.; Eperon, G. E.; Snaith, H. J. and Giustino, F. 'Steric engineering of metal-halide perovskites with tunable optical band gaps'. *Nature Communications*, 2014, **5**, 5757.

[66] Nelson, J. *The physics of solar cells*. Imperial College Press, 2003.

[67] Davies, C. L.; Filip, M. R.; Patel, J. B.; Crothers, T. W.; Verdi, C.; Wright, A. D.; Milot, R. L.; Giustino, F.; Johnston, M. B. and Herz, L. M. 'Bimolecular recombination in methylammonium lead triiodide perovskite is an inverse absorption process'. *Nature Communications*, 2018, **9**, 293.

[68] Hall, R. N. 'Electron-hole recombination in germanium'. *Physical Review*, 1952, **87**, 387.

[69] Shockley, W. and Read, J. W. T. 'Statistics of the recombinations of holes and electrons'. *Physical Review*, 1952, **87**, 835.

[70] Rivas, A. and Ausin, V. 'Optically induced F-centre-interstitial recombination in γ-irradiated KCl'. *J. Phys. C : Solid State Phys*, 1977, **10**, 1089–1096.

[71] Hall, T. P. P.; Hughes, A. E. and Pooley, D. 'Optical studies of colour centres formed in KCI by electron-hole recombination'. *J. Phys. C : Solid State Phys*, 1976, **9**.

[72] Song, K. S. and Williams, R. T. *Self-trapped excitons*. Springer Berlin Heidelberg, 1993.

[73] Wright, A. D.; Buizza, L. R. V.; Savill, K. J.; Longo, G.; Snaith, H. J.; Johnston, M. B. and Herz, L. M. 'Ultrafast excited-state localization in $Cs_2AgBiBr_6$ double perovskite'. *Journal of Physical Chemistry Letters*, 2021, **12**.

[74] Zelewski, S. J.; Urban, J. M.; Surrente, A; Maude, D. K.; Kuc, A; Schade, L; Johnson, R. D.; Dollmann, M; Nayak, P. K.; Snaith, H. J. *et al.* 'Revealing the nature of photoluminescence emission in the metal-halide double perovskite $Cs_2AgBiBr_6$'. *J. Mater. Chem. C*, 2019, **7**, 8350–8356.

[75] Hoye, R. L. Z.; Eyre, L.; Wei, F.; Brivio, F.; Sadhanala, A.; Sun, S.; Li, W.; Zhang, K. H. L.; MacManus-Driscoll, J. L.; Bristowe, P. D. *et al.* 'Fundamental carrier lifetime exceeding 1 µs in $Cs_2AgBiBr_6$ double perovskite'. *Advanced Materials Interfaces*, 2018, **5**, 1800464.

[76] Slavney, A. H.; Hu, T.; Lindenberg, A. M. and Karunadasa, H. I. 'A bismuth-halide double perovskite with long carrier recombination lifetime for photovoltaic applications'. *The Journal of the America Chemical Society*, 2016, **7**, 2138–2141.

[77] Kentsch, R.; Scholz, M.; Horn, J.; Schlettwein, D.; Oum, K. and Lenzer, T. 'Exciton dynamics and electron–phonon coupling affect the photovoltaic performance of the $Cs_2AgBiBr_6$ double perovskite'. *The Journal of Physical Chemistry C*, 2018, **122**, 25940–25947.

[78] Volonakis, G.; Filip, M. R.; Haghighirad, A. A.; Sakai, N.; Wenger, B.; Snaith, H. J. and Giustino, F. 'Lead-free halide double perovskites via heterovalent substitution of noble metals'. *The Journal of Physical Chemistry Letters*, 2016, 1254–1259.

[79] Xiao, Z.; Meng, W.; Wang, J. and Yan, Y. 'Thermodynamic stability and defect chemistry of bismuth-based lead-free double perovskites'. *ChemSusChem*, 2016, **9**, 2628–2633.

[80] Sansom, H. C.; Whitehead, G. F.; Dyer, M. S.; Zanella, M.; Manning, T. D.; Pitcher, M. J.; Whittles, T. J.; Dhanak, V. R.; Alaria, J.; Claridge, J. B. *et al.* '$AgBiI_4$ as a lead-free solar absorber with potential application in photovoltaics'. *Chemistry of Materials*, 2017, **29**, 1538–1549.

[81] Iyoda, F.; Nishikubo, R.; Wakamiya, A. and Saeki, A. 'Ag-(Bi, Sb, In, Ga)-I solar cells: Impacts of elemental composition and additives on the charge carrier dynamics and crystal structures'. *ACS Applied Energy Materials*, 2020.

[82] Khazaee, M.; Sardashti, K.; Chung, C.-C.; Sun, J.-P.; Zhou, H.; Bergmann, E.; Dunlap-Shohl, W. A.; Han, Q.; Hill, I. G.; Jones, J. L. *et al.* 'Dual-source evaporation of silver bismuth iodide films for planar junction solar cells'. *Journal of Materials Chemistry A*, 2019, **7**, 2095–2105.

[83] Turkevych, I.; Kazaoui, S.; Ito, E.; Urano, T.; Yamada, K.; Tomiyasu, H.; Yamagishi, H.; Kondo, M. and Aramaki, S. 'Photovoltaic Rudorffites: Lead-Free Silver Bismuth Halides Alternative to Hybrid Lead Halide Perovskites'. *ChemSusChem*, 19 2017, **10**, 3754–3759.

[84] Sansom, H. C.; Longo, G.; Wright, A. D.; Buizza, L. R. V.; Zanella, M.; Gibbon, J. T.; Abda-Jalebi, M.; Pitcher, M. J.; Dyer, M. S.; Manning, T. D. *et al.* 'Highly absorbing lead-free semiconductor Cu_2AgBiI_6 for photovoltaic applications from the quaternary CuI−AgI−BiI_3 phase space'. *Journal of the American Chemical Society*, 2021, **143**, 3983–3992.

[85] Sansom, H. C.; Buizza, L. R. V.; Zanella, M.; Gibbon, J. T.; Pitcher, M. J.; Dyer, M. S.; Manning, T. D.; Dhanak, V. R.; Herz, L. M.; Snaith, H. J. *et al.* 'Chemical control of the dimensionality of the octahedral network of solar absorbers from the CuI-AgI-BiI_3 phase space by synthesis of 3D $CuAgBiI_5$'. 2021, **Under Review**.

[86] Buizza, L. R. V.; Wright, A. D.; Longo, G.; Sansom, H. C.; Xia, C. Q.; Rosseinsky, M. J.; Johnston, M. B.; Snaith, H. J. and Herz, L. M. 'Charge-carrier mobility and localization in semiconducting Cu_2AgBiI_6 for photovoltaic applications'. *ACS Energy Lett.*, 2021, **6**, 1729–1739.

[87] Buizza, L. R. V.; Sansom, H. C.; Wright, A. D.; Ulatowski, A. M.; Johnston, M. B.; Snaith, H. J. and Herz, L. M. 'Interplay of structure, charge-carrier localisation and dynamics in copper-silver-bismuth-halide semiconductors'. *Advanced Functional Materials*, 2021, **Accepted for Publication**.

[88] Fabini, D. H.; Seshadri, R. and Kanatzidis, M. G. 'The underappreciated lone pair in halide perovskites underpins their unusual properties'. *MRS Bulletin*, 2020, **45**, 467–477.

[89] Egger, D. A.; Bera, A.; Cahen, D.; Hodes, G.; Kirchartz, T.; Kronik, L.; Lovrincic, R.; Rappe, A. M.; Reichman, D. R. and Yaffe, O. 'What remains unexplained about the properties of halide perovskites?' *Advanced Materials*, 2018, **30**, 1800691.

[90] Whalley, L. D.; Skelton, J. M.; Frost, J. M. and Walsh, A. 'Phonon anharmonicity, lifetimes, and thermal transport in $CH_3NH_3PbI_3$ from many-body perturbation theory'. *Physical Review B*, 2016, **94**, 220301.

[91] Xiao, Z.; Meng, W.; Wang, J.; Mitzi, D. B. and Yan, Y. 'Searching for promising new perovskite-based photovoltaic absorbers: The importance of electronic dimensionality'. *Materials Horizons*, 2017, **4**, 206–216.

[92] Xiao, Z.; Song, Z. and Yan, Y. 'From lead halide perovskites to lead-free metal halide perovskites and perovskite derivatives'. *Advanced Materials*, 2019, **31**, 1803792.

[93] Zhao, X.-G.; Yang, D.; Ren, J.-C.; Sun, Y.; Xiao, Z. and Zhang, L. 'Rational design of halide double perovskites for optoelectronic applications'. *Joule*, 2018, **2**, 1662–1673.

[94] Filip, M. R.; Hillman, S.; Haghighirad, A. A.; Snaith, H. J. and Giustino, F. 'Band gaps of the lead-free halide double perovskites $Cs_2BiAgCl_6$ and $Cs_2BiAgBr_6$ from theory and experiment'. *The Journal of Physical Chemistry Letters*, 2016, **7**, 2579–2585.

[95] Shi, H. and Du, M. H. 'Discrete electronic bands in semiconductors and insulators: Potential high-light-yield scintillators'. *Physical Review Applied*, 2015, **3**, 054005.

[96] Volonakis, G.; Haghighirad, A. A.; Milot, R. L.; Sio, W. H.; Filip, M. R.; Wenger, B.; Johnston, M. B.; Herz, L. M.; Snaith, H. J. and Giustino, F. '$Cs_2InAgCl_6$: A new lead-free halide double perovskite with direct band gap'. *Journal of Physical Chemistry Letters*, 2017, **8**, 772–778.

[97] Wehrenfennig, C.; Liu, M.; Snaith, H. J.; Johnston, M. B. and Herz, L. M. 'Charge-carrier dynamics in vapour-deposited films of the organolead halide perovskite $CH_3NH_3PbI_{3-x}Cl_x$'. *Energy Environ. Sci.*, 2014, **7**, 2269–2275.

[98] Li, S.; Luo, J.; Liu, J. and Tang, J. 'Self-trapped excitons in all-inorganic halide perovskites: Fundamentals, status, and potential applications'. *The Journal of Physical Chemistry Letters*, 2019, **10**, 1999–2007.

[99] Smith, M. D. and Karunadasa, H. I. 'White-light emission from layered halide perovskites'. *Accounts of Chemical Research*, 2018, **51**, 619–627.

[100] Tsai, H.; Nie, W.; Blancon, J.-C.; Stoumpos, C. C.; Asadpour, R.; Harutyunyan, B.; Neukirch, A. J.; Verduzco, R.; Crochet, J. J.; Tretiak, S. *et al.* 'High-efficiency two-dimensional Ruddlesden-Popper perovskite solar cells'. *Nature*, 2016, **536**, 312–316.

[101] McCall, K. M.; Stoumpos, C. C.; Kostina, S. S.; Kanatzidis, M. G. and Wessels, B. W. 'Strong electron-phonon coupling and self-trapped excitons in the defect halide perovskites $A_3M_2I_9$ (A = Cs, Rb; M = Bi, Sb)'. *Chemistry of Materials*, 2017, **29**, 4129–4145.

[102] Benin, B. M.; Dirin, D. N.; Morad, V.; Wörle, M.; Yakunin, S.; Rainò, G.; Nazarenko, O.; Fischer, M.; Infante, I. and Kovalenko, M. V. 'Highly emissive self-trapped excitons in fully inorganic zero-dimensional tin halides'. *Angewandte Chemie International Edition*, 2018, **57**, 11329–11333.

[103] He, Y. and Galli, G. 'Perovskites for solar thermoelectric applications: A first principle study of $CH_3NH_3AI_3$ (A = Pb and Sn)'. *Chemistry of Materials*, 2014, **26**, 5394–5400.

[104] Saito, T.; Iwasaki, T.; Kurosawa, S.; Yoshikawa, A. and Den, T. 'BiI_3 single crystal for room-temperature gamma ray detectors'. *Nuclear Instruments and Methods in Physics Research Section A: Accelerators, Spectrometers, Detectors and Associated Equipment*, 2016, **806**, 395–400.

[105] Landau, L. D. 'On the motion of electrons in a crystal lattice'. *Physikalische Zeitschrift der Sowjetunion*, 1933, **3**, 644–5.

[106] Pekar, S. 'Local quantum states of electrons in an ideal ion crystal'. *Zh. Eksperim. i Teor. Fiz.*, 1946, **16**, 347.

[107] Holstein, T. 'Studies of polaron motion: Part II. The "small" polaron'. *Annals of Physics*, 1959, **8**, 343–389.

[108] Feynman, R. P. 'Slow electrons in a polar crystal'. *Physical Review*, 1955, **97**, 660–665.

[109] Franchini, C.; Reticcioli, M.; Setvin, M. and Diebold, U. 'Polarons in materials'. *Nature Reviews Materials 2021 6:7*, 7 2021, **6**, 560–586.

[110] Wang, Z.; Lin, Q.; Chmiel, F. P.; Sakai, N.; Herz, L. M. and Snaith, H. J. 'Efficient ambient-air-stable solar cells with 2D-3D heterostructured butylammonium-caesium-formamidinium lead halide perovskites'. *Nature Energy*, 2017, **2**, 17135.

[111] Frost, J. M. 'Calculating polaron mobility in halide perovskites'. *Physical Review B*, 2017, **96**, 195202.

[112] Sendner, M.; Nayak, P. K.; Egger, D. A.; Beck, S.; Müller, C.; Epding, B.; Kowalsky, W.; Kronik, L.; Snaith, H. J.; Pucci, A. *et al.* 'Optical phonons in methylammonium lead halide perovskites and implications for charge transport'. *Materials Horizons*, 2016, **3**, 613–620.

[113] Munson, K. T.; Swartzfager, J. R. and Asbury, J. B. 'Lattice anharmonicity: A double-edged sword for 3D perovskite-based optoelectronics'. *ACS Energy Letters*, 2019, **4**, 1888–1897.

[114] Meggiolaro, D.; Ambrosio, F.; Mosconi, E.; Mahata, A. and De Angelis, F. 'Polarons in metal halide perovskites'. *Advanced Energy Materials*, 2020, **10**, 1902748.

[115] McClure, E. T.; Ball, M. R.; Windl, W. and Woodward, P. M. 'Cs_2AgBiX_6 (X = Br, Cl): New visible light absorbing, lead-free halide perovskite semiconductors'. *Chemistry of Materials*, 2016, **28**, 1348–1354.

[116] Koh, T. M.; Shanmugam, V.; Schlipf, J.; Oesinghaus, L.; Müller-Buschbaum, P.; Ramakrishnan, N.; Swamy, V.; Mathews, N.; Boix, P. P. and Mhaisalkar, S. G. 'Nanostructuring mixed-dimensional perovskites: A route toward tunable, efficient photovoltaics'. *Advanced Materials*, 2016, **28**, 3653–3661.

[117] Kang, B. and Biswas, K. 'Exploring polaronic, excitonic structures and luminescence in Cs_4PbBr_6/$CsPbBr_3$'. *The Journal of Physical Chemistry Letters*, 2018, **9**, 830–836.

[118] Schlipf, M.; Poncé, S. and Giustino, F. 'Carrier lifetimes and polaronic mass enhancement in the hybrid halide perovskite $CH_3NH_3PbI_3$ from multiphonon Fröhlich coupling'. *Physical Review Letters*, 2018, **121**, 086402.

[119] Poncé, S.; Schlipf, M. and Giustino, F. 'Origin of low carrier mobilities in halide perovskites'. *ACS Energy Letters*, 2019, **4**, 456–463.

[120] Williams, R. and Song, K. 'The self-trapped exciton'. *Journal of Physics and Chemistry of Solids*, 1990, **51**, 679–716.

[121] Cortecchia, D.; Yin, J.; Petrozza, A. and Soci, C. 'White light emission in low-dimensional perovskites'. *Journal of Materials Chemistry C*, 2019, **7**, 4956–4969.

[122] Dotzler, C.; Williams, G. V. M.; Edgar, A.; Schweizer, S.; Henke, B.; Spaeth, J. M.; Bittar, A.; Hamlin, J. and Dunford, C. 'The effect of X-ray, γ-ray, and UV radiations on the optical properties of $RbCdF_3$:Mn^{2+}'. *Journal of Applied Physics*, 2006, **100**, 033102.

[123] Kim, Y.; Kim, J. S. and Lee, T. 'Strategies to improve luminescence efficiency of metal-halide perovskites and light-emitting diodes'. *Advanced Materials*, 2019, **31**, 1804595.

[124] Le, Q. V.; Jang, H. W. and Kim, S. Y. 'Recent advances toward high-efficiency halide perovskite light-emitting diodes: Review and perspective'. *Small Methods*, 2018, **2**, 1700419.

[125] Wei, H. and Huang, J. 'Halide lead perovskites for ionizing radiation detection'. *Nature Communications*, 2019, **10**, 1066–undefined.

[126] Kakavelakis, G.; Gedda, M.; Panagiotopoulos, A.; Kymakis, E.; Anthopoulos, T. D. and Petridis, K. 'Metal halide perovskites for high-energy radiation detection'. *Advanced Science*, 2020, 2002098–undefined.

[127] Landau, L. D. and Pekar, S. I. 'Effective mass of a polaron'. *Translated and reprinted from Zh. Eksp. Teor. Fiz*, 1948, **18**, 419–423.

[128] Fröhlich, H.; Pelzer, H. and Zienau, S. 'XX. Properties of slow electrons in polar materials'. *The London, Edinburgh, and Dublin Philosophical Magazine and Journal of Science*, 1950, **41**, 221–242.

[129] Fröhlich, H. 'Electrons in lattice fields'. *Advances in Physics*, 1954, **3**, 325–361.

[130] Feynman, R. P.; Hellwarth, R. W.; Iddings, C. K. and Platzman, P. M. 'Mobility of slow electrons in a polar crystal'. *Physical Review*, 1962, **127**, 1004–1017.

[131] Ōsaka, Y. 'Polaron state at a finite temperature'. *Progress of Theoretical Physics*, 1959, **22**, 437–446.

[132] Ōsaka, Y. 'Theory of polaron mobility'. *Progress of Theoretical Physics*, 1961, **25**, 517–536.

[133] Marshall, J. T. and Mills, L. R. 'Second-order correction to Feynman's path-integral calculation of the polaron self-energy'. *Physical Review B*, 1970, **2**, 3143–3146.

[134] Devreese, J. T. and Alexandrov, A. S. 'Fröhlich polaron and bipolaron: recent developments'. *Reports on Progress in Physics*, 2009, **72**, 066501.

[135] Herz, L. M. 'How lattice dynamics moderate the electronic properties of metal-halide perovskites'. *Journal of Physical Chemistry Letters*, 2018, **9**, 6853–6863.

[136] Hellwarth, R. W. and Biaggio, I. 'Mobility of an electron in a multimode polar lattice'. *Physical Review B*, 1999, **60**, 299–307.

[137] Yaffe, O.; Guo, Y.; Tan, L. Z.; Egger, D. A.; Hull, T.; Stoumpos, C. C.; Zheng, F.; Heinz, T. F.; Kronik, L.; Kanatzidis, M. G. *et al.* 'Local polar fluctuations in lead halide perovskite crystals'. *Phys. Rev. Lett.*, 2017, **118**, 136001.

[138] Mayers, M. Z.; Tan, L. Z.; Egger, D. A.; Rappe, A. M. and Reichman, D. R. 'How lattice and charge fluctuations control carrier dynamics in halide perovskites'. *Nano Letters*, 2018, **18**, 8041–8046.

[139] Zhao, D.; Skelton, J. M.; Hu, H.; vorakiat, C. La-o; Zhu, J.-X.; Marcus, R. A.; Michel-Beyerle, M.-E.; Lam, Y. M.; Walsh, A. and Chia, E. E. M. 'Low-frequency optical phonon modes and carrier mobility in the halide perovskite $CH_3NH_3PbBr_3$ using terahertz time-domain spectroscopy'. *Applied Physics Letters*, 2017, **111**, 201903.

[140] Lan, Y.; Dringoli, B. J.; Valverde-Chávez, D. A.; Ponseca, C. S.; Sutton, M.; He, Y.; Kanatzidis, M. G. and Cooke, D. G. 'Ultrafast correlated charge and lattice motion in a hybrid metal halide perovskite'. *Science Advances*, 2019, **5**, eaaw5558.

[141] Batignani, G.; Fumero, G.; Srimath Kandada, A. R.; Cerullo, G.; Gandini, M.; Ferrante, C.; Petrozza, A. and Scopigno, T. 'Probing femtosecond lattice displacement upon photo-carrier generation in lead halide perovskite'. *Nature Communications*, 2018, **9**, 1971.

[142] Puppin, M; Polishchuk, S; Colonna, N; Crepaldi, A; Dirin, D. N.; Nazarenko, O; De Gennaro, R; Gatti, G; Roth, S; Barillot, T *et al.* 'Evidence of large polarons in photoemission band mapping of the perovskite semiconductor $CsPbBr_3$'. *Physical Review Letters*, 2019, **124**, 206402.

[143] Neutzner, S.; Thouin, F.; Cortecchia, D.; Petrozza, A.; Silva, C. and Kandada, A. R. S. 'Exciton-polaron spectral structures in two-dimensional hybrid lead-halide perovskites'. *Physical Review Materials*, 2018, **2**, 064605.

[144] Manna, D.; Kangsabanik, J.; Das, T. K.; Das, D.; Alam, A. and Yella, A. 'Lattice dynamics and electron–phonon coupling in lead-free $Cs_2AgIn_{1-x}Bi_xCl_6$ double perovskite nanocrystals'. *The Journal of Physical Chemistry Letters*, 2020, **11**, 2113–2120.

[145] Steele, J. A.; Puech, P.; Keshavarz, M.; Yang, R.; Banerjee, S.; Debroye, E.; Kim, C. W.; Yuan, H.; Heo, N. H.; Vanacken, J. *et al.* 'Giant electron-phonon coupling and deep conduction band resonance in metal halide double perovskite'. *ACS Nano*, 2018, **12**, 8081–8090.

[146] Toyozawa, Y. 'Self-trapping of an electron by the acoustical mode of lattice vibration. I'. *Progress of Theoretical Physics*, 1961, **26**, 29–44.

[147] Toyozawa, Y. 'A proposed model of excitonic mechanism for defect formation in alkali halides'. *Journal of the Physical Society of Japan*, 1978, **44**, 482–488.

[148] Tasker, P. and Stoneham, A. 'An appraisal of the molecular model for the V_k centre'. *Journal of Physics and Chemistry of Solids*, 1977, **38**, 1185–1189.

[149] Stoneham, A. M.; Gavartin, J.; Shluger, A. L.; Kimmel, A. V.; Mũoz Ramo, D.; Rønnow, H. M.; Aeppli, G. and Renner, C. 'Trapping, self-trapping and the polaron family'. *Journal of Physics Condensed Matter*, 2007, **19**, 255208.

[150] Bridges, F; Daviesl; G; Robertson, J and Stoneham, A. M. 'The spectroscopy of crystal defects: a compendium of defect nomenclature'. *J. Phys.: Condens. Matter*, 1990, **2**, 2875–2928.

[151] Sio, W. H.; Verdi, C.; Poncé, S. and Giustino, F. 'Ab initio theory of polarons: Formalism and applications'. *Physical Review B*, 2019, **99**, 235139.

[152] Emin, D. and Holstein, T. 'Adiabatic theory of an electron in a deformable continuum'. *Physical Review Letters*, 1976, **36**, 323–326.

[153] Kabanov, V. V. and Mashtakov, O. Y. 'Electron localization with and without barrier formation'. *Physical Review B*, 1993, **47**, 6060–6064.

[154] Mott, N. F. and Stoneham, A. M. 'The lifetime of electrons, holes and excitons before self-trapping'. *J. Phys. C: Solid State Phys*, 1977, **10**, 3391.

[155] Unuma, Y.; Masumoto, Y.; Shionoya, S. and Nishimura, H. 'Dynamical aspects of self-trapping of 1s Excitons in RbI and KI'. *Journal of the Physical Society of Japan*, 1983, **52**, 4277–4282.

[156] Morrissey, F. X.; Mance, J. G.; Van Pelt, A. D. and Dexheimer, S. L. 'Femtosecond dynamics of exciton localization: self-trapping from the small to the large polaron limit'. *Journal of Physics: Condensed Matter*, 2013, **25**, 144204.

[157] Tomimoto, S.; Nansei, H.; Saito, S.; Suemoto, T.; Takeda, J. and Kurita, S. 'Femtosecond dynamics of the exciton self-trapping process in a quasi-one-dimensional halogen-bridged platinum complex'. *Physical Review Letters*, 1998, **81**, 417–420.

[158] Giustino, F. 'Electron-phonon interactions from first principles'. *Reviews of Modern Physics*, 2017, **89**, 015003.

[159] Sio, W. H.; Verdi, C.; Poncé, S. and Giustino, F. 'Polarons from first principles, without supercells'. *Physical Review Letters*, 2019, **122**, 246403.

[160] Lin, H.; Zhou, C.; Tian, Y.; Siegrist, T. and Ma, B. 'Low-dimensional organometal halide perovskites'. *ACS Energy Letters*, 2017, **3**, 54–62.

[161] Yin, J.; Li, H.; Cortecchia, D.; Soci, C. and Brédas, J.-L. 'Excitonic and polaronic properties of 2D hybrid organic–inorganic perovskites'. *ACS Energy Letters*, 2017, **2**, 417–423.

[162] Srimath Kandada, A. R. and Silva, C. 'Exciton polarons in two-dimensional hybrid metal-halide perovskites'. *The Journal of Physical Chemistry Letters*, 2020, **11**, 3173–3184.

[163] Maughan, A. E.; Ganose, A. M.; Candia, A. M.; Granger, J. T.; Scanlon, D. O. and Neilson, J. R. 'Anharmonicity and octahedral tilting in hybrid vacancy-ordered double perovskites'. *Chemistry of Materials*, 2018, **30**, 472–483.

[164] Maughan, A. E.; Ganose, A. M.; Almaker, M. A.; Scanlon, D. O. and Neilson, J. R. 'Tolerance factor and cooperative tilting effects in vacancy-ordered double perovskite halides'. *Chemistry of Materials*, 2018, **30**, 3909–3919.

[165] 'Alternative Lone-Pair ns2-Cation-Based Semiconductors beyond Lead Halide Perovskites for Optoelectronic Applications'. *Advanced Materials*, 32 2021, **33**, 2008574.

[166] Ganose, A. M.; Savory, C. N. and Scanlon, D. O. 'Beyond methylammonium lead iodide: prospects for the emergent field of ns2 containing solar absorbers'. *Chemical Communications*, 1 2016, **53**, 20–44.

[167] Yu, P. Y. and Cardona, M. *Fundamentals of semiconductors : physics and materials properties*. Springer: Heidelberg Dordrecht London New York, 2010.

[168] Zhao, T.; Shi, W.; Xi, J.; Wang, D. and Shuai, Z. 'Intrinsic and extrinsic charge transport in $CH_3NH_3PbI_3$ perovskites predicted from first-principles'. *Scientific Reports*, 2016, **6**, 19968.

[169] Munson, K. T.; Kennehan, E. R.; Doucette, G. S. and Asbury, J. B. 'Dynamic disorder dominates delocalization, transport, and recombination in halide perovskites'. *Chem*, 2018, **4**, 2826–2843.

[170] Kojima, A.; Teshima, K.; Shirai, Y. and Miyasaka, T. 'Organometal halide perovskites as visible-light sensitizers for photovoltaic cells'. *J Am Chem Soc*, 2009, **131**, 6050.

[171] Baikie, T.; Fang, Y.; Kadro, J. M.; Schreyer, M.; Wei, F.; Mhaisalkar, S. G.; Graetzel, M. and White, T. J. 'Synthesis and crystal chemistry of the hybrid perovskite $(CH_3NH_3)PbI_3$ for solid-state sensitised solar cell applications'. *Journal of Materials Chemistry A*, 2013, **1**, 5628.

[172] Gehrmann, C. and Egger, D. A. 'Dynamic shortening of disorder potentials in anharmonic halide perovskites'. *Nature Communications*, 2019, **10**, 3141.

[173] Mahata, A.; Meggiolaro, D. and De Angelis, F. 'From large to small polarons in lead, tin, and mixed lead–tin halide perovskites'. *The Journal of Physical Chemistry Letters*, 2019, **10**, 1790–1798.

[174] Milot, R. L.; Eperon, G. E.; Snaith, H. J.; Johnston, M. B. and Herz, L. M. 'Temperature-dependent charge-carrier dynamics in $CH_3NH_3PbI_3$ perovskite thin films'. *Advanced Functional Materials*, 2015, **25**, 6218–6227.

[175] Davies, C. L.; Borchert, J.; Xia, C. Q.; Milot, R. L.; Kraus, H.; Johnston, M. B. and Herz, L. M. 'Impact of the organic cation on the optoelectronic properties of formamidinium lead triiodide'. *The Journal of Physical Chemistry Letters*, 2018, **9**, 4502–4511.

[176] Neukirch, A. J.; Nie, W.; Blancon, J.-C.; Appavoo, K.; Tsai, H.; Sfeir, M. Y.; Katan, C.; Pedesseau, L.; Even, J.; Crochet, J. J. *et al.* 'Polaron stabilization by cooperative lattice distortion and cation rotations in hybrid perovskite materials'. *Nano Letters*, 2016, **16**, 3809–3816.

[177] Neukirch, A. J.; Abate, I. I.; Zhou, L.; Nie, W.; Tsai, H.; Pedesseau, L.; Even, J.; Crochet, J. J.; Mohite, A. D.; Katan, C. *et al.* 'Geometry distortion and small polaron binding energy changes with ionic substitution in halide perovskites'. *The Journal of Physical Chemistry Letters*, 2018, **9**, 7130–7136.

[178] Bretschneider, S. A.; Ivanov, I.; Wang, H. I.; Miyata, K.; Zhu, X. and Bonn, M. 'Quantifying polaron formation and charge carrier cooling in lead-iodide perovskites'. *Advanced Materials*, 2018, **30**, 1707312.

[179] Munson, K. T.; Swartzfager, J. R.; Gan, J. and Asbury, J. B. 'Does dipolar motion of organic cations affect polaron dynamics and bimolecular recombination in halide perovskites?' *The Journal of Physical Chemistry Letters*, 2020, **11**, 3166–3172.

[180] Pérez-Osorio, M. A.; Milot, R. L.; Filip, M. R.; Patel, J. B.; Herz, L. M.; Johnston, M. B. and Giustino, F. 'Vibrational properties of the organic-inorganic halide perovskite $CH_3NH_3PbI_3$ from theory and experiment: Factor group analysis, first-principles calculations, and low-temperature infrared spectra'. *The Journal of Physical Chemistry C*, 2015, **119**, 25703–25718.

[181] Filippetti, A.; Mattoni, A.; Caddeo, C.; Saba, M. I. and Delugas, P. 'Low electron-polar optical phonon scattering as a fundamental aspect of carrier mobility in methylammonium lead halide $CH_3NH_3PbI_3$ perovskites'. *Physical Chemistry Chemical Physics*, 2016, **18**, 15352–15362.

[182] Savill, K. J.; Ulatowski, A. M.; Farrar, M. D.; Johnston, M. B.; Snaith, H. J. and Herz, L. M. 'Impact of tin fluoride additive on the properties of mixed tin-lead iodide perovskite semiconductors'. *Advanced Functional Materials*, 2020, 2005594.

[183] Klug, M. T.; Milot, R. L.; Patel, J.; Green, T.; Sansom, H. C.; Farrar, M.; Ramadan, A. J.; Martani, S.; Wang, Z.; Wenger, B. *et al.* 'Metal composition influences optoelectronic quality in mixed-metal lead-tin triiodide perovskite solar absorbers'. *Energy & Environmental Science*, 2020, **13**, 1776–1787.

[184] Kahmann, S.; Shao, S. and Loi, M. A. 'Cooling, scattering, and recombination — The role of the material quality for the physics of tin halide perovskites'. *Advanced Functional Materials*, 2019, **29**, 1902963.

[185] Cinquanta, E.; Meggiolaro, D.; Motti, S. G.; Gandini, M.; Alcocer, M. J. P.; Akkerman, Q. A.; Vozzi, C.; Manna, L.; De Angelis, F.; Petrozza, A. *et al.* 'Ultrafast THz probe of photoinduced polarons in lead-halide perovskites'. *Physical Review Letters*, 2019, **122**, 166601.

[186] Motti, S. G.; Krieg, F.; Ramadan, A. J.; Patel, J. B.; Snaith, H. J.; Kovalenko, M. V.; Johnston, M. B. and Herz, L. M. '$CsPbBr_3$ nanocrystal films: Deviations from bulk vibrational and optoelectronic properties'. *Advanced Functional Materials*, 2020, 1909904.

[187] Zhao, Q.; Hazarika, A.; Schelhas, L. T.; Liu, J.; Gaulding, E. A.; Li, G.; Zhang, M.; Toney, M. F.; Sercel, P. C. and Luther, J. M. 'Size-dependent lattice structure and confinement properties in $CsPbI_3$ perovskite nanocrystals: Negative surface energy for stabilization'. *ACS Energy Letters*, 2020, **5**, 238–247.

[188] Boehme, S. C.; Brinck, S. ten; Maes, J.; Yazdani, N.; Zapata, F.; Chen, K.; Wood, V.; Hodgkiss, J. M.; Hens, Z.; Geiregat, P. *et al.* 'Phonon-mediated and weakly size-dependent electron and hole cooling in $CsPbBr_3$ nanocrystals revealed by atomistic simulations and ultrafast spectroscopy'. *Nano Letters*, 2020, **20**, 1819–1829.

[189] Zheng, K.; Abdellah, M.; Zhu, Q.; Kong, Q.; Jennings, G.; Kurtz, C. A.; Messing, M. E.; Niu, Y.; Gosztola, D. J.; Al-Marri, M. J. *et al.* 'Direct experimental evidence for photoinduced strong-coupling polarons in organolead halide perovskite nanoparticles'. *The Journal of Physical Chemistry Letters*, 2016, **7**, 4535–4539.

[190] Liu, C.; Tsai, H.; Nie, W.; Gosztola, D. J. and Zhang, X. 'Direct spectroscopic observation of the hole polaron in lead halide perovskites'. *The journal of physical chemistry letters*, 2020, **11**, 6256–6261.

[191] Ambrosio, F.; Meggiolaro, D.; Mosconi, E. and De Angelis, F. 'Charge localization, stabilization, and hopping in lead halide perovskites: Competition between polaron stabilization and cation disorder'. *ACS Energy Letters*, 2019, **4**, 2013–2020.

[192] Iaru, C. M.; Geuchies, J. J.; Koenraad, P. M.; Vanmaekelbergh, D. and Silov, A. Y. 'Strong carrier-phonon coupling in lead halide perovskite nanocrystals'. *ACS Nano*, 2017, **11**, 11024–11030.

[193] Yang, L.; Wei, K.; Xu, Z.; Li, F.; Chen, R.; Zheng, X.; Cheng, X. and Jiang, T. 'Nonlinear absorption and temperature-dependent fluorescence of perovskite $FAPbBr_3$ nanocrystal'. *Optics Letters*, 2018, **43**, 122.

[194] Li, J.; Yuan, X.; Jing, P.; Li, J.; Wei, M.; Hua, J.; Zhao, J. and Tian, L. 'Temperature-dependent photoluminescence of inorganic perovskite nanocrystal films'. *RSC Advances*, 2016, **6**, 78311–78316.

[195] Wright, A. D.; Volonakis, G.; Borchert, J.; Davies, C. L.; Giustino, F.; Johnston, M. B. and Herz, L. M. 'Intrinsic quantum confinement in formamidinium lead triiodide perovskite'. *Nature Materials*, 2020, **19**, 1201 –1206.

[196] Hutter, E. M.; Gélvez-Rueda, M. C.; Bartesaghi, D.; Grozema, F. C. and Savenije, T. J. 'Band-like charge transport in $Cs_2AgBiBr_6$ and mixed antimony–bismuth $Cs_2AgBi_{1-x}Sb_xBr_6$ halide double perovskites'. *ACS Omega*, 2018, **3**, 11655–11662.

[197] Sharma, M.; Yangui, A.; Whiteside, V. R.; Sellers, I. R.; Han, D.; Chen, S.; Du, M.-H. and Saparov, B. '$Rb_4Ag_2BiBr_9$: A lead-free bisible light absorbing halide semiconductor with improved stability'. *Inorganic Chemistry*, 2019, **58**, 4446–4455.

[198] Luo, J.; Wang, X.; Li, S.; Liu, J.; Guo, Y.; Niu, G.; Yao, L.; Fu, Y.; Gao, L.; Dong, Q. *et al.* 'Efficient and stable emission of warm-white light from lead-free halide double perovskites'. *Nature*, 2018, **563**, 541–545.

[199] Zeng, R.; Zhang, L.; Xue, Y.; Ke, B.; Zhao, Z.; Huang, D.; Wei, Q.; Zhou, W. and Zou, B. 'Highly efficient blue emission from self-trapped excitons in stable Sb^{3+}-doped $Cs_2NaInCl_6$ double perovskites'. *The Journal of Physical Chemistry Letters*, 2020, **11**, 2053–2061.

[200] Yang, B.; Hong, F.; Chen, J.; Tang, Y.; Yang, L.; Sang, Y.; Xia, X.; Guo, J.; He, H.; Yang, S. *et al.* 'Colloidal synthesis and charge-carrier dynamics of $Cs_2AgSb_{1-y}Bi_yX_6$ (X: Br, Cl; $0 \leq y \leq 1$) double perovskite nanocrystals'. *Angewandte Chemie International Edition*, 2019, **58**, 2278–2283.

[201] Connor, B. A.; Leppert, L.; Smith, M. D.; Neaton, J. B. and Karunadasa, H. I. 'Layered halide double perovskites: Dimensional reduction of $Cs_2AgBiBr_6$'. *Journal of the American Chemical Society*, 2018, **140**, 5235–5240.

[202] Smith, I. C.; Hoke, E. T.; Solis-Ibarra, D.; McGehee, M. D. and Karunadasa, H. I. 'A layered hybrid perovskite solar-cell absorber with enhanced moisture stability'. *Angewandte Chemie International Edition*, 2014, **53**, 11232–11235.

[203] Hu, T.; Smith, M. D.; Dohner, E. R.; Sher, M.-J.; Wu, X.; Trinh, M. T.; Fisher, A.; Corbett, J.; Zhu, X.-Y.; Karunadasa, H. I. *et al.* 'Mechanism for broadband white-light emission from two-dimensional (110) hybrid perovskites'. *The Journal of Physical Chemistry Letters*, 2016, **7**, 2258–2263.

[204] Thouin, F.; Valverde-Chávez, D. A.; Quarti, C.; Cortecchia, D.; Bargigia, I.; Beljonne, D.; Petrozza, A.; Silva, C. and Kandada, A. R. S. 'Phonon coherences reveal the polaronic character of excitons in two-dimensional lead halide perovskites'. *Nature Materials*, 2019, **18**, 349–356.

[205] Milot, R. L.; Sutton, R. J.; Eperon, G. E.; Haghighirad, A. A.; Hardigree, J. M.; Miranda, L.; Snaith, H. J.; Johnston, M. B. and Herz, L. M. 'Charge-carrier dynamics in 2D hybrid metal-halide perovskites'. *Nano Letters*, 2016, **16**, 7001–7007.

[206] Yangui, A.; Garrot, D.; Lauret, J. S.; Lusson, A.; Bouchez, G.; Deleporte, E.; Pillet, S.; Bendeif, E. E.; Castro, M.; Triki, S. *et al.* 'Optical investigation of broadband white-light emission in self-assembled organic-inorganic perovskite $(C_6H_{11}NH_3)_2PbBr_4$'. *The Journal of Physical Chemistry C*, 2015, **119**, 23638–23647.

[207] Dohner, E. R.; Hoke, E. T. and Karunadasa, H. I. 'Self-assembly of broadband white-light emitters'. *Journal of the American Chemical Society*, 2014, **136**, 1718–1721.

[208] Dohner, E. R.; Jaffe, A.; Bradshaw, L. R. and Karunadasa, H. I. 'Intrinsic white-light emission from layered hybrid perovskites'. *Journal of the American Chemical Society*, 2014, **136**, 13154–13157.

[209] Cortecchia, D.; Yin, J.; Bruno, A.; Lo, S.-Z. A.; Gurzadyan, G. G.; Mhaisalkar, S.; Brédas, J.-L. and Soci, C. 'Polaron self-localization in white-light emitting hybrid perovskites'. *Journal of Materials Chemistry C*, 2017, **5**, 2771–2780.

[210] Luo, B.; Liang, D.; Sun, S.; Xiao, Y.; Lian, X.; Li, X.; Li, M.-D.; Huang, X.-C. and Zhang, J. Z. 'Breaking forbidden transitions for emission of self-trapped excitons in two dimensional $(F_2CHCH_2NH_3)_2CdBr_4$ perovskite through Pb alloying'. *The Journal of Physical Chemistry Letters*, 2020, **11**, 199–205.

[211] Urban, J. M.; Chehade, G.; Dyksik, M.; Menahem, M.; Surrente, A.; Trippé-Allard, G.; Maude, D. K.; Garrot, D.; Yaffe, O.; Deleporte, E. *et al.* 'Revealing excitonic phonon coupling in $(PEA)_2(MA)_{n-1}Pb_nI_{3n+1}$ 2D layered perovskites'. *Journal of Physical Chemistry Letters*, 2020, **11**, 5830–5835.

[212] Dyksik, M.; Duim, H.; Zhu, X.; Yang, Z.; Gen, M.; Kohama, Y.; Adjokatse, S.; Maude, D. K.; Loi, M. A.; Egger, D. A. *et al.* 'Broad tunability of carrier effective masses in two-dimensional halide perovskites'. *ACS Energy Letters*, 2020, 3609–3616.

[213] Thouin, F.; Srimath Kandada, A. R.; Valverde-Chávez, D. A.; Cortecchia, D.; Bargigia, I.; Petrozza, A.; Yang, X.; Bittner, E. R. and Silva, C. 'Electron–phonon couplings inherent in polarons drive exciton dynamics in two-dimensional metal-halide perovskites'. *Chemistry of Materials*, 2019, **31**, 7085–7091.

[214] Seitz, M.; Magdaleno, A. J.; Alcázar-Cano, N.; Meléndez, M.; Lubbers, T. J.; Walraven, S. W.; Pakdel, S.; Prada, E.; Delgado-Buscalioni, R. and Prins, F. 'Exciton diffusion in two-dimensional metal-halide perovskites'. *Nature Communications*, 2020, **11**, 2035.

[215] Esmaielpour, H.; Whiteside, V. R.; Sourabh, S.; Eperon, G. E.; Precht, J. T.; Beard, M. C.; Lu, H.; Durant, B. K. and Sellers, I. R. 'Role of exciton binding energy on LO phonon broadening and polaron formation in $(BA)_2PbI_4$ Ruddlesden-Popper films'. *Journal of Physical Chemistry C*, 2020, **124**, 9496–9505.

[216] Baranowski, M. and Plochocka, P. 'Excitons in metal-halide perovskites'. *Advanced Energy Materials*, 2020, 1903659.

[217] Straus, D. B.; Parra, S. H.; Iotov, N.; Gebhardt, J.; Rappe, A. M.; Subotnik, J. E.; Kikkawa, J. M. and Kagan, C. R. 'Direct observation of electron-phonon coupling and slow vibrational relaxation in organic-inorganic hybrid perovskites'. *Journal of the American Chemical Society*, 2016, **138**, 13798–13801.

[218] Smith, M. D.; Connor, B. A. and Karunadasa, H. I. 'Tuning the luminescence of layered halide perovskites'. *Chemical Reviews*, 2019, **119**, 3104–3139.

[219] Kahmann, S.; Tekelenburg, E. K.; Duim, H.; Kamminga, M. E. and Loi, M. A. 'Extrinsic nature of the broad photoluminescence in lead iodide-based Ruddlesden–Popper perovskites'. *Nature Communications*, 2020, **11**, 1–8.

[220] Knutson, J. L.; Martin, J. D. and Mitzi, D. B. 'Tuning the band gap in hybrid tin iodide perovskite semiconductors using structural templating'. 2005, **44**, 4699–4705.

[221] Li, J.; Wang, J.; Ma, J.; Shen, H.; Li, L.; Duan, X. and Li, D. 'Self-trapped state enabled filterless narrowband photodetections in 2D layered perovskite single crystals'. *Nature Communications*, 2019, **10**, 806.

[222] Birowosuto, M. D.; Cortecchia, D.; Drozdowski, W.; Brylew, K.; Lachmanski, W.; Bruno, A. and Soci, C. 'X-ray scintillation in lead halide perovskite crystals'. *Scientific Reports*, 2016, **6**, 37254.

[223] Zhou, C.; Tian, Y.; Yuan, Z.; Lin, H.; Chen, B.; Clark, R.; Dilbeck, T.; Zhou, Y.; Hurley, J.; Neu, J. *et al.* 'Highly efficient broadband yellow phosphor based on zero-dimensional tin mixed-halide perovskite'. *ACS Applied Materials and Interfaces*, 2017, **9**, 44579–44583.

[224] Lewis, J. T.; Kolopus, J. L.; Sonder, E. and Abraham, M. M. 'Reorientation and motion of the self-trapped hole in $KMgF_3$'. *Physical Review B*, 1973, **7**, 810–818.

[225] Maughan, A. E.; Ganose, A. M.; Scanlon, D. O. and Neilson, J. R. 'Perspectives and design principles of vacancy-ordered double perovskite halide semiconductors'. *Chemistry of Materials*, 2019, **31**, 1184–1195.

[226] Saparov, B.; Hong, F.; Sun, J. P.; Duan, H. S.; Meng, W.; Cameron, S.; Hill, I. G.; Yan, Y. and Mitzi, D. B. 'Thin-film preparation and characterization of $Cs_3Sb_2I_9$: A lead-free layered perovskite semiconductor'. *Chemistry of Materials*, 2015, **27**, 5622–5632.

[227] Kaltzoglou, A.; Antoniadou, M.; Kontos, A. G.; Stoumpos, C. C.; Perganti, D.; Siranidi, E.; Raptis, V.; Trohidou, K.; Psycharis, V.; Kanatzidis, M. G. *et al.* 'Optical-vibrational properties of the Cs_2SnX_6 (X = Cl, Br, I) defect derovskites and hole-transport efficiency in dye-sensitized solar cells'. *Journal of Physical Chemistry C*, 2016, **120**, 11777–11785.

[228] Liu, C.; Wang, Y.; Geng, H.; Zhu, T.; Ertekin, E.; Gosztola, D.; Yang, S.; Huang, J.; Yang, B.; Han, K. *et al.* 'Asynchronous photoexcited electronic and structural relaxation in lead-free perovskites'. *Journal of the American Chemical Society*, 2019, **141**, 13074–13080.

[229] Jing, Y.; Liu, Y.; Zhao, J. and Xia, Z. 'Sb^{3+} doping-induced triplet self-trapped excitons emission in lead-free Cs_2SnCl_6 nanocrystals'. *The Journal of Physical Chemistry Letters*, 2019, **10**, 7439–7444.

[230] Luo, R.; Zhang, S.; Zhao, S.; Li, J.; Kang, F.; Yu, K. and Wei, G. 'Ultrasmall blueshift of near-infrared fluorescence in phase-stable Cs_2SnI_6 thin films'. *Physical Review Applied*, 2020, **14**, 014048.

[231] Saidaminov, M. I.; Mohammed, O. F. and Bakr, O. M. 'Low-dimensional-networked metal halide perovskites: The next big thing'. *ACS Energy Letters*, 2017, **2**, 889–896.

[232] Zhou, C.; Lin, H.; Tian, Y.; Yuan, Z.; Clark, R.; Chen, B.; Van De Burgt, L. J.; Wang, J. C.; Zhou, Y.; Hanson, K. *et al.* 'Luminescent zero-dimensional organic metal halide hybrids with near-unity quantum efficiency'. *Chemical Science*, 2018, **9**, 586–593.

[233] Zhang, R.; Mao, X.; Yang, Y.; Yang, S.; Zhao, W.; Wumaier, T.; Wei, D.; Deng, W. and Han, K. 'Air-stable, lead-free zero-dimensional mixed bismuth-antimony perovskite single crystals with ultra-broadband emission'. *Angewandte Chemie International Edition*, 2019, **58**, 2725–2729.

[234] Yin, J.; Maity, P.; De Bastiani, M.; Dursun, I.; Bakr, O. M.; Brédas, J. L. and Mohammed, O. F. 'Molecular behavior of zero-dimensional perovskites'. *Science Advances*, 2017, **3**, e1701793.

[235] Kondo, S; Amaya, K and Saito, T. 'Localized optical absorption in Cs_4PbBr_6'. *J. Phys.: Condens. Matter*, 2002, **14**, 2093–2099.

[236] Yangui, A.; Roccanova, R.; Wu, Y.; Du, M.-H. and Saparov, B. 'Highly efficient broad-band luminescence involving organic and inorganic molecules in a zero-dimensional hybrid lead chloride'. *The Journal of Physical Chemistry C*, 2019, **123**, 22470–22477.

[237] Jun, T.; Sim, K.; Iimura, S.; Sasase, M.; Kamioka, H.; Kim, J. and Hosono, H. 'Lead-free highly efficient blue-emitting $Cs_3Cu_2I_5$ with 0D electronic structure'. *Advanced Materials*, 2018, **30**, 1804547.

[238] Lian, L.; Zheng, M.; Zhang, W.; Yin, L.; Du, X.; Zhang, P.; Zhang, X.; Gao, J.; Zhang, D.; Gao, L. *et al.* 'Efficient and reabsorption-free radioluminescence in $Cs_3Cu_2I_5$ nanocrystals with self-trapped excitons'. *Advanced Science*, 2020, **7**, 2000195.

[239] Morad, V.; Shynkarenko, Y.; Yakunin, S.; Brumberg, A.; Schaller, R. D. and Kovalenko, M. V. 'Disphenoidal zero-dimensional lead, tin, and germanium halides: Highly emissive singlet and triplet self-trapped excitons and X-ray scintillation'. *Journal of the American Chemical Society*, 2019, **141**, 9764–9768.

[240] Zhou, C.; Lin, H.; Neu, J.; Zhou, Y.; Chaaban, M.; Lee, S.; Worku, M.; Chen, B.; Clark, R.; Cheng, W. *et al.* 'Green emitting single-crystalline bulk assembly of metal halide clusters with near-unity photoluminescence quantum efficiency'. *ACS Energy Letters*, 2019, **4**, 1579–1583.

[241] Zhou, C.; Lin, H.; Shi, H.; Tian, Y.; Pak, C.; Shatruk, M.; Zhou, Y.; Djurovich, P.; Du, M.-H. and Ma, B. 'A zero-dimensional organic seesaw-shaped tin bromide with highly efficient strongly Stokes-shifted deep-red emission'. *Angewandte Chemie*, 2018, **130**, 1033–1036.

[242] Zhou, C.; Lin, H.; Worku, M.; Neu, J.; Zhou, Y.; Tian, Y.; Lee, S.; Djurovich, P.; Siegrist, T. and Ma, B. 'Blue emitting single crystalline assembly of metal halide clusters'. *Journal of the American Chemical Society*, 2018, **140**, 13181–13184.

[243] Peng, H.; Yao, S.; Guo, Y.; Zhi, R.; Wang, X.; Ge, F.; Tian, Y.; Wang, J. and Zou, B. 'Highly efficient self-trapped exciton emission of a $(MA)_4Cu_2Br_6$ single crystal'. *Journal of Physical Chemistry Letters*, 2020, **11**, 4703–4710.

[244] Akkerman, Q. A.; Abdelhady, A. L. and Manna, L. 'Zero-dimensional cesium lead halides: History, properties, and challenges'. *Journal of Physical Chemistry Letters*, 2018, **9**, 2326–2337.

[245] Yuan, Z.; Zhou, C.; Tian, Y.; Shu, Y.; Messier, J.; Wang, J. C.; Burgt, L. J. van de; Kountouriotis, K.; Xin, Y.; Holt, E. *et al.* 'One-dimensional organic lead halide perovskites with efficient bluish white-light emission'. *Nature Communications*, 2017, **8**, 14051.

[246] Du, M. H. 'Emission trend of multiple self-trapped excitons in luminescent 1D copper halides'. *ACS Energy Letters*, 2020, 464–469.

[247] Peeters, F. M. and Devreese, J. T. 'Magneto-optical absorption of polarons'. *Physical Review B*, 1986, **34**, 7246–7259.

[248] Yang, S.; Brant, A. T.; Giles, N. C. and Halliburton, L. E. 'Intrinsic small polarons in rutile TiO_2'. *Physical Review B - Condensed Matter and Materials Physics*, 2013, **87**, 125201.

[249] Huber, D. L. 'Contribution of polaron hopping to the electron paramagnetic resonance linewidth in $La_{1-x}Ca_xMnO_3$ and related materials'. *Journal of Magnetism and Magnetic Materials*, 2012, **324**, 2113–2115.

[250] Fox, M. *Optical properties of solids*. Oxford University Press, 2010.

[251] Elliott, R. J. 'Intensity of optical absorption by excitons'. *Physical Review*, 1957, **108**.

[252] Andor. *An introduction to gated intensified cameras (ICCDs)- Oxford Instruments*. https://andor.oxinst.com/learning/view/article/intensified-ccd-cameras.

[253] Richter, J. M.; Abdi-Jalebi, M.; Sadhanala, A.; Tabachnyk, M.; Rivett, J. P.; Pazos-Outón, L. M.; Gödel, K. C.; Price, M.; Deschler, F. and Friend, R. H. 'Enhancing photoluminescence yields in lead halide perovskites by photon recycling and light out-coupling'. *Nature Communications*, 2016, **7**, 13941.

[254] Johnston, D. C. 'Stretched exponential relaxation arising from a continuous sum of exponential decays'. *Physical Review B*, 2006, **74**, 184430.

[255] Beard, M. C.; Turner, G. M. and Schmuttenmaer, C. A. 'Terahertz spectroscopy'. *J. Phys. Chem. B*, 2002, **106**, 7146 –7159.

[256] Rehman, W.; Milot, R. L.; Eperon, G. E.; Wehrenfennig, C.; Boland, J. L.; Snaith, H. J.; Johnston, M. B. and Herz, L. M. 'Charge-carrier dynamics and mobilities in formamidinium lead mixed-halide perovskites'. *Advanced Materials*, 2015, **27**, 7938–7944.

[257] Wu, Q and Zhang, X.-C. 'Free-space electro-optic sampling of terahertz beams'. *Appl. Phys. Lett.*, 1995, **67**, 3523–3525.

[258] Seifert, T.; Jaiswal, S.; Martens, U.; Hannegan, J.; Braun, L.; Maldonado, P.; Freimuth, F.; Kronenberg, A.; Henrizi, J.; Radu, I. *et al.* 'Efficient metallic spintronic emitters of ultrabroadband terahertz radiation'. *Nature Photonics*, 2016, **10**, 483–488.

[259] Hieftje, G. M. 'Signal-to-noise enhancement through instrumental techniques'. *Analytical Chemistry*, 1972, **44**, 69A–78A.

[260] Davies, C. L.; Patel, J. B.; Xia, C. Q.; Herz, L. M. and Johnston, M. B. 'Temperature-dependent refractive index of quartz at terahertz frequencies'. *Journal of Infrared, Millimeter, and Terahertz Waves*, 2018, **39**, 1236–1248.

[261] Ulatowski, A. M.; Herz, L. M. and Johnston, M. B. 'Terahertz conductivity analysis for highly doped thin-film semiconductors'. *Journal of Infrared, Millimeter, and Terahertz Waves*, 2020, **41**, 1431–1449.

[262] La-O-Vorakiat, C.; Cheng, L.; Salim, T.; Marcus, R. A.; Michel-Beyerle, M. E.; Lam, Y. M. and Chia, E. E. 'Phonon features in terahertz photoconductivity spectra due to data analysis artifact: A case study on organometallic halide perovskites'. *Applied Physics Letters*, 2017, **110**, 123901.

[263] Joyce, H. J.; Baig, S. A. and Parkinson, P. 'A review of the electrical properties of semiconductor nanowires: Insights gained from terahertz conductivity spectroscopy'. *Semicond. Sci. Technol*, 2016, **31**, 103003.

[264] Kittel, C. *Introduction to Solid State Physics, 8th edition.* Wiley & Sons, New York, NY, 2004.

[265] Sansom, H. C. 'Copper and Silver Bismuth Iodide Semiconductors as Potential Solar Cell Absorber Materials'. University of Liverpool, 2018. https://livrepository.liverpool.ac.uk/3028034.

[266] Speakman, S. A. *Profile Fitting for Analysis of XRPD Data using HighScore Plus v3.* MIT. http://prism.mit.edu/xray.

[267] Chemistry (UCL), D. of. *Whole Pattern Fitting: I. Pawley Method.* http://pd.chem.ucl.ac.uk/pdnn/solve1/pawley.htm.

[268] Rietveld, H. 'A profile refinement method for nuclear and magnetic structures'. *J. Appl. Cryst.*, 2 1969, **2**, 65–71.

[269] Rietveld, H. 'Line profiles of neutron powder-diffraction peaks for structure refinement'. *Acta. Cryst.*, 1 1967, **22**, 151–152.

[270] Longo, G.; Mahesh, S.; Buizza, L. R. V.; Wright, A. D.; Ramadan, A. J.; Abdi-Jalebi, M.; Nayak, P. K.; Herz, L. M. and Snaith, H. J. 'Understanding the performance-limiting factors of $Cs_2AgBiBr_6$ double-perovskite solar cells'. *ACS Energy Letters*, 2020, **5**, 2200–2207.

[271] Slotcavage, D. J.; Karunadasa, H. I. and Mcgehee, M. D. 'Light-induced phase segregation in halide-perovskite absorbers'. *ACS Energy Letters*, 2016, **1**, 1199.

[272] Eperon, G. E.; Stranks, S. D.; Menelaou, C.; Johnston, M. B.; Herz, L. M. and Snaith, H. J. 'Formamidinium lead trihalide: a broadly tunable perovskite for efficient planar heterojunction solar cells'. *Energy & Environmental Science*, 2014, **7**, 982.

[273] Yi, C.; Luo, J.; Meloni, S.; Boziki, A.; Ashari-Astani, N.; Grätzel, C.; Zakeeruddin, S. M.; Röthlisberger, U. and Grätzel, M. 'Entropic stabilization of mixed A-cation ABX_3 metal halide perovskites for high performance perovskite solar cells'. *Energy & Environmental Science*, 2016, **9**, 656–662.

[274] Mitzi, D. B.; Chondroudis, K. and Kagan, C. R. 'Organic-inorganic electronics'. *IBM Journal of Research and Development*, 2001, **45**, 29–45.

[275] Ishihara, T.; Takahashi, J. and Goto, T. 'Optical properties due to electronic transitions in two-dimensional semiconductors $(C_nH_{2n+1}NH_3)_2PbI_4$'. *Physical Review B*, 1990, **42**, 11099–11107.

[276] Yao, K.; Wang, X.; Xu, Y.-x.; Li, F. and Zhou, L. 'Multilayered perovskite materials based on polymeric-ammonium cations for stable large-area solar cell'. *Chemistry of Materials*, 2016, **28**, 3131–3138.

[277] Stoumpos, C. C.; Cao, D. H.; Clark, D. J.; Young, J.; Rondinelli, J. M.; Jang, J. I.; Hupp, J. T. and Kanatzidis, M. G. 'Ruddlesden-Popper hybrid lead iodide perovskite 2D homologous semiconductors'.

[278] Grancini, G; Roldán-Carmona, C; Zimmermann, I; Mosconi, E; Lee, X; Martineau, D; Narbey, S; Oswald, F; De Angelis, F; Graetzel, M *et al.* 'One-Year stable perovskite solar cells by 2D/3D interface engineering.' *Nature Communications*, 2017, **8**, 15684.

[279] Hu, Y.; Schlipf, J.; Wussler, M.; Petrus, M. L.; Jaegermann, W.; Bein, T.; Müller-Buschbaum, P. and Docampo, P. 'Hybrid perovskite/perovskite heterojunction solar cells'. *ACS Nano*, 2016, **10**, 5999–6007.

[280] Yuan, M.; Quan, L. N.; Comin, R.; Walters, G.; Sabatini, R.; Voznyy, O.; Hoogland, S.; Zhao, Y.; Beauregard, E. M.; Kanjanaboos, P. *et al.* 'Perovskite energy funnels for efficient light-emitting diodes'. *Nature Nanotechnology*, 2016, **11**, 872–877.

[281] Li, P.; Zhang, Y.; Liang, C.; Xing, G.; Liu, X.; Li, F.; Liu, X.; Hu, X.; Shao, G. and Song, Y. 'Phase pure 2D perovskite for high-performance 2D-3D heterostructured perovskite solar cells'. *Advanced Materials*, 2018, **0**, 1805323.

[282] Stewart, J. E. 'Vibrational spectra of primary and secondary aliphatic amines'. *The Journal of Chemical Physics*, 1959.

[283] Layton, E. M.; Kross, R. D. and Fassel, V. A. 'Correlation of bond length with stretching frequency for carbon-oxygen and carbon-nitrogen systems'. *The Journal of Chemical Physics*, 1956, **25**, 135–138.

[284] Wang, Y. and Poirier, R. A. 'Factors that influence the C=N stretching frequency in imines'. *Journal of Physical Chemistry A*, 1997.

[285] Kucharska, E.; Hanuza, J.; Ciupa, A.; Maczka, M. and Macalik, L. 'Vibrational properties and DFT calculations of formamidine-templated Co and Fe formates'. *Vibrational Spectroscopy*, 2014, **75**, 45–50.

[286] Coates, J. *Interpretation of infrared spectra, a practical approach.* Wiley, 2006.

[287] Ramis, G. and Busca, G. 'FTIR spectra of adsorbed n-butylamine'. *Journal of Molecular Structure*, 1989, **193**, 93–100.

[288] Frost, J. M.; Butler, K. T.; Brivio, F.; Hendon, C. H.; Schilfgaarde, M. van and Walsh, A. 'Atomistic origins of high-performance in hybrid halide perovskite solar cells'. *Nano Letters*, 2014, **14**, 2584–2590.

[289] Even, J.; Pedesseau, L.; Dupertuis, M. A.; Jancu, J. M. and Katan, C. 'Electronic model for self-assembled hybrid organic/perovskite semiconductors: Reverse band edge electronic states ordering and spin-orbit coupling'. *Physical Review B - Condensed Matter and Materials Physics*, 2012, **86**, 205301.

[290] Even, J.; Pedesseau, L.; Katan, C.; Kepenekian, M.; Lauret, J. S.; Sapori, D. and Deleporte, E. 'Solid-state physics perspective on hybrid perovskite semiconductors'. *Journal of Physical Chemistry C*, 2015, **119**, 10161.

[291] Matsuishi, K.; Ishihara, T.; Onari, S.; Chang, Y. H. and Park, C. H. 'Optical properties and structural phase transitions of lead-halide based inorganic-organic 3D and 2D perovskite semiconductors under high pressure'. *physica status solidi (b)*, 2004, **241**, 3328–3333.

[292] Nandi, P.; Giri, C.; Swain, D.; Manju, U.; Mahanti, S. D. and Topwal, D. 'Temperature dependent photoinduced reversible phase separation in mixed-halide perovskite'. *ACS Applied Energy Materials*, 2018, **1**, 3807–3814.

[293] Yu, C.; Chen, Z.; J. Wang, J.; Pfenninger, W.; Vockic, N.; Kenney, J. T. and Shum, K. 'Temperature dependence of the band gap of perovskite semiconductor compound $CsSnI_3$'. *Journal of Applied Physics*, 2011, **110**, 063526.

[294] Saidi, W. A.; Poncé, S. and Monserrat, B. 'Temperature dependence of the energy levels of methylammonium lead iodide perovskite from first-principles'. *The Journal of Physical Chemistry Letters*, 2016, **7**, 5247–5252.

[295] Saidi, W. A. and Kachmar, A. 'Effects of electron–phonon coupling on electronic properties of methylammonium lead iodide perovskites'. *The Journal of Physical Chemistry Letters*, 2018, **9**, 7090–7097.

[296] Huang, L. and Lambrecht, W. R. L. 'Electronic band structure, phonons, and exciton binding energies of halide perovskites $CsSnCl_3$, $CsSnBr_3$, and $CsSnI_3$'. *Physical Review B*, 2013, **88**, 165203.

[297] Noh, J. H.; Im, S. H.; Heo, J. H.; Mandal, T. N. and Seok, S. I. 'Chemical management for colorful, efficient, and stable inorganic-organic hybrid nanostructured solar cells'. *Nano Letters*, 2013, **13**, 1764–1769.

[298] Hu, M.; Bi, C.; Yuan, Y.; Bai, Y. and Huang, J. 'Stabilized wide bandgap $MAPbBr_xI_{3-x}$ perovskite by enhanced grain size and improved crystallinity'. *Advanced Science*, 2016, **3**, 1500301.

[299] Yun, J. S.; Seidel, J.; Kim, J.; Soufiani, A. M.; Huang, S.; Lau, J.; Jeon, N. J.; Seok, S. I.; Green, M. A. and Ho-Baillie, A. 'Critical role of grain boundaries for ion migration in formamidinium and methylammonium lead halide perovskite solar cells'. *Advanced Energy Materials*, 2016, **6**, 1600330.

[300] Shao, Y.; Fang, Y.; Li, T.; Wang, Q.; Dong, Q.; Deng, Y.; Yuan, Y.; Wei, H.; Wang, M.; Gruverman, A. *et al.* 'Grain boundary dominated ion migration in polycrystalline organic-inorganic halide perovskite films'. *Energy & Environmental Science*, 2016, **9**, 1752–1759.

[301] Parrott, E. S.; Milot, R. L.; Stergiopoulos, T.; Snaith, H. J.; Johnston, M. B. and Herz, L. M. 'Effect of structural phase transition on charge-carrier lifetimes and defects in $CH_3NH_3SnI_3$ perovskite'. *J. Phys. Chem. Lett.*, 2016, **7**, 1321–1326.

[302] Noel, N. K.; Abate, A.; Stranks, S. D.; Parrott, E. S.; Burlakov, V. M.; Goriely, A. and Snaith, H. J. 'Enhanced photoluminescence and solar cell performance *via* Lewis base passivation of organic-inorganic lead halide perovskites'. *ACS Nano*, 2014, **8**, 9815–9821.

[303] Crothers, T. W.; Milot, R. L.; Patel, J. B.; Parrott, E. S.; Schlipf, J.; Müller-Buschbaum, P.; Johnston, M. B. and Herz, L. M. 'Photon reabsorption masks intrinsic bimolecular charge-carrier recombination in $CH_3NH_3PbI_3$ perovskite'. *Nano Letters*, 2017, **17**, 5782–5789.

[304] Gélvez-Rueda, M. C.; Hutter, E. M.; Cao, D. H.; Renaud, N.; Stoumpos, C. C.; Hupp, J. T.; Savenije, T. J.; Kanatzidis, M. G. and Grozema, F. C. 'Interconversion between free charges and bound excitons in 2D hybrid lead halide perovskites'. *The Journal of Physical Chemistry C*, 2017, **121**, 26566–26574.

[305] Schade, L.; Wright, A. D.; Johnson, R. D.; Dollmann, M.; Wenger, B.; Nayak, P. K.; Prabhakaran, D.; Herz, L. M.; Nicholas, R.; Snaith, H. J. *et al.* 'Structural and optical properties of $Cs_2AgBiBr_6$ double perovskite'. *ACS Energy Letters*, 2019, **1**, 299–305.

[306] Bartesaghi, D.; Slavney, A. H.; Gélvez-Rueda, M. C.; Connor, B. A.; Grozema, F. C.; Karunadasa, H. I. and Savenije, T. J. 'Charge carrier dynamics in $Cs_2AgBiBr_6$ double perovskite'. *The Journal of Physical Chemistry C*, 2018, **122**, 4809–4816.

[307] Bo, W.; Weihua, N.; Qiang, X.; Manukumara, M.; Minjun, F.; Senyun, Y.; Jianhui, F.; Stener, L.; Tingting, Y.; Feng, W. *et al.* 'Strong self-trapping by deformation potential limits photovoltaic performance in bismuth double perovskite'. *Science Advances*, 2021, **7**, eabd3160.

[308] Hu, Z.; Wang, Z.; Kapil, G.; Ma, T.; Iikubo, S.; Minemoto, T.; Yoshino, K.; Toyoda, T.; Shen, Q. and Hayase, S. 'Solution-processed air-stable copper bismuth iodide for photovoltaics'. *ChemSusChem*, 2018, **11**, 2930–2935.

[309] Ke, W.; Stoumpos, C. C.; Zhu, M.; Mao, L.; Spanopoulos, I.; Liu, J.; Kontsevoi, O. Y.; Chen, M.; Sarma, D.; Zhang, Y. *et al.* 'Enhanced photovoltaic performance and stability with a new type of hollow 3D perovskite {en}$FASnI_3$'. *Science Advances*, 2017, **3**, e1701293.

[310] Emin, D. 'Lattice relaxation and small-polaron hopping motion'. *Physical Review B*, 1971, **4**, 3639–3651.

[311] Fourcroy, P. H.; Carré, D.; Thévet, F. and Rivet, J. 'Structure du tétraiodure de cuivre(I) et de bismuth(III), CuBiI4'. *Acta Crystallographica Section C Crystal Structure Communications*, 1991, **47**, 2023–2025.

[312] Varshni, Y. P. 'Temperature dependence of the energy gap in semiconductors'. *Physica*, 1967, **34**, 149–154.

[313] D'Innocenzo, V.; Grancini, G.; Alcocer, M. J. P.; Kandada, A. R. S.; Stranks, S. D.; Lee, M. M.; Lanzani, G.; Snaith, H. J. and Petrozza, A. 'Excitons versus free charges in organo-lead tri-halide perovskites'. *Nature Communications*, 2014, **5**, 3586.

[314] Pelant, I. and Valenta, J. *Luminescence spectroscopy of semiconductors*. Oxford University Press, 2012.

[315] Hong, X.; Ishihara, T. and Nurmikko, A. V. 'Dielectric confinement effect on excitons in PbI_4-based layered semiconductors'. *Physical Review B*, 1992, **45**, 6961–6964.

[316] Biega, R. I.; Filip, M. R.; Leppert, L. and Neaton, J. B. 'Chemically localized resonant excitons in silver-pnictogen halide double perovskites'. *Journal of Physical Chemistry Letters*, 2021, **12**, 2057–2063.

[317] Locardi, F.; Sartori, E.; Buha, J.; Zito, J.; Prato, M.; Pinchetti, V.; Zaffalon, M. L.; Ferretti, M.; Brovelli, S.; Infante, I. *et al.* 'Emissive Bi-doped double perovskite $Cs_2Ag_{1-x}Na_xInCl_6$ nanocrystals'. *ACS Energy Letters*, 2019, **4**, 1976–1982.

[318] Brandt, R. E.; Kurchin, R. C.; Hoye, R. L. Z.; Poindexter, J. R.; Wilson, M. W. B.; Sulekar, S.; Lenahan, F.; Yen, P. X. T.; Stevanović, V.; Nino, J. C. *et al.* 'Investigation of bismuth triiodide (BiI_3) for photovoltaic applications'. *The Journal of Physical Chemistry Letters*, 2015, **6**, 4297–4302.

[319] Williamson, B. W.; Eickemeyer, F. T. and Hillhouse, H. W. 'Solution-processed BiI_3 films with 1.1 eV quasi-Fermi level splitting: the role of water, temperature, and solvent during processing'. *ACS Omega*, 2018, **3**, 12713–12721.

[320] Hamdeh, U. H.; Nelson, R. D.; Ryan, B. J.; Bhattacharjee, U.; Petrich, J. W. and Panthani, M. G. 'Solution-processed BiI_3 thin films for photovoltaic applications: improved carrier collection via solvent annealing'. *Chemistry of Materials*, 2016, **28**, 6567–6574.

[321] Fischbach, J. U.; Fröhlich, D. and Kabler, M. N. 'Recombination luminescence lifetimes and the self-trapped excition in alkali halides'. *Journal of Luminescence*, 1973, **6**, 29–43.

[322] Hirai, M.; Suzuki, Y.; Hattori, H.; Ehara, T. and Kitamura, E. 'Picosecond laser photolysis on photo-induced defect formation process in KI crystal'. *Journal of the Physical Society of Japan*, 1987, **56**, 2948–2963.

[323] Tokizaki, T.; Makimura, T.; Akiyama, H.; Nakamura, A.; Tanimura, K. and Itoh, N. 'Femtosecond cascade-excitation spectroscopy for nonradiative deexcitation and lattice relaxation of the self-trapped exciton in NaCl'. *Physical Review Letters*, 1991, **67**, 2701–2704.

[324] Lietard, A.; Piani, G.; Briant, M.; Gaveau, M.-A.; Faisan, S.; Mazet, V.; Soep, B.; Mestdagh, J.-M. and Poisson, L. 'Self-trapping relaxation decay investigated by time-resolved photoelectron spectroscopy'. *Physical Chemistry Chemical Physics*, 2018, **20**, 11206–11214.

[325] Emin, D.; Seager, C. H. and Quinn, R. K. 'Small-polaron hopping motion in some chalcogenide glasses'. *Physical Review Letters*, 1972, **28**, 813–816.

[326] Onoda-Yamamuro, N.; Matsuo, T. and Suga, H. 'Dielectric study of $CH_3NH_3PbX_3$ (X = Cl, Br, I)'. *Journal of Physics and Chemistry of Solids*, 1992, **53**, 935–939.

[327] Savenije, T. J.; Ponseca, C. S.; Kunneman, L.; Abdellah, M.; Zheng, K.; Tian, Y.; Zhu, Q.; Canton, S. E.; Scheblykin, I. G.; Pullerits, T. *et al.* 'Thermally activated exciton dissociation and recombination control the carrier dynamics in organometal halide perovskite'. *The Journal of Physical Chemistry Letters*, 2014, **5**, 2189–2194.

[328] Iguchi, E.; Ueda, K. and Jung, W. H. 'Conduction in $LaCoO_3$ by small-polaron hopping below room temperature'. *Physical Review B*, 1996, **54**, 17431–17437.

[329] Hulea, I. N.; Fratini, S.; Xie, H.; Mulder, C. L.; Iossad, N. N.; Rastelli, G.; Ciuchi, S. and Morpurgo, A. F. 'Tunable Fröhlich polarons in organic single-crystal transistors'. *Nature Materials*, 2006, **5**, 982–986.

[330] Fishchuk, I. I.; Kadashchuk, A.; Hoffmann, S. T.; Athanasopoulos, S.; Genoe, J.; Bässler, H. and Köhler, A. 'Unified description for hopping transport in organic semiconductors including both energetic disorder and polaronic contributions'. *Physical Review B*, 2013, **88**, 125202.

[331] Coropceanu, V.; Cornil, J.; Silva Filho, D. A. da; Olivier, Y.; Silbey, R. and Brédas, J.-L. 'Charge transport in organic semiconductors'. *Chemical Reviews*, 2007, **107**, 926–952.

[332] Slavney, A. H.; Connor, B. A.; Leppert, L. and Karunadasa, H. I. 'A pencil-and-paper method for elucidating halide double perovskite band structures'. *Chemical Science*, 2019, **10**, 11041–11053.

[333] Canali, C.; Jacoboni, C.; Nava, F.; Ottaviani, G. and Alberigi-Quaranta, A. 'Electron drift velocity in silicon'. *Physical Review B*, 1975, **12**, 2265.

[334] Norton, P.; Braggins, T. and Levinstein, H. 'Impurity and lattice scattering parameters as determined from Hall and mobility analysis in n-type silicon'. *Physical Review B*, 1973, **8**, 5632.

[335] Kao, Y. C. and Eknoyan, O. 'Electron and hole carrier mobilities for liquid phase epitaxially grown GaP in the temperature range 200-550 K'. *Journal of Applied Physics*, 1983, **54**, 2468–2471.

[336] Casey, H. C.; Ermanis, F. and Wolfstirn, K. B. 'Variation of electrical properties with Zn concentration in GaP'. *Journal of Applied Physics*, 1969, **40**, 2945–2958.

[337] Burgos-Caminal, A.; Moreno-Naranjo, J. M.; Willauer, A. R.; Paraecattil, A. A.; Ajdarzadeh, A. and Moser, J. E. 'Hot carrier mobility dynamics unravel competing subpicosecond processes in lead halide perovskites'. *Journal of Physical Chemistry C*, 2021, **125**, 98–106.

[338] Dey, A.; Richter, A. F.; Debnath, T.; Huang, H.; Polavarapu, L. and Feldmann, J. 'Transfer of direct to indirect bound excitons by electron intervalley scattering in $Cs_2AgBiBr_6$ double perovskite nanocrystals'. *ACS Nano*, 2020, **14**, 5855–5861.

[339] Papalazarou, E.; Faure, J.; Mauchain, J.; Marsi, M.; Taleb-Ibrahimi, A.; Reshetnyak, I.; Roekeghem, A. V.; Timrov, I.; Vast, N.; Arnaud, B. *et al.* 'Coherent phonon coupling to individual Bloch states in photoexcited bismuth'. *Physical Review Letters*, 2012, **108**, 256808.

[340] Hase, M.; Mizoguchi, K.; Harima, H.; Nakashima, S. ichi and Sakai, K. 'Dynamics of coherent phonons in bismuth generated by ultrashort laser pulses'. *Physical Review B - Condensed Matter and Materials Physics*, 1998, **58**, 5448–5452.

[341] Jia, L.; Ma, W. and Zhang, X. 'Ultrafast carrier dynamics in polycrystalline bismuth telluride nanofilm'. *Applied Physics Letters*, 2014, **104**, 241911.

[342] 'Ultrafast dynamics of photoexcited coherent phonon in Bi_2Te_3 thin films'. *Applied Physics Letters*, 2008, **92**, 011108.

[343] Scholz, M.; Oum, K. and Lenzer, T. 'Pronounced exciton and coherent phonon dynamics in BiI_3'. *Physical Chemistry Chemical Physics*, 2018, **20**, 10677–10685.

[344] Scholz, M.; Flender, O.; Oum, K. and Lenzer, T. 'Pronounced exciton dynamics in the vacancy-ordered bismuth halide perovskite $(CH_3NH_3)_3Bi_2I_9$ observed by ultrafast UV-vis-NIR transient absorption spectroscopy'. *Journal of Physical Chemistry C*, 2017, **121**, 12110–12116.

[345] Scholz, M.; Morgenroth, M.; Oum, K. and Lenzer, T. 'Exciton and coherent phonon dynamics in the metal-deficient defect perovskite $(CH_3NH_3)_3Sb_2I_9$'. *Journal of Physical Chemistry C*, 2018, **122**, 5854–5863.

[346] Jana, M. K.; Janke, S. M.; Dirkes, D. J.; Dovletgeldi, S.; Liu, C.; Qin, X.; Gundogdu, K.; You, W.; Blum, V. and Mitzi, D. B. 'Direct-bandgap 2D silver-bismuth iodide double perovskite: The structure-directing influence of an oligothiophene spacer cation'. *Journal of the American Chemical Society*, 2019, **141**, 7955–7964.

[347] Wang, L.; Bao, Y.; Wang, S.; Wang, F.; Xie, C.; Butler, K. T. and Fan, X. 'Revealing the potential crystal structures of earth-abundant nontoxic photovoltaic $CuBiI_4$'. *Crystal Growth & Design*, 2021, **21**, 2850–2855.

[348] Patnaik, J. R. and Sunandana, C. S. 'Studies on gamma silver iodide'. *Journal of Physics and Chemistry of Solids*, 1998, **59**, 1059–1069.

[349] Kumar, P. S.; Dayal, P. B. and Sunandana, C. S. 'On the formation mechanism of γ-AgI thin films'. *Thin Solid Films*, 1999, **357**, 111–118.

[350] Bulakhe, R. N.; Shinde, N. M.; Thorat, R. D.; Nikam, S. S. and Lokhande, C. D. 'Deposition of copper iodide thin films by chemical bath deposition (CBD) and successive ionic layer adsorption and reaction (SILAR) methods'. *Current Applied Physics*, 2013, **13**, 1661–1667.

[351] Li, T.; Zhao, X.; Yang, D.; Du, M. H. and Zhang, L. 'Intrinsic defect properties in halide double perovskites for optoelectronic applications'. *Physical Review Applied*, 2018, **10**, 041001.

[352] Kirchartz, T.; Márquez, J. A.; Stolterfoht, M. and Unold, T. 'Photoluminescence-based characterization of halide perovskites for photovoltaics'. *Advanced Energy Materials*, 2020, **10**, 1904134.

[353] Lakhwani, G.; Rao, A. and Friend, R. H. 'Bimolecular recombination in organic photovoltaics'. *Annual Review of Physical Chemistry*, 2014, **65**, 557–581.

[354] Groves, C. and Greenham, N. C. 'Bimolecular recombination in polymer electronic devices'. *Physical Review B - Condensed Matter and Materials Physics*, 2008, **78**, 155205.

[355] Xia, C. Q.; Peng, J.; Poncé, S.; Patel, J. B.; Wright, A. D.; Crothers, T. W.; Rothmann, M. U.; Borchert, J.; Milot, R. L.; Kraus, H. *et al.* 'Limits to electrical mobility in lead-halide perovskite semiconductors'. *J. Phys. Chem. Lett.*, 2021, **12**, 3607–3617.

[356] Savill, K. J.; Klug, M. T.; Milot, R. L.; Snaith, H. J. and Herz, L. M. 'Charge-carrier cooling and polarization memory loss in formamidinium tin triiodide'. *The Journal of Physical Chemistry Letters*, 2019, 6038–6047.

[357] Yang, Y.; Ostrowski, D. P.; France, R. M.; Zhu, K.; Lagemaat, J. V. D.; Luther, J. M. and Beard, M. C. 'Observation of a hot-phonon bottleneck in lead-iodide perovskites'. *Nature Photonics*, 2016, **10**, 53–59.

[358] Price, M. B.; Butkus, J.; Jellicoe, T. C.; Sadhanala, A.; Briane, A.; Halpert, J. E.; Broch, K.; Hodgkiss, J. M.; Friend, R. H. and Deschler, F. 'Hot-carrier cooling and photoinduced refractive index changes in organic-inorganic lead halide perovskites'. *Nature Communications*, 2015, **6**, 1–8.

[359] Hutter, E. M.; Gélvez-Rueda, M. C.; Osherov, A.; Bulović, V.; Grozema, F. C.; Stranks, S. D. and Savenije, T. J. 'Direct–indirect character of the bandgap in methylammonium lead iodide perovskite'. *Nature Materials*, 2017, **16**, 115–120.

[360] Dakshinamurthy, A. C. and Sudakar, C. 'Bandgap engineering and sublattice distortion driven bandgap bowing in $Cs_2Ag_{1-x}Na_xBiCl_6$ double perovskites'. *Applied Physics Letters*, 2021, **118**, 131902.

[361] Slavney, A. H.; Leppert, L.; Bartesaghi, D.; Gold-Parker, A.; Toney, M. F.; Savenije, T. J.; Neaton, J. B. and Karunadasa, H. I. 'Defect-induced band-edge reconstruction of a bismuth-halide double perovskite for visible-light absorption'. *Journal of the American Chemical Society*, 2017, **139**, 5015–5018.

[362] Du, K. zhao; Meng, W.; Wang, X.; Yan, Y. and Mitzi, D. B. 'Bandgap engineering of lead-free double perovskite $Cs_2AgBiBr_6$ through trivalent metal alloying'. *Angewandte Chemie International Edition*, 2017, **56**, 8158–8162.

[363] Schade, L.; Mahesh, S.; Volonakis, G.; Zacharias, M.; Wenger, B.; Schmidt, F.; Kesava, S. V.; Prabhakaran, D.; Abdi-Jalebi, M.; Lenz, M. *et al.* 'Crystallographic, optical, and electronic properties of the $Cs_2AgBi_{1-x}In_xBr_6$ double perovskite: Understanding the fundamental photovoltaic efficiency challenges'. *ACS Energy Letters*, 2021, **6**, 1073–1081.

[364] Ibn-Mohammed, T.; Koh, S. C.; Reaney, I. M.; Acquaye, A.; Schileo, G.; Mustapha, K. B. and Greenough, R. 'Perovskite solar cells: An integrated hybrid lifecycle assessment and review in comparison with other photovoltaic technologies'. *Renewable and Sustainable Energy Reviews*, 2017, **80**, 1321–1344.

[365] Leccisi, E. and Fthenakis, V. 'Life-cycle environmental impacts of single-junction and tandem perovskite PVs: A critical review and future perspectives'. *Progress in Energy*, 2020, **2**, 032002.